UNIVERSITY *of the*
WESTERN CAPE

Magmatic-petrogenetic & structural relationships of the Peninsula Granite of the Cape Granite Suite (CGS) with the Malmesbury Group, Sea Point contact, Saldania Belt, South Africa

by

Musa Mhlanga

Thesis submitted in fulfilment of the requirements for the degree of Master of Science in the Faculty of Natural Sciences at the University of the Western Cape

Supervisor: Dr. Russell Bailie

Co-supervisor: Dr. Juergen Reinhardt

Department of Earth Sciences
November, 2020

Declaration

I, Musa Mhlanga, hereby declare that this Masters (MSc.) thesis, submitted to the Faculty of Natural Sciences at the University of the Western Cape, is my work and has not been previously submitted either entirely or partly to any other university or institution of higher education for obtaining a qualification.

Signature: ______________________

Musa Mhlanga

Date: 27/10/2020 Place: Nelspruit, Mpumalanga, South Africa

Abstract

The Sea Point contact, Cape Town, South Africa, exposes the contact between the Neoproterozoic Malmesbury Group metasedimentary rocks of the Pan-African Saldania belt and the intrusive S-type Peninsula Granite of the Neoproterozoic-Paleozoic Cape Granite Suite (CGS). The exposure outcrops over an area of approximately 170 m × 60 m with the northern end of the exposure being characterized by the country rock–microgranite intrusive contact. Heading further south, the outcrop transitions to the main contact zone, which is a predominantly gradational zone marked by sheets of compositionally variable granitic injections (collectively referred to as hybrid granite phases) concordant to the country rock structure, before reaching the main pluton area comprising the voluminous coarse-grained porphyritic granite. Using a combined study incorporating field, structural, geochemical, isotopic and U-Pb geochronological data, the intrusive contact is investigated to determine the construction history of the pluton and delineate possible emplacement mechanisms.

The granitic phases, which vary from fine-grained leucocratic, medium-grained porphyritic to coarse-grained porphyritic, are peraluminous, magnesian to ferroan, and alkali-calcic. Based on the linear trends between the whole-rock major and trace element content of the granites vs. maficity (molar Fe + Mg), their initial Sr ratios and εNd(t) values, the granites of the study area are consistent with the currently proposed petrogenetic model for the CGS (e.g. Stevens et al., 2007; Villaros et al., 2009a; Harris & Vogeli, 2010); i.e., they are crustally derived and their chemical variability is controlled primarily by peritectic assemblage entrainment.

The fractional crystallization of K-feldspar is identified as the primary mechanism for the local geochemical variability of the granites. The fractionation of K-feldspar as a mechanism of variability was evaluated using binary log-log diagrams of Ba, Sr and Eu and is interpreted to have taken place at levels close to the emplacement site after source entrainment processes. Although there is outcrop evidence, particularly in the main contact zone, to suggest that local assimilation and filter pressing took place, this was not reflected by the whole-rock and isotope geochemistry of the granites. This suggests that these processes are very localized and will need further rigorous testing to ascertain the extent to which they caused variability. Outcrop evidence for assimilation includes gradational country rock-granite contacts and the ductile behaviour of the country rock, whereas the occurrence of K-feldspar megacrysts

embedded in the country rock at the main contact zone suggests melt accumulation and escape consistent with the filter pressing mechanism. In the case of the latter, the melt fraction of the granite was easily mobilized and driven out compared to the crystal fraction (K-feldspars) during the emplacement of the granites.

Field relationships and the structural interpretation of the Malmesbury Group country rocks and the granites reveal that: (1) the various granites are late syn-tectonic and (2) were emplaced as incrementally assembled, repeated pulses of inclined granitic sheets more or less normal (i.e. at high angles) to the regional NE-SW shortening (D_1) of the Malmesbury fore-arc during the Saldanian orogeny. Given the lack of a controlling shear zone in facilitating granite emplacement in the study area, the pre-existing planar anisotropies (bedding planes and foliations) in the country rock provided preferential pathways for magma emplacement and propagation during deformation. This implies that the tensile strength normal and parallel to the bedding and foliation anisotropy of the country rock was larger than the regional differential stress ($\sigma_1 - \sigma_3$, with $\sigma_1 \geq \sigma_2 \geq \sigma_3$), allowing for magma emplacement relative to shortening. Sheet propagation is interpreted to have occurred through the balance of the following conditions: (1) density contrasts between host rocks and magmas, (2) the pressure differential along the subvertical fractures/sheets, and (3) the melt pressure equalling the lithostatic pressure to keep the magma pathways open and being sufficiently high such that it exceeds the sum of σ_1 and the tensile strength of the rock parallel to σ_1.

The crystallization ages of the dated granite samples are identical within error and vary between 538.7 ± 3.6 Ma and 542.7 ± 2.9 Ma. They, therefore, cannot prove which granite phase intruded first and which one proceeded and so forth. Field relationships, however, suggests that the microgranites were first to intrude given their fine-grained nature and the localized chilled contacts they show with the country rock. The various coarser-grained and porphyritic phases were next to intrude, with their coarse grain-sizes and lack of chilled margins with the country rock suggesting that the time interval between their successive emplacements was not too long; this prevented the country rock from completely cooling down between each magma batch. Magma stoping and the ductile flow of the host material (owing to highly viscous magma flow) to accommodate granite emplacement are interpreted to be secondary emplacement processes.

Acknowledgements

A word of thanks and gratitude is extended to the following people, societies, councils and institutions:

- The Heritage Society of the Western Cape and the Heritage Committee of the Geological Society of South Africa for giving the Department of Earth Sciences, University of the Western Cape (UWC), special permission to sample the Sea Point contact outcrop.
- The Council for Geoscience for funding my accommodation and living expenses as well as some of the running costs incurred for certain analyses related to this thesis.
- My principal supervisor, Dr. Russell Bailie, for his patience, understanding, continuous support and insights on numerous topics spanning igneous petrology, igneous geochemistry, geochronology, structural geology and igneous-related emplacement processes. He is also thanked for providing critical feedback and revisions for all the thesis chapter drafts submitted. I have learned a lot under his supervision.
- My co-supervisor, Dr. Juergen Reinhardt, for providing his insights regarding the structural geology and metamorphism aspects of the thesis. His explanations, as well as the clarifications, edits and ideas he provided, are highly appreciated.
- My family, in particular, my mother Elisa Mhlanga, for their thoughts, prayers, words of encouragement and asking for constant updates with regards to the status of my thesis.
- The Central Analytical Facilities, Stellenbosch University, staff members: (i) Dr. Laura Bracciali for performing the geochronology analysis. Before the geochronology analysis was conducted, Mareli Grobbelaar is thanked for her assistance with sample preparation & training and Madeline Frazenburg is thanked for helping with SEM CL imaging. (ii) Dr. Cynthia Sanchez-Garrido, Mareli Grobbelaar and Riana Rossouw for performing the major- & trace-element analyses.
- Dr. Petrus le Roux, of the Department of Geological Sciences, University of Cape Town, for performing the isotope analyses.
- Richard Harrison, Janine Botha and Brett Burgell of the Department of Earth Sciences at UWC for their assistance in the preparation of thin sections and sample preparation for geochemistry and geochronology analyses.
- My friends, and fellow MSc. candidates, Aidan Leetz, Carmenlite van Wyk and Sharmoney Wilson. Aidan and Carmenlite are thanked for helping me with field mapping and Sharmoney is thanked for assisting with geochemistry- and plot editing-software.
- All my friends whom I did not acknowledge individually. Know that your well-wishes and the belief you had in me spurred me on to complete the thesis. You are all greatly appreciated.

CONTENTS PAGE

1 **Introduction** ... 1

2 **Geological setting** ... 4

2.1 Saldania belt ... 4

2.2 The western Saldania belt ... 4

2.2.1 Swartland complex (lower domain) ... 8

2.2.2 The Malmesbury Group (upper domain) ... 9

2.2.3 The Cape Granite Suite ... 11

3 **Methodology** ... 13

3.1 Sampling ... 13

3.2 Analytical procedures ... 13

3.2.1 Whole-rock major- and trace element-geochemistry analyses ... 13

3.2.2 Rb-Sr and Sm-Nd isotopic analyses ... 15

3.2.3 U-Pb zircon geochronology ... 16

3.3 Mapping and geochemistry software ... 17

4 **Lithological descriptions** ... 18

4.1 Introduction ... 18

4.2 Malmesbury Group ... 20

4.2.1 Interlayered metasiltstone and metamudstone outcrops ... 20

4.2.2 Metamudstones ... 22

4.3 Main S-type coarse-grained porphyritic granite ... 25

4.3.1 Inclusion trails and growth zone textures of feldspar megacrysts (both K-feldspar and plagioclase) ... 30

4.3.2 Enclaves ... 33

4.3.3 Aplites ... 35

4.3.4 Magmatic structures ... 36

4.4 S-type microgranites (fine-grained granite) ... 37

4.5 Lit-par-lit zone ... 39

4.5.1 Petrographic descriptions of the hybrid granite phases ... 39

4.5.2 Field descriptions of the hybrid granites ... 44

4.5.3 Features of the country rock in the lit-par-lit zone ... 50

5 **Structural geology** ... 57

5.1 Introduction ... 57

5.2 Structure of the country rock ... 57

5.2.1 Bedding S_0 ... 59

5.2.2 S_1 foliation 60
5.2.3 Crenulation cleavage S_2 64
5.2.4 Relationships between cordierite growth and deformation 66
5.2.5 Folding 69
5.3 Shear sense indicators in the lit-par-lit zone 79
5.3.1 Grain-tail complexes: K-feldspars and hornfels xenoliths 80
5.3.2 *En échelon* vein arrays (tension gash veins) at dilation sites 84
5.3.3 Shear band foliation 86
5.4 Porphyritic S-type granite 91
5.4.1 Shape preferred orientation (SPO) of K-feldspar megacrysts 91
6 **Geochemistry** 96
6.1 Introduction 96
6.2 Major element composition of the granites 96
6.3 Trace element composition of the granites 103
6.4 Major element composition of the Malmesbury Group metasedimentary rocks 109
6.4.1 Weathering and weathering indices 112
6.5 Trace element composition of the Malmesbury Group metasedimentary rocks 114
6.5.1 Provenance 114
6.5.2 Tectonic setting 118
6.6 Sr and Nd radiogenic isotope geochemistry 119
6.6.1 Sr and Nd isotope geochemistry results for the granite phases 119
6.6.2 Sr and Nd isotope geochemistry results for the metasedimentary sample (SP16) 120
7 **U-Pb geochronology** 122
7.1 Introduction 122
7.2 Zircon descriptions 122
7.3 U-Pb ages 127
7.3.1 Microgranite (Sample SP19) 127
7.3.2 Fine-grained porphyritic hybrid granite (Sample SP33) 132
7.3.3 Coarse-grained porphyritic hybrid granite (Sample SP43-A) 132
8 **Discussion** 135
8.1 Geochemistry of the S-type granites 135
8.1.1 Introduction 135
8.1.2 Source characterization 137
8.1.3 Mechanisms/processes for geochemical variation 138
8.2 Geochemistry of the Malmesbury Group metasedimentary rocks 150
8.2.1 Introduction 150

8.2.2 Sediment provenance and tectonic setting 150
8.3 Metamorphism of the country rock 154
8.3.1 Introduction 154
8.3.2 Reactions expected for low-grade pelitic rocks undergoing contact metamorphism..... 154
8.4 Structural interpretation of the country rock 157
8.4.1 Introduction 157
8.4.2 Deformation 157
8.5 Granite emplacement 160
8.5.1 Introduction 160
8.5.2 Depth of emplacement 160
8.5.3 Granite emplacement relative to regional deformation 161
8.5.4 Proposed granite emplacement mechanisms for the study area 166
8.6 The origin of K-feldspar megacrysts 172
8.6.1 Introduction 172
8.6.2 The origin of K-feldspar megacrysts in the porphyritic granite phases 173
8.6.3 K-feldspar megacrysts in the country rocks – a case for an igneous/magmatic origin 174
8.6.4 K-feldspar megacrysts in the country rocks – a case for late-stage growth 177
8.7 K-feldspar megacryst defined magmatic foliation: implications and conclusions 179
9 **Conclusions** 180
9.1 Geochemistry summary 180
9.2 Granite emplacement processes summary 181
9.3 Recommendations 183
References 184
Appendix list 197

List of figures

Figure 2.1: Distribution of Neoproterozoic units in the Pan-African/Brasiliano tectonic belts in southern Africa and southeastern South America (after Frimmel, 2009) and the stratigraphic subdivision of the Saldania belt and its extent along the southwestern and southern portions of the Western Cape Province (after Gresse et al., 2006)……5

Figure 2.2: A summary of the proposed lithostratigraphic subdivision of the Western Saldania belt (after Kisters & Belcher, 2018)……7

Figure 2.3: Geological map of the western Saldania belt (after Kisters & Belcher, 2018) and the regional extent of the S-type Peninsula Pluton and its contact with the Tygerberg Fm metasedimentary rocks at Sea Point (modified after Farina et al., 2012)……12

Figure 4.1: Geological map of the Sea Point contact outcrop……19

Figure 4.2: Metasiltstone-metamudstone xenoliths in the lit-par-lit zone……20

Figure 4.3: Typical appearance of the interlayered metasiltstone-metamudstones lithologies at both the outcrop- and thin section-scale……21

Figure 4.4: Outcrop photograph of the appearance of the metamudstone in the northern portion of the study area……22

Figure 4.5: The appearance of the metamudstone in the lit-par-lit zone……23

Figure 4.6: Thin section photomicrographs of the mineral constituents that make up the metamudstone……24

Figure 4.7: Field appearance of the S-type porphyritic coarse-grained granite and the various features associated with it……26

Figure 4.8: Thin section photomicrographs of the mineral constituents of the S-type coarse-grained porphyritic granite and some of its common textural features……27

Figure 4.9: Thin section photomicrographs showing some of the textural features involving Bt……29

Figure 4.10: Outcrop photographs of variably-sized and shaped K-feldspar megacrysts which form part of the coarse-grained S-type granite……30

Figure 4.11: Thin section photomicrographs of the textural features of Kfs megacrysts……31

Figure 4.12: Thin section photomicrographs of the typical textural features of Pl phenocrysts……32

Figure 4.13: Outcrop photographs of the compositionally variable enclaves in occurrence within the S-type porphyritic granite outcropping at the southern- and northern-end of the study area respectively……34

Figure 4.14: Outcrop and thin section view of the aplite bodies associated with the S-type coarse-grained porphyritic granite……35

Figure 4.15: Magmatic structures outcropping in the study area……37

Figure 4.16: Outcrop photographs of the microgranite outcropping in the northern- and southern-portion of the study area respectively……38

Figure 4.17: Thin section photomicrographs of the microgranite mineralogy and its textural features……40

Figure 4.18: Thin section photomicrographs of the various hybrid granite phases that occur in the lit-par-lit zone……41

Figure 4.19: Stacked bar plots provided to give a visual/graphical representation of the mineral abundances given for each hybrid granite described in Table 4.1. ……42

Figure 4.20: Transect of area 7 showing a portion of the northern coarse-grained porphyritic granite sheet in contact or adjacent to a lit-par-lit section……44

Figure 4.21: Transect of area 8 showing the contact between the northern coarse-grained porphyritic granite sheet and an adjacent medium to coarse-grained porphyritic hybrid granite and Malmesbury lit-par-lit section……45

Figure 4.22: Close up view of the close association between the country rock and the hybrid granite in area 7……46

Figure 4.23: Thin section photomicrographs of the contact relationship between the hybrid granite phases and Malmesbury Group country rock in the lit-par-lit zone……47

Figure 4.24: Outcrop photographs depicting the relationship between fine-grained hybrid granite phases and the medium- and coarse-grained hybrid granite phases within the lit-par-lit section demarcated by area 8……49

Figure 4.25: Outcrop photographs and thin section photomicrographs of various feldspar grains preserved within the metamudstone country rock in the lit-par-lit zone……51

Figure 4.26: Outcrop photographs of various hornfels xenoliths in the study area incorporated into or surrounded by the metamudstone country rock……52

Figure 4.27: Transect of area 4 depicting a xenolith-rich zone in the study area……53

Figure 4.28: Outcrop photographs of some of the xenoliths located within the xenolith-rich zone of area 4……54

Figure 4.29: Outcrop photograph of a rotated country rock xenolith with preserved S_1 foliation planes……55

Figure 4.30: The appearance of some of the ductiley deformed country rock bodies within the lit-par-lit zone….56

Figure 5.1: Simplified geological map of the Sea Point contact comparing foliation and bedding orientation in the lit-par-lit zone and northern Malmesbury Group outcrops……58

Figure 5.2: Lower hemisphere equal-area projections comparing bedding orientation measured from the southern end, lit-par-lit zone and the northern end of the study area respectively……59

Figure 5.3: Thin section photomicrograph of a portion of sample SP17 (interlayered metamudstone-metasiltstone) to illustrate the microstructural relationship between the S_1 foliation and the bedding (S_0)……60

Figure 5.4: Thin section photomicrographs of the well-developed domainal structure characterizing the metamudstones exposed in the study area……62

Figure 5.5: Lower hemisphere equal-area projections comparing S_1 foliation orientation measured from the southern end, lit-par-lit zone and the northern end of the study area respectively……63

Figure 5.6: Bending/folding of the Malmesbury banding in area 8 resulting in an orientation change, of the banding, from an initial roughly NW-SE orientation towards a more NNW-SSE orientation, with the maximum curvature (of this banding) closing or directed towards the SSW direction……64

Figure 5.7: Thin section photomicrographs of the development of a crenulation cleavage (S_2) after folding of the primary foliation (S_1)……65

Figure 5.8: Malmesbury Group metamudstone outcrops showing evidence of a sub-horizontal S_2 crenulation cleavage……65

Figure 5.9: Lower hemisphere equal-area projections for S_2 orientation measured at the northern portion of the study area at stations F1 and F3……66

Figure 5.10: Thin section photomicrographs of syn-tectonic Crd porphyroblasts……68

Figure 5.11: Evidence of F_1 folding in the southern portion of the study area……70

Figure 5.12: A close-up view of the fold hinge area of Figure 5.11……72

Figure 5.13: Outcrop photographs of folded Malmesbury country rock structures intruded by various hybrid phases in the lit-par-lit zone……73

Figure 5.14: Outcrop photograph of a fairly large scale antiformal fold structure exposed in the northern portion of the study area (i.e. area 11)……74

Figure 5.15: Tight to isoclinal folding of the Malmesbury Group in the northern portion of the study area (i.e. area 10)……76

Figure 5.16: Antiformal fold structure, closing towards the WNW direction, exposed in the northern portion of the study area at area 9……77

Figure 5.17: Lower hemisphere equal-area projections of the plunge and plunge direction of the fold axes and the associated dip direction and dip of the axial plane as determined from the bedding orientation readings taken from the folded bed limbs at area 2, area 9 and area 11……78

Figure 5.18: The three types of grain-tail complexes and their use as shear sense indicators (after Passchier & Trouw, 2005)……81

Figure 5.19: Grain-tail complexes of the σ- and δ- type characterized by subhedral K-feldspar grains lodged within a Malmesbury Group host at various locations in the lit-par-lit zone……82

Figure 5.20: σ-type Malmesbury Group hornfels xenoliths sitting within a more biotite-rich metamudstone host in the lit-par-lit zone……83

Figure 5.21: Simplified geological map of the Sea Point contact map showing the locations/stations of suitable shear sense indicators in the study area……84

Figure 5.22: En échelon tension gash veins in the lit-par-lit zone……85

Figure 5.23: The two types of foliation pairs, C- and C'-type, that are characterized by foliation curvature relative to the shear plane and their differences in geometry (after Passchier & Trouw, 2005)……87

Figure 5.24: Thin section photomicrographs highlighting the development of a C/S fabric in sample SP14……88

Figure 5.25: Outcrops showing evidence of a C/S fabric at stations SC1 and SC4 respectively……89

Figure 5.26: Sub-vertical surfaces showing evidence of a C/S fabric at stations SC2 and SC3 respectively……90

Figure 5.27: Examples of three mutually perpendicular surfaces observed and their associated equal-area lower hemisphere projections that show the preferred orientation of the K-feldspar megacrysts on each respective surface and the inferred magmatic foliation plane per station……92

Figure 5.28: Examples of two mutually perpendicular surfaces observed and their associated equal-area lower hemisphere projections that show the preferred orientation of the K-feldspar megacrysts on each respective surface and the inferred magmatic foliation plane per station……93

Figure 5.29: Simplified map of the Sea Point contact depicting all the station locations used for SPO analysis and their associated preferred K-feldspar megacryst orientations and resultant magmatic foliation plane……94

Figure 6.1: Major element classification plots for the various granite phases of the study area……100

Figure 6.2: Select major elements vs. maficity plots for the various granite phases of the study area……102

Figure 6.3: Select REE and HFSE vs. maficity plots for the various granite phases of the study area……105

Figure 6.4: Select LILE vs. maficity plots for the various granite phases of the study area……106

Figure 6.5: REE and multi-element spider plots for the various granite phases of the study area……107

Figure 6.6: Geochemical classification of the Malmesbury metasedimentary rocks of the study area using the log (SiO_2/Al_2O_3) vs. log (Fe_2O_3/K_2O) diagram (after Herron, 1988)……112

Figure 6.7: A-CN-K and CIA ternary diagram showing the weathering trend for the Malmesbury Group metasedimentary rocks of the study area……114

Figure 6.8: Various provenance and degree of weathering plots for the Malmesbury metasedimentary rocks of the study area……116

Figure 6.9: Trace element tectonic discrimination diagrams for the Malmesbury metasedimentary rocks of the study area……118

Figure 7.1: CL images of oscillatory zoned zircon grains……124

Figure 7.2: CL images of zircons with unzoned cores and those which are elongate……125

Figure 7.3: CL images of unzoned and irregularly zoned zircons……126

Figure 7.4: U-Pb concordia diagram of inherited and igneous ages of zircon grains from sample SP19……128

Figure 7.5: U-Pb concordia diagram of inherited and igneous ages of zircon grains from sample SP33…… 133

Figure 7.6: U-Pb concordia diagram of inherited and igneous ages of zircon grains from sample SP43A……134

Figure 8.1: Whole-rock isotope plots for the various granite phases of the study area……138

Figure 8.2: Binary log-log diagrams of Ba vs. Sr, Ba vs. Eu, Ba/Sr vs. Sr, and Rb/Sr vs. Sr modelled at 30% fractional crystallization……141

Figure 8.3: Rare earth element (A, C) and multi-element spider (B, D) plots for the various granite phases of the study area normalized to average trace element values of Farina et al. (2012) and Frimmel et al. (2013)……146

Figure 8.4: Plot of 3(Na + K)/Fe versus Si/Fe……147

Figure 8.5: Whole-rock isotope plots for the various Malmesbury Group samples……151

Figure 8.6: Contoured lower hemisphere equal-area projections of bedding and S_1 foliation poles together with the orientation of their respective principal stresses……158

Figure 8.7: Lower hemisphere equal-area projections for S_2 orientation (as contoured poles) measured at the northern portion of the study area……159

Figure 8.8: Rock block photographs of samples SP5, SP43D and SP43B showing the contact relationships between various fine, medium and coarse-grained porphyritic granites pulses and the metamudstone country rock……163

Figure 8.9: Thin section photomicrographs highlighting the apparent foliation deflections in the biotite-rich Malmesbury Group metamudstone bands at the contact areas with the voluminous and porphyritic medium-grained porphyritic hybrid granite intrusions……164

Figure 8.10: Model for a Weertman buoyancy-driven fracture/dyke (modified after Melosh, 2011)……176

List of tables

Table 2.1: A summary of the lithology and depositional environments of the various formations of the Malmesbury Group……9

Table 4.1: Mineralogy, grain sizes, abundances and textural features of the hybrid granite phases in the lit-par-lit zone……42

Table 6.1: Statistical summary of the major element composition of the various granite phases of the study area……97

Table 6.2: Whole-rock major, trace and REE geochemistry of the various granite phases of the study area……98

Table 6.3: Statistical summary of selected trace element compositions of the various granite phases of the study area……103

Table 6.4: Whole-rock major, trace and REE geochemistry of the Malmesbury metasedimentary rocks of the study area……110

Table 6.5: Whole−rock Sm-Nd isotopic data for the S-type Peninsula Pluton granites and the single Malmesbury Group metasedimentary rock of the study area……121

Table 6.6: Whole−rock Rb-Sr isotopic data for the S-type Peninsula Pluton granites and the single Malmesbury Group metasedimentary rock of the study area……121

Table 7.1: LA-ICP-MS U-Pb geochronological data for zircons of sample SP19……129

Table 7.2: LA-ICP-MS U-Pb geochronological data for zircons of sample SP33……130

Table 7.3: LA-ICP-MS U-Pb geochronological data for zircons of sample SP43A……131

1 Introduction

The Earth's continental crust is comprised of large amounts of granitic rocks that have remained stable and above sea level for billions of years; these granites play a fundamental role in establishing and developing the continental crust (Taylor & McLennan, 1995, Petford et al., 2000; Kemp & Hawkesworth, 2003). The process of how large volumes of granitic magma are extracted from and ascend through the lower to mid-upper crust to be emplaced at structurally higher levels can be conveniently subdivided into four steps: magma generation, segregation, ascent and emplacement (Brown, 1994; Petford et al., 2000). The processes related to the first three steps fall outside the scope of this study but will be referenced to some degree at various points of the thesis. Recent descriptions and/or summaries of the first three steps are provided by Clemens (2012) and Brown (2013).

Granite emplacement mechanisms are plentiful and are still a subject of much debate among researchers (Nédélec & Bouchez, 2015). Emplacement is the mechanism by which volumes of magma are accommodated in the crust (Clemens, 2012). The classic interpretation of pluton growth by the solidification of large molten magma chambers emplaced over short periods by overall inflation is now disregarded as it requires enormous amounts of space (Paterson et al., 1996; Petford et al., 2000). This is referred to as the 'space problem' (e.g. Bowen, 1948; Buddington, 1959) and it has been a major point of contention throughout the years. A better understanding of tectonic forces coupled with the quantification of stresses and strains and the introduction of high-resolution geochronology has led to the proposal of new emplacement mechanisms that have partly resolved the space problem (Burchardt, 2018). Some of the more current proposed emplacement mechanisms include: **(1)** The incremental growth of a pluton by an amalgamation of successive magmatic injections and dykes (e.g. Clemens & Mawer, 1992; Annen & Sparks, 2002; Glazner et al., 2004; Belcher & Kisters, 2006; Menand, 2011; Annen, 2011; Miller et al., 2011; Farina et al., 2012; Annen et al., 2015). There is, however, a debate on whether magma pulses were injected via dyking (Petford, 1996), or by diapirism (Miller & Patterson, 1999). **(2)** Magmatic stoping, defined as the process of completely disconnecting and surrounding a piece of host rock by magma, resulting in the movement of the block relative to its position before emplacement (e.g. Paterson et al., 2008; Clarke & Erdmann, 2008). **(3)** Crustal assimilation, where magma creates space for itself by melting its way upwards through the surrounding wall rock (e.g. Jung et al., 1999; Winter, 2010). **(4)** Deformation-controlled emplacement. Structural studies have demonstrated strong links between regional deformation and the ascent and emplacement of both felsic and mafic magmas (Cruden & Weinberg, 2018). For example, the role played by active faults and shear zones (which are both sites of dilation and enhanced porosity), and pre-existing country rock structures in controlling the emplacement and growth of magma bodies at depth have been described (e.g. Hutton et al., 1990; McCaffrey, 1992; Neves et al., 1996; Holdsworth et al., 1999; Passchier et al., 2005).

First described by Clarke Abel (1818) but described in greater detail (and subsequently made famous) by Charles Darwin (1844), the Sea Point contact (Cape Town, South Africa) provides an example of a well-exposed intrusive contact between the S-type Peninsula Granite (of the Neoproterozoic-Paleozoic Cape Granite Suite) and metasedimentary country rocks of the Neoproterozoic Malmesbury Group. Despite subsequent descriptions of the contact being undertaken (e.g. Walker & Mathias, 1946; Von Veh, 1983, Theron, 1984), there has yet to be a more recent study that describes the contact in greater detail (i.e. an integrated study that involves structural mapping, petrography, geochemistry and geochronology of the exposed granites and country rocks). The outcrop exposes a variety of S-type granite phases at a more localized scale compared to the rest of the Peninsula Pluton. The main contact zone not only provides evidence of the intimate association between the granite phases and the country rock, resulting in a hybrid rock of mixed character, it also shows the concordant (i.e. subparallel to the lithological boundaries of country rock e.g. bedding and foliation) nature of granite intrusion into the country rock. Furthermore, the main contact zone also contains numerous shear sense indicators, magma flow indicators and evidence of ductile behaviour and folding of the country rock. With all the features listed above, it is apparent that the contact records the fundamental features of a magmatic intrusion and can, therefore, provide clues as to the methods by which an intrusion occurs, relative to a certain tectonic regime, and the processes that accompany this event.

The primary aim of the thesis is to identify the plausible modes of emplacement of the granites in the study area and to shed light on the main mechanisms that influence pluton emplacement in general. Also, another aim involves linking the tectonic or structural development/evolution of the study area to magma emplacement and how structure and tectonics influenced the magma emplacement mechanisms. To fulfil the aim, detailed mapping of the Sea Point contact outcrop was undertaken and involved describing the intrusive relationships of the various granite phases with each other as well as with the country rock, measuring the orientations of the structural features of the country rock and examining the predominant shear sense direction that typifies the study area. In addition, the relative orientations of the K-feldspar megacrysts were measured using the shape preferred orientation technique (SPO). This aided in establishing the orientation of the K-feldspar megacryst defined magmatic foliation. Analytical procedures, in the form of U-Pb zircon geochronology and whole-rock major and trace element geochemistry, were undertaken to assist in the interpretation of the magmatic processes that gave rise to the granitic rocks exposed at the contact and the timing of their emplacement. Additional aims of the thesis include describing the extent to which the host metasedimentary rocks of the Malmesbury Group in the study area were metamorphosed by the heat of the granite as well as investigating the origin of K-feldspar megacrysts embedded in the country rock in the main contact zone.

2 Geological setting

2.1 Saldania belt

The Saldania orogenic belt is a volcano-sedimentary succession, of a low-grade metamorphic nature, that is situated along the southern and southwestern portions of the Western Cape Province of South Africa and the Kalahari Craton (Fig. 2.1B) (Grese et al., 2006; Chemale et al., 2011). It forms part of the Neoproterozoic Pan-African/Brasiliano tectonic belts, in southern Africa and southeastern South America (Fig. 2.1A), that record the oblique closure of the Adamastor Ocean related to the construction of southwestern Gondwana ca. 550-500 million years ago (Frimmel & Fölling, 2004; Gresse et al., 2006; Frimmel, 2009). The Saldania belt is commonly subdivided into two branches, namely the E-W trending southern branch and the NW-SE trending western branch (Frimmel, 2009; Chemale et al., 2011) (Fig. 2.1B). The western branch (or western Saldania belt), where the study area is located, is the main exposure of the Saldania belt. The southern branch is exposed within large unroofed anticlinal hinges of the Permo-Triassic Cape Fold Belt and comprises the **Kango Group** (Oudtshoorn area), the **Kaaimans Group** (George area) and the **Gamtoos Group** (Port Elizabeth area) (Rozendaal et al., 1999; Gresse et al., 2006; Chemale et al., 2011) (Fig. 2.1B). The aforementioned groups are comprised of quartzites, phyllites, schists, marble and calc-silicates and are intruded by various metamafic and granitic intrusions.

2.2 The western Saldania belt

The western Saldania belt is a NW-SE trending, low-grade (i.e. lower greenschist-facies) metamorphic fold belt that outcrops at a much larger extent (approx. 180 × 100 km) compared to the Southern Branch (Scheepers, 1995; Rozendaal et al., 1999; Belcher & Kisters, 2003; Chemale et al., 2011). The metamorphism of the belt is attributed to the deformation and folding during the Pan African orogenic event or Saldanian orogeny (i.e. convergence of the Kalahari and the Rio de la Plata cratons during Gondwana assembly) (Scheepers, 1995; Rozendaal et al., 1999; Belcher & Kisters, 2003; Chemale et al., 2011). Supracrustal rocks (outcropping to the north and northeast of Cape Town), collectively referred to as the Malmesbury Group, underlie the western Saldania Belt.

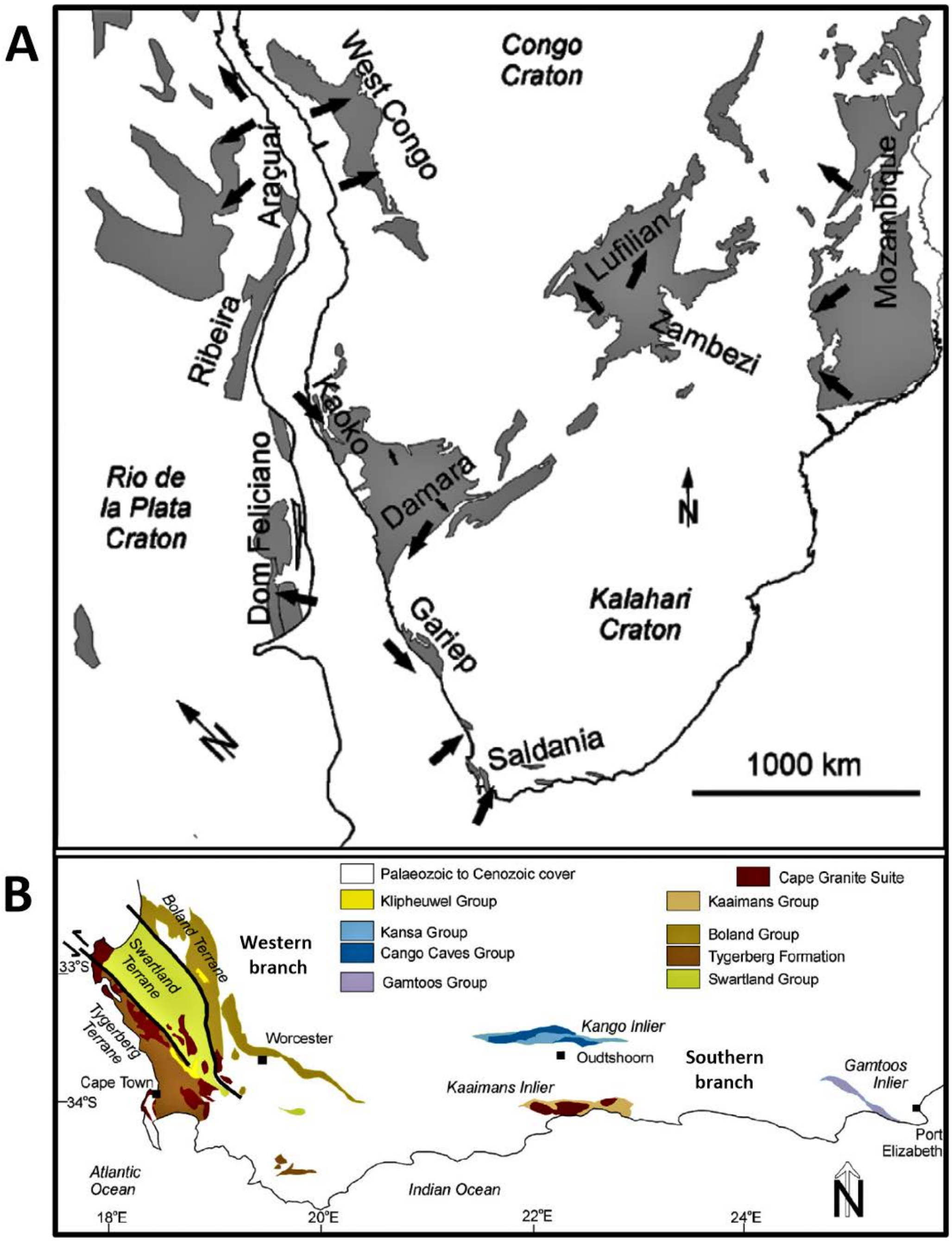

Figure 2.1*: (A) The Distribution of Neoproterozoic units in the Pan-African/Brasiliano tectonic belts located in southern Africa and southeastern South America (shown in an Upper Cretaceous Gondwana break-up position) (after Frimmel, 2009). The arrows in each of the belts indicate the main orogenic kinematic transport directions. (B) The stratigraphic subdivision of the Saldania belt and its extent along the southwestern and southern portions of the Western Cape Province (after Gresse et al., 2006); figure obtained from Frimmel et al. (2013).*

The Malmesbury Group is overlain by younger rocks of the Cape Supergroup which constitute much of the geology underlying the Western Cape (Fig. 2.3A). Volumetrically minor rocks of the Klipheuwel Group also form part of the lithological component of the western Saldania belt (Fig. 2.3A). They are mainly clastic sedimentary rocks and unconformably overlie folded strata of the Malmesbury Group and plutons of the Cape Granite Suite (CGS) but are located below the regional unconformity with the overlying Cape Supergroup (Kisters & Belcher, 2018). Regional sub-vertical, NW-SE trending strike-slip faults, in the form of the Colenso and Piketberg-Wellington fault zones (the largest structural features of the western Saldania belt), cross-cut the western Saldania belt (Hartnady et al., 1974; Theron et al., 1992; Kisters et al., 2002; Belcher, 2003; Frimmel et al., 2011, 2013) (Figs. 2.1B, 2.3A). The Colenso fault is more prominent and better exposed (Kisters & Belcher, 2018). It extends ~180 km parallel to the Atlantic Coast and is defined by mylonitic and brecciated outcrops along its extent, with an initial sinistral shear sense (Kisters et al., 2002). Subsequently, the fault reversed to dextral shearing at ~539 ± 4 Ma with dextral movement continuing until ~520 Ma (Kisters et al., 2002). The Piketberg-Wellington fault is only poorly exposed and its actual trace and location are not well established (Kisters & Belcher, 2018).

The lithostratigraphic subdivision of the western Saldania belt has been highly contentious. The currently accepted lithostratigraphic subdivision of the belt by the South African Committee for Stratigraphy (SACS, 1980) is from Gresse et al. (2006). The subdivision of Gresse et al. (2006) owes its origin to Hartnady et al. (1974), which proposed the western Saldania belt to be underlain by three allochthonous or para-autochthonous terranes or domains (north-eastern, central and south-western) separated by prominent terrane bounding strike-slip fault zones (i.e. Colenso & Piketberg-Wellignton fault zones) (Fig. 2.1B, 2.2A). Von Veh (1983) later named these three terranes the Boland, Swartland and Tygerberg Terranes for the north-eastern, central and south-western terranes respectively (Fig. 2.1B, 2.2A). Frimmel et al. (2013) recognized two terranes instead, namely the Malmesbury Terrane and the Boland Zone (terrane). In this subdivision, the Malmesbury Terrane is a combination of the previous Tygerberg and Swartland terranes of Gresse et al. (2006) (Fig. 2.2B). The subdivision by Frimmel et al. (2013) identifies the Piketberg−Wellington Fault as a terrane boundary (separating the Malmesbury terrane in the southwest from an autochthonous Boland Zone in the northeast), whereas the Colenso Fault is considered to be a reactivated deeper ancient basement structure.

In a more recent publication, Kisters and Belcher (2018) argue that previous subdivisions of the Malmesbury Group into three terranes (separated by terrane bounding strike-slip fault zones) cannot be upheld. The reasons provided for this include: (i) the similarity of the lithologies and structural features in large parts of the belt (e.g. gradational lithological contacts are common across and on either side of the faults and the contiguity of structures without any major breaks is observed); (ii) the uniformly low grades of metamorphism (i.e. no sharp metamorphic breaks exist); and (iii) the age of sedimentation in the three domains is similar and can be constrained to the Neoproterozoic between ca. 600 and 550 Ma (Kisters, 2016; Kisters & Belcher, 2018).

Based on all the arguments outlined above, Kisters and Belcher (2018) propose a new subdivision for the western Saldania belt comprising of two domains with distinct structural and strain histories. The lower domain, termed the Swartland Complex, is structurally more complex and lithologically heterogeneous, whereas the upper domain, termed the Malmesbury Group, is structurally simpler and covers a larger area (Figs. 2.2C, 2.3A). The two domains are separated by a major tectonostratigraphic break (or an inferred unconformity) (Fig. 2.2C).

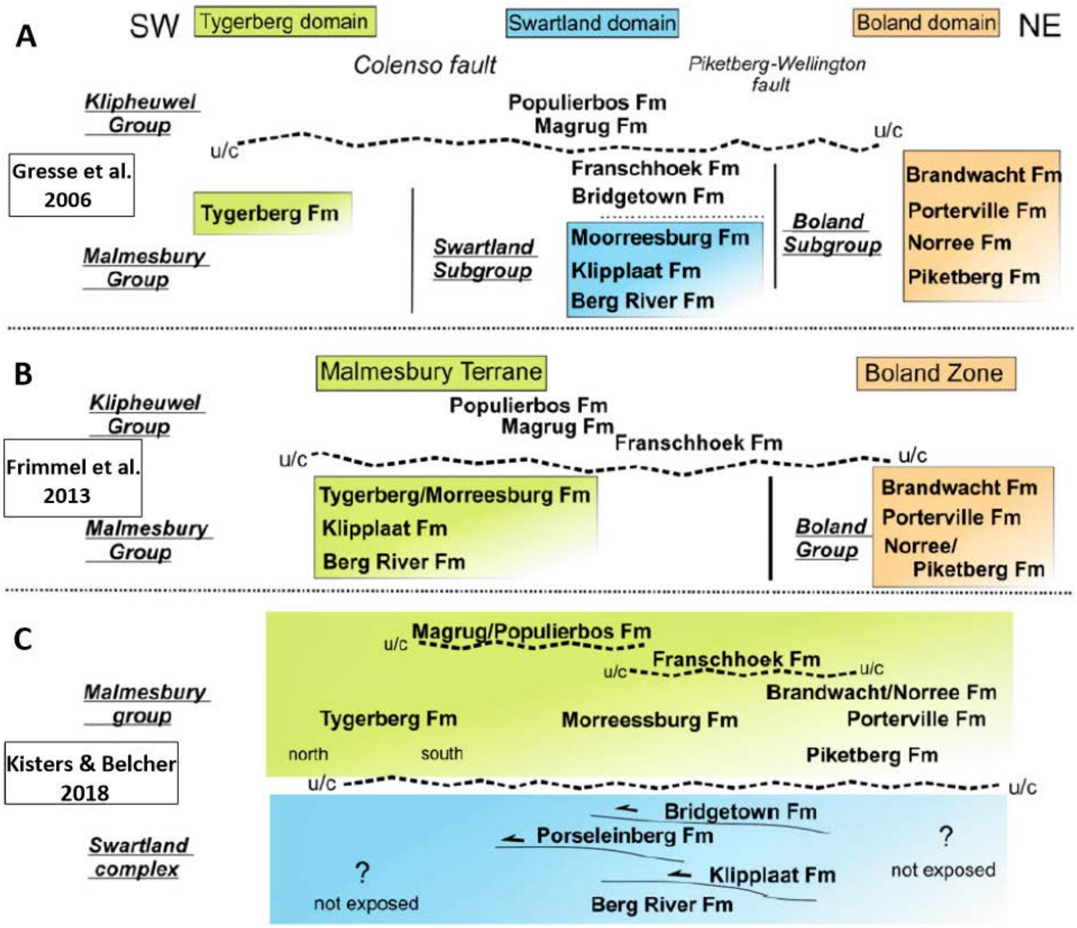

Figure 2.2: *A summary of the proposed lithostratigraphic subdivision of the western Saldania belt (after Kisters & Belcher, 2018). The figure is described in more detail in the text.*

The tectonic setting proposed by Kisters and Belcher (2018) for the two domains is as a section through a fore-arc along the western margin of the Kalahari Craton that formed during the Late Neoproterozoic to Cambrian (Rowe et al., 2010; Kisters & Belcher, 2018). During the closure of the Adamastor Ocean and southeast-directed oblique subduction of this oceanic crust beneath the Kalahari Craton, a mélange-like, imbricated, 20-25 km thick accretionary prism was formed (i.e. Swartland complex) comprising marine sediments and slivers of oceanic crust (Hartnady et al., 1974; Belcher, 2003; Kisters & Belcher, 2018). The late-Neoproterozoic to Cambrian fore-arc basin fill of the Malmesbury Group mantles this complex (Kisters & Belcher, 2018). The lithological assemblages and strains in the overlying Malmesbury Group mark a sharp break against the underlying mélange-like rocks of the Swartland complex, although the actual contacts between the two are not exposed (Kisters & Belcher, 2018).

2.2.1 Swartland complex (lower domain)

The Swartland complex is subdivided into four formations (abbreviated Fm here), namely the Berg River Fm, Klipplaat Fm, Porseleinberg Fm and Bridgetown Fm (Kisters & Belcher, 2018) (Fig. 2.2C). Collectively, the Swartland Complex mostly comprises quartz-sericite schists, chlorite-muscovite schists and phyllites, chlorite- and talc-carbonate schists, quartzites and muscovite quartzites, sheared chert horizons, graphitic schists and massive to well-bedded limestones (Hartnady et al., 1974; Theron et al., 1992; Belcher, 2003; Belcher & Kisters, 2003; Gresse et al., 2006; Kisters & Belcher, 2018). They are mainly exposed in the cores of the regional-scale antiforms (F_2 folds) of the Swartland and Spitskop domes (Fig. 2.3A). The characteristic features of the rocks in the Swartland complex include a pervasive bedding-parallel phyllitic foliation/fabric (S_1) and foliation parallel (i.e. transposed) quartz and quartz-carbonate veins (Belcher, 2003; Kisters & Belcher, 2003; Kisters & Belcher, 2018). Despite the pervasive fabrics, the predominantly metapelitic sequence and interlayered metapsammite units of the Swartland complex preserve characteristics of an originally marine, metaturbiditic succession (Theron et al., 1992; Belcher, 2003; Kisters & Belcher, 2018).

2.2.2 The Malmesbury Group (upper domain)

The Malmesbury Group of the upper domain (Fig. 2.3A) is subdivided into seven formations comprising the Tygerberg Fm, Morreesburg Fm, Piketberg Fm, Porterville Fm, Brandwacht Fm, Noree Fm, and Franschhoek Fm (Fig. 2.2C). A summary of the lithologies and depositional setting of the formations is provided in Table 2.1. The metasedimentary rocks exposed in the study area belong to the Tygerberg Formation of the Malmesbury Group.

***Table 2.1**: A summary of the lithology and depositional environments of the various formations (Fm) of the Malmesbury Group. The prefix "meta-" is assumed for all lithological descriptions owing to the metamorphism (lower greenschist facies) of the western Saldania belt.*

Formation	Lithology	Depositional setting
Tygerberg	Greywacke-dominated succession with intercalated shales and siltstones; has minor quartzite and some impure carbonate and conglomerate beds (Hartnady et al., 1974; Von Veh, 1983; Rowe et al., 2010; Frimmel et al., 2013).	Proximal and shallow-marine conditions of deposition; soft-sediment deformation features are common suggesting a rapid deposition of the sediments, but also indicating seismic activity in the unconsolidated sediments (Von Veh, 1983; Theron et al., 1992).
Morreesburg	Interlayered greywacke and shale units (resembling those of the Tygerberg Fm) (Von Veh, 1983; Belcher & Kisters, 2003).	Proximal and shallow-marine conditions of deposition (Theron et al., 1992; Kisters & Belcher, 2018).
Franschhoek	Quartzites, feldspathic greywackes and conglomerates, with only minor intercalated shales; also comprises tuffs and amygdaloidal lavas and intrusive quartz-porphyry dykes (Theron et al., 1992; Gresse et al., 2006).	Fluvial depositional environment; basin infilling was accomplished by dispersal systems that initially contributed small pebbles to boulders up to 30 cm in diameter (Tankard et al., 2012).
Piketberg, Porterville, Norree and Brandwacht formations	Sandstone and feldspathic sandstone interlayered with siltstone and shale, greywacke, gritty sandstone, conglomerate units and impure limestones; the Brandwacht Fm also contains metavolcanic units of andesitic composition intercalated with conglomerates, greywackes and metapelites (Kisters & Belcher, 2018).	Near-shore marine to deltaic and fluvial and non-marine depositional environment for the mainly coarse-clastic rocks; the conglomerates of the Piketberg and Porterville formations contain pebbles of vein quartz, phyllite and greywacke, suggesting a proximal source for the sediments (Gresse & Theron, 1992; Rozendaal et al., 1999; Frimmel et al., 2013).

In general, the Malmesbury Group is a predominantly clastic marine sedimentary succession comprising mostly alternating layers of dark-grey to black, fine-grained metagreywacke, metapelite, metasandstone, metalimestone, metaconglomerate and minor metavolcanic rocks (Hartnady et al., 1974; Theron et al., 1992; Scheepers, 1995; Gresse et al., 2006; Chemale et al., 2011). The depositional ages, ca. 560-555 Ma (Armstrong et al., 1998; Frimmel et al., 2013), have only been assigned to the upper portions of the Malmesbury Group (e.g.

from metaturbidites of the Tygerberg Formation) as the base of the group is not exposed (Kisters & Belcher, 2018). These ages correspond well with U-Pb ages from a felsic tuff of the metavolcanic Bloubergstrand Member in the Tygerberg Formation (north of Cape Town) which indicates an age of volcanism of ca. 554.5 ± 5 Ma (Kisters et al., 2015). This age helps to constrain the age of deposition of the Malmesbury Group and also indicates/confirms that volcanism of the Bloubergstrand Member occurred towards the end of sedimentation of the Tygerberg Formation (Kisters et al., 2015). The age is also, within error, identical to the emplacement of the earliest granites of the syn-, late- to post-tectonic Cape Granite Suite (CGS) (Kisters et al., 2015). The granites of the CGS (550-510 Ma) are intrusive into the Malmesbury Group (Belcher, 2003; Gresse et al., 2006; Farina et al., 2012; Frimmel et al., 2013; Kisters & Belcher, 2018) (Fig. 2.3A). The intrusion of the granites locally metamorphosed the rocks of the Malmesbury Group to lower amphibolite facies (Rozendaal et al., 1999, Chemale et al., 2011). The lower greenschist facies of the Malmesbury Group, a metamorphic grade obtained before CGS granite intrusion, indicates upper crustal levels of metamorphism. The CGS intrusions then intruded at that level as indicated by the low grade of the country rocks they intruded (Scheepers, 1995; Rozendaal et al., 1999; Belcher & Kisters, 2003).

The rocks of the Malmesbury Group lack the bedding-parallel foliation (S_1) characteristic of the Swartland complex, instead, primary bedding (S_0) together with depositional features (e.g. soft-sediment deformation structures) are well preserved (e.g. Von Veh, 1983; Theron et al., 1992; Rowe et al., 2010; Frimmel et al., 2013; Kisters & Belcher, 2018); the latter were used for constraining the environment of deposition as summarized in Table 2.1. Most of the structural features present in the rocks of the Malmesbury Group are related to D_2, the main deformation phase of the western Saldania belt, developed during the NE-SW regional shortening of the belt during the Saldanian orogeny. As a result, the rocks of the Malmesbury Group are folded into northerly to northwest-trending, doubly plunging and more or less upright or southwest-verging F_2 folds (Kisters & Belcher, 2018). Associated with the F_2 folds is an upright, broadly axial planar cleavage (S_2) which is prominent in the shale units of the Malmesbury Group but is weak or absent in psammitic rocks (Kisters & Belcher, 2018).

2.2.3 The Cape Granite Suite

The 550-510 Ma CGS crops out over a distance of more than 500 km along the southern and western Cape coast (Scheepers, 2000). The CGS comprises mainly S-, and I- type granitoid rocks (or plutons), and minor A-type granites, that formed during the Saldanian orogeny (Scheepers & Armstrong, 2002; Scheepers et al., 2006; Chemale et al., 2011) (Fig. 2.3A).

The syn- to late-tectonic S-type granites are the oldest of the granitoid intrusives and are located mainly in the south−western section of the western Saldania belt (Scheepers, 1995; Scheepers & Armstrong, 2002; Da Silva et al., 2000; Frimmel et al., 2013) (Fig. 2.3A). They have a peraluminous to metaluminous composition and have been subdivided into four main S-type plutons, namely the Darling, Saldanha, Stellenbosch, and Peninsula plutons. These plutons were emplaced between ca. 550 and 535 Ma and as late as ca. 525 Ma for the latest phases in the central Darling batholith (Da Silva et al., 2000; Villaros et al. 2009b). The main S-type CGS–Malmesbury contact zone is located at Sea Point, Cape Town (i.e. the location of the study area), where the Peninsula Pluton is intrusive into the metasedimentary rocks of the Tygerberg Formation (Fig. 2.3B). The Peninsula Pluton is largely undeformed and is the southernmost body among the S-type granites of the CGS. It outcrops along the Cape Peninsula, a piece of land stretching southward from Cape Town to Cape Point (Farina et al., 2012) (Fig. 2.3B). In general, the S-type granites have a compositional variation from leucogranite to granodiorite and are composed of quartz, biotite, muscovite, plagioclase, cordierite, large K-feldspar phenocrysts and some minor garnet. Processes that control the diversification of the chemistry (i.e. compositional variation) of the S-type granites have been constrained by Stevens et al. (2007) and Villaros et al. (2009a). S-type granitic magmatism was accompanied by the extrusion of the intracaldera, S-type, rhyolite ignimbrites (~542 Ma) of the Saldanha Bay Volcanic Complex (Clemens et al., 2017).

The regional Colenso Fault zone separates the S-type granites (to the west) from the I-type granites (to the east) (Scheepers, 1995; Scheepers & Schoch, 2006; Stevens et al., 2007; Villaros et al., 2009b) (Fig. 2.3A). The I−type granites form elongate, northwest-trending plutons and are also intrusive into the rocks of the central Swartland domain/complex (Kisters & Belcher, 2018) (Fig. 2.3A). They are metaluminous to slightly peraluminous and comprise monzogranites, granites, and alkali feldspar granites (Scheepers, 1995). The I-type granites are slightly younger (compared to the S-types), with emplacement ages falling between 540 and 520 Ma (Armstrong et al., 1998; Da Silva et al., 2000; Scheepers & Armstrong, 2002).

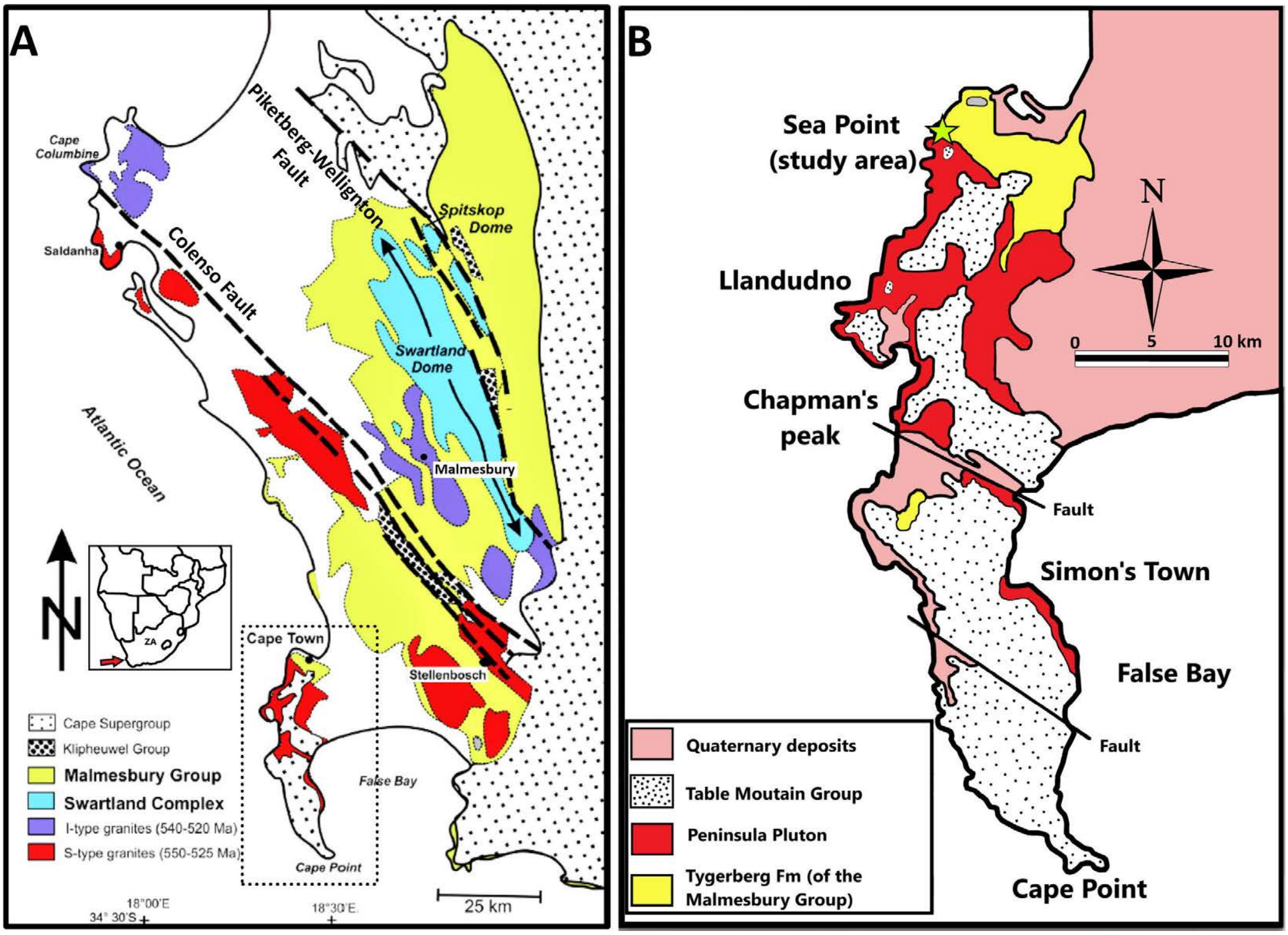

Figure 2.3*: (A) Geological map of the western Saldania belt (modified after Kisters & Belcher, 2018) subdivided based on the proposed lithostratigraphic subdivision by Kisters & Belcher (2018). Localities/distributions of the intrusive S- and I-type granites of the CGS, Klipheuwel Group and Cape Supergroup are also shown. Blank areas on the map correspond to regions with less than 1% outcrop. (B) A close-up view of the area demarcated by a dashed rectangle in (A) that shows the regional extent of the S-type Peninsula Pluton and its contact with the Tygerberg Fm (of the Malmesbury Group) metasedimentary rocks at Sea Point (i.e. the location of the study area; represented by the yellow star) (modified after Farina et al., 2012). The distribution of the overlying Table Mountain Group (of the Cape Supergroup) is also shown.*

A third (and minor) variety of granites associated with the CGS, referred to as the A-type granites, mark the conclusion of the CGS magmatism (Scheepers, 1995; Scheepers & Armstrong, 2002). They have an estimated age of intrusion ranging between ~525 and 510 Ma. The initial stages of the A-types had a high-K calc-alkaline composition becoming more intermediate at the final stages of magmatism (Scheepers, 1995; Scheepers & Armstrong, 2002).

3 Methodology

3.1 Sampling

The Sea Point contact outcrop is a heritage site and is of particular interest to the geological community, both locally and internationally, as well as to the general public from both a general scientific viewpoint as well as historically. For these reasons, sampling was restricted to sites away from the visually obvious areas (i.e. sites not readily visible from the viewing platform/parking bay; Fig. 4.1) and was done with a chisel and hammer with no drilling of any kind involved. Such sites of sampling included the gullies, which are worn into the outcrop by tides and waves, and along jointed surfaces where signs of any removal of material will be less obvious; this will, in turn, preserve the natural appearance of the outcrop. Sampling targeted the least weathered outcrops of the various granite phases as well as the metamorphosed Malmesbury Group country rock. Their GPS locations were recorded and are provided in Appendix A.

All of the samples were prepared at the Department of Earth Sciences, University of the Western Cape (UWC) for petrography, whole-rock major- and trace element-geochemical analysis as well as geochronology analysis. A total of 50 thin sections were made for petrographic analysis. An additional 12 probe sections were produced for a future K-feldspar microprobe study.

3.2 Analytical procedures

3.2.1 Whole-rock major- and trace element-geochemistry analyses

A total of 25 samples of the various granite (19 samples) and metasedimentary (6 samples) lithologies outcropping at the Sea Point contact outcrop were prepared at the Department of Earth Sciences (UWC) for whole-rock major- and trace element-geochemical analysis. The preparation involved the crushing of samples and milling them to a very fine powder. Cleaning procedures (i.e. quartz run and cleaning of surfaces with acetone) between each sample run (on both the crusher and milling bowl) were strictly adhered to for avoidance of cross-contamination.

After preparation, both major and trace element analysis was done at the Central Analytical Facilities (CAF), Stellenbosch University (SUN). Major element analysis was determined by XRF (X-ray fluorescence) spectrometry on fused glass beads. The glass beads were prepared by mixing 1 g of rock powder with 10 g of trace element- and REE-free flux [(lithium metaborate/tetraborate mixture ($LiBO_2$ = 32.83%, $Li_2B_4O_7$ = 66.67%, LiI = 0.50%)]. The XRF spectrometry analysis was performed on a PANalytical Axios Wavelength Dispersive spectrometer fitted with a 3kW Rhodium tube. The control standards used in the calibration for major element analyses were BE-N (basalt reference values), JB-1 (basalt (depleted) reference values), BHVO-1 (basalt reference values), JG-1 (granodiorite reference values), and WITS-G (granite reference values). Loss on ignition (LOI) was calculated by weight difference after ignition at 1000°C.

A Resonetics 193nm Excimer laser ablation system (LA) connected to an Agilent 7700 Inductively Coupled Plasma Mass Spectrometer (ICP-MS) was used to analyse the trace element concentration of fused glass discs. The operating conditions for the laser were set to a frequency of 10Hz and a fluence of 8 J/cm^2. 2 spots of 100µm per sample were created during the laser ablation analysis. Laser ablation was performed in helium gas at a flow rate of 0.35L/min and mixed with argon (0.9L/min) and nitrogen (0.007L/min) before being introduced into the ICP plasma. Each analysis incorporated a background acquisition of 15 seconds (gas blank) followed by 35 seconds of data acquisition from the sample. The calibration standard, NIST SRM 610 (National Institute of Standards and Technology Standard Reference Materials), was run every 15-20 samples, with a quality control standard (BCR and BHVO) run at the beginning of the sequence as well as a calibration standard throughout. The data was processed using the *Iolite v 3.34* software (Paton et al., 2011).

3.2.2 Rb-Sr and Sm-Nd isotopic analyses

Rb (Rubidium)-Sr (Strontium) and Sm (Samarium)-Nd (Neodymium) isotope analysis for 7 samples were done at the Department of Geological Sciences, University of Cape Town (UCT). 6 of the samples were various granite-types and 1 was a metasedimentary country rock.

To obtain the Rb, Sr, Sm and Nd concentrations in each sample a Thermo XSeries II ICP-MS at UCT was used after the dissolution of the samples with concentrated HF and HNO_3, and dilution with 5% HNO_3 containing an internal standard. Concentrations were determined in duplicate for each sample. The international standard BHVO-2 was analysed with every batch of samples as a measure to assess accuracy and precision.

Following concentration analysis, separation of Sr and Nd fractions in the same sample dissolutions were undertaken by chromatographic techniques as described by Míková and Denková (2007), after that described by Pin and Zalduegui (1997) and Pin et al. (1994). All isotope analyses were performed with a Nu Instruments NuPlasma HR ICP-MS coupled to a DSN-100 desolvating nebuliser at UCT. Sr is analysed as a 200ppb 0.2% HNO_3 solution. All Sr isotope analyses of unknowns are referenced to bracketing analyses of the NIST SRM987 reference standard, using a reference value for $^{87}Sr/^{86}Sr$ of 0.710255. The international reference material BHVO-2 gave a value of 0.703486 ± 10 relative to a value of 0.703479 ± 20 reported by Weis et al. (2006). The long-term UCT average is 0.703487 ± 44 (n = 124). All Sr isotope data are corrected for Rb interference using the measured signal for ^{85}Rb and the natural $^{85}Rb/^{87}Rb$ ratio. Instrumental mass fractionation is corrected using the exponential law and a $^{86}Sr/^{88}Sr$ value of 0.1194.

Nd isotopes are analysed as 50 ppb 2% HNO_3 solutions using a Nu Instruments DSN-100 desolvating nebuliser. JNdi-1 is used as a reference standard, with a $^{143}Nd/^{144}Nd$ reference value of 0.512115 (Tanaka et al., 2000). The BHVO-2 reference material gave values of 0.512990 ± 12, relative to a value of 0.512984 ± 11 reported by Weis et al. (2006). All Nd isotope data are corrected for Sm and Ce interference using the measured signals for ^{147}Sm and ^{140}Ce, and the natural Sm and Ce isotope abundances. Instrumental mass fractionation is corrected using the exponential law and a $^{146}Nd/^{144}Nd$ value of 0.7219.

3.2.3 U-Pb zircon geochronology

A total of 3 samples (all granites) were selected for U-Pb zircon age dating. The zircon grains were extracted from the selected granite whole-rock samples by the following sequential steps: (i) crushing, milling and sieving of samples at the Department of Earth Sciences, UWC; (ii) hand washing followed by gravity separation, using a super panner or Wilfley table, at the Mineral Separation Laboratory, SUN; (iii) magnetic separation using a Frantz magnetic separator at the Thin Section Laboratory, SUN; and (iv) heavy liquid separation at the Mineral Separation Laboratory, SUN. After the extraction process, the desired zircon grains for analysis were handpicked (using a needle) with aid of a binocular microscope and mounted in epoxy discs. The discs were polished, carbon-coated and imaged by cathodoluminescence using a Leo® 1450VP scanning electron microscope (SEM) at the CAF.

LA ICP-MS U-Pb measurements were carried out in the Earthlab at the University of the Witwatersrand (Johannesburg, South Africa) employing an Applied Spectra (AS) RESOlution 193 nm ArF excimer laser system coupled to a Thermo Scientific Element XR magnetic sector-field ICP-MS. At the start of each analytical session, the mass spectrometer was tuned by ablating a line scan on the NIST610 glass. The torch position, lenses and gas flows were tuned while measuring ^{206}Pb, ^{238}U and ^{238}U^{16}O to get stable signals and maximum sensitivity for ^{206}Pb and ^{238}U while maintaining low oxide rates (ThO+/Th < 0.2 %) and Th/U ratio > 0.9.

The laser sampling protocol employed a 24 µm static spot and a fluence of 2.5 J/cm^2 and took place in a SE-155 dual-volume ablation cell using a continuous flow of He gas combined with Argon (incorporated into the cell funnel) and a small volume of N_2 (added after the cell) to enhance signal stability and sensitivity, respectively. Each analytical session included up to 400 measurements. Before the gas blank measurement, each spot was pre-ablated by firing two laser shots to remove common Pb from the surface that may have been introduced during the sample preparation.

During each analytical session the zircon reference materials GJ-1 (Jackson et al., 2004), Plešovice (Sláma et al., 2008) and 91500 (Wiedenbeck et al., 1995) were measured between groups of 12 unknowns. Zircon GJ-1 was used as a matrix-matched primary reference material to correct for mass discrimination on measured isotope ratios in unknown samples and simultaneous correction for instrumental drift. The GJ-1 isotopic ratios used for the correction are those reported by Horstwood et al. (2016). Plešovice and 91500 were used as secondary reference materials to validate the results and assess the quality of the data for each analytical session.

Data reduction was performed with the software package *Iolite v.3.5* (Paton et al., 2011), combined with *VizualAge* (Petrus & Kamber, 2012). An exponential model of laser-induced elemental fractionation (LIEF) obtained by combining the isotopic ratios of the primary reference material from the entire session is used to correct for time-dependent down-hole elemental fractionation in the unknowns, under the assumption of similar fractionation behaviour in the reference material and the unknowns. After correction for LIEF and drift and normalization to the main reference material (performed in Iolite), uncertainty components for systematic errors are propagated by quadratic addition according to the recommendations of Horstwood et al. (2016). All absolute ages and uncertainties were calculated with *Isoplot v. 4.15* (Ludwig, 2012).

3.3 Mapping and geochemistry software

All base maps were acquired from Google Earth and were subsequently digitized using *Surfer 16*, distributed by Golden Software®, after field mapping. All the stereonets/stereoplots for structural readings were generated using the *Stereonet 10* software by Allmendinger et al. (2013) and Cardoza et al. (2013). Geochemical plots were generated using *GCDkit 5.0* by Janoušek et al. (2006) and *ioGAS*™ 64 distributed by REFLEX.

4 Lithological descriptions

4.1 Introduction

The Sea Point contact outcrops over an area of approximately 170 m × 60 m and shows a transition from Malmesbury Group rocks (in the northern portions) through a complex zone comprised of various phases of S-type granitic- and metasedimentary-rocks (main contact zone) before reaching the main pluton area, to the south, comprising the coarse-grained porphyritic S-type granite (Fig. 4.1). Also occurring within the extent of the exposure are fine-grained varieties of the S-type granite, typically referred to as a microgranite (Theron et al., 1992) (Fig. 4.1). Towards the southern portion of the exposure, these microgranites are semi-porphyritic, while in the north, they occur mostly as non-porphyritic concordant sheets. The main contact zone, or lit-par-lit zone, acquired its complex nature from the fact that various phases of granite and the country rock are intimately associated resulting in a hybrid rock of mixed character. This is the reason why the term "hybrid granite" is used to identify the granite phases and the variety of grain sizes and textures they display within this zone. The term lit-par-lit is used to describe a zone of rocks, which have been penetrated, or injected by numerous thin, roughly parallel sheets of molten material (usually granitic) along bedding or cleavage planes of the host rock (Sawyer, 2008).

This chapter describes the lithology of both the Malmesbury Group country rock and the intrusive granitic phases of the Peninsula Pluton as observed at the outcrop scale as well as in thin section. Moreover, a detailed account of the contact relationships between the country rocks and the granitic phases, as well as the relationship of the granite phases with each other, is also described. All mineral abbreviations used in this chapter (as well as the ensuing chapters thereafter) follow those recommended by Kretz (1983), Spear (1993), Fettes (2007) and Winter (2010).

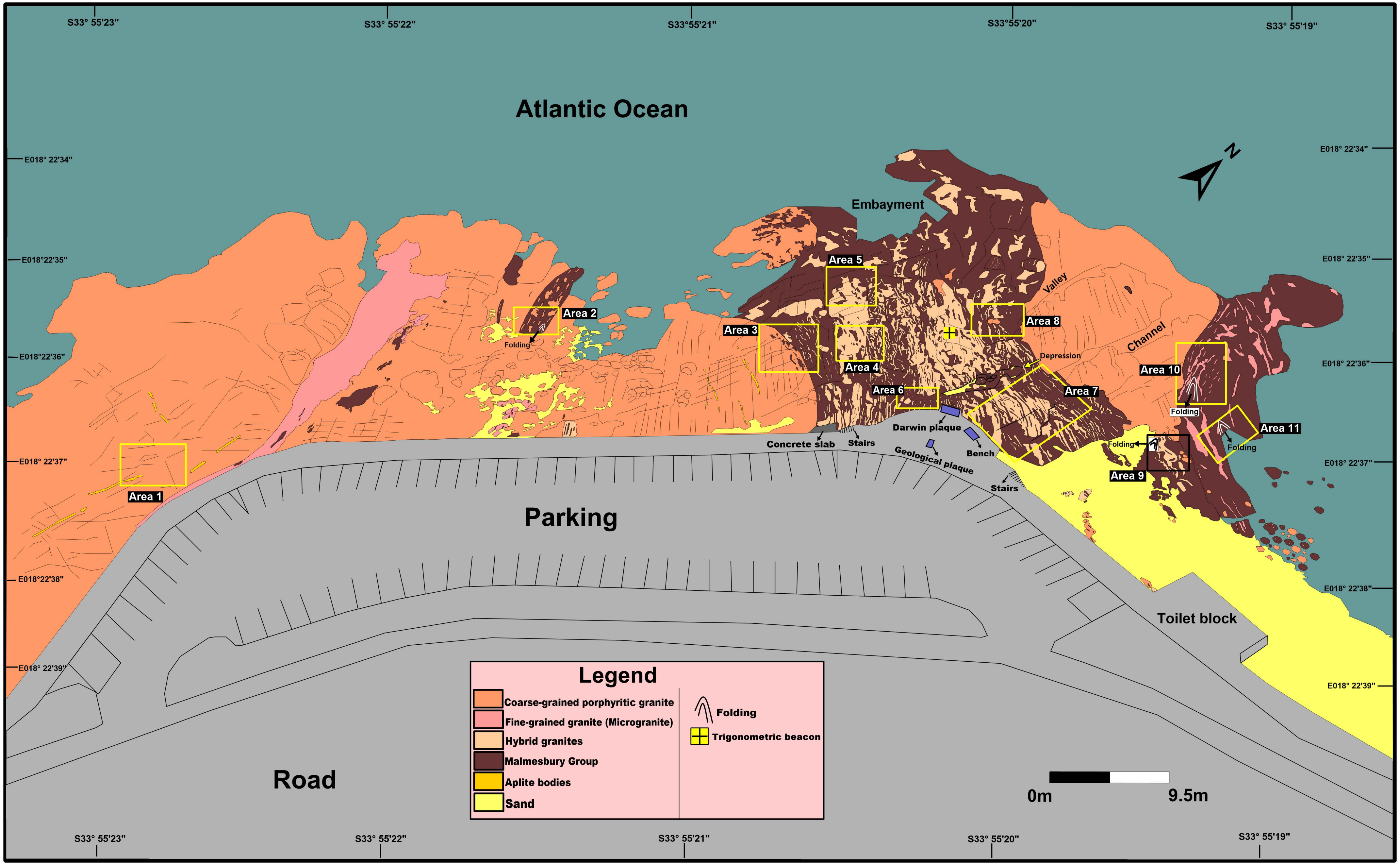

Figure 4.1: *Geological map of the Sea Point contact outcrop. Areas demarcated with rectangles are representative locations (referenced in the text) selected either to describe the lithology and the changes associated with it as one moves from one area to the next or to mark out where geological structures (e.g. folds) outcrop. The various black solid lines, cutting across the coarse-grained porphyritic granite as well portions of the Malmesbury Group and hybrid granite phases in the lit-par-lit zone, are used to indicate the variably oriented exhumation joints developed along the aforementioned lithologies in the study area.*

4.2 Malmesbury Group

4.2.1 Interlayered metasiltstone and metamudstone outcrops

The interlayered metasiltstone-metamudstone lithologies outcrop predominantly in the southern portion of the study area, where they occur as various small (Fig. 4.3A) to relatively large bodies (Fig. 4.3B) or as xenoliths (Fig. 4.2), with the latter being more common in the lit-par-lit zone. Primary fabrics in sedimentary rocks can be in the form of bedding and lamination defined by layers of different composition or texture, typically reflecting environmental change during deposition (Winter, 2009). As such, the presence of the variably thick metasiltstone banding interposed in the metamudstone layers represents the initial bedding (S_0) (Figs. 4.2, 4.3C, D).

In the field, the metasiltstones layers have a thickness up to 3 cm (Fig. 4.3A), however, the majority are millimetre-sized and are fairly hard to discern without careful observation (Fig. 4.3B). In thin section, they are fine-grained and are characterized by a granoblastic-textured matrix defined predominantly by interlocking, equigranular to partly inequigranular quartz grains (0.05-0.4 mm; 65 vol. %) (Fig. 4.3E, F). Biotite (0.025-0.3 mm) is next most abundant at 18 vol. %, followed by orthoclase (0.075-0.25 mm; 10 vol. %), sericite (typically <0.1 mm; 4 vol. %) and chlorite (<0.1 mm; 2 vol. %) (Fig. 4.3E, F). Detrital zircon, apatite and opaques occur as accessory mineral phases. The orthoclase grains are subhedral, commonly sericitized (explaining the presence of sericite in the matrix) and have inclusions of quartz and biotite grains. The quartz grains are subhedral to anhedral with minor sub-grain domains and typical undulose extinction microstructures. The biotite grains are subhedral to tabular and commonly chloritized (explaining the presence of chlorite in the matrix), with minor inclusions of zircon.

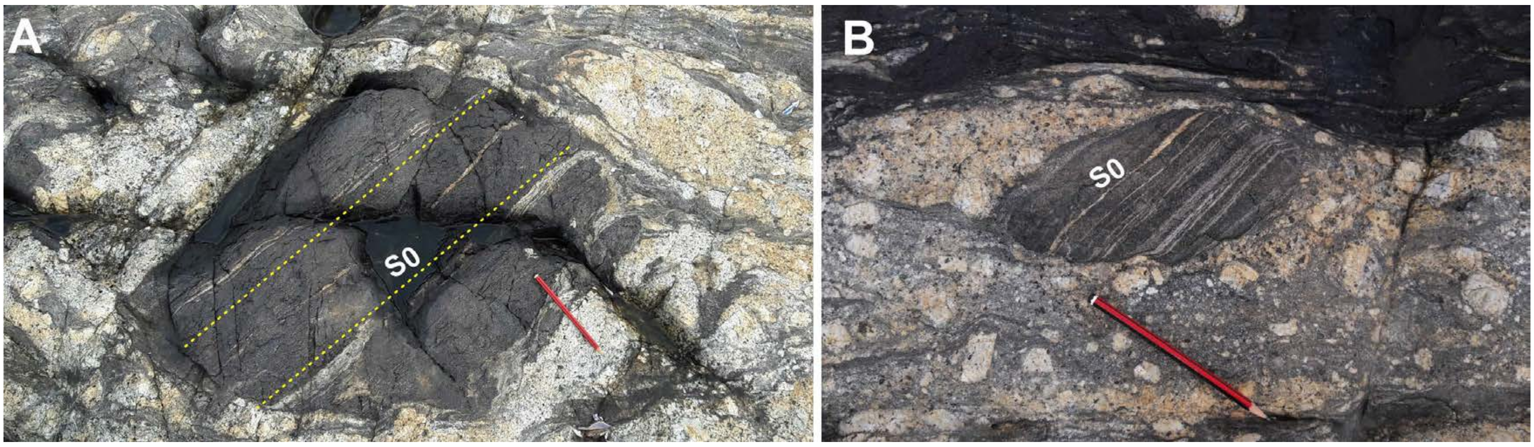

***Figure 4.2**: Metasiltstone-metamudstone xenoliths in the lit-par-lit zone. The orientation of S_0 in the xenoliths differs from the main Malmesbury Group.*

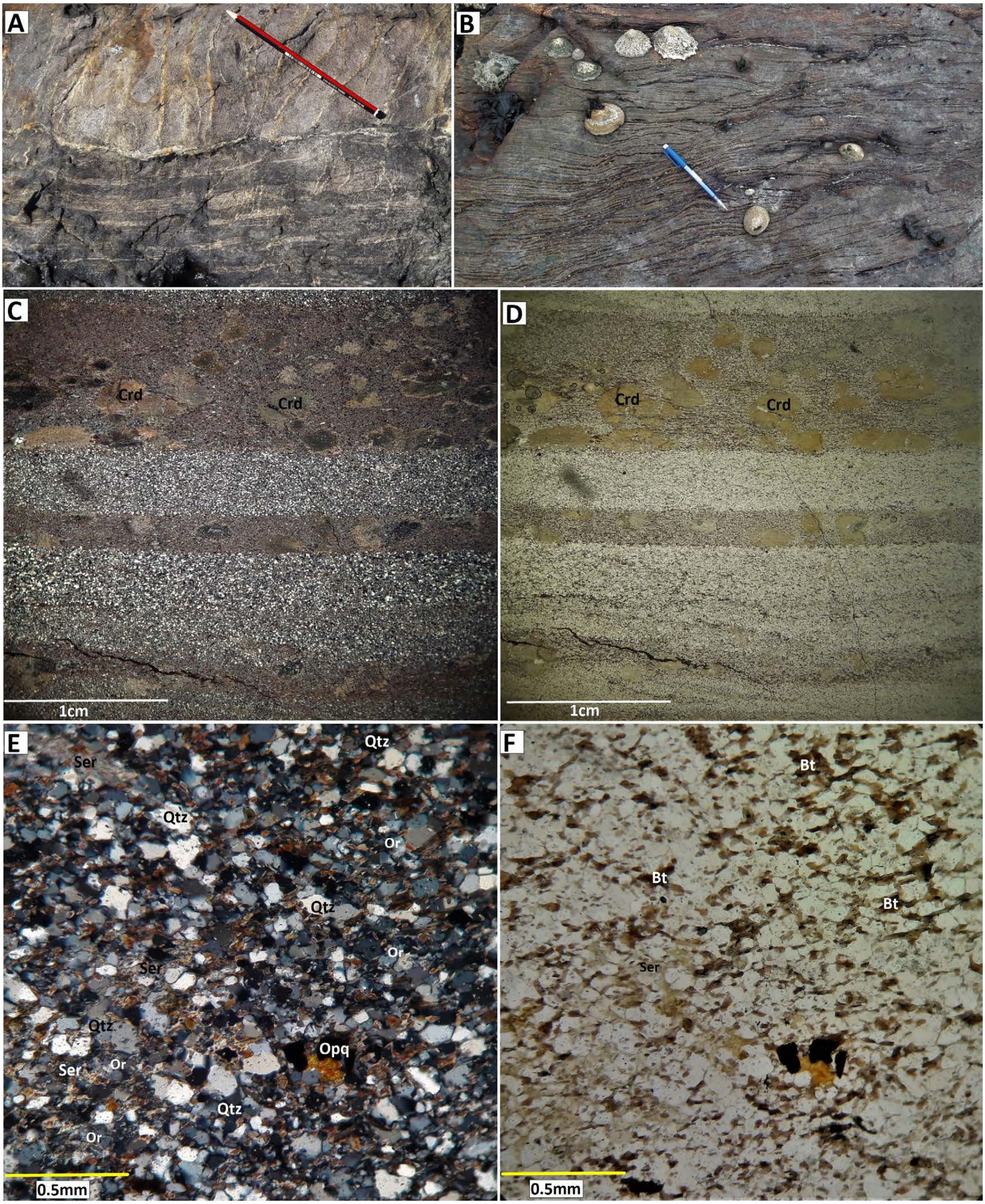

Figure 4.3*: (A) & (B) Typical appearance of the interlayered metasiltstone-metamudstone outcrops in the southern section of the study area. Discernible layers of different composition are visible and have average widths varying from > 1cm (A) down to mm sized widths (B). (C) & (D) Thin section view of the metasiltstone-metamudstone outcrops, one in cross polars (C) and the other plane-polarized (D). The metasiltstone layers are more coarse-grained compared to the biotite (Bt)-rich metamudstone layers. Note how the pinitized (or altered) cordierite (Crd) porphyroblasts are developed predominantly in the metamudstone layers as opposed to the metasiltstone layers. (E) & (F) Thin section photomicrographs of a zoomed-in portion of one of the metasiltstone layers in (C) & (D). Apart from a few partly inequigranular quartz (Qtz) grains, the metasiltstones have a predominantly granoblastic-polygonal texture, consisting of Qtz, orthoclase (Or) and Bt. Alteration products in the form of sericite (Ser) and accessory opaques (Opq) also occur. Length of pencil in (A) = 17cm & length of clutch pencil in (B) = 15 cm; both point to the north.*

4.2.2 Metamudstones

The metamudstones are the dominant lithological component of the Malmesbury Group in the study area. They outcrop as a dark-grey to black coloured succession that is fine-grained. These rocks range from weakly to highly foliated, with the highly foliated rocks having a well-developed vertical to sub-vertical axial planar foliation and a much shallower crenulation cleavage developed within them. Most of the metamudstones outcrop predominantly as splintery and fractured hornfelsic-type rock masses (Fig. 4.5A), however, in the northern portion of the study area, they occur as bedded outcrops (Fig. 4.4). In both cases, the metamudstones tend to have millimetre- to centimetre-sized cordierite crystals giving them a 'spotted' look or nodular texture (Figs. 4.3C, D, 4.5B, C). At the outcrop scale, however, some of the cordierite grains are not always easy to recognise especially when they are fine-grained. In this case, the fine-grained cordierite crystals commonly do not stand out against an equally or darker appearance of their metamudstone host which masks the appearance of the cordierite grains.

Figure 4.4: *Outcrop photograph of the appearance of the metamudstone in the northern portion of the study area as bedded features that make up the dominantly exposed northeast dipping and NW-SE trending fold limb. Intruded along this limb is the microgranite (left portion). Oppositely dipping SW limb is poorly exposed and largely submerged in the ocean. Length of clipboard: 35cm. The direction of view is NW.*

Figure 4.5*: (A) Appearance of the metamudstone in the lit-par-lit zone. Injected principally along (or sub-parallel) to the country rock fabrics are various hybrid granite phases and other finer-grained quartzofeldspathic vein material. (B) A portion of a metamudstone outcrop with a cluster of relatively coarse, rounded, equidimensional cordierite grains. (C) A zoomed-in portion of the area demarcated by a black rectangle in (B) for a clearer view of the cordierite grains. Length of GPS = 9.5cm; diameter of 50 cent coin = 2.2 cm.*

Petrographically, the metamudstones are biotite-rich and comprised of a granoblastic-polygonal textured matrix, with an overall size range between 0.075-0.5 mm, comprising quartz (30-40 vol. %), biotite (25-30% vol. %), orthoclase (15-20 vol. %) and plagioclase (5-10 vol. %) (Fig. 4.6). Cordierite (15-25 vol. %) mainly occur as porphyroblasts (Fig. 4.3C, D) but finer-grained varieties also occur (e.g. Fig. 4.6). Muscovite does not occur as a primary matrix mineral and, is instead, an alteration product, along with sericite and chlorite, replacing cordierite. Tourmaline, zircon and opaques occur as accessory phases. The platy to elongate millimetre- to centimetre-sized zircon-rich biotite grains commonly show a well-defined preferential alignment and thus define the foliation in the study area.

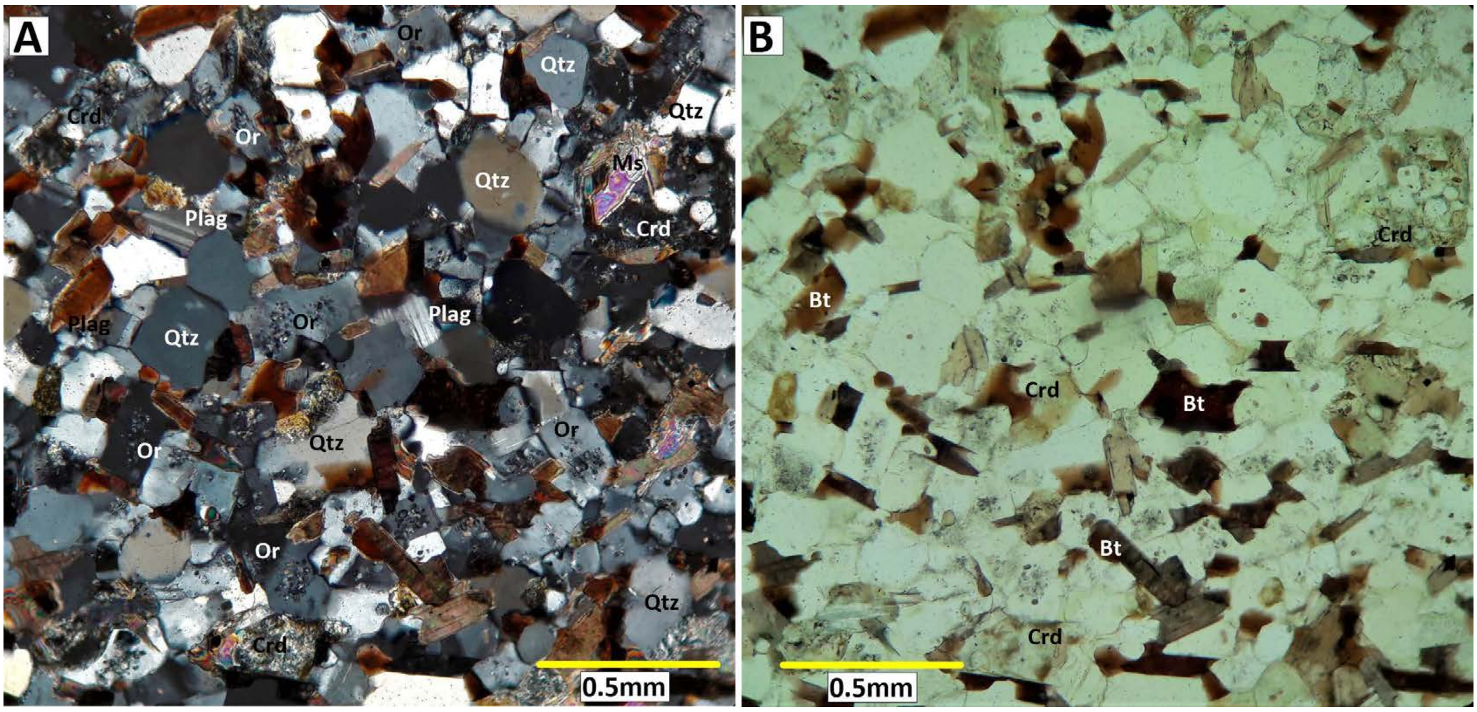

Figure 4.6*: Thin section photomicrographs, in cross polars (A) and plane-polarized light (B), of the mineral constituents that make up the metamudstone. The granoblastic-polygonal textured matrix is defined by minerals of quartz (Qtz), plagioclase (Pl), orthoclase (Or), biotite (Bt) and altered cordierite (Crd).*

The cordierite grains are typically equidimensional with a sub-elliptical (Fig. 4.5C) to irregular elongate-lenticular geometry (far-top left and right portions of Fig. 4.3C, D) and increase in size (0.35-6mm; e.g. Fig. 4.5C) approaching the intrusive contact. In thin section, the cordierite spots seldom show sector twinning but are poikiloblastic with numerous inclusions (in order of decreasing abundance) of biotite, quartz, muscovite, opaques and chlorite (Appendix B; Fig. B1).

Cordierite is extremely reactive along the retrograde path of metamorphism and its breakdown is a potential monitor of retrogression and hydrothermal activity, including the composition of fluids (Ogiermann, 2002). The term used to describe this breakdown is known as pinitization and the fine-grained products that result from the alteration are termed 'pinite' (Deer et al., 2013). All the cordierite grains present within the metamudstone lithologies have experienced some form of alteration or pinitization (suggesting that the alteration is highly pervasive), albeit to varying degrees ranging from minimal to a complete replacement of primary cordierite. Four distinct types of alteration are observed and are recognized primarily on their composition and textural relationship with the cordierite. Because the interpretation of the origin of each type of cordierite alteration in the metamudstones is not one of the objectives of this thesis, the types of alteration are described in more detail in Appendix B1.

4.3 Main S-type coarse-grained porphyritic granite

The S-type coarse-grained porphyritic granite of the Peninsula Pluton is the most common rock type in the study area. It occurs as a weathered, slightly cream white to grey voluminous granitic mass marked by a series of joints (with one set trending NW-SE to NNW-SSE and the other set trending NE-SW to NNE-SSW) which crosscut each other in most localities but do not offset each other (Fig. 4.7A). It is the coarsest granite phase at the Sea Point contact outcrop and is characterized by large (2.5-10 cm in length) cream white K-feldspar phenocrysts (or megacrysts for the larger varieties) which are set in a relatively coarse-grained matrix comprising quartz (1-4.5 mm; 35 vol.%), smaller K-feldspars (1.5-4 mm; 30 vol.%), plagioclase (2-5.5 mm; 20 vol.%), biotite (2-2.5 mm; 8 vol.%), cordierite (2-6.5 mm; 5 vol.%) and muscovite (0.05-1 mm; 2 vol.%) (Fig. 4.8A). Tourmaline, zircon, apatite, opaques, rutile and garnet occur as accessory phases. In general, the main coarse-grained porphyritic granite is largely undeformed and only shows a few microstructures in the form of undulose extinction and subgrain boundaries. These are shown by the quartz grains (both the phenocrystic quartz variety and the smaller subhedral to anhedral quartz grains which occupy interstitial sites in the matrix).

The coarse-grained porphyritic granite in the northern section of the map (Fig. 4.1), which outcrops over a distance of approximately 25 meters laterally, retains the same overall mineralogical and compositional characteristics as its southern counterpart, except that it is more biotite-rich. Furthermore, there are similarities in the mineralogy and textural features between the main coarse-grained porphyritic phase and the hybrid granites in the form of the medium- and coarse-grained porphyritic hybrids. Due to this, some of the common features between the aforementioned phases (e.g. biotite-quartz clots, feldspar megacrysts and pinitized cordierite grains) shall be described collectively in this section to avoid repetition in the lit-par-lit zone section where the hybrid phases are discussed separately.

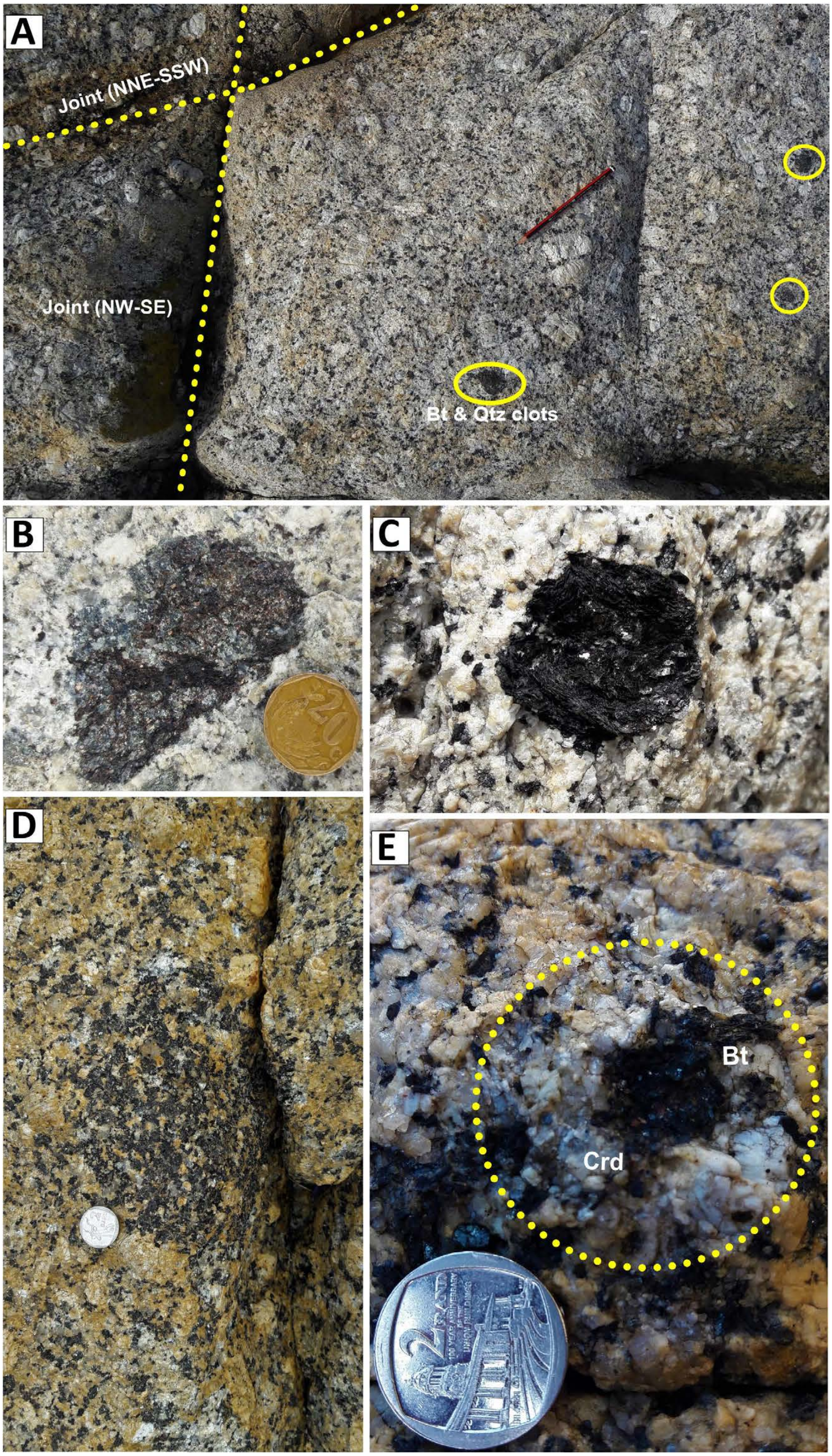

Figure 4.7*: Outcrop appearance of the S-type coarse-grained porphyritic granite and the various features associated with it. (A) Coarse-grained porphyritic granite body, with a series of biotite (Bt)-quartz (Qtz) clots developed within it, cross-cut by two sets of joints. One set assumes a dominantly NW-SE orientation while the other trends in a NNE-SSW direction (pencil points to the north). (B) Close-up view of a subhedral Bt-Qtz clot dominated by Qtz as opposed to Bt. (C) Close-up view of a sub-rounded Bt-Qtz clot dominated by Bt as opposed to Qtz. (D) Fairly large rounded Bt-dominated Bt-Qtz clot feature exposed at the northern coarse-grained porphyritic granite sheet. (E) Outcrop appearance of Cordierite (Crd). The grain is being replaced (pinitized) by Bt from the core outwards. Diameter of 2 rand coin = 2.2 cm; diameter of 20 cent coin = 1.9 cm.*

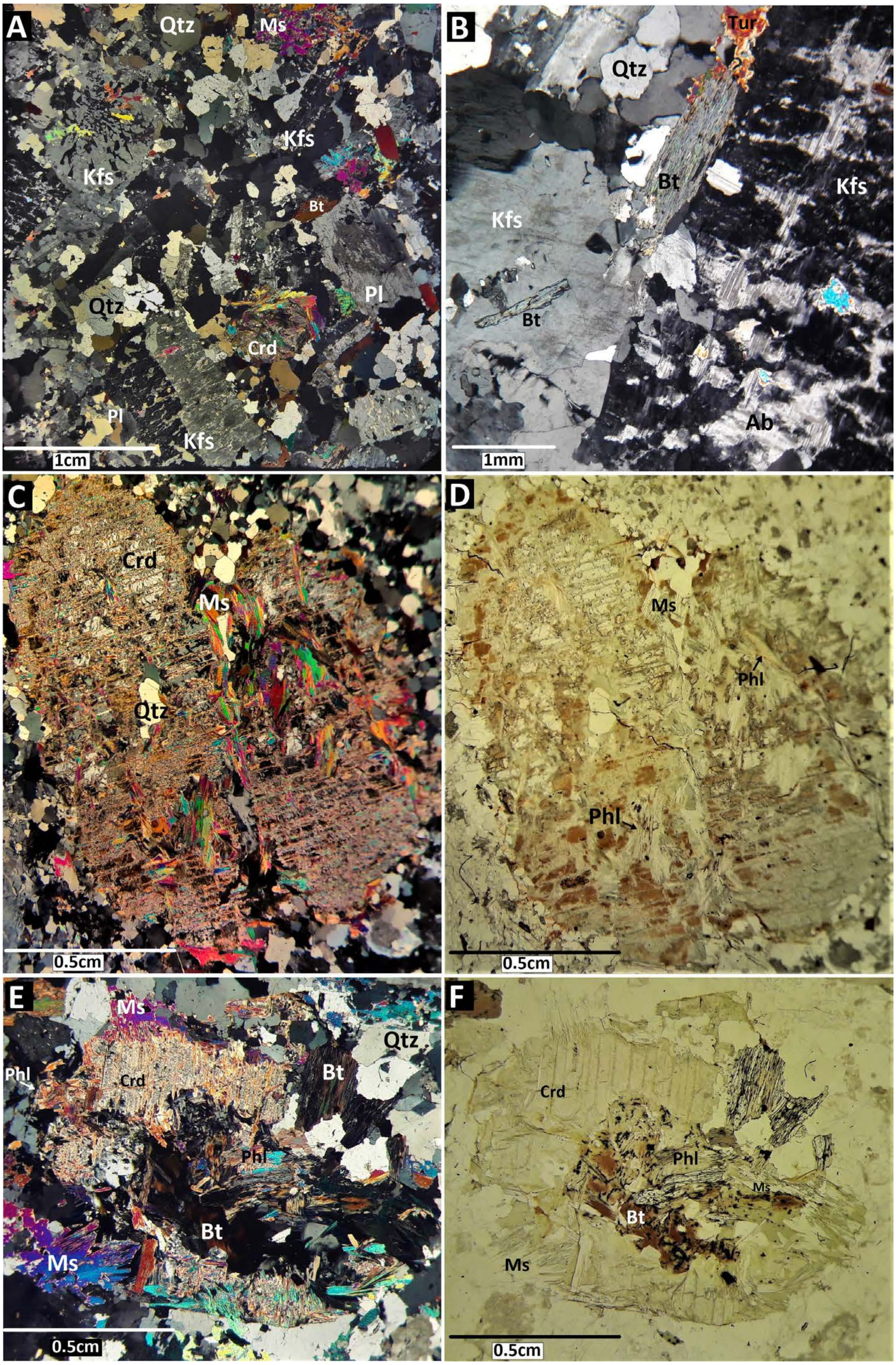

Figure 4.8*: Thin section photomicrographs, in cross polars and plane-polarized light, of some of the common textural features of the S-type coarse-grained porphyritic granite. (A) Mineral constituents comprising the coarse-grained porphyritic granite; it is characterized by K-feldspar (Kfs) phenocrysts sitting within a coarse matrix comprising Qtz, Pl, Bt, muscovite (Ms) and Crd. (B) Close-up view of a Kfs grain showing exsolution textures as evidenced by exsolved lamellae of twinned albite (Ab) within its body. (C) & (D) Crd grain affected by alteration, but complete alteration never took place as evidenced by remnants of Crd. (E) & (F) Crd grain affected by a more severe form of alteration. The alteration constituents are comprised of micaceous material in the form of Ms, Chl, Ser, Bt and phlogopite (Phl). Other mineral abbreviations not mentioned in the description: Tur-Tourmaline.*

The K-feldspar grains can be subdivided into two types based on grain size and shape: (1) 2.5-10 cm long, commonly Carlsbad-twinned (e.g. bottom mid-portion of Fig 4.8A, Fig. 4.10B), euhedral to subhedral crystals (e.g. 4.10A) which gives the rock its distinctly porphyritic texture, (2) 1.5-4 mm subhedral to anhedral grains that form part of the matrix. Both K-feldspar types occur as one of two varieties, microcline (less common) or orthoclase (more common). Both K-feldspar varieties commonly exhibit perthitic exsolution textures (bottom mid-portion of Fig. 4.8A; Fig. 4.11). The exsolution takes one of two forms: (1) microperthite which is more defined within the K-feldspar grains in the groundmass or matrix, and (2) coarse vein perthite with clearly discernable twinned albite-rich plagioclase lamellae which are visible within the more K-feldspar megacrystic variety (Fig. 4.8B). Due to the occurrence of orthoclase and microcline, even within the same thin section, further use of the term “K-feldspar” will be used to refer to the occurrence of either orthoclase and/or microcline henceforth. An additional texture shown by the K-feldspar grains is a granophyric texture defined by branching quartz rods set in a single crystal of feldspar (e.g. Winter, 2010) (upper-left portion of Fig. 4.8A).

All the cordierite grains have experienced pinitization to some degree, with the severity of pinitization varying from grain to grain. Some grains retain traces of the original cordierite grain (Figs. 4.8C, D), whereas some are completely altered to pinite (representing a severe or heavy form of alteration) (Fig. 4.8E, F). The alteration affecting the cordierite grains in all the granite phases exposed in the study area is not varied (i.e. does not consist of several types) as is the case within the metamudstones (Appendix B1; Fig. B1). Instead, the most common cordierite alteration type in the various granite phases involves aggregates of fine- to medium-grained micaceous material (some too fine-grained to be identified) replacing cordierite. The aggregates in question are comprised of chlorite, muscovite (white mica), biotite and phlogopite (green-brown Ti-poor biotite) (Fig. 4.8C–F). This is similar to Type I alteration in the metamudstones (Appendix B1).

The biotite grains not involved in the replacement of cordierite are present in one of two forms: (1) matrix-occupying individual grains (with sizes up to 4.5 mm) and (2) those which form part of biotite-quartz clots. The individual biotite grains that form part of the matrix range from being partially chloritized (Fig. 4.9B) to being completely transformed to chlorite, with the latter locally resembling amorphous grains (Fig. 4.9C, D). These chloritized biotite grains commonly have needle-like inclusions of exsolved rutile (more distinct within the more strongly altered biotite grains) arranged in a rectilinear pattern to define a sagenitic texture (e.g. Gary et al., 1972) (Fig. 4.9C, D). The occurrence of sagenitic rutile within a biotite host is a very common feature amongst all the various granitic phases exposed in the study area. Another common feature observed is the replacement of biotite by tourmaline (Fig. 4.9A).

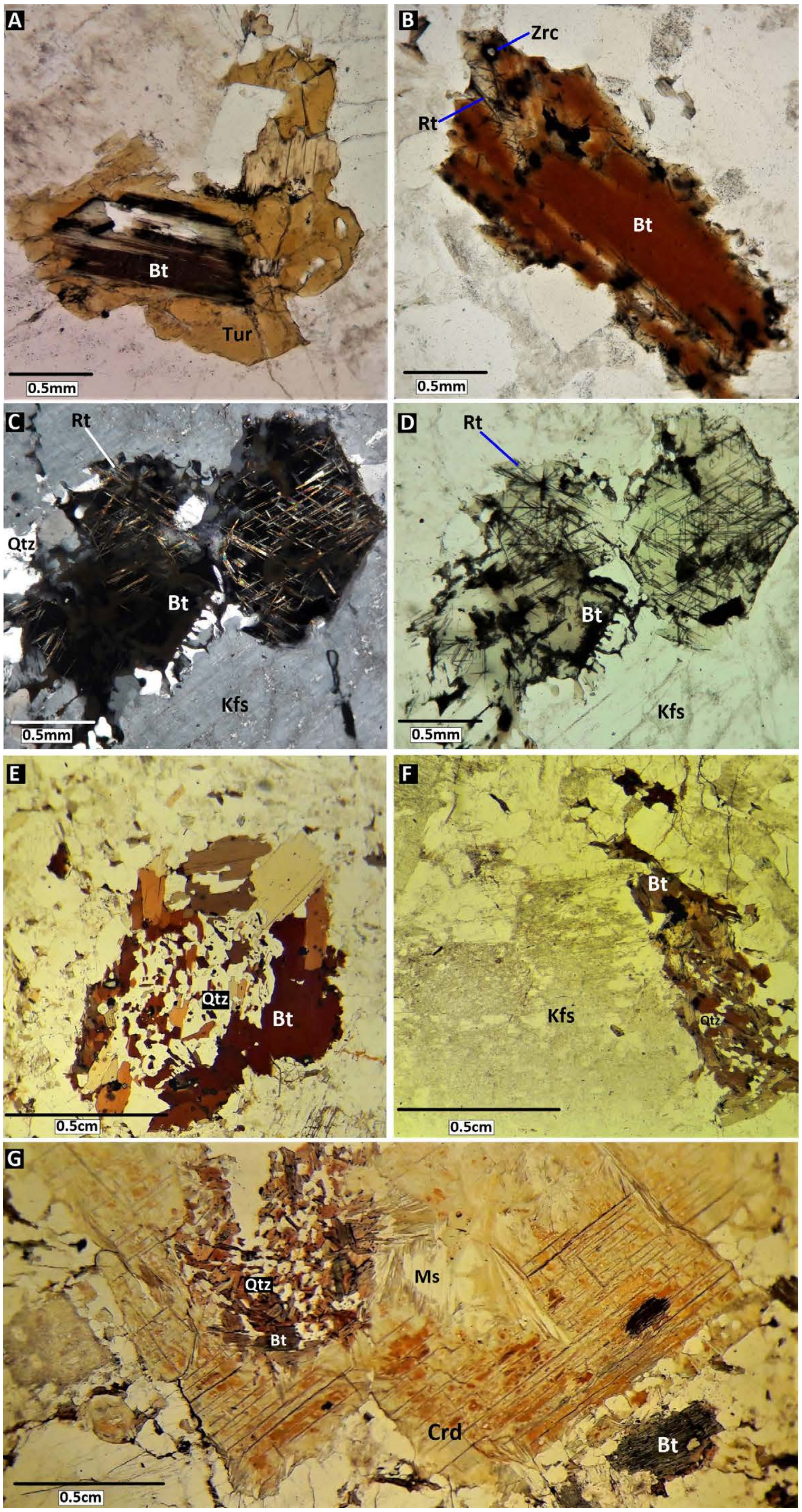

Figure 4.9: *Thin section photomicrographs, in cross polars and plane-polarized light, showing some of the textural features involving Bt. (A) Chloritized Bt grain being replaced by Tur. (B) Partially chloritized Bt grain with radiation haloes caused by zircon (Zrc). The reddish-brown colour of the Bt grain suggests a high Ti content (Deer et al., 2013). Small needles of rutile (Rt) occur as inclusions. (C) & (D) Highly chloritized Bt grain, resembling amorphous like-material, with well-developed needle-like inclusions of Rt that are arranged in a rectilinear pattern to define a sagenitic texture. The Bt grains are hosted in a Kfs host and rimmed by a reaction texture involving wormy-intergrowths of Qtz reacting with the surrounding Kfs host. (E) Thin section view of the various Bt-Qtz clots that are widespread in the coarse-grained porphyritic granite. They are also locally involved in the replacement of Kfs- (F) or Crd-grains (G).*

The biotite-quartz clots are rounded to subhedral (Figs. 4.7A–D, 4.9E) and are widespread throughout the main coarse-grained porphyritic phase and porphyritic hybrid phases but are absent within the more biotite-poor leucocratic fine-grained granites and aplitic phases. They have an average size of 1-3 cm but can attain sizes up to 7.5 cm (in width). Typically, they tend to have finer-grained quartz and biotite compared to the surrounding matrix. Additionally, the biotite fractions within the clots tend to predominate over the quartz fraction (Figs. 4.7C, D), however, on a less common basis the converse, also occurs (Fig. 4.7B). Petrographically, three types of biotite-quartz clots occur and are described in Appendix B2.

4.3.1 Inclusion trails and growth zone textures of feldspar megacrysts (both K-feldspar and plagioclase)

In the field, most of the K-feldspar megacrysts observed are poikilitic to semi-poikilitic and commonly have crystallographically oriented biotite inclusions aligned relative to the internal zonation of the K-feldspar grains (Fig. 4.10A, C). The biotite inclusions have smaller sizes (< 0.3 cm) than those in the host granites in all cases. Moreover, in some settings, particularly noticeable on weathered surfaces, inclusions of small plagioclase crystals are aligned along zone boundaries of the K-feldspar grains (Fig. 4.10C).

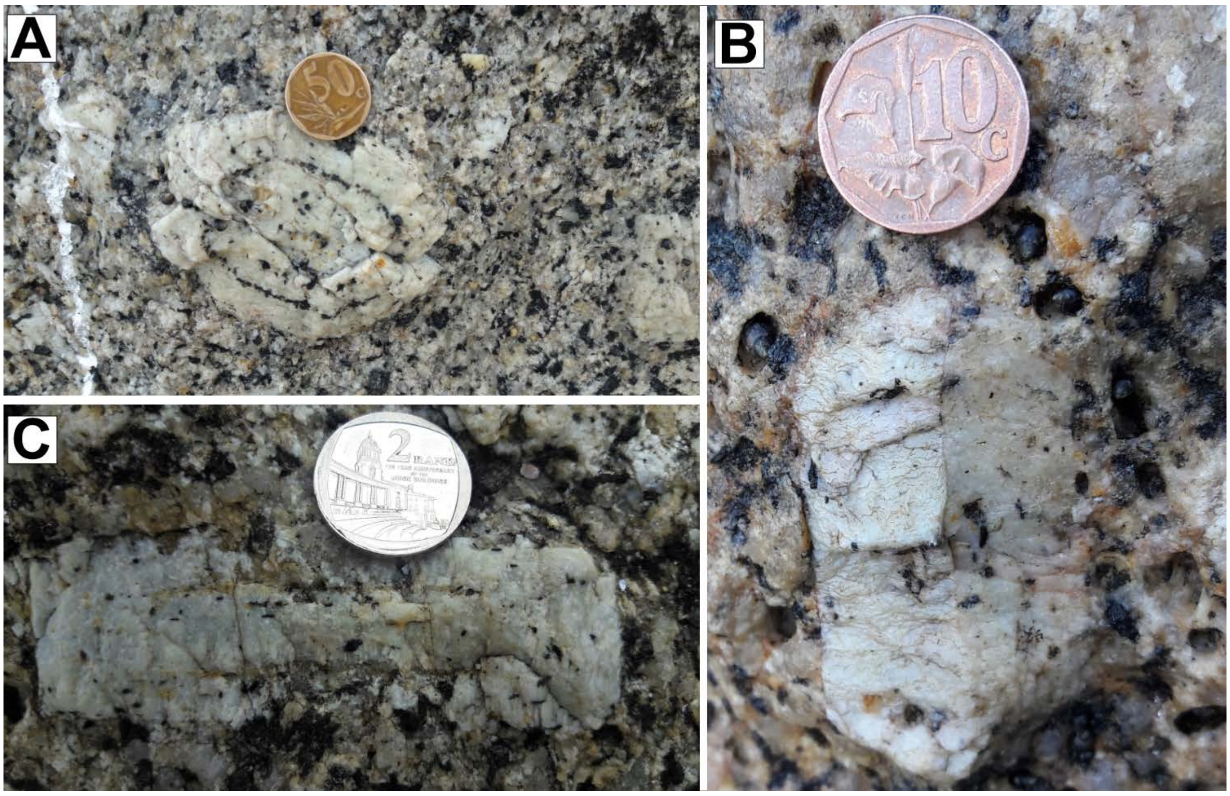

Figure 4.10*: Outcrop photographs of variably-sized and shaped K-feldspar megacrysts which form part of the coarse-grained S-type granite. (A) Poikilitic subhedral K-feldspar measuring 10 cm in length. Note the well-defined zone parallel arrangement of biotite inclusions relative to the inner core or inner-zone boundary of the megacryst. (B) Euhedral K-feldspar grain showing Carlsbad twinning (diameter of 10c coin = 1.6 cm). (C) Poikilitic euhedral K-feldspar grain on a weathered surface locally showing an alignment of small plagioclase (trace of yellowish coloured minerals) and biotite crystals along the inner zone boundaries of the grain.*

Petrographically, the K-feldspar grains show evidence of concentric zoning, however, it is usually not well-defined due to the occurrence of perthite exsolution textures, which mask the appearance of zoning (Fig. 4.11B). Where discernible, the zoning is usually recognizable in one of two ways: (i) slight differences in colour within the K-feldspar grain (with the rotation of the microscope stage at a fixed point), reflecting one composition in the interior of the crystal and a gradually changing composition toward the outer edge of the crystal (e.g. Winter, 2010), and (ii) preferential alignment of inclusion minerals relative to the zone boundary they occur within (Fig. 4.11B).

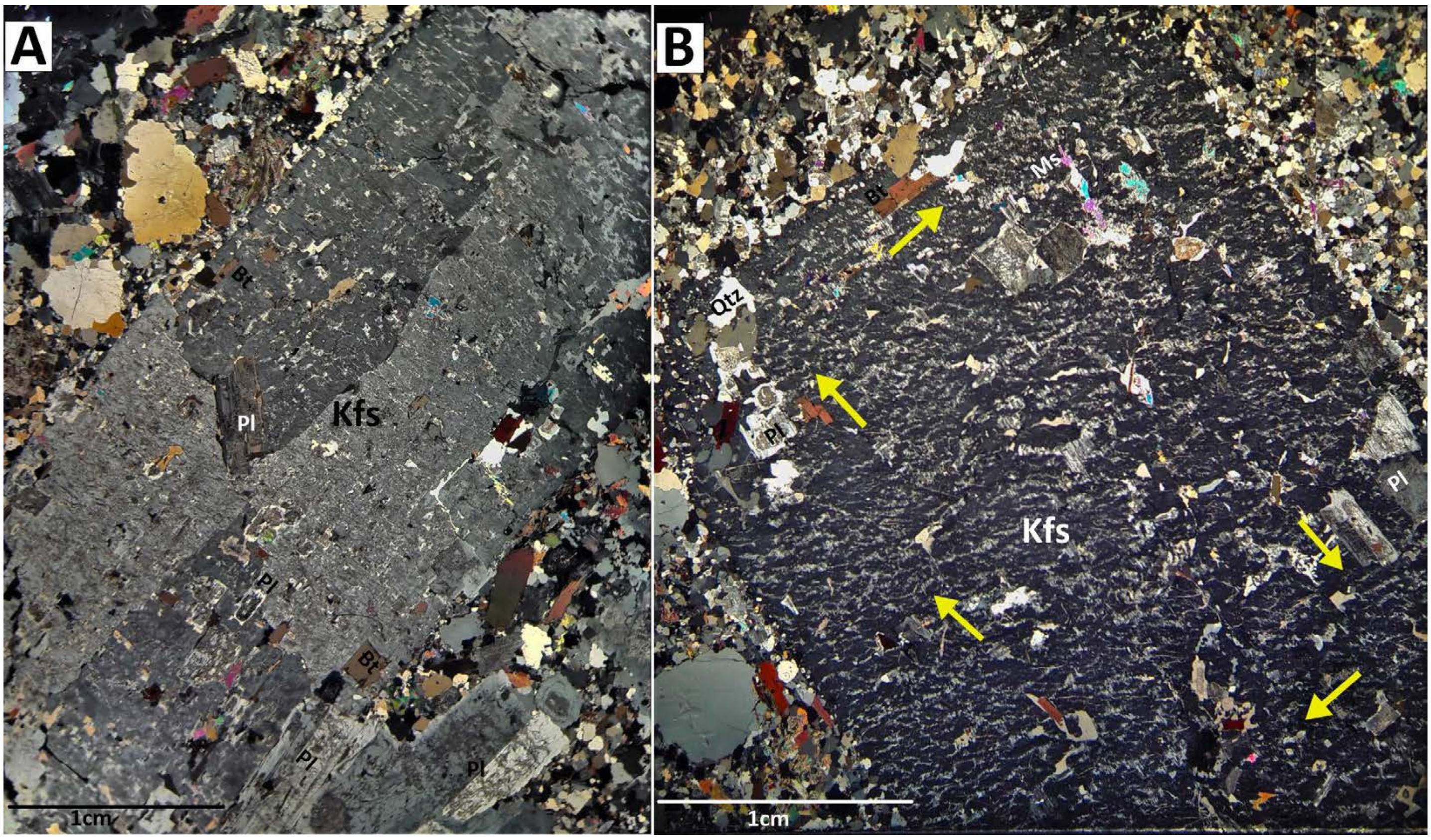

__Figure 4.11__: (A) Thin section photomicrograph of a sector twinned Kfs megacryst in sample SP32/2 (medium-grained porphyritic granite) in cross polars. (B) Thin section photomicrograph of a part of a Kfs megacryst in sample SP34 (medium-grained porphyritic hybrid granite) in cross polars showing zonally arranged inclusions, principally Pl and Bt. The rim of the Kfs grain has preferentially aligned fine-grained inclusions of Qtz. An inner and outer zone (described in more detail in the text) is distinguished based on the arrangement/distribution of the inclusions in the core and rim of the grain.

The type of inclusions occurring in the K-feldspar grains, in order of decreasing abundance, include quartz, biotite, plagioclase, muscovite, opaques and garnet. The quartz grains, in particular, show a marked parallel alignment commonly near the outer margin of the K-feldspar grain (Fig. 4.11A, B). In some of the K-feldspar megacrysts, plagioclase and biotite inclusions show a marked alignment of their long axes parallel to the zones in which they occur (Fig. 4.11A, B). The zones in which they occur are commonly the outer boundary of the inner zone and a change of orientation of the inclusions at the border of the zones is also observable in certain cases as well (Fig. 4.11B). The K-feldspar megacrysts also show evidence of sector (or cyclic) twinning (Fig. 4.11A).

The plagioclase phenocrysts show evidence of zoning to a much better extent relative to the K-feldspar megacrysts. The zoning is characterized by several fairly well-developed oscillating zones of different compositions (Fig. 4.12A). One of the most common textural features shown by the plagioclase grains within all the granite phases is the strong alteration (i.e. sericitization) of the inner core relative to the outer core/rim, which remains relatively unaltered (Fig. 4.12D). Another prevalent textural feature shown by the plagioclase grains is the occurrence of cumulophyric textures defined by multiple-grain clusters of adhering plagioclase phenocrysts (Winter, 2010) (Fig. 4.12C). Carlsbad twinning also occurs but is rare (Fig. 4.12B).

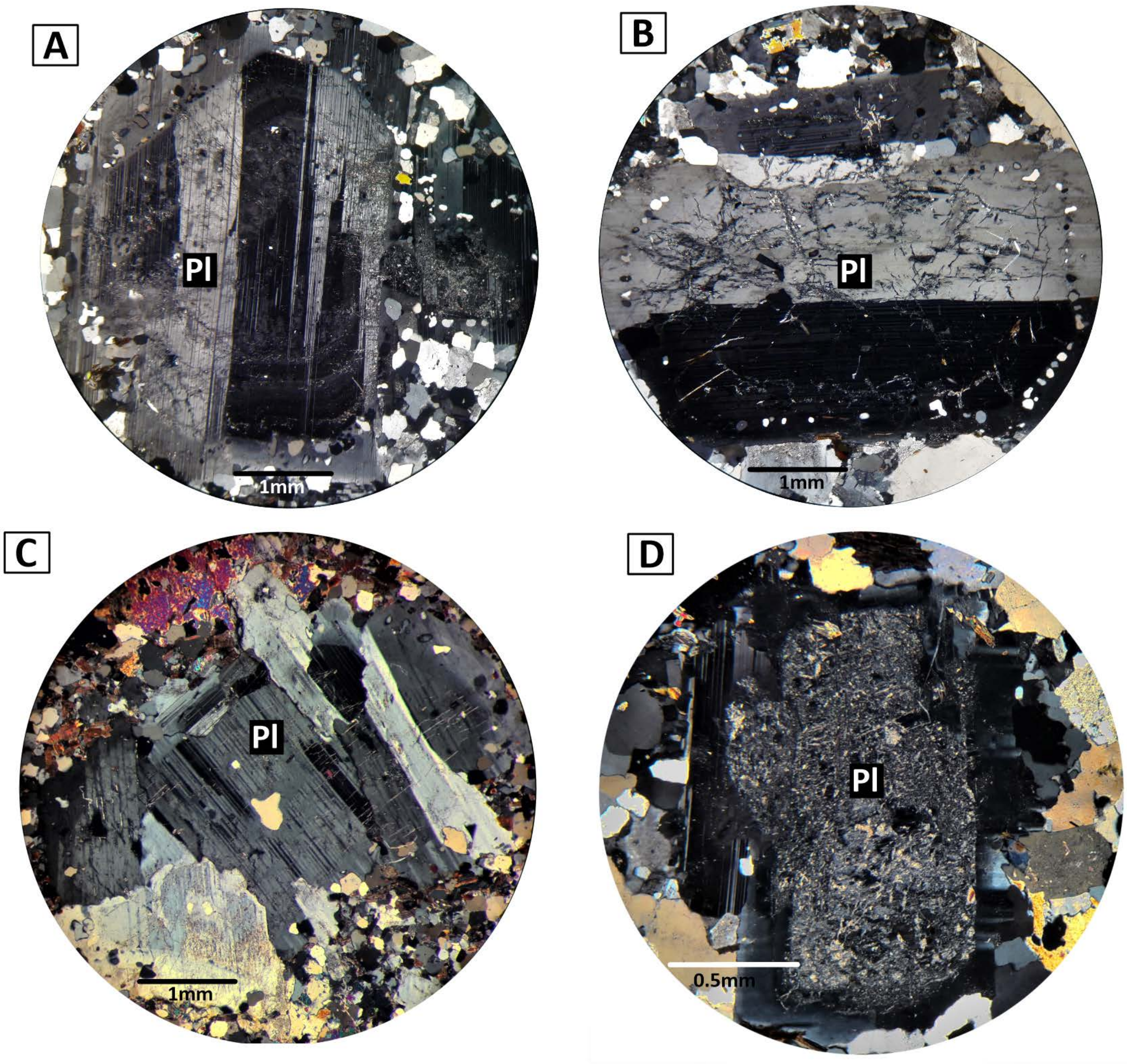

Figure 4.12*: Thin section photomicrographs, in cross polars, of the typical textural features of Pl phenocrysts within the various granite phases exposed in the study area. (A) Pl in sample SP36/2 characterized by oscillatory zoned boundaries. The grain also has broad polysynthetic twins, some of which are wedge-shaped and indicative of deformation. (B) Carls-bad twinned Pl grain in sample SP42 with a well-developed alignment of Qtz along the outer edge of the inner zone boundary. The outermost-rim is entirely inclusion-free. (C) An aggregate of interlocking Pl crystals in sample SP4 defining a cumulophyric texture. (D) An example of one of the more common textural features shown by Pl phenocrysts whereby the core structures of the grains are more altered relative to their rims; Pl grain occurs in sample SP11/1.*

4.3.2 Enclaves

Although the population of enclaves within the S-type granite exposed at the Sea Point contact is relatively low, those observed are compositionally variable and include: (i) mafic micro-granitoid varieties (Fig. 4.13G), (ii) biotite-granite varieties (Fig. 4.13A, C) and (iii) granodiorite varieties (Fig. 4.13B, D, E). The mafic micro-granitoid enclaves are present as dark grey sub-rounded or oval-shaped bodies (as large as 12cm) which define sharp contacts with the host granite (Fig. 4.13G). They are comprised of biotite (most abundant), quartz, K-feldspar and plagioclase and occur either as isolated individual bodies or as multiple bodies defining a cluster (Fig. 4.13G). Although not always the case, some of the micro-granitoid enclaves have inclusions of rounded subhedral K-feldspar grains (bottom left portion of Fig. 4.13G) which are much smaller than the K-feldspar megacrysts in the surrounding matrix of the host granite.

Biotite-granite enclaves occur either as fairly large (Fig. 4.13A) 20 cm (length) porphyritic masses or smaller sized (6-10 cm in length) masses (Fig. 4.13C). Both types are comprised of biotite, quartz, K-feldspar and plagioclase. Moreover, they both host rounded to sub-rounded biotite clots (Fig. 4.13A, C). The fairly large-sized biotite-granite enclave population form gradational contacts with the granite host due to having K-feldspar megacrysts inclusions which are similar in size and texture to the granite host (Fig. 4.13A). In contrast, the smaller biotite-granite enclaves define fairly sharp contacts with the host granite due to their fine-grained sizes and having K-feldspar inclusions of much smaller size (< 1cm) compared to the host (Fig. 4.13C).

The granodioritic enclaves are present as small sub-rounded bodies (Fig. 4.13D; 5-10 cm in length) or as fairly large, angular, irregularly shaped bodies (Fig. 4.13B, E). Both types have mostly sharp contacts with the host granite, however, the fairly large granodioritic enclave bodies tend to show gradational contacts (e.g. 4.13E). They are composed of biotite, quartz, K-feldspar and minor plagioclase. In some cases, these enclaves can be locally porphyritic by having similarly sized K-feldspar megacrysts as the host granite (Fig. 4.13B, E). An explanation that accounts for why all the compositionally variable enclaves in the study area have varying sizes and different contact relationships with the host coarse-grained porphyritic granite is provided in Appendix B3.

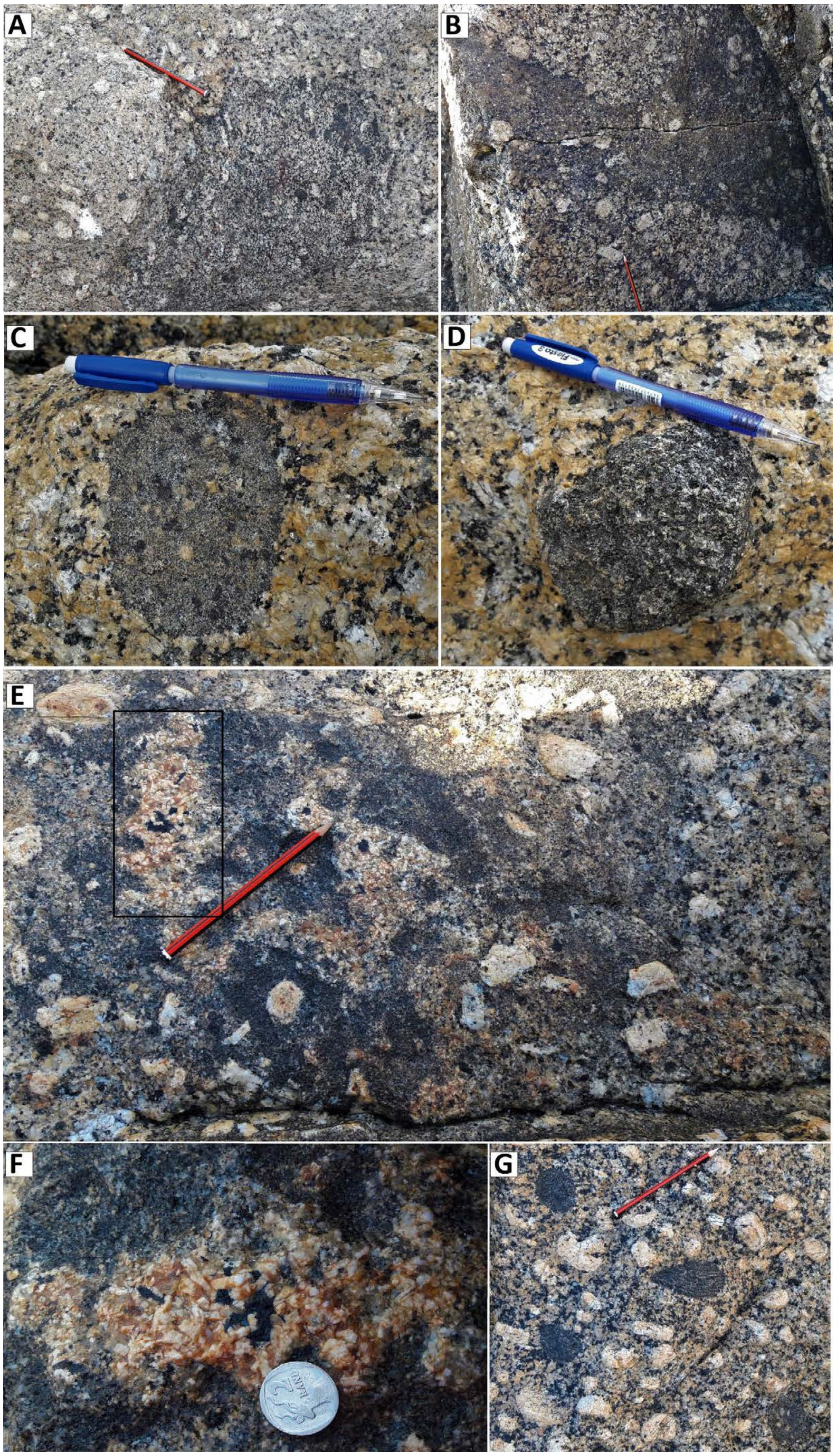

***Figure 4.13**: Outcrop photographs of the compositionally variable enclaves in occurrence within the S-type porphyritic granite outcropping at the southern- (A) and northern- (B, C, D, E, F, G) portion of the study area respectively. (A) Sub-rounded coarse-grained porphyritic biotite-granite enclave, with a cluster of biotite clots (top right portion of A), defining a gradational contact with the host granite. (B) Locally porphyritic and irregularly shaped granodiorite enclave defining a sharp boundary with the host granite. (C) & (D) The other variations of the biotite-granite and granodiorite enclaves respectively; both form local sharp contacts with their host. (C) Is rounded to ovoid, fine-to medium-grained, partly porphyritic and also has small rounded biotite clots as in (A). (D) Is rounded, fairly coarse-grained as (B) but is non-porphyritic. (E) A portion of an irregularly shaped granodiorite enclave, which forms fairly gradational contacts with the host at that portion of the outcrop. Occurring within the enclave are irregularly shaped quartzofeldspathic patches with accumulations of K-feldspar (demarcated by black-square); (F) is a close-up view of said features. The K-feldspar grains (0.5-1.5 cm) are smaller than those of the surrounding host granite. (G) Typical appearance of the microgranitoid enclaves. They are biotite-rich, small sub-rounded to oval-shaped bodies forming sharp boundaries with the host granite. Pencils point to the north.*

4.3.3 Aplites

The main coarse-grained porphyritic granite also contains fine-grained, white-grey to tan-brown leucocratic aplitic bodies. They are present either as elongate vein-like bodies that traverse the granitic body (Fig. 4.14A), semi-rounded to semi-tabular bodies (Fig. 4.14C), or as small (< 20 cm in length) rounded blob-like bodies protruding out of the host granite (Fig. 4.14D). The latter two are less common. The aplite bodies are mostly oriented in an E-W to WNW-ESE direction and traverse at an oblique angle to the NNE-SSW joint set and are roughly subparallel to the NW-SE joint set cutting across the S-type pluton (Fig. 4.14A). The aplitic bodies define a predominantly sharp contact with the host granite but there are instances where the contact is locally gradational (Fig. 4.14C). These aplitic bodies have different sizes (up to 6.5 m in length and 0.8 m in width) and are mostly composed of quartz (0.13-1 mm; 38 vol. %), K-feldspar (0.5-2.5 mm; 35 vol. %) and plagioclase (0.75-1 mm; 25 vol. %) to define an overall equigranular to partly inequigranular texture (Fig. 4.14B). They have minimal biotite (<1mm; 1 vol. %) and muscovite (0.075-0.5 mm; 1 vol. %) content and have accessory phases of apatite, monazite, opaques and tourmaline.

***Figure 4.14**: Outcrop and thin section view of the aplite bodies associated with the S-type coarse-grained porphyritic granite. (A) The most common form of the aplite present as an elongate and narrow body traversing across the granite body at an angle sub-parallel to the NNW-SSE exhumation joint set which cross-cut the granite; pencil points to the north. There are, however, a few aplite bodies which traverse at an angle oblique to this joint set. (B) Thin section photomicrograph, in cross-polars, of the mineralogy of the aplites. They are dominantly quartzofeldspathic and mica poor, with the K-feldspars commonly showing exsolution textures. (C) and (D) are the less common forms of the aplite. (C) A semi-rounded, pod-like form of the aplite defining a gradational contact with the host granite. (D) Aplites outcropping as rounded blob-like masses protruding out of the host granite.*

4.3.4 Magmatic structures

The coarse-grained porphyritic S-type granite of the study area hosts a few magmatic structures. Such magmatic structures include mafic schlieren (mechanical concentration of mafic minerals; Fig. 4.15C, D) and megacrystic magma pipes or tubes (mechanical concentrations of K-feldspar; Fig. 4.15A, B).

Crystal-laden batches of magma or megacrystic pipes are the most commonly occurring magmatic structural feature in the study area. Megacrystic pipes, or simply ‘pipes’, are defined by Farina et al. (2012) as enclosed cylindrical-shaped accumulations of megacrysts that consist of more than 70 vol.% of K-feldspar megacrysts. They are more prominent in the lit-par-lit zone and the northern coarse-grained granite sheet, where they can reach vertical lengths of up to approximately 5.5 m and widths of 2 m (Fig. 4.15A). In the southern portion of the mapped area, where the main S-type pluton predominates, the pipes are less prominent and smaller in length (up to 1.5 m) and width (up to 0.5 m) (Fig. 4.15C). In general, the pipes consist of the same mineralogy as described for the host granite, and the numerous K-feldspar megacrysts, that define these accumulations, are similar to those occurring within the host granite in terms of size, shape and texture.

Schlieren structures are present as thin to relatively thick (1-8.5 cm), elongate dark coloured bands with large amounts of biotite and either show an association with K-feldspar accumulations (Fig. 4.15C) or occur independently from them (Fig. 4.15D). The schlieren structures associated with K-feldspar accumulations occur as thin and relatively faint bands bordering the K-feldspar accumulations and are concentrated mostly in the southern portion of the mapped area (Area 1; Fig. 4.1). Those that have no association with K-feldspar accumulations are usually present as thicker, curved tube-like masses showing evidence of a regular repeated gradation or alternation defined by biotite-rich layers and K-feldspar-quartz layers, with both layers being finer-grained than the surrounding host granite (Fig. 4.15D).

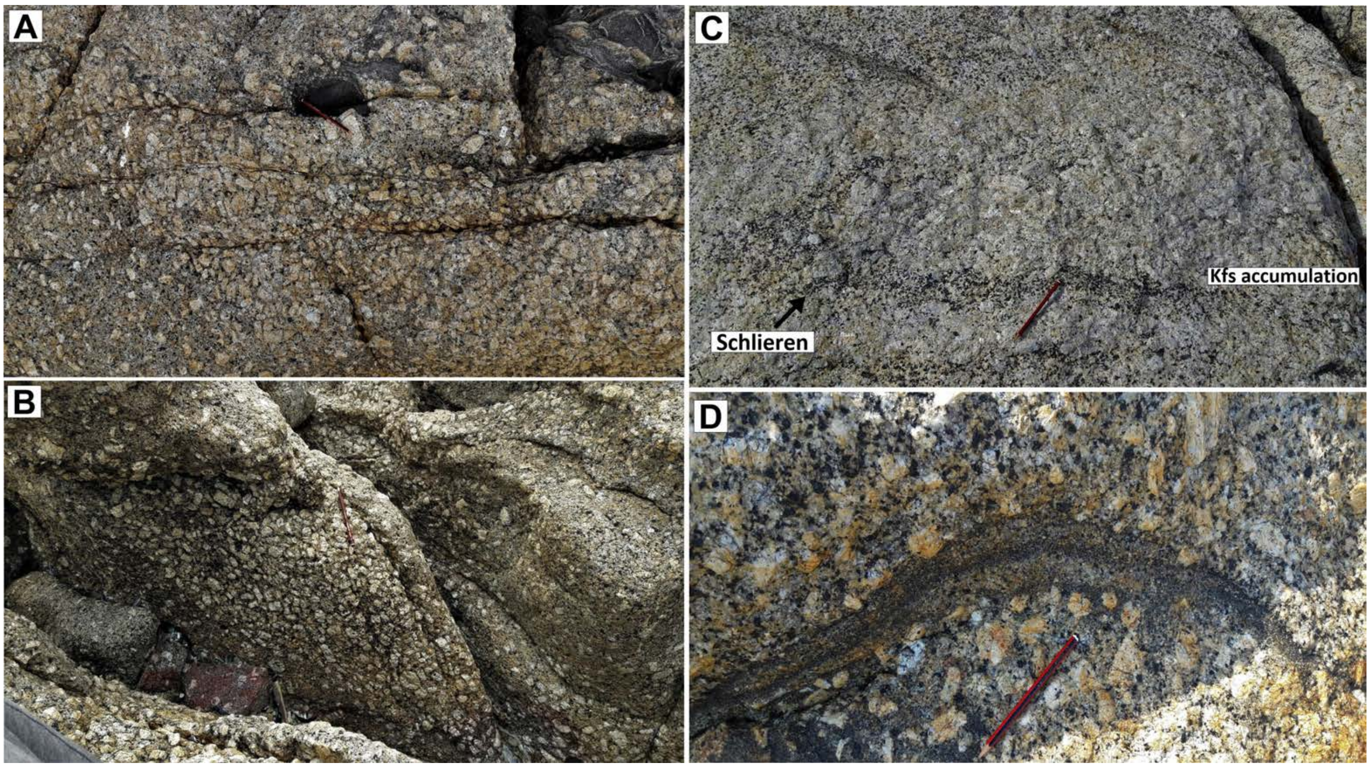

***Figure 4.15**: Magmatic structures outcropping in the study area. (A) & (B) Outcrop photographs of K-feldspar megacryst accumulations in the northern coarse-grained porphyritic granite sheet developed on a sub-horizontal surface (A) and sub-vertical surface (B). Note the fairly well-defined alignment defined by the preferred orientation of the long axes of the K-feldspars on the subvertical surface in (B). (C) & (D) Schlieren structures preserved within the host coarse-grained porphyritic granite exposed in the southern- (C) and northern-portion (D) of the study area respectively. (C) Local K-feldspar megacryst accumulation with biotite-rich schlieren layers rimming the margins of the K-feldspar accumulations. (D) Curved or bow-shaped schlieren not associated with K-feldspar accumulations. Note the repeated alternations of biotite-rich layers and quartzofeldspathic layers.*

4.4 S-type microgranites (fine-grained granite)

The microgranite outcrops in two areas within the mapped area, the northern-most region and to the south (Fig. 4.1). From these two regions/areas, it is observed that the contacts between the microgranite with the Malmesbury Group country rock are mostly sharp and evidence of chilled margins are also left preserved. At the northern end of the study area (Fig. 4.1), the micrograntes are present as approximately 8-15 m (on average) long, slightly orange to tan-brown masses (Fig. 4.16A). The microgranites have intruded adjacent to, or along the foliation and/or bedding planes of the Malmesbury country rock, however, they also show evidence of crosscutting relationships with the country rock as well (Fig. 4.16A, B). Although largely non-porphyritic, the microgranite to the north can be locally porphyritic comprising 1.5-5 cm euhedral to subhedral K-feldspar megacrysts (and 1-3 cm plagioclase grains) set within a finer-grained matrix. To the south, the microgranite is locally porphyritic to semi-porphyritic. In areas where the country rock is in contact with the microgranite, the microgranite at the southern end is also clearly intruded primarily sub-parallel to the bedding (Fig. 4.16B). Furthermore, the microgranite to the south forms a transitional or gradational boundary with the adjacent coarse-grained porphyritic granite where both are in direct contact. When both granite types are not in direct contact, the relationship becomes hard to define.

Figure 4.16*: Outcrop photographs of the microgranite outcropping in the northern- (A) and southern-portion (B) of the study area respectively. (A) Slightly orange to tan-brown microgranite intruded along the country rock; the direction of view is SSE. The rock mass outcrops in regions further north from the fairly large scale anticlinal folded structure as shown in Fig. 4.1. (B) Semi-porphyritic microgranite intruded subparallel to the bedding (pencil is oriented subparallel to the compositional banding) of the country rock; the direction of view is NNE. Locally, crosscutting relations do occur as shown by the obliquely oriented microgranite vein (middle-right portion of B) that cuts across the country rock.*

Petrographically, the microgranites are largely undeformed. They are defined by an equigranular texture and are comprised of, in order of decreasing abundance, quartz (0.25-1 mm; 35 vol. %), K-feldspar (0.75-3 mm; 30 vol. %), plagioclase (0.5-2 mm; 28 vol. %), muscovite (0.075-1.5 mm; 4 vol. %), biotite (0.1-2.5 mm; 2 vol. %) and pinitized cordierite (0.25-1.5 mm; 1 vol. %) (Fig. 4.17A). The larger sized K-feldspar, plagioclase and biotite grains in the matrix locally give the microgranite a semi-porphyritic texture (Fig. 4.17B). Tourmaline can reach up to 2 vol.% in sample SP3 (Fig. 4.17D), however, in all other microgranite samples collected, it occurs as an accessory phase along with zircon, apatite, monazite, opaques and rutile (in biotite).

The quartz grains show typical undulose structures and local subgrain boundaries (e.g. bottom- to mid-left portion of Fig. 4.17C). The biotite grains are commonly chloritized and the K-feldspar grains (whether it is the megacrystic variety within the semi-porphyritic microgranites or the smaller varieties forming part of the matrix), are partially sericitized and commonly show Carlsbad twinning and perthitic exsolution textures. The plagioclase grains (both phenocryst and matrix varieties) are also sericitized with the inner core being more sericitized compared to the outer rim. Similar to the main coarse-grained granite, cordierite alteration in the microgranites (Fig. 4.17E) resembles Type I alteration in the metamudstones (Appendix B1). Some of the cordierite grains occurring in the microgranites, however, have an additional phase in the form of tourmaline which forms part of the alteration assemblage (Fig. 4.17F).

4.5 Lit-par-lit zone

The lit-par-lit zone extends laterally (across strike) over a distance of approximately 40 meters. It defines a mostly gradational zone marked by a series of roughly WNW-ESE to NW-SE trending, non-crosscutting sheets of granitic material which traverse along or subparallel to the foliation and bedding structures of Malmesbury Group country rocks. Also, various hydrothermal-related quartz to quartzofeldspathic veins, as well as quartz-tourmaline veins (of various widths and extents), which made use of structural weaknesses within the pre-existing lithology, crosscut the country rock as well as the various granite phases. This adds to the complex nature of the zone.

4.5.1 Petrographic descriptions of the hybrid granite phases

The various hybrid granite phases that outcrop in the lit-par-lit zones are as follows:

(i) Fine-grained phases and their sub-varieties in the form of the fine-grained porphyritic and fine-grained non-porphyritic phases respectively.
(ii) Variably weathered medium- and coarse-grained phases; they both tend to be porphyritic and are the most voluminous hybrid phases in the lit-par-lit zone.

Best exposed in areas 7 and 8 of the mapped area (Fig. 4.1), these hybrid phases mostly pass laterally into each other (gradationally) and show no significant evidence of crosscutting relations relative to each other nor do they show any significant deformational features. Because all of these aforementioned phases have the same mineralogy and textural features as the main coarse-grained porphyritic phase (section 4.3) and the microgranite (section 4.4), the petrographic features of the hybrid granites are summarized in Table 4.1 to avoid repetition (in the text).

In general, the fine-grained non-porphyritic hybrid granite in the lit-par-lit zone (e.g. Fig. 4.18D) resembles the microgranite occurring in the northern portion of the study area in terms of overall appearance, mineral composition and texture. The fine-grained porphyritic granite (Fig. 4.18A) is porphyritic (with phenocrysts of quartz, K-feldspar, plagioclase, biotite and cordierite) and has various biotite-quartz clots.

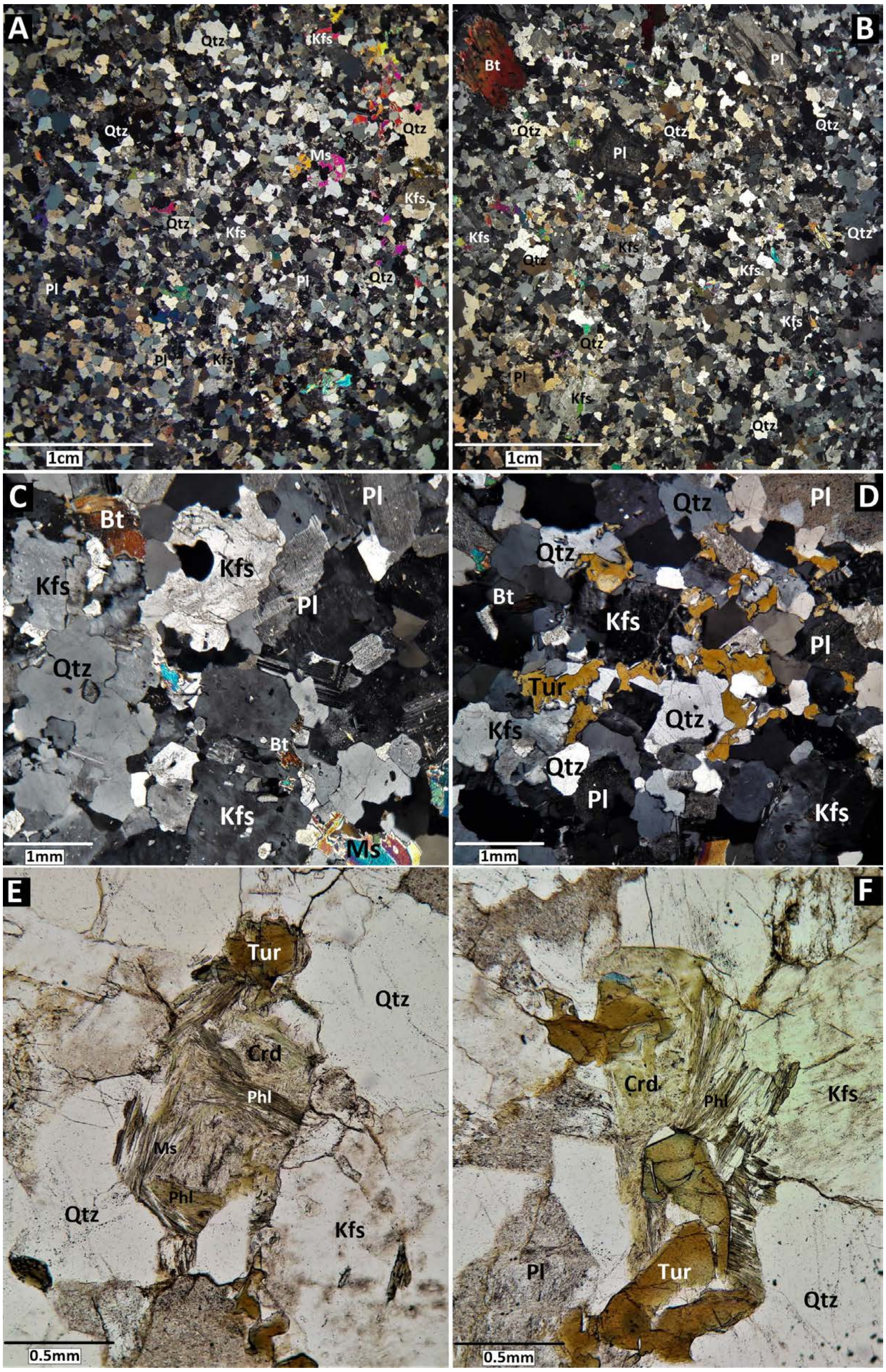

Figure 4.17*: Thin section photomicrographs, in cross polars and plane-polarized light, of the mineralogy and textural features of the microgranite. (A) Typical equigranular and fine-grained matrix associated with the microgranite. It comprises Qtz, Kfs, Pl, with minor amounts of Bt and Ms. (B) Porphyritic to semi-porphyritic microgranite with phenocrysts of Pl, Bt, Qtz and Kfs sitting within a finer-grained matrix. (C) A close-up view of the matrix forming minerals in (A). (D) Tur clusters which occur in some of the microgranite samples. (E) & (F) Crd grains replaced by an alteration assemblage of Ms, Bt, Phl and chlorite along with an additional constituent in the form of Tur.*

The medium- (Fig. 4.18B) and coarse-grained porphyritic hybrid phases (as well as intermediate varieties that incorporate aspects of both; Fig. 4.18C) resemble the main coarse-grained porphyritic phase at the southern end of the study area in terms of overall appearance, mineral composition and texture. The only differences between the phases come in the form of grain size (the main phase granite has overall coarser grain sizes), and the fact that the hybrid medium- and coarse-grained phases have a slightly higher biotite content.

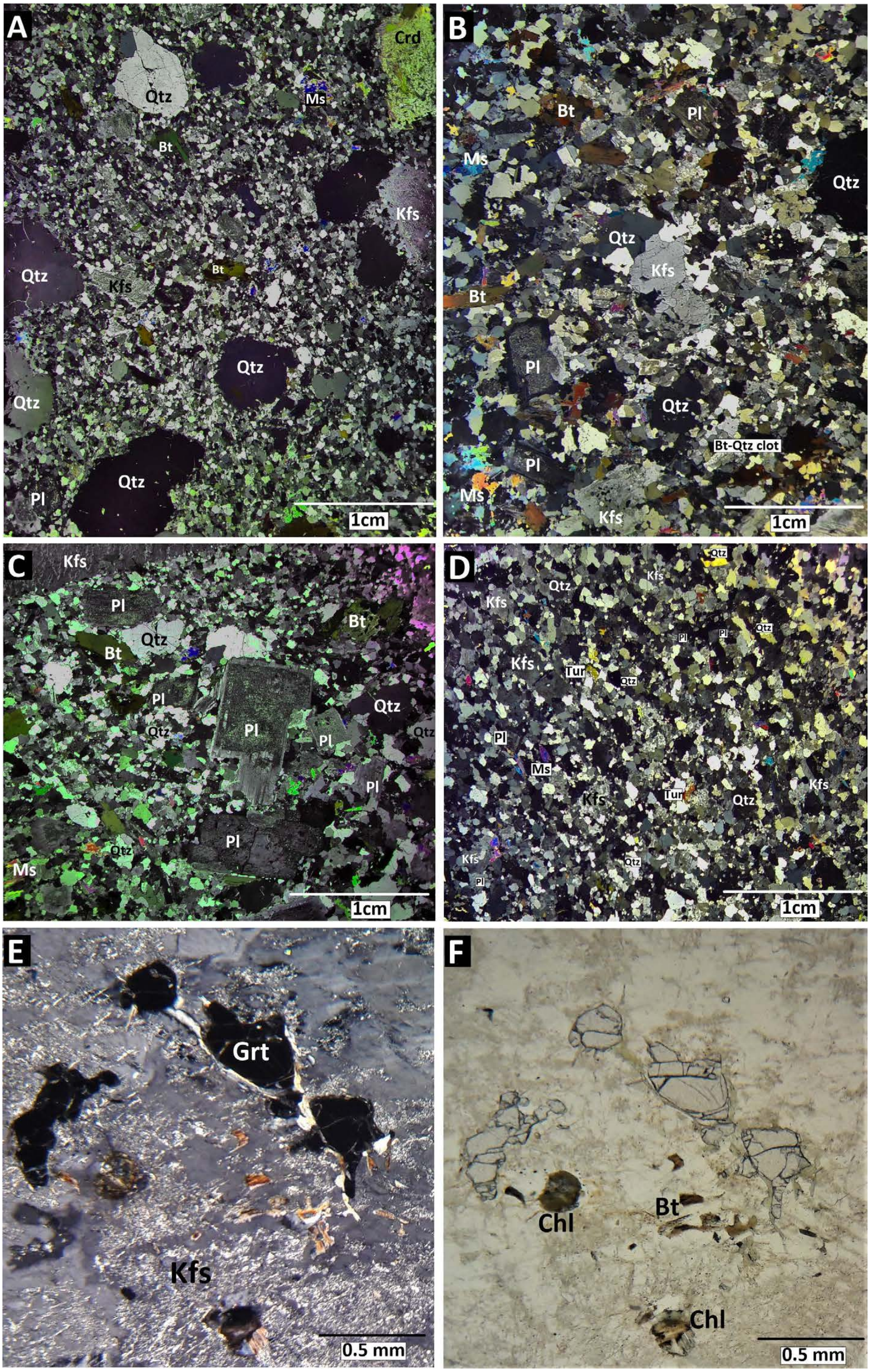

***Figure 4.18**: Thin section photomicrographs of the various hybrid granite phases that occur in the lit-par-lit zone (in cross-polars). (A) Fine-grained porphyritic hybrid granite. (B) Example of a medium-grained porphyritic hybrid granite phase. (C) Medium- to coarse-grained hybrid granite phase. (D) Fine-grained non-porphyritic hybrid granite phase. (E) & (F) Inclusion-free subhedral garnet (Grt) inclusions rimmed by chlorite (Chl) and preserved within in a Kfs megacryst. The Grt grains are observed more readily in the medium- and coarse-grained hybrid phases compared to the main phase granite (most likely due to a larger sample set for the hybrid granites). From petrographic studies, all Grt grains occur exclusively as inclusions within K-feldspar megacrysts, and evidence of Grt as a normal matrix mineral or Crd pseudomorphs after Grt, as described by Farina et al. (2012), was not observed.*

Table 4.1: Mineralogy, grain sizes, abundances and textural features of the hybrid granite phases in the lit-par-lit zone.

Hybrid granite phase	Mineralogy, grain sizes and abundances	Textural features
Fine-grained non-porphyritic	**Matrix**: is fine-grained, with average crystal sizes between **0.1-3 mm**. It comprises quartz (38 vol. %), K-feldspar (29 vol. %), plagioclase (26 vol. %), muscovite (4 vol. %), biotite (2 vol. %) and cordierite (1 vol. %). **Accessory phases**: zircon, apatite, monazite, opaques and tourmaline.	Overall equigranular matrix. **Quartz**: undulose extinction and local sub-grain boundaries. **K-feldspars**: perthite exsolution textures, partially sericitized and Carls-bad twinning. **Plagioclase**: sericitized (core more altered compared to rim). **Cordierite**: commonly altered or pinitized.
Fine-grained porphyritic	**Phenocrysts**: quartz (3-8 mm; 6 vol. %), K-feldspar (1.5-5 mm; 4 vol. %), plagioclase (1-3 mm; 3 vol. %), biotite (1-4 mm; 2 vol. %) and cordierite (3-7 mm; 2 vol. %). **Matrix**: is fine-grained, with overall crystal sizes between **0.1-3 mm**. It comprises quartz (30 vol. %), K-feldspar (24 vol. %), plagioclase (22 vol. %) and minor biotite (4 vol. %) and muscovite (2 vol. %) and cordierite (1 vol. %). **Accessory phases**: zircon, apatite, monazite, opaques and tourmaline.	**Phenocrystic quartz**: undulose extinction. **Matrix quartz**: undulose extinction and local sub-grain boundaries. **Biotite** (both phenocryst and matrix variety): commonly chloritized, shows mottled and sagenitic textures. **K-feldspars** (both phenocryst and matrix variety): perthite exsolution textures, partially sericitized and Carls-bad twinning. **Plagioclase**: (both phenocryst and matrix variety): sericitized (core more altered compared to rim) and common cumulophyric textures. **Cordierite** (both phenocryst and matrix variety): commonly altered or pinitized. **Biotite-quartz clots are common**.
Medium-grained porphyritic	**Phenocrysts**: K-feldspar (4mm to > 1cm; 6 vol. %), plagioclase (2.5-7.5 mm; 5 vol. %), quartz (2-6 mm; 4 vol. %) and pinitized cordierite (2- 6 mm; 2 vol. %). **Matrix**: is medium grained, with average crystal sizes between **1-3.5 mm**. Quartz (30 vol. %), K-feldspar (20 vol. %), plagioclase (18 vol. %), biotite (8 vol. %), cordierite (4 vol. %) and muscovite (3 vol. %). **Accessory phases**: garnet, tourmaline, zircon, opaques, monazite and apatite.	**Phenocrystic quartz**: undulose extinction. **Matrix quartz**: undulose extinction and local sub-grain boundaries. **Biotite** (both phenocryst and matrix variety): commonly chloritized, shows mottled and sagenitic textures. **K-feldspars** (both phenocryst and matrix variety): perthite exsolution textures, partially sericitized, sector twinning and Carls-bad twinning. **Plagioclase**: (both phenocryst and matrix variety): sericitized (core more altered compared to rim) and common cumulophyric textures. **Cordierite** (both phenocryst and matrix variety): commonly altered or pinitized. **Biotite-quartz clots are common**. Some are inclusions in a k-feldspar host with symplectic intergrowths of biotite and quartz.
Coarse-grained porphyritic	**Phenocrysts**: K-feldspar (4mm to > 1cm; 8 vol. %), plagioclase (2.5-7 mm; 6 vol. %), quartz (2.5-8.5 mm; 4 vol. %) and pinitized cordierite (2-6.5 mm; 2 vol. %). **Matrix**: is coarse-grained, with average crystal sizes between **2–5 mm**. It comprises quartz (28 vol. %), K-feldspar (20 vol. %), plagioclase (18 vol. %), biotite (10 vol. %), cordierite (2 vol. %) and muscovite (2 vol. %). **Accessory phases**: garnet, tourmaline, zircon, opaques, monazite and apatite.	**Phenocrystic quartz**: commonly shows undulose extinction. **Matrix quartz**: undulose extinction and local sub-grain boundaries. **Biotite** (both phenocryst and matrix variety): commonly chloritized, shows mottled and sagenitic textures. **K-feldspars** (both phenocryst and matrix variety): perthite exsolution textures, partially sericitized, sector twinning and Carls-bad twinning. **Plagioclase**: (both phenocryst and matrix variety): sericitized (core more altered compared to rim) and common cumulophyric textures. **Cordierite** (both phenocryst and matrix variety): commonly altered or pinitized **Biotite-quartz clots are common**. Some are inclusions in a k-feldspar host with symplectic intergrowths of biotite and quartz.

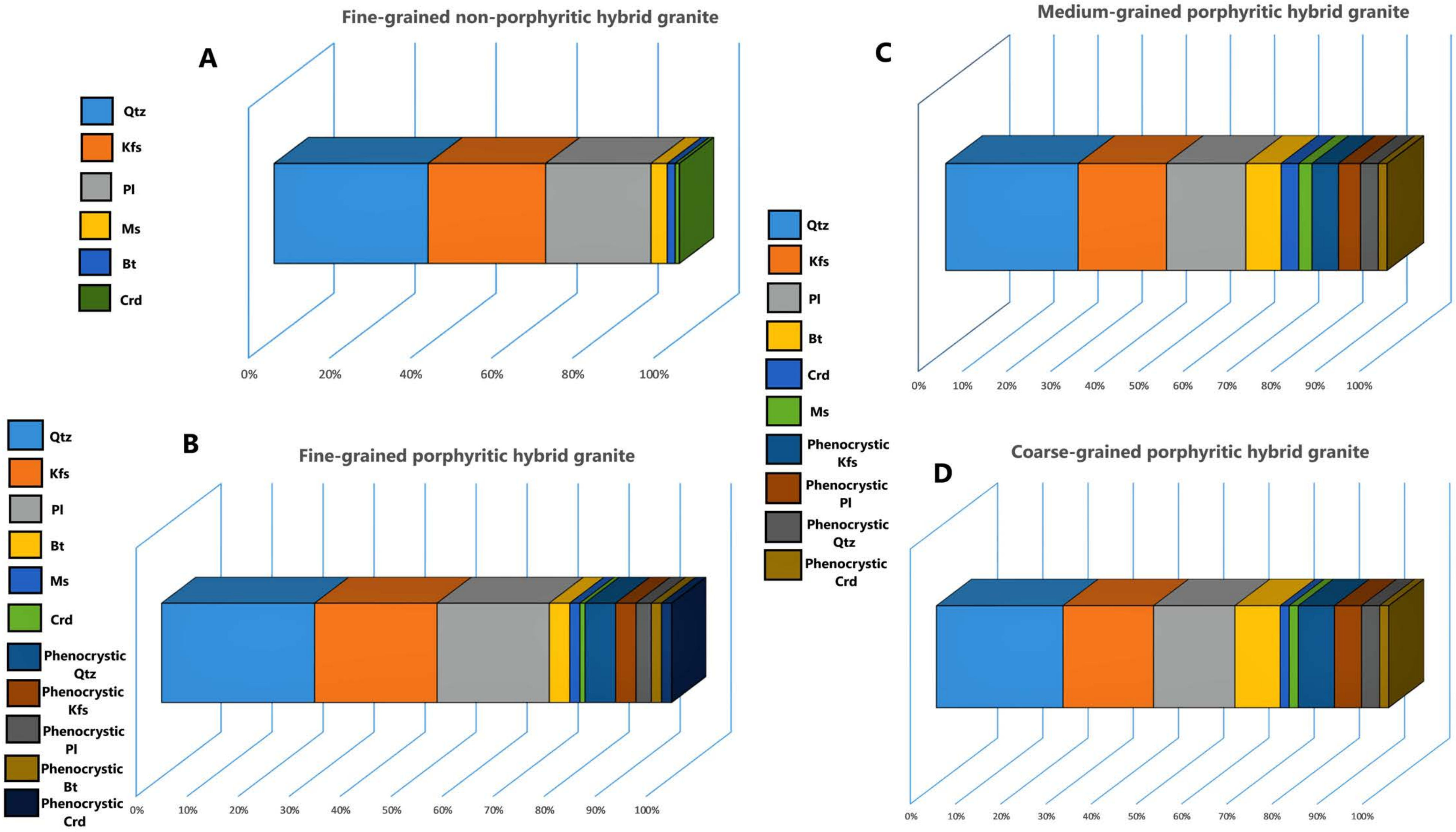

Figure 4.19: 100% stacked bar plots provided to give a visual/graphical representation of the mineral abundances given for each hybrid granite described in Table 4.1. The length of the bar represents 100% percent of a rock and each different colour segment on the bar is the abundance (in vol. %) of a particular mineral in said rock. (C) and (D) share the same legend.

4.5.2 Field descriptions of the hybrid granites

Areas 7 and 8 (Fig. 4.1), as previously mentioned, provide the best exposure and representative examples of the various hybrid phases within the mapped area. As a result, both areas will be used for describing the relationship between the hybrid granite phases and the country rock as well as their relationships amongst each other. Area 7 (Figs. 4.1, 4.20) provides an excellent example of the lit-par-lit nature of the contact zone. Conversely, area 8 showcases a portion of the main contact zone where the well-defined lit-par-lit type contact between the granites and the country rock becomes less apparent as one traverses NW to WNW from the trig beacon towards the wave-cut platform closer to the ocean (Figs. 4.1, 4.21). In both areas, the medium- and coarse-grained porphyritic hybrid phases are more voluminous compared to the other hybrid granite phases and have biotite content that varies from one locality to the next.

Figure 4.20: Transect of area 7 showing a portion of the northern coarse-grained porphyritic granite sheet (bottom-left) in contact or adjacent to a lit-par-lit section (or zone). In the lit-par-lit section, the various hybrid granite phases (typical widths ranging from 0.1-1.5 m) are intruded primarily sub-parallel to the country rock as 'finger-like' intrusions. The direction of view is SE.

Figure 4.21: *Transect of area 8 showing the contact between the northern coarse-grained porphyritic granite sheet and an adjacent medium to coarse-grained porphyritic hybrid granite and Malmesbury lit-par-lit section. The direction of view is to the E.*

4.5.2.1 Relationship between the hybrid granites and the country rock

Despite localized occurrences of sharp contacts in the lit-par-lit zone, in general, the various hybrid granites have gradational contacts with the surrounding country rocks in which they exhibit a banded or interlayered appearance (Fig. 4.22). Evidence for a gradational contact can be seen at both the outcrop (Fig. 4.22) and thin section scale (Fig. 4.23). Overall, this gradational-type contact steadily diminishes as one heads further south away from the lit-par-lit zone and into the main S-type pluton, where the amount/spacing of granite sheeting increases giving way to more massive outcrops of granite.

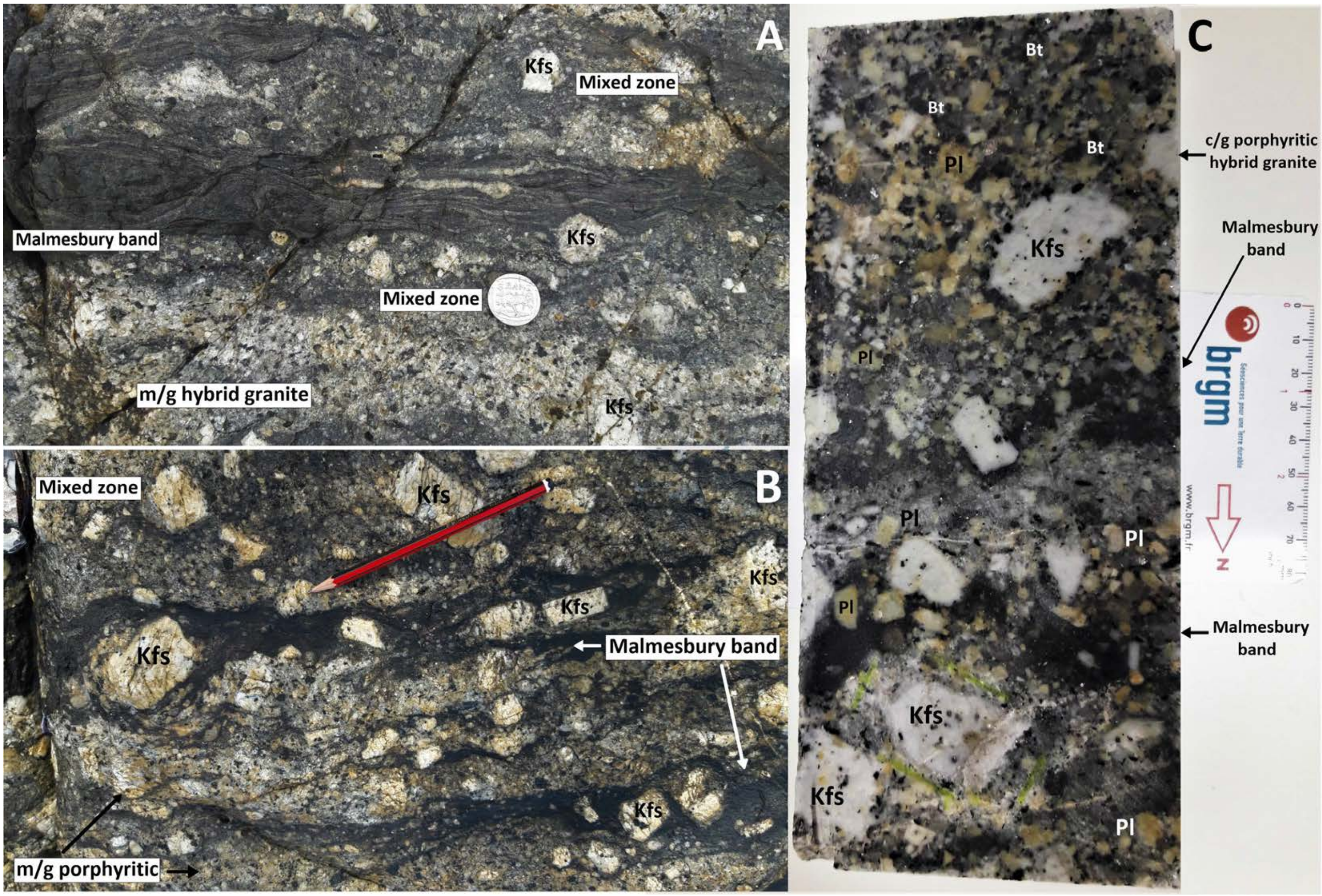

Figure 4.22*: Close up view of the close association between the country rock and the hybrid granite in area 7. (A) The Malmesbury banding is markedly more feldspathic, conversely, the medium-grained (m/g) hybrid granite band (bottom half of A) is itself markedly biotite-rich. 'Mixed' or hybrid zones where the distinction between the country rock and granite is not clear also exist (e.g. top-half and mid-portion of A) (diameter of 5 rand coin = 2.6 cm). (B) Biotite-rich medium-grained porphyritic granite phase injected sub-parallel to a series of Malmesbury country rock bands that have K-feldspar megacrysts incorporated within them (pencil points to the north). (C) A block sample of sample SP32 (a coarse-grained (c/g) porphyritic hybrid granite in contact with the Malmesbury Group country rock) that shows the gradational nature of the country rock–granite contact at the rock-block scale. Note the concentration of feldspar phenocrysts in the Malmesbury bands. The K-feldspar megacryst demarcated by a green marker (bottom-mid left portion) is one of the megacrysts chosen for a future K-feldspar chemical probe study.*

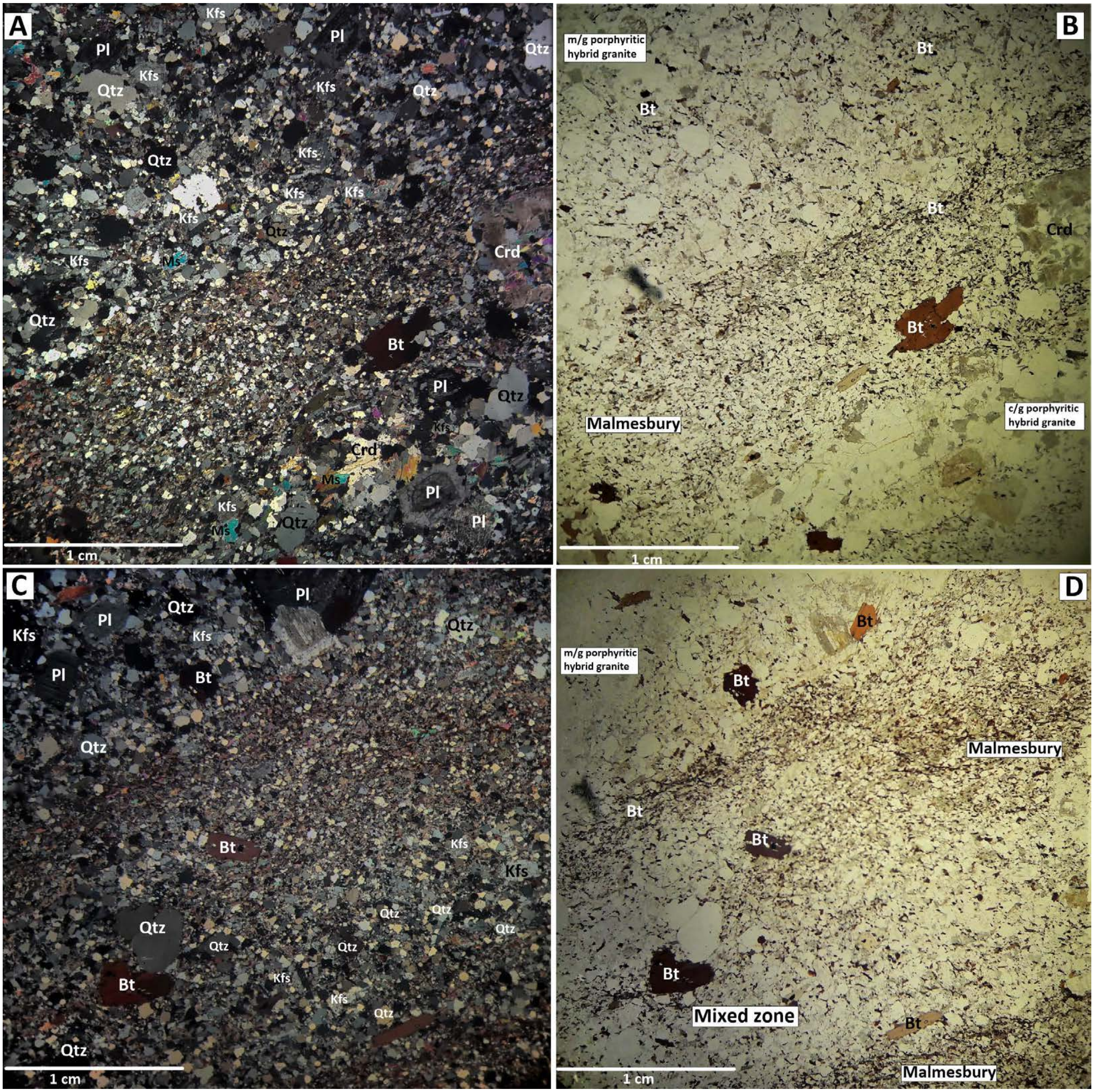

Figure 4.23*: Thin section photomicrographs, in cross- and plane-polarized light, of the contact relationship between the hybrid granite phases and the Malmesbury Group country rock in the lit-par-lit zone. The contact relationships are primarily gradational as opposed to sharp. (A) Injections of m/g and c/g porphyritic hybrid granite phases in contact with a Bt-rich quartzofeldspathic Malmesbury country rock band. Note, in (B), how the m/g porphyritic granite phase has Bt grains of similar size and texture to those in the Malmesbury band. Conversely, note how the Malmesbury band has large grains of Qtz, Bt and Crd similar to those in the c/g porphyritic granite. The aforementioned grains do not attain such large sizes in the metamudstone lithologies that are not in direct contact with the granite (e.g. Fig. 4.6). (C) & (D) Contact between a m/g porphyritic hybrid granite phase and the Malmesbury country rock. A 'mixed' or hybrid zone has developed (in the bottom-half of D) where the country rock is indistinguishable from the granite.*

4.5.2.2 Relationship between the various hybrid granite phases

The fine-grained hybrid phases, in area 8, and the geological features they display as well as their relationship with the other medium- and coarse-grained porphyritic hybrid phases and the country rock are as follows:

(i) They transition laterally into the surrounding medium- and coarse-grained porphyritic phases. This is seen, for example, in Figure 4.24A where there is a progressive gradation to finer grain sizes as one transitions from the porphyritic/crystal-rich coarse-grained hybrid granite into the fine-grained hybrid granite.

(ii) They locally occur as pinch-out or boudinaged features sandwiched between the country rock bands and the coarse-grained porphyritic phase (Fig. 4.24C). Some of the medium-grained porphyritic hybrid granite phases are also locally boudinaged (Fig. 4.24E).

(iii) The country rock–fine-grained non-porphyritic phase contact relationship tends to be partly- to fully-incorporated by the various medium- and coarse-grained hybrid phases (Fig. 4.24D).

Moreover, the fine-grained non-porphyritic hybrid phase also forms a gradational contact with the fine-grained porphyritic phase (Fig. 4.24F). The sizes of the megacrysts within the fine-grained porphyritic hybrid phase vary in size (typically between 0.5-3 cm), abundance, and distribution, resulting in a rock type varying from semi-porphyritic to porphyritic (Fig. 4.24F). Commonly or wherever both the fine-grained hybrid granite varieties are intruded into the country rock, thin wispy remnants (or xenoliths) of the country rock are evident (e.g. Fig. 4.24A). In contrast, larger xenoliths of the country rock are incorporated within the medium- and coarse-grained hybrid granite phases (e.g. Fig. 4.27).

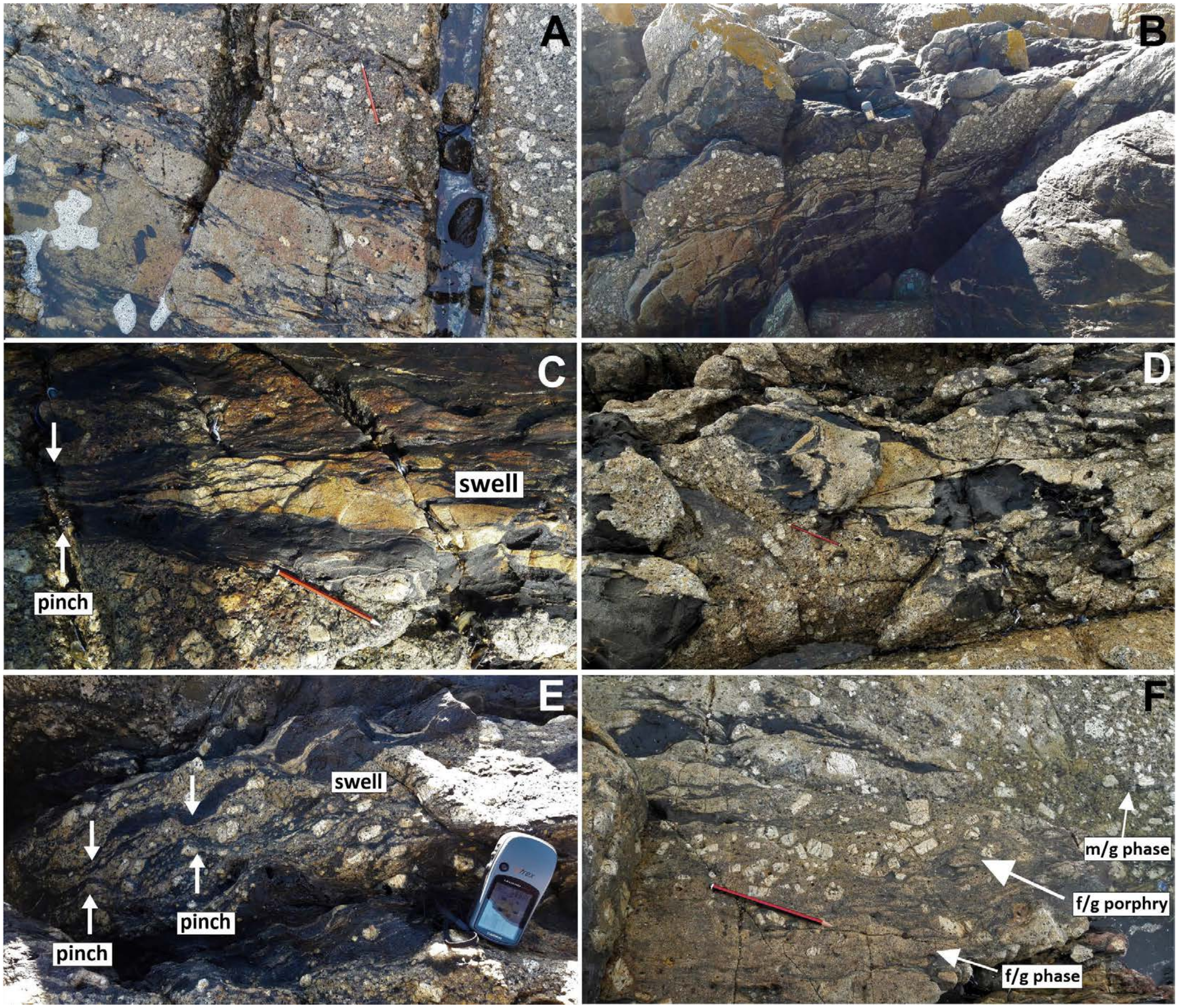

__Figure 4.24__: Outcrop photographs depicting the relationship between fine-grained hybrid granite phases and the medium- and coarse-grained hybrid granite phases in area 8. Features associated with some of the hybrid phases are also shown. (A) Fine-grained non-porphyritic phase, with small wispy remnants of the country rock, transitioning laterally into the medium-grained porphyritic phase, which locally exhibits K-feldspar alignment in a roughly NW-SE to WNW-ESE direction. (B) Vertical surface depicting the contact relationships between three lithologies: a coarse-grained porphyritic hybrid granite phase, a fine-grained non-porphyritic hybrid granite phase and the country rock. Note the appearance of the fine-grained non-porphyritic phase which is present as ropy, disaggregated bodies within the country rock. (C) Fine-grained non-porphyritic hybrid granite phase occurring as a pinch-out feature 'sandwiched' between the country rock and the medium- to coarse-grained hybrid phase. (D) Contact between the country rock and the fine-grained non-porphyritic phase that is incorporated by a medium- to coarse-grained porphyritic hybrid phase. (E) Boudinaged medium-grained porphyritic hybrid granitic phase in the country rock. (F) Gradational contact relationship defined by the following three hybrid granite phases: fine-grained (f/g) non-porphyritic, fine-grained porphyritic and medium-grained porphyritic.

4.5.3 Features of the country rock in the lit-par-lit zone

4.5.3.1 Preservation of feldspar megacrysts in the country rocks

Variably sized feldspar grains, in the form of K-feldspar and plagioclase, are embedded within the metamudstone country rock in the lit-par-lit zone (Fig. 4.25), with or without other phenocrysts such as biotite and quartz. Of the two feldspar grains, however, K-feldspar megacrysts are the ones most commonly preserved in the country rock (Fig. 4.25A, B). Although there are a few feldspar grains that are preserved in complete isolation within the country rock, the majority of the feldspars are associated with and/or surrounded by various trails of quartzofeldspathic granitic material (Fig. 4.25B, C, D). These trails or injections are typically thin and hard to discern using the microscope. This is because their grain size and composition are largely similar to the mineralogy of the host country rock. The trails are most visible where they have coarse grain sizes (bottom-left portion of Fig. 4.25C).

4.5.3.2 Xenoliths

The majority of the xenoliths occurring in the lit-par-lit zone are biotite-rich metamudstone xenoliths (Figs. 4.27, 4.28). Other xenoliths types, outcropping to a lesser extent, are in the form of the darkened country rock xenoliths which are metamorphosed to a greater degree compared to the surrounding country rock. They are smaller (largest up to 30 cm), rounded to blocky and tend to be more cordierite-rich compared to the surrounding metamudstone (Fig. 4.26). These hornfels xenoliths outcrop predominantly in area 7 (Fig. 4.1, 4.20) and are preserved mostly within the metamudstone and/or occur as rotated blocks rimmed by various fine- and medium-grained hybrid granite phases (Fig. 4.26A).

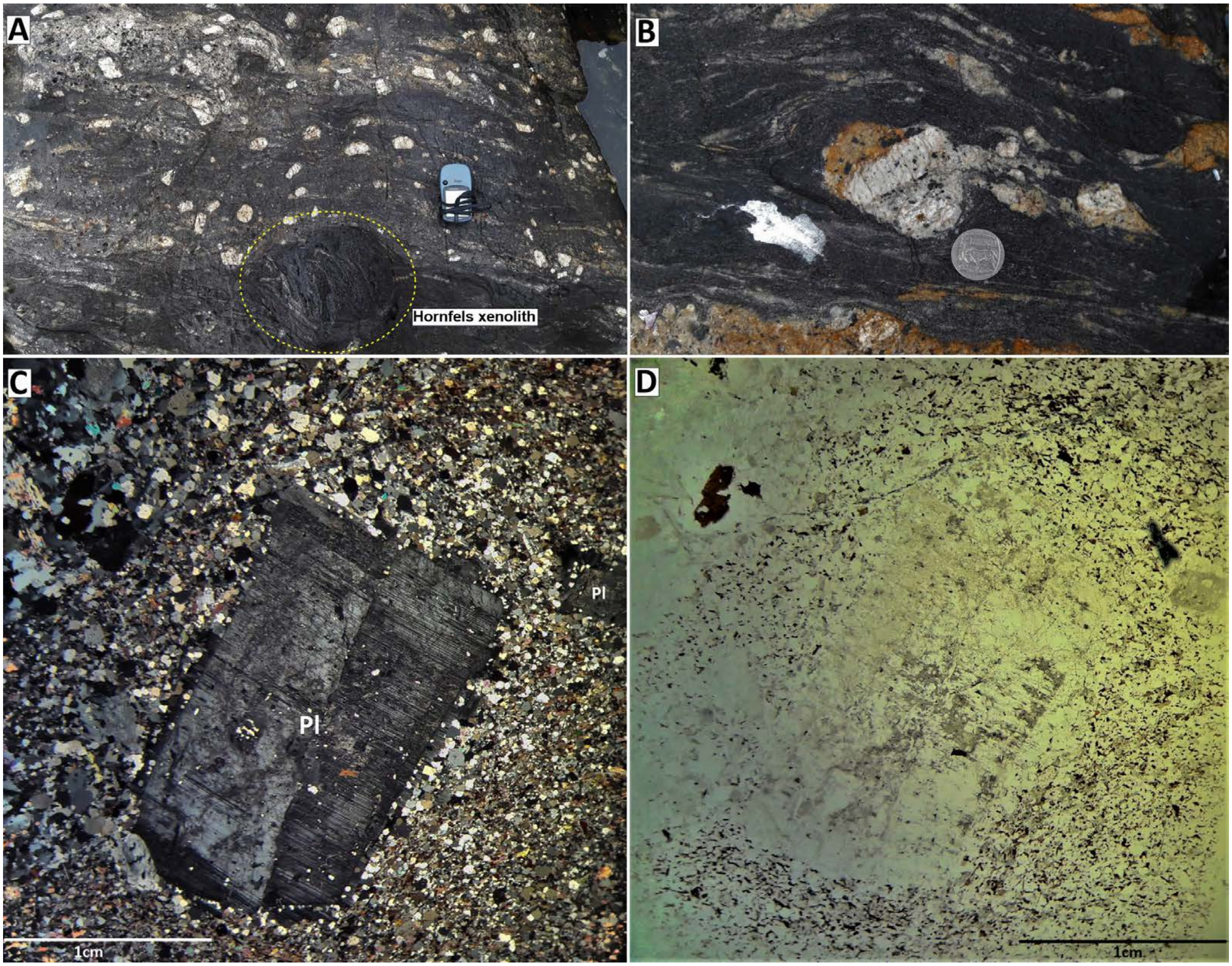

***Figure 4.25**: Outcrop photographs and thin section photomicrographs of various feldspar grains preserved within the metamudstone country rock in the lit-par-lit zone. (A) Country rock intruded by various fine- and medium-grained hybrid granite phases/injections in area 7. Some of the K-feldspar grains embedded within the country rock have quartzofeldspathic trails attached to them, whereas others do not. Also present in (A) is a much darker hornfels xenolith in a metamudstone host. (B) Rotated K-feldspar megacryst within the country rock located in area 7 (the direction of view is NNE). The megacryst appears to have been rotated in the direction of magma flow as evident from the deflection of flow, defined by the fine-grained granitic material, around the K-feldspar megacryst. Magma flow, using this feature, is interpreted to be oriented in a WNW-ESE direction with the direction of flow being ESE. (C) & (D) Thin section photomicrograph, in cross polars and plane-polarized light, of a Pl grain preserved within a country rock portion. The Pl grain shows Carls-bad twinning and is compositionally zoned, with the rim of the Pl having well-oriented fine-grained quartz inclusions arranged parallel to the margin of the grain. In (D), note how the country rock foliation wraps around the Pl and envelops relics of granite (i.e. the coarse-grained quartzofeldspathic granitic material attached to the Pl in the bottom-left portion of C and D).*

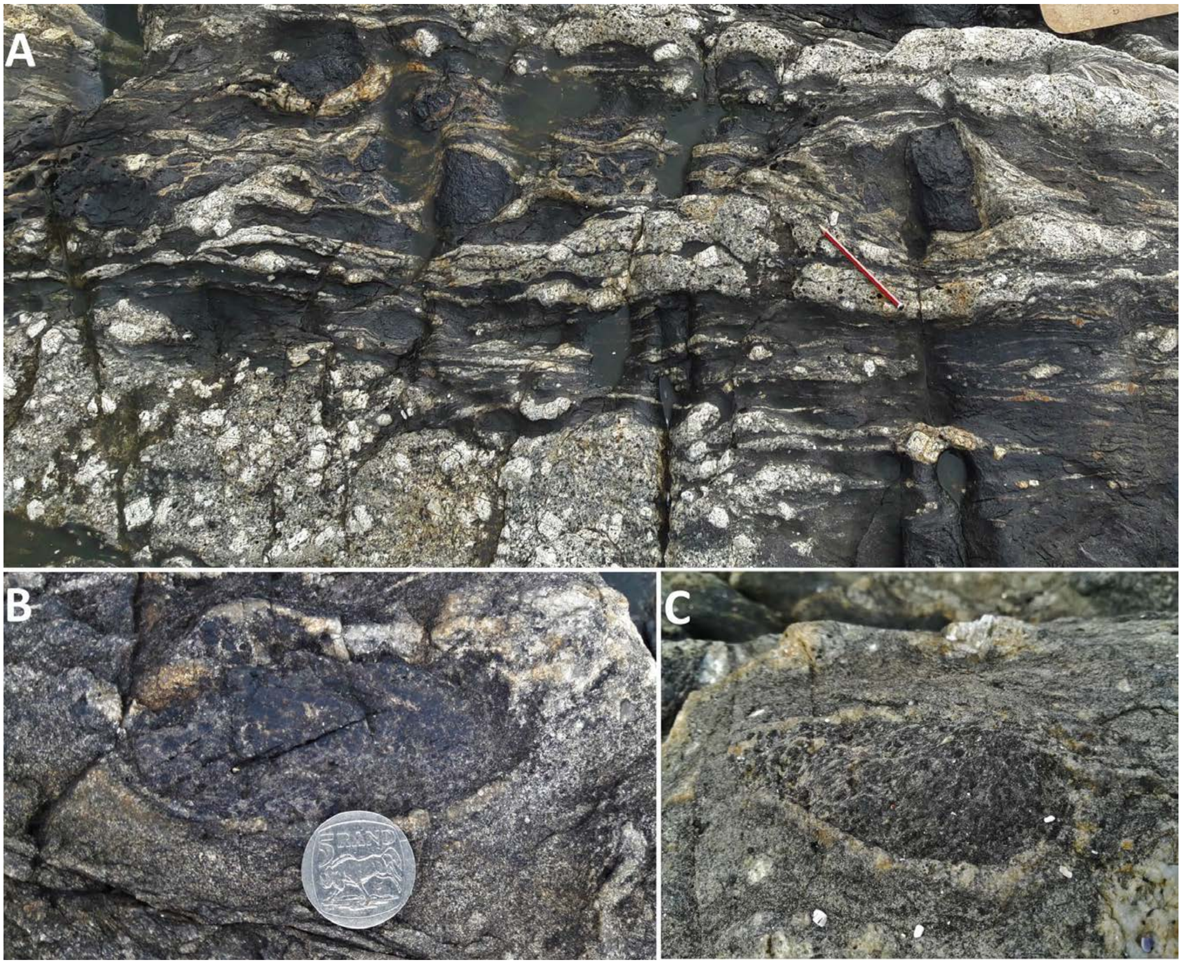

***Figure 4.26**: Outcrop photographs of various hornfels xenoliths in the study area incorporated into or surrounded by the metamudstones. All examples are located in area 7. (A) Several hornfels xenoliths rimmed by various fine- and medium-grained hybrid granite phases that are intruded subparallel to the country rock fabric (pencil points north). (B) & (C) Close-up views of some of the hornfels xenoliths; they are cordierite-rich, as evident from the numerous rounded and equidimensional dark spots developed within them. Both are also rimmed by fine-grained granitic material.*

The more common biotite-rich metamudstone xenoliths outcrop in area 4 (Fig. 4.1). A transect of area 4 is shown in Figure 4.27. The area shows a xenolith-rich medium- to coarse-grained porphyritic hybrid granite (on left of Fig. 4.27) in contact with an adjacent lit-par-lit section (on the right of Fig. 4.27). The metamudstone xenoliths within this xenolith-rich zone can attain sizes up to 1.5 m in length and are irregularly-shaped to elongate. Some of the xenoliths still have the predominant S_1 foliation preserved within them, however, the S_1 foliation has a different orientation to the main Malmesbury Group S_1 foliation (i.e. the internal S_1 in the xenoliths is rotated against the external S_1 in the wall rocks) (e.g. Fig. 4.29).

Figure 4.27: Transect of area 4 depicting a xenolith-rich zone in the study area. This area has a significant amount of xenoliths of various size and shape (demarcated by yellow outlines) that are incorporated into the medium- to coarse-grained hybrid granite. Adjacent to this zone is a lit-par-lit section (the portion/section to the right of the photo) defined by metamudstone bands which are intruded by fine- to medium-grained porphyritic hybrid granite veins. Portions of this lit-par-lit section show an intimate association between the hybrid granite and the country rock giving rise to a country rock section that is more feldspathic and locally porphyritic. The direction of view is WNW.

Some of the xenoliths have undergone stretching or extension (in a direction more or less parallel to the long axis of the xenoliths) to such an extent that they experienced necking and pinching out (Fig. 4.28C). This direction of extension is approximately WNW-ESE, parallel to the overall contact zone (Fig. 4.28C). These elongated xenoliths, along with some of the distended and disconnected granitic material and phenocrysts occurring around the xenoliths (Figs. 4.28D, 4.29), are all good indicators of magmatic flow. For the case of the elongated xenoliths (e.g. Fig. 4.28C), the direction of magma flow is evident from: (i) granitic material around the xenolith core appearing to be dragged in one direction as they flowed around the xenolith core as the core itself was being rotated in the direction of magma flow (i.e. WNW) (central portion of Fig. 4.28C), or (ii) the tail of the xenolith (left of Fig. 4.28C), being dragged and extending (with reference to the long axis of the xenolith) in the direction of magma flow as the xenolith body was rotated.

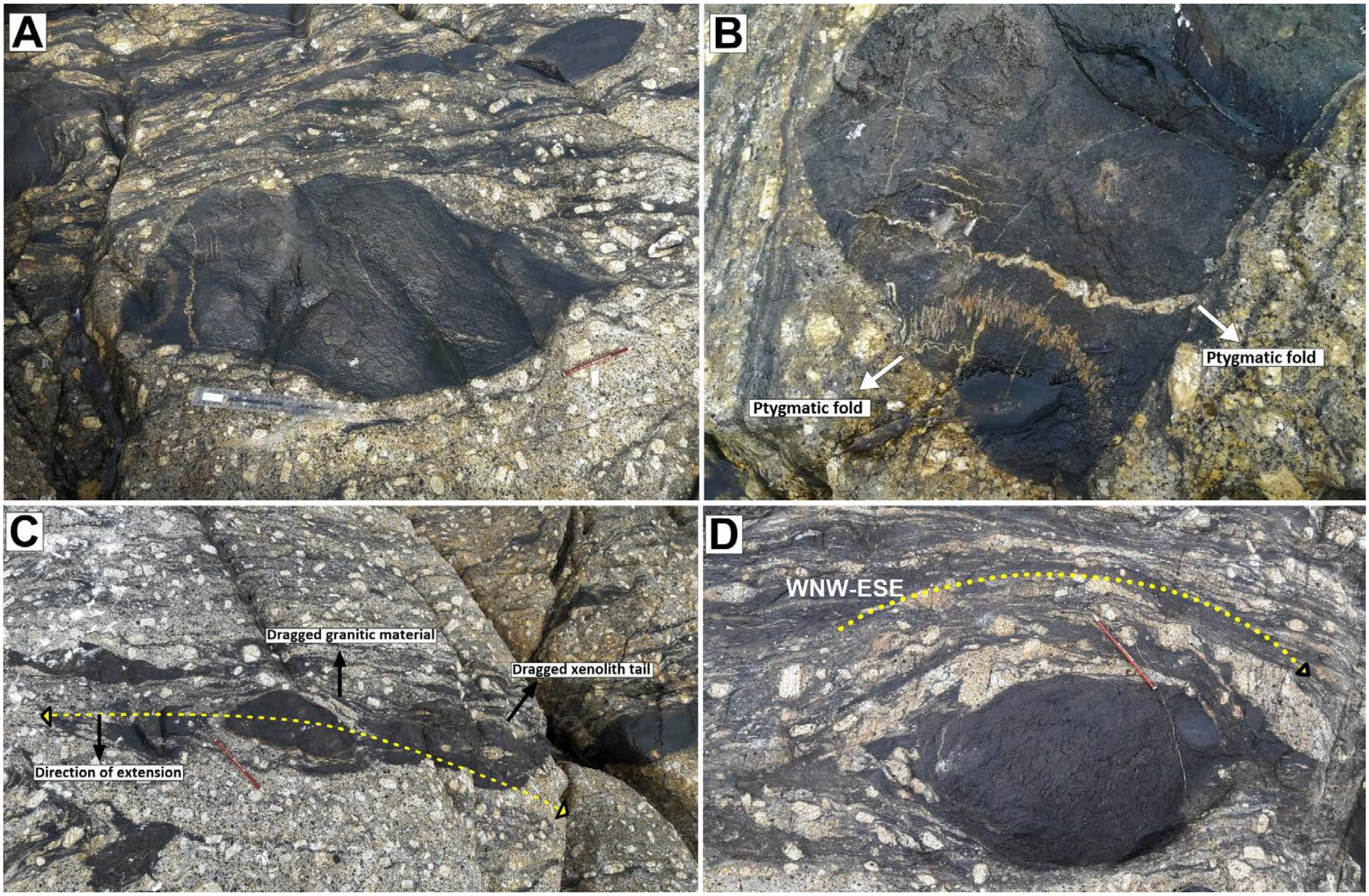

Figure 4.28*: Outcrop photographs of some of the xenoliths located within the xenolith-rich zone of area 4. (A) Metamudstone xenolith flanked by an array of preserved remnants of the original country rock occurring as distended and separated slivers in the extensive granitic mass (length of ruler = 30 cm); the direction of view is SSW. (B) Zoomed in section of the bottom-left portion of the xenolith portrayed in (A) showing the occurrence of cross-cutting and irregularly-shaped quartzofeldspathic fine-grained veinlets; both veins are folded (ptygmatic folds) and the enveloping foliation is more or less axial planar. (C) A distended and necked (or 'pinched') xenolith body that appears to also have been rotated as well. This xenolith is useful for inferring magma flow direction as explained in the text; the direction of view is SSW (D) A xenolith that appears to have been rotated in the direction of magma flow as evident from the fine- to medium-grained hybrid granite phases deflected around the xenolith body; the direction of view is NNE. The general orientation of magma flow is inferred to be WNW-ESE.*

For the examples shown in Figures 4.28D and 4.29, the presence of magma flow can be observed from the deflection patterns of the various fine- to medium-grained hybrid granite material around the xenolith bodies as the material flowed around the rotated xenolith bodies. The magma flow direction inferred from all the features depicted in Figures 4.28C, D and 4.29, is consistently WNW-ESE oriented, an orientation corresponding to or subparallel to the WNW-ESE orientation of the Malmesbury banding as well as the orientation of the granitic banding/veins in the lit-par-lit zone. The direction in which magma flowed was towards the WNW.

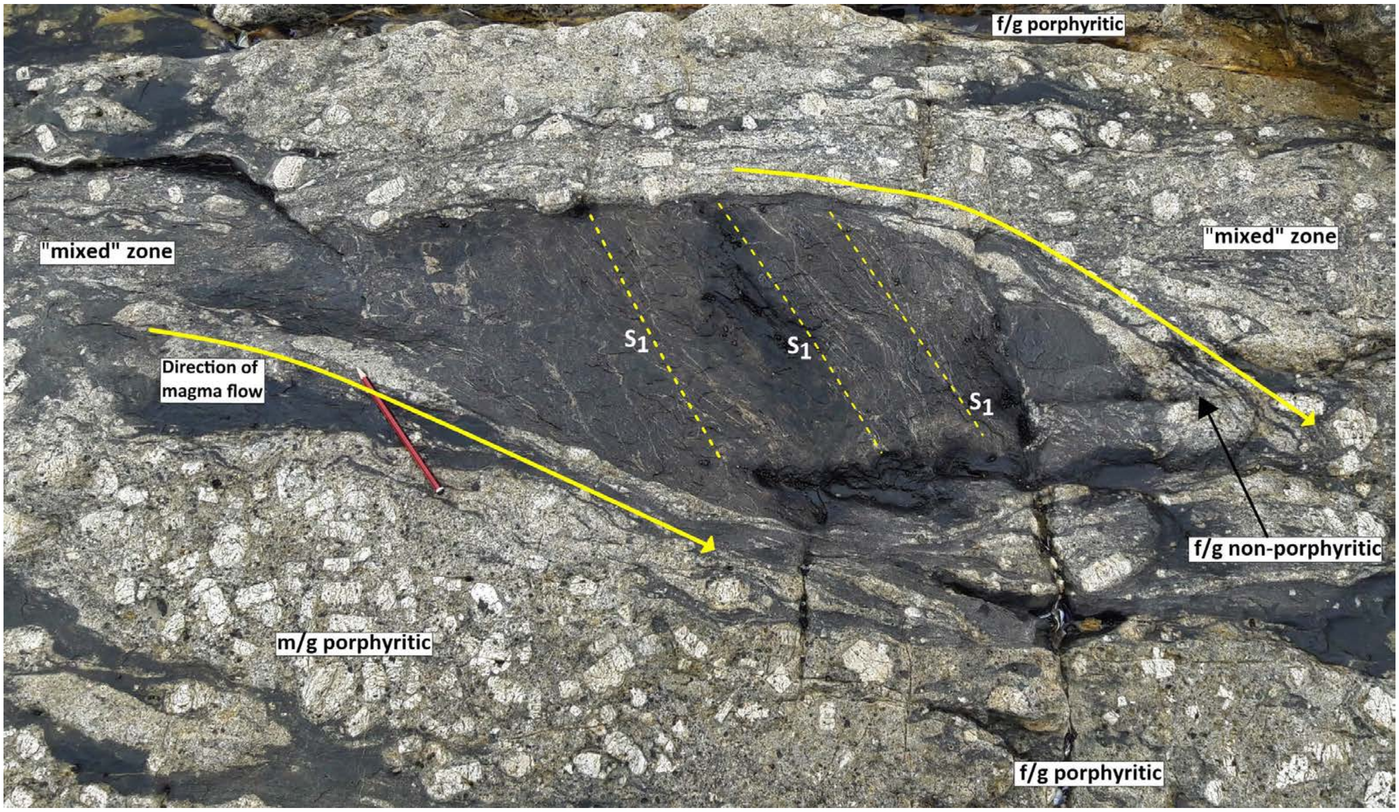

***Figure 4.29**: Outcrop photograph of a rotated country rock xenolith with preserved S_1 foliation planes (shown by yellow dashed lines). The foliation planes are intruded by fine-grained quartzofeldspathic material. The xenolith appears to have been rotated in the direction of magmatic flow (WNW-ESE oriented). Various granitic phases surrounding the xenolith namely, the medium-grained porphyritic granite, fine-grained porphyritic granite (commonly rimming the xenolith body) and fine-grained non-porphyritic granite, transition laterally into each other to define an overall gradational contact. The tail of the xenolith (in the upper-left portion of the photograph) extends in the direction of magma flow. Outcrop located in area 8. The direction of view is NNE.*

Fine-grained quartzofeldspathic vein material (1.5-6 mm in width and up to 20 cm in length) are commonly observed to crosscut the xenoliths and locally exhibit sharp ptygmatic folding (Fig. 4.28A, B). Ptygmatic folds represent conditions where the folded material is of a much greater viscosity than the surrounding medium (Godfrey, 1954). These ptygmatic folds are commonly oriented roughly NNE-SSW, an orientation perpendicular to the trend of the Malmesbury and granitic banding (i.e. WNE-ESE). Their orientation also shows the orientation (more or less) of shortening (NNE-SSW) which is perpendicular to the direction of extension (WNW-ESE).

4.5.3.3 Evidence of the ductile behaviour of the country rock

In the study area, some of the country rocks show evidence of ductile behaviour at both the outcrop and microscopic scale. At the outcrop scale, this ductile behaviour is especially evident in area 3 (Fig. 4.1), where the country rock bodies have a wavy appearance and are elongated (Fig. 4.30). Moreover, some of the granitic material/veinlets, within the country rock, help highlight the ductility of the country rock because they occur as pinch-and-swell structures or boudins (Fig. 4.30). Boudins are more or less regularly shaped and spaced fragments formed by stretching of competent layers and are usually developed within a host rock/matrix that deforms plastically (Fossen, 2010). Out of the two Malmesbury Group lithologies that outcrop in the study area, the metamudstones are the ones depicting all the characteristics of ductile behaviour. This, therefore, suggests that of the two rock lithologies, the metasiltstone is relatively competent, whereas the metamudstone lithologies had the greater capacity to behave in a ductile fashion. Evidence of ductile behaviour is not widespread but is instead restricted to local scales in the lit-par-lit zone.

Figure 4.30*: The appearance of some of the country rock bodies in the lit-par-lit zone. They are more elongated and have a characteristic wavy appearance suggesting ductile behaviour. (A) Interlayered metasiltstone-metamudstone body intruded by the medium- to coarse-grained porphyritic hybrid granite phase. The granite intrusions are locally boudinaged (white arrows) between the country rock bands. (B) Biotite-rich metamudstone body intruded by various granite phases namely, the porphyritic medium-grained phase and fine-grained non-porphyritic hybrid phase. Note the competency contrast between the fine-grained non-porphyritic hybrid phase and the metamudstone layer as seen by the moderate pinch-and-swell structures developed in the former giving them a lenticular boudin-like shape and suggesting a higher competency over the latter. Localized hornfels xenoliths (upper- and mid-right portions of B) also occur. The outcrop is located to the immediate east of the trig beacon (Fig. 4.1). Pencil points to the north.*

5 Structural geology

5.1 Introduction

This chapter describes the structural features associated with the Malmesbury Group country rock and the S-type granites of the Peninsula Pluton. Although the latter are largely undeformed (as described in the Lithological descriptions chapter), a study involving K-feldspar megacrysts, which are a defining feature of the main coarse-grained porphyritic granite, was performed. The study involved measuring the relative orientation of K-feldspar megacrysts using the SPO technique to investigate the occurrence of a possible (K-feldspar megacryst-defined) magmatic foliation (or magmatic flow) and its orientation.

For the Malmesbury Group country rocks, at least two deformation events, D_1 and D_2, are identified. Therefore, the resultant orientation changes of the country rock fabric, e.g. bedding, foliation and fold structures, after the advent of the two deformation events are discussed. Moreover, a brief microstructural description of the main axial planar foliation (S_1) (associated with D_1) and a crenulation cleavage (S_2) (associated with D_2) are discussed. Also, an interpretation of cordierite porphyroblast growth relative to deformation is provided. Shear sense indicators are prevalent and localized within the country rock occurring in the lit-par-lit zone; they will also be described in this chapter. All the orientation data for planar structures in this chapter (as well as the ensuing chapters thereafter) are reported as dip direction and dip angle.

5.2 Structure of the country rock

The deformation stages and fold/foliation generations for the Malmesbury Group rocks of the Tygerberg Formation described in this thesis are primarily based on the chronology observed in the outcrop and thin section. They correspond to the stages of deformation proposed by Hartnady et al. (1974) and Theron et al. (1992) who state that the Tygerberg Formation (Tygerberg terrane in the classification they utilized) of the Malmesbury Group is characterised by at least two major deformation events developed during the Saldanian orogeny. The first is the major deformational phase (D_1) of the Saldanian orogeny, defined by slightly inclined to upright and tight, slightly southwest-verging F_1 folds with a northwesterly plunge, a slight inclination towards the northeast, and a pervasive subvertical axial planar cleavage, S_1. The second deformation event (D_2) was much weaker than D_1 and gave rise to broad, open F_2 folds, with axial surfaces largely oriented NNE-SSW and a weakly developed sub-horizontal to gently dipping S_2 crenulation cleavage. The D_1 of Hartnady et al. (1974) corresponds to the D_2 event recognized by Belcher (2003), Belcher & Kisters (2003) and Kisters & Belcher (2018). The aforementioned researchers recognize D_1 as a regional S_0/S_1 fabric developed only in the schistose rocks of the Swartland complex, with the lithologies of the Malmesbury Group only having S_0 as a primary fabric. The D_1 deformation phase they describe is marked by an event of low-angle thrusting related to the development of intrafolial F_1 folds, accompanied by the development of a bedding-sub-parallel schistosity, S_1 (Belcher, 2003).

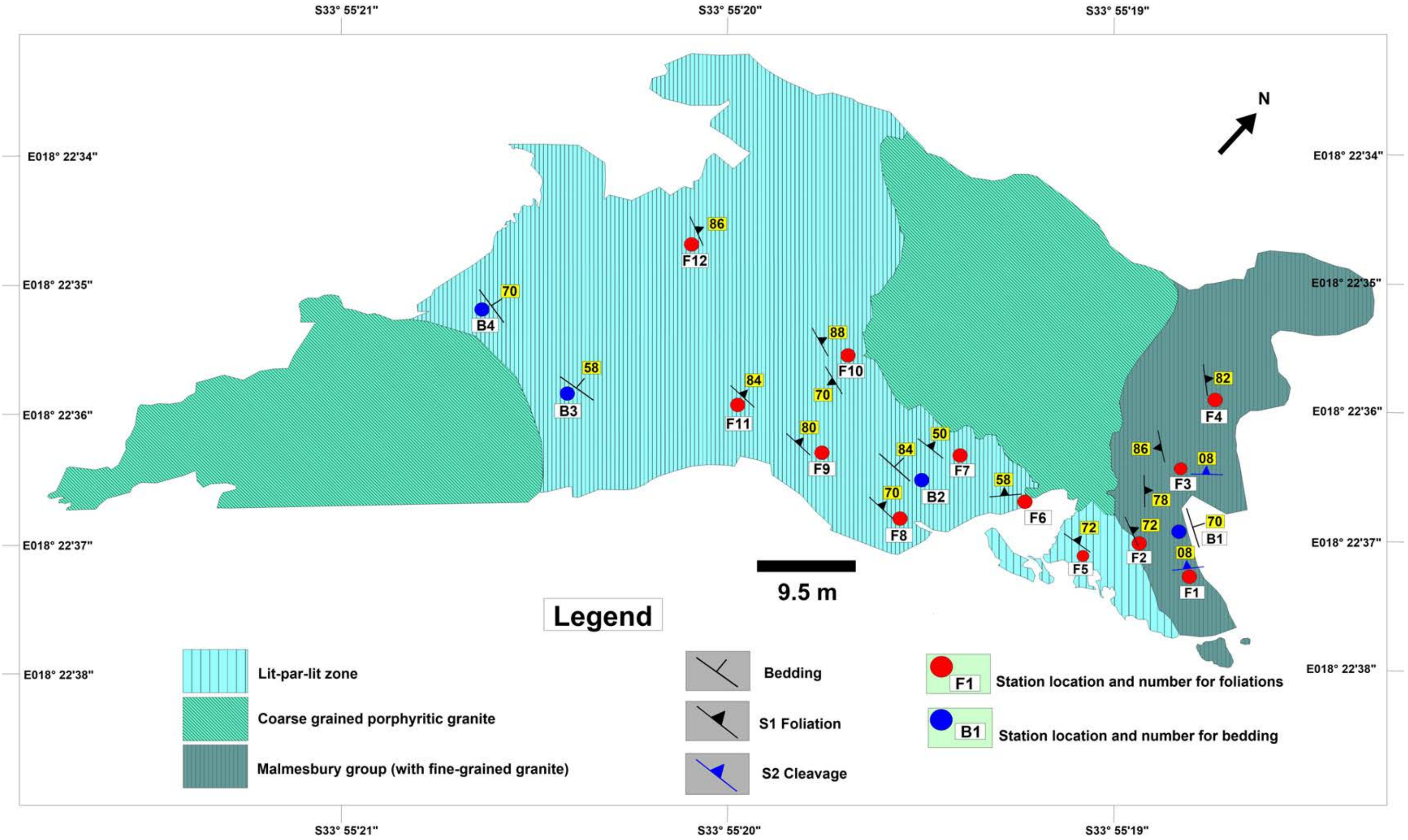

Figure 5.1: *Simplified geological map of the Sea Point contact comparing foliation and bedding orientation in the lit-par-lit zone and northern Malmesbury Group outcrops. The small Malmesbury Group outcrops to the south are excluded because they do not cover a large enough extent that warrants the observation of bedding and foliation variation on a large scale. A portion of the main coarse-grained porphyritic phase at the southern end is also excluded due to not showing any significant structural features.*

5.2.1 Bedding S_0

Reliable locations for measuring S_0 bedding orientation are located in the small Malmesbury outcrop located in area 2 (Fig. 4.1) and the northern-most portion of the study area (i.e. station B1; Fig. 5.1). In the lit-par-lit zone, care was taken to take readings from larger segments of *in situ* country rocks that have not been passively rotated within granite magma such as seen in the metasiltstone-metamudstone xenoliths (e.g. Fig. 4.2).

Beginning from the northern end of the study area, S_0 is mostly vertical to sub-vertical and trends NW-SE (Fig. 5.2C). Within the lit-par-lit zone, S_0 orientation varies from E-W to WNW-ESE trending (Fig. 5.2B). For example station B2 (Fig. 5.1), which is located toward the eastern end of the lit-par-lit zone, has S_0 planes that trend E-W (e.g. 002/84, 002/86, 008/82) but change (or curve) to WNW-ESE trending (014/62, 018/60), as one heads towards stations B3 and B4, located along the western portions of the lit-par-lit zone (Fig. 5.1).

Towards the southern portion of the mapped area, S_0 trends WNW-ESE to E-W and dips towards the NE and SW (Fig. 5.2A). This is largely the same orientation as observed within the lit-par-lit zone.

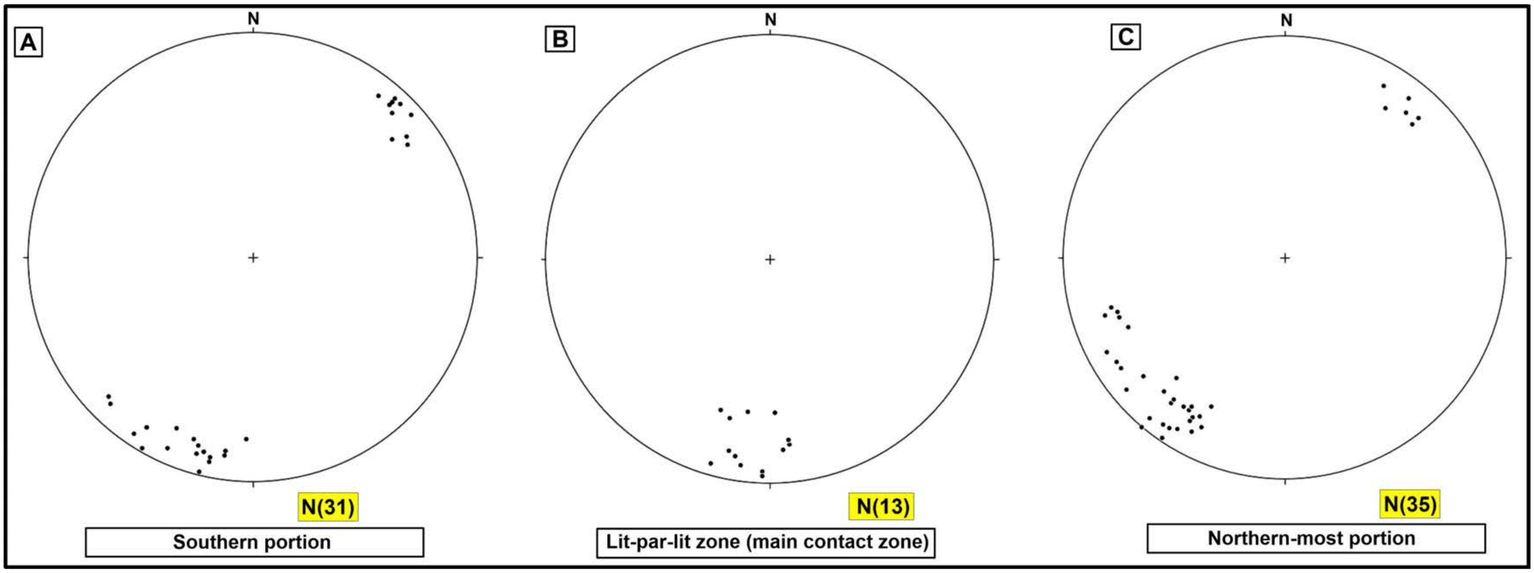

Figure 5.2: *Lower hemisphere equal-area projections (stereonets) comparing bedding orientation (as poles to planes) measured from the southern end (A), lit-par-lit zone (B) and northern end (C) of the study area respectively*

5.2.2 S_1 foliation

The earliest foliation, S_1, in the Malmesbury Group country rocks is an axial planar foliation to the F_1 folds and is generally at a very low angle to the bedding (Fig. 5.3). The close association between S_0 and S_1, in terms of orientation, suggests that the two planes are generally subparallel in most parts of the Malmesbury Group outcrop and differentiation of the overall bedding attitude relative to the S_1 foliation is especially difficult except in the hinge zones of F_1 folds. In these hinge zones, bedding and foliation are more distinctly oblique to one another.

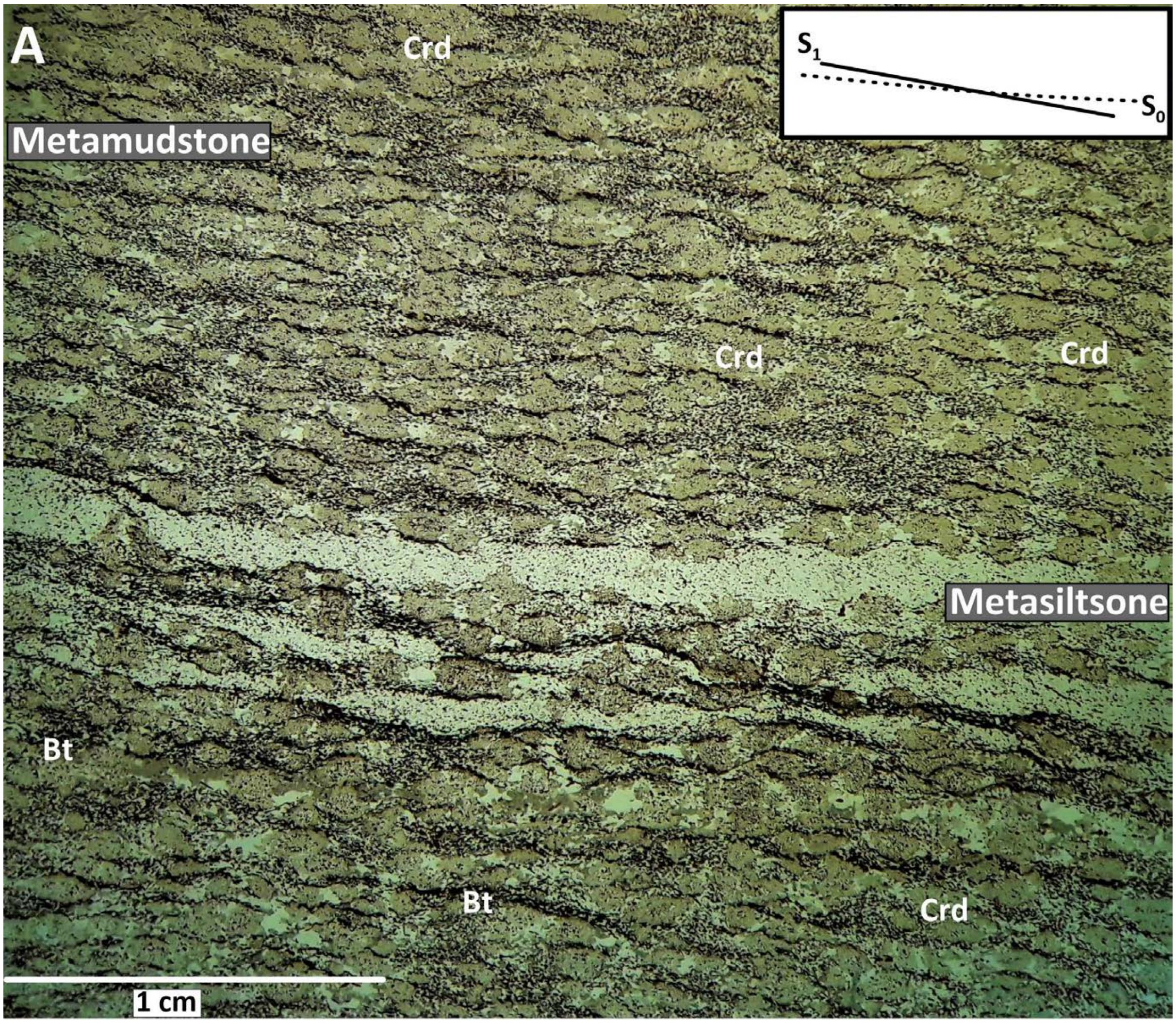

Figure 5.3*: Thin section photomicrograph of a portion of sample SP17 (interlayered metamudstone-metasiltstone) under plane-polarized light. The thicker metamudstone layers have a strongly developed S_1 foliation, defined by preferentially aligned Bt grains, and host Crd porphyroblasts. The metasiltstone layers are thinner, largely quartzofeldspathic with minimal Bt content. The microstructural relationship between the S_1 foliation and the metasiltstone layers (used as a proxy for initial bedding in this case) is illustrated (sketch in the top-right corner). The S_1 foliation in this sample is generally at a low angle relative to the bedding (S_0).*

In both the metamudstone and the interlayered metasiltstone-metamudstone lithologies, the foliated metamudstones are characterized by a domainal structure or, more accurately, a spaced anastomosing foliation due to the presence of lens-shaped microlithons (Passchier & Trouw, 2005) (Fig. 5.4). A domainal structure is a kind of structural layering or lamination composed of domains of strongly developed foliation that alternate with domains with less-developed foliation (i.e. microlithons) (Davis et al., 2011). In the metamudstone samples of the study area, the spacing between these domains typically ranges from 0.15-1.25 mm. The S_1 foliation, defined by strongly aligned, variably chloritized and zircon-rich biotite grains, within the 'foliation domains' can also be classified as a penetrative or pervasive foliation as it tends to be developed throughout the rock.

The microlithons may have sharply defined boundaries, but are more commonly gradationally bounded on either side by the foliation domains (Fig. 5.4C, D). The microlithons generally show little or no preferred orientation, with the majority of the deformation instead being strongly partitioned into the biotite-selvedges (i.e. foliation domains) which show a stronger alignment compared to the microlithons. The microlithons are biotite-poor, generally lenticular- to lens-shaped and are composed of a granoblastic-polygonal textured matrix defined predominantly by quartz and a few orthoclase and plagioclase grains along with strongly pinitized cordierite grains (Fig. 5.4C, D). The latter are commonly enveloped by the biotite grains (Fig. 5.4C, D).

In the northern portion of the study area (i.e. stations F2–F4, Fig. 5.1), S_1 foliations are NW-SE trending and dip either to the NE or SW, but the majority of the planes show a predominant NE dip (Fig. 5.5C). This is largely the same for the southern portion (Fig. 5.5A). In the lit-par-lit zone, S_1 foliation planes vary from trending WNW-ESE to E-W and they dip mostly to the N and NNE directions, however, a few of the planes dip to the SW and are especially prevalent around station F9 and F10 (Figs. 5.1, 5.5B). Despite the varying orientation of the S_1 planes in the lit-par-lit zone, a clear change in the orientation of S_1 is apparent as one traverses from a generalized direction of east towards the west across the lit-par-lit zone.

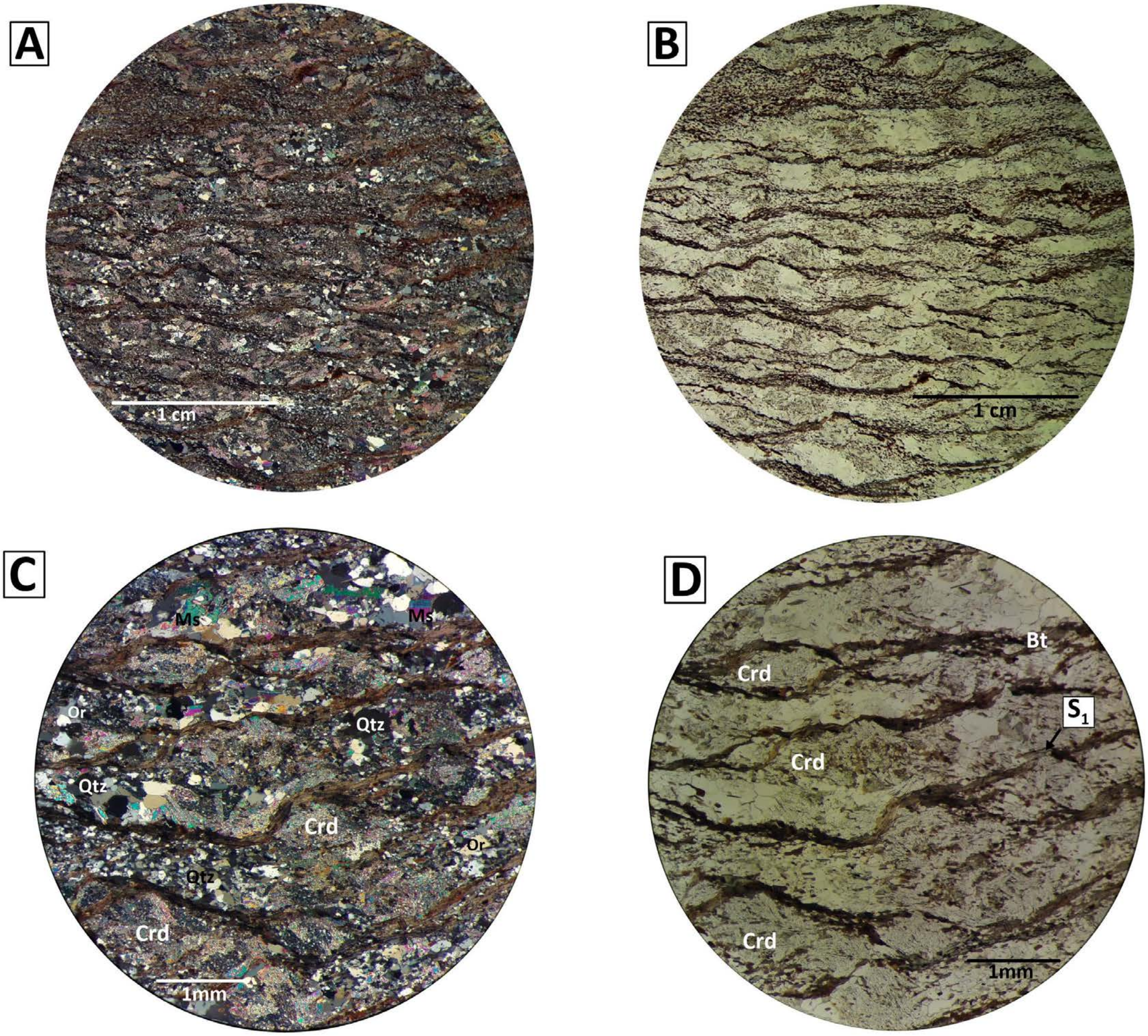

Figure 5.4*: (A) & (B) Thin section photomicrographs, in cross polars and plane-polarized light, of the domainal structure characterizing the metamudstone outcrops of the Malmesbury Group exposed in the study area. The domainal structure is composed of domains of strongly developed foliation (*S_1*) that alternate with domains with less-developed foliation (i.e. microlithons). (C) & (D) Thin section photomicrographs of a close-up view of both (A) and (B) respectively. The anastomosing nature of the *S_1* foliation can be well seen from this close-up view.*

A prime example of this is observed through a traverse from station F7 towards F12 (Fig. 5.1). F7 is comprised of roughly E-W trending (e.g. 002/50, 004/82, 002/64) S_1 planes whereas those in F12 are WNW-ESE (e.g. 026/86, 032/84, 030/88) trending. This change in orientation signifies a curve of the S_1 foliation from E-W trending in the eastern sections of the zone towards WNW-ESE heading further westward (or WNW) towards the ocean (Fig. 5.1).

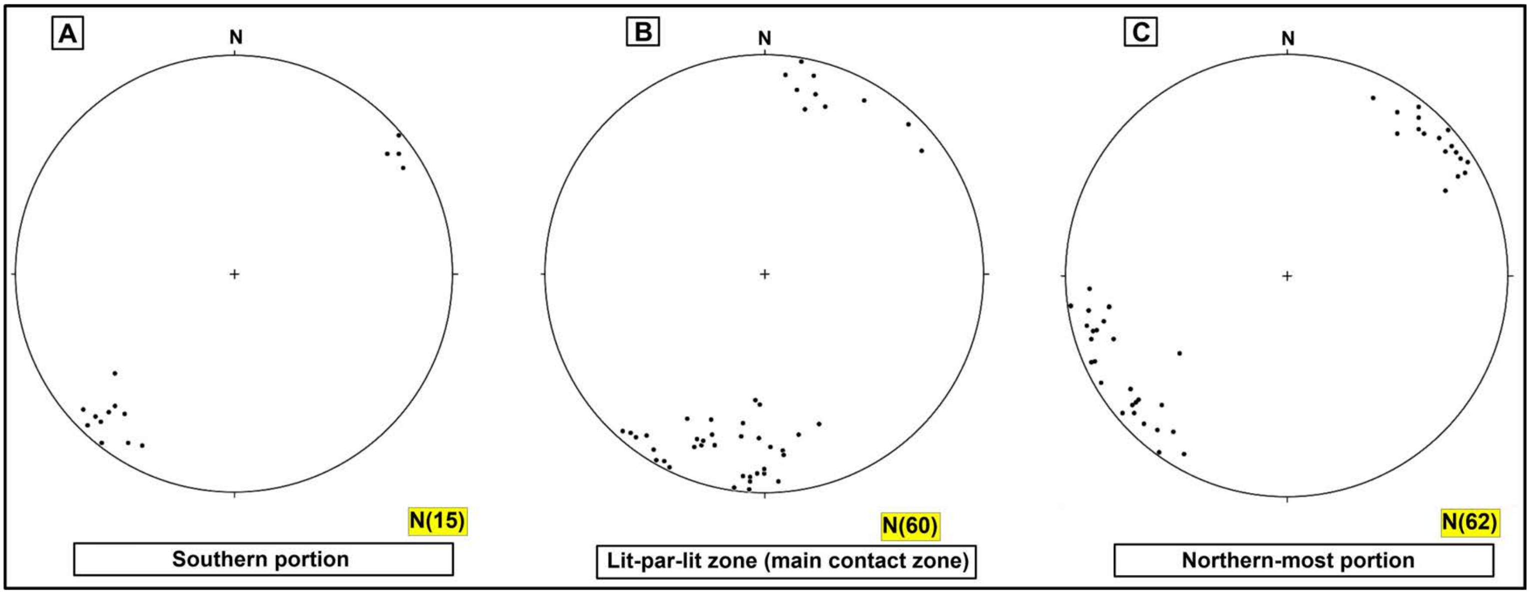

Figure 5.5*: Lower hemisphere equal-area projections comparing S_1 foliation orientation (as poles to planes) measured from the southern end (A), lit-par-lit zone (B) and northern end (C) of the study area respectively.*

The Malmesbury banding in area 8 around the valley area to the immediate WNW of station F9 (Figs. 4.1, 5.1, 5.6A) also displays some form of curvature. The Malmesbury banding is roughly E-W oriented but changes towards a more NNW-SSE orientation (Fig. 5.6A). Figure 5.6B depicts the banding at a localized scale. At this localized scale, the hybrid granite (dominantly comprised of the medium- to coarse-grained porphyritic hybrid granite) is concentrated along the limbs of the folded Malmesbury banding. The concentration of the granite along the limbs of this structure is also reflected on a larger scale as a folded pattern can be seen on the overall Sea Point contact map at area 8 (Fig. 4.1).

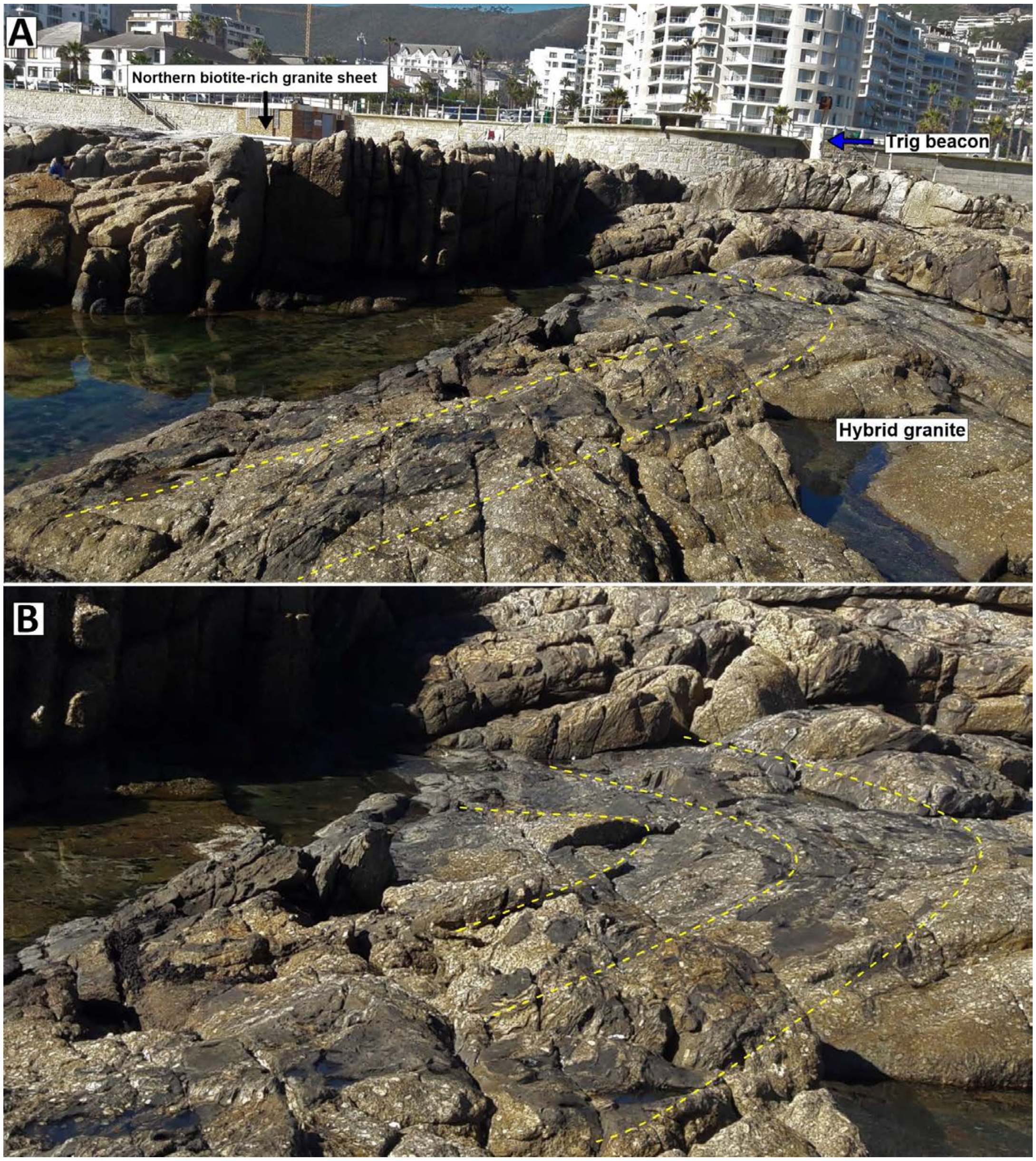

Figure 5.6*: (A) Bending/folding of the Malmesbury banding in area 8 resulting in an orientation change, of the banding, from an initial roughly E-W orientation towards a more NNW-SSE orientation. (B) Close-up view of a portion in (A) that shows maximum curvature of the banding. Hybrid granite intrusions follow the Malmesbury curvature as alluded by the concentration of granitic material along the limbs of the Malmesbury banding. The direction of view is to the E.*

5.2.3 Crenulation cleavage S_2

Crenulation occurs when an earlier foliation is shortened sub-parallel to the foliation plane causing the development of microfolds along the axial surface (Passchier & Trouw, 2005). In thin section, the S_1 planes in the foliated metamudstone samples of the study area are typically crenulated into unbroken waveforms of small asymmetric folds (gentle crenulations) due to the subsequent D_2 deformation. Commonly, no new grains have grown parallel to the axial surface of the stacked microfolds, and S_1 remains the dominant fabric in the rock (Fig. 5.7B).

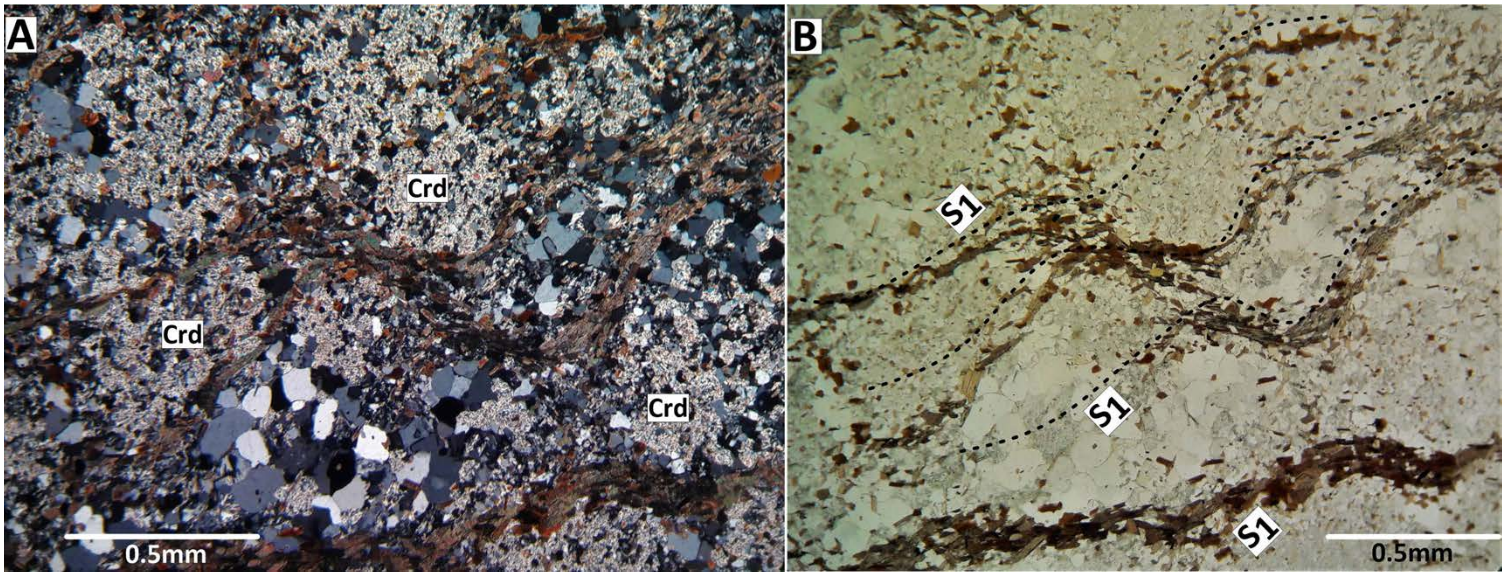

Figure 5.7: *Thin section photomicrographs, in cross polars and plane-polarized light, of the development of crenulations after the folding of S_1.*

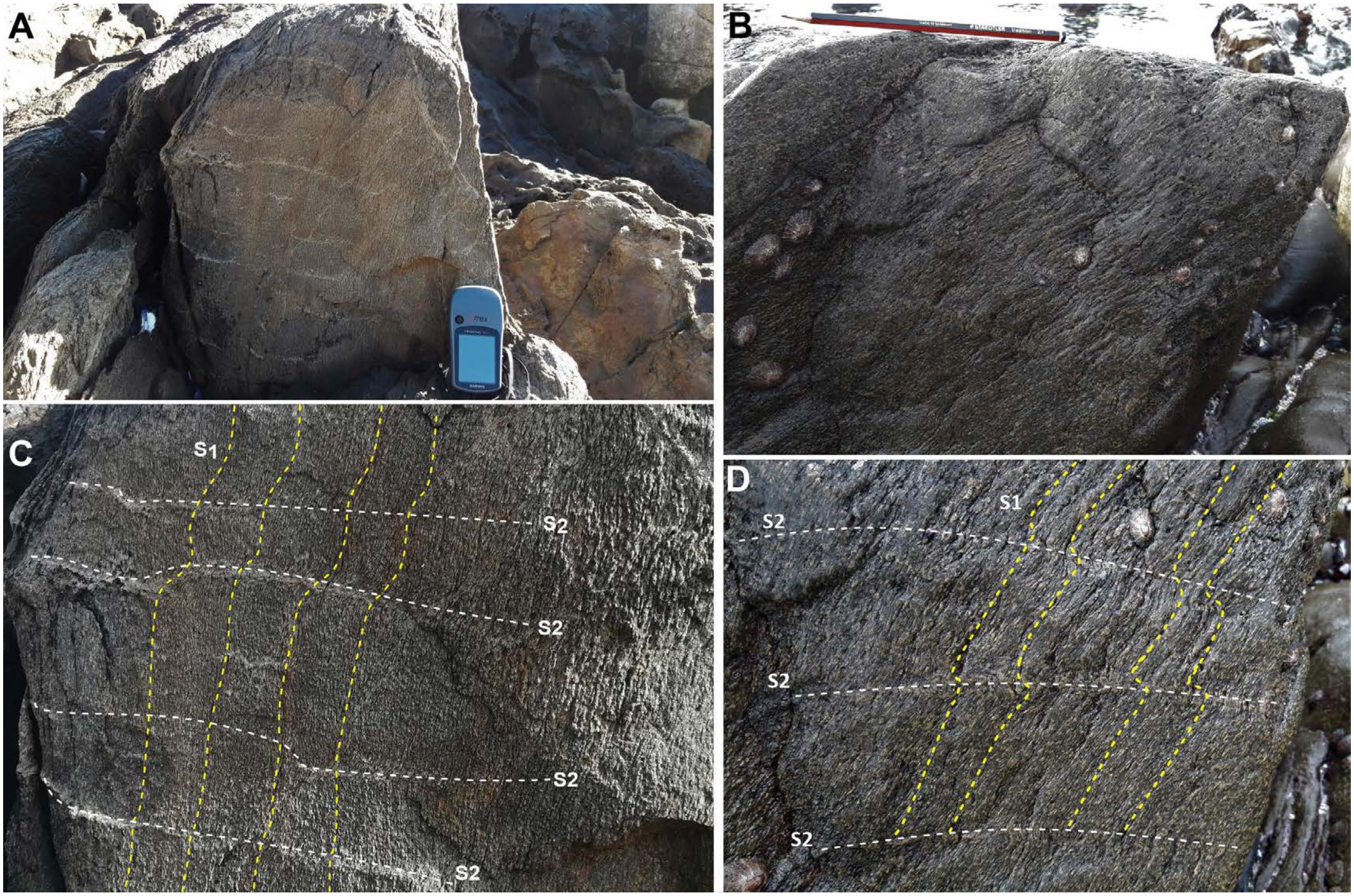

Figure 5.8: *(A) & (B) Malmesbury Group metamudstone outcrops showing evidence of a sub-horizontal S_2 crenulation cleavage; the direction of view for (A) is NW and that of (B) is NNE. (C) & (D) Are zoomed-in portions of the surfaces in (A) and (B) (respectively) showing a well-developed, closely-spaced sub-vertical foliation (S_1) (yellow dashed lines) affected by a more widely spaced sub-horizontal S_2 cleavage (white dashed lines). Given the spacing, the crenulations resemble kink bands, where S_1 foliations are kinked by the S_2 cleavage.*

At the outcrop scale, S_2 is poorly developed and fine-grained. It outcrops within two localities in the northern portion of the study area at stations F1 (Figs. 5.1, 5.8B, D) and F3 (Figs. 5.1, 5.8A, C) respectively. At these stations, but more well-developed at station F3, the S_1 foliation is closely spaced and is affected by a more widely spaced S_2 crenulation cleavage (Fig. 5.8C, D). At these two stations, S_2 is observed to be a sub-horizontal WSW-ENE oriented plane that is shallowly dipping largely towards the NNW (Fig. 5.9).

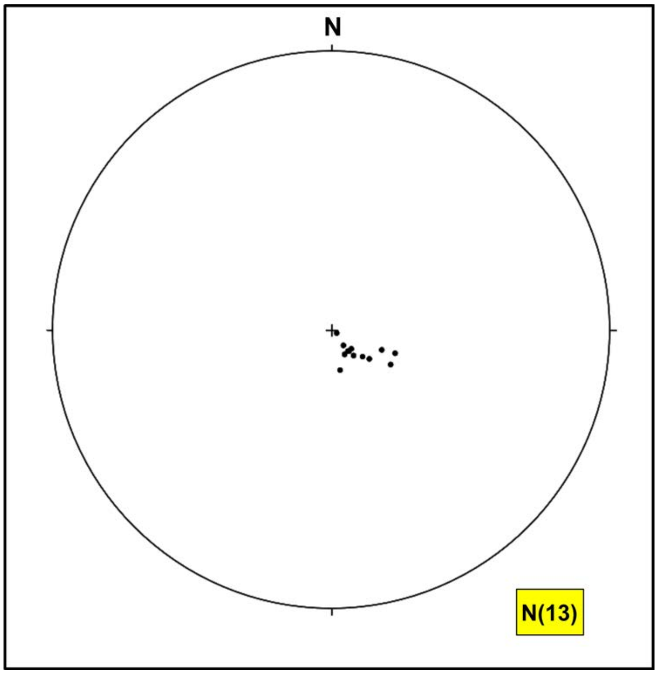

***Figure 5.9**: Lower hemisphere equal-area projections for S_2 cleavage orientation (as poles to planes) measured at the northern portion of the study area at stations F1 and F3 (Figs. 5.1, 5.8).*

5.2.4 Relationships between cordierite growth and deformation

Porphyroblasts with inclusion patterns contain information that can be useful in deciphering:

(i) The conditions and processes (pressure-temperature conditions; changes of compositional parameters) involved during nucleation and growth of porphyroblasts (Passchier & Trouw, 2005).

(ii) The relative timing of porphyroblast growth relative to deformation and metamorphism because the inclusions in the porphyroblast reflect the structure in the rock at the time of their growth (Passchier & Trouw, 2005; Raith et al., 2012).

Based on the timing of growth relative to the observed deformation, porphyroblasts can be classified as pre-, inter-, syn- or post-tectonic (Passchier & Trouw, 2005). Pre-tectonic porphyroblasts predate deformation. Inter-tectonic porphyroblasts have grown over a secondary foliation, and are surrounded by a matrix affected by a later deformation. Syn-tectonic porphyroblasts have grown during a single phase of deformation, and post-tectonic porphyroblasts post-date deformation (Passchier & Trouw, 2005).

The cordierite grains, developed within the metamudstones of the study area, show evidence of predominantly syn-tectonic growth relative to the main phase of deformation, D_1. Evidence for syn-tectonic growth include:

(i) A deflection of the matrix foliation, S_1 or S_e, around the cordierite porphyroblasts and a general planar pattern of S_1 within the cordierite (S_i) that is continuous with Se (Van der Pluijm & Marshak, 2004; Fig. 5.10C, D). For most of the cordierite porphyroblasts, both S_e and S_i are defined by biotite grains, with the included biotite grains having much smaller sizes (<0.5 mm) than the surrounding matrix/groundmass.

(ii) Curved or spiral inclusion trails within the cordierite porphyroblasts (S_i) which are continuous and connected with the matrix foliation (S_e) despite their different patterns relative to Se (Vernon & Clarke, 2008; Fig. 5.10B, E). There are two types of curved inclusion trails, one which is defined by small (0.075-0.15 mm) rounded opaque grains (Fig. 5.10A) and the other which is commonly defined by biotite and quartz (0.1-0.35 mm) grains (Fig. 5.10E). The magnitude of curvature, for both varieties, generally decreases from the core of the cordierite grains (where it is most pronounced) to the rim (where it becomes less pronounced).

(iii) Development of strain shadows as the matrix foliation is deflected around the cordierite porphyroblasts (Fig. 5.10E). The asymmetry of the strain shadows indicates a dextral shear sense for the cordierite grain shown in Fig. 5.10E.

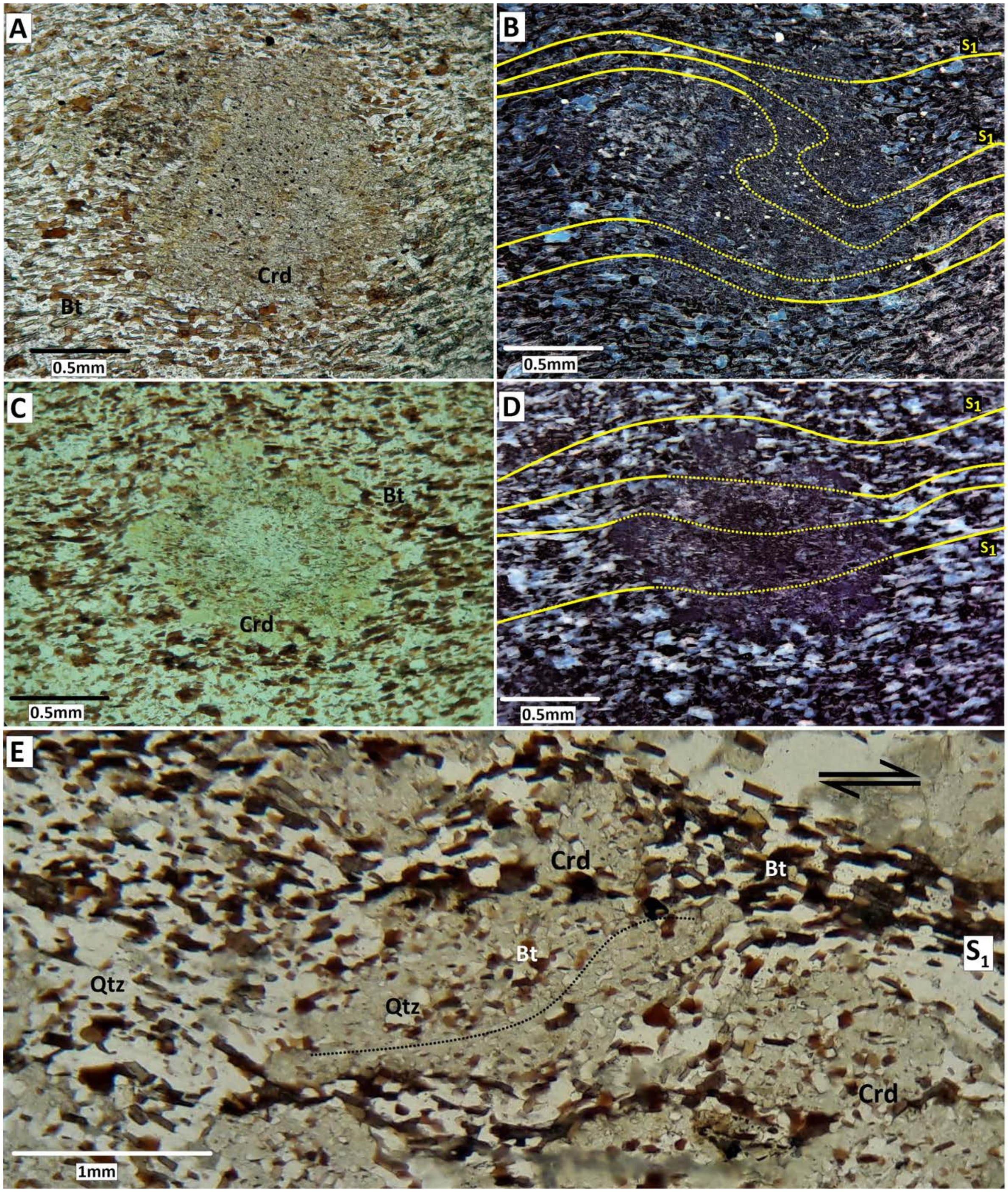

Figure 5.10: *Thin section photomicrographs of syn-tectonic Crd porphyroblasts. (A) Plane-polarized view of a sub-rounded Crd porphyroblast in sample SP44. (B) is the same photomicrograph as (A) but with a negative filter applied for a better view of the matrix-inclusion-porphyroblasts relationships at play. A deflection of the external* S_1 *foliation (defined by Bt and indicated by the solid yellow lines) around the Crd porphyroblast together with a rotation of the internal* S_1 *foliation (defined by small opaque inclusions; indicated by the yellow dashed lines) relative to the external* S_1 *foliation can be observed. (C) A sub-rounded Crd grain in sample SP44 taken in plane-polarized light (C) and applied with a negative filter (D) for the same reason as mentioned previously. A deflection of the external* S_1 *foliation around the Crd porphyroblasts and a general planar pattern of* S_1 *(within the Crd) that is continuous with the external foliation can be observed. (E) Plane-polarized view of a set of rotated Crd grains in sample SP17. The fairly large Crd grain in the centre of (E) is a syn-tectonic Crd porphyroblast with curved inclusion patterns (comprised of aligned Qtz & Bt grains; indicated by the black dashed line) and strain shadows of quartz (bottom left-mid portion of E). The asymmetry of the strain shadows implies/indicates a dextral shear sense.*

5.2.5 Folding

Regional (or first-order) folds commonly have minor (second-order) folds associated with them. This implies that both were formed during the same deformation phase and stress field and so have the same geometric features (e.g. the axial surfaces of the minor and large scale folds are parallel) (Fossen, 2010). This geological phenomenon applies to the various fold structures exposed in the study area. Most of these second-order folds in the study area are recognizable from the various folded patterns shown by the granite phases which now trace the outline of the original folded structure as a result of having intruded along the limbs and hinge zones of the original folds (e.g. Figs. 5.13, 5.15). Commonly, as a result, the originally folded beds of the country rock are no longer exposed or apparent whenever such folded granite features are observed.

One of the few places, in the study area, where the original folded bedding structure of the country rock is left intact (and not completely overprinted by the granite intrusions) occurs in area 2 in the southern portion of the study area (Figs. 4.1, 5.11). In this area, an interlayered metamudstone-metasiltstone outcrop, representing S_0 bedding, has been folded into a tight antiformal fold (Fig. 5.11). The hinge of the fold also marks one of the few areas where S_0 can be distinguished from S_1 foliation because, here, the two planar features are not subparallel to each other as evidenced by a SW dipping S_1 axial planar foliation cutting across the limbs of the folded S_0 structure (upper central portion of Fig. 5.11A, B; seen more clearly in Fig. 5.12A). This F_1 fold has smaller higher-order parasitic folds towards the hinge area (Fig. 5.12B). Depending upon which limb (on the left or right side if facing toward the fold hinge) higher-order parasitic folds are observed from when an observer is looking down the axial direction of a lower order fold, they display "Z" (clockwise) or "S" (anti-clockwise) local apparent vergence directed toward the hinge zone (Burg, 2017; Fig. 5.12B). In this case, the minor (S and Z) folds verge towards the hinge zone of a larger scale antiform located in the NW direction (Fig. 5.12B).

Figure 5.11: *(A) Evidence of* F_1 *folding in the southern portion of the study area. Quartz veins in the bottom-left and bottom-central portion of (A) occur along the folded limbs. (B) Annotated depiction of (A) showing the trace or outline of the fold (white solid lines). The yellow dashed line represents the trace of a non-planar axial surface that characterizes this fold. Evidence of small porphyritic granite bands or veinlets having made use of the folded limbs for propagation during intrusion is located on the top right portion of (A) and (B) but seen more clearly in the right-portion of Fig. 5.12A. White trails in (A), which mask the appearance of the fold, are trails left behind by various oceanic gastropods. The direction of view is WNW.*

At the hinge of this F_1 fold (Figs. 5.11, 5.12A), S_1 is axial planar and trends WNW-ESE while dipping steeply to the SW (e.g. 202/88, 204/86, 196/88). The axial surface is non-planar. This is evident from the limbs further away from the hinge area (i.e. the bottom mid-right portion of Fig. 5.11B) yielding an axial surface orientation of 176/77 whereas the hinge area of the fold has an axial surface oriented at 212/70. According to Burg (2017), the axes of parasitic folds are habitually closely parallel to the axis of the major fold with which they are associated and are said to be congruous. Thus, for this reason, all elements needed for the classification purposes of this fold was restricted to the limbs occurring in the hinge zone instead of those further away from the hinge. Therefore, with a measured axial surface oriented in a WNW-ESE (189°) direction that dips to the SW at an angle of 71°, a fold hinge with a trend of 116° that plunges moderately to the SE at an angle of 40° and an interlimb angle of 34°, this fold can be classified as a steeply inclined moderately plunging tight fold.

The limbs have unequal lengths and their leaning direction suggests a relative sense of movement, termed the apparent vergence (Burg, 2017) (which is different from the use of the same term to refer to the direction of the next anticlinal closure or hinge of a larger fold as previously discussed). Based on this, the F_1 fold has a north-easterly vergence (a direction perpendicular to the fold axis) based on the “leaning” or verging direction of the fold hinge towards the NNE direction (Fig. 5.11B).

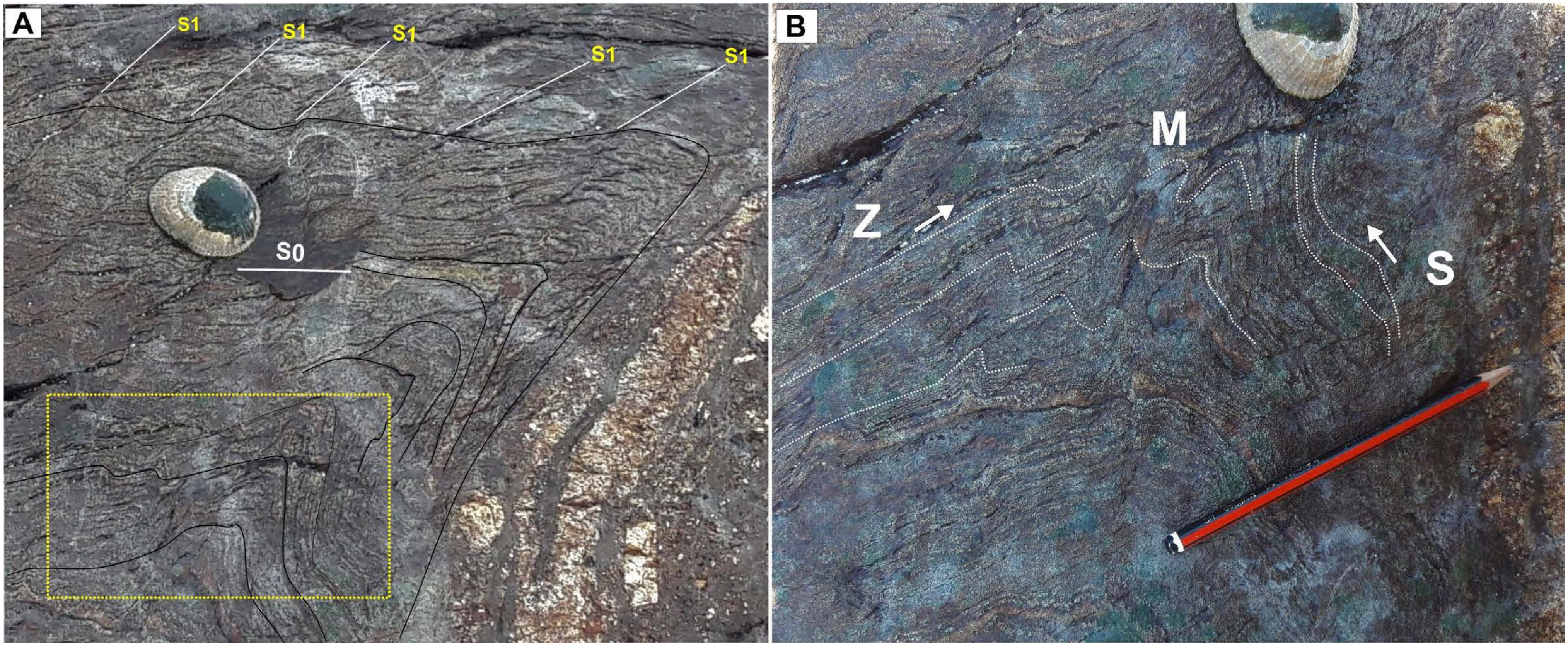

Figure 5.12: (A) A close-up view of the fold hinge in Fig 5.11. Note how the earlier S_0 fabric is crenulated by the later S_1 foliation. (B) A close-up view of the portion of (A) demarcated by the yellow rectangle to show how the sense of symmetry of minor folds varies around the profile of the F_1 fold. S and Z folds indicate the limbs of the fold whereas M folds indicate the hinge region. The minor folds verge (indicated by white arrows) towards the hinge zone of the larger scale antiform located in the NW direction. The direction of view is WNW. Pencil points north.

In the lit-par-lit zone, folded features are not readily exposed due to the prevalence of granite intrusions. Those which are visible (to some extent) have been intruded by the various hybrid granite phases to define what looks like folded granitic material. These folded features are embedded within the country rock, however, traces of the original bedded structures are no longer visible. This makes it particularly difficult to measure their orientation for classification purposes.

***Figure 5.13**: Outcrop photographs of folded Malmesbury country rock structures intruded by various hybrid phases in the lit-par-lit zone. Traces of the originally folded country rock beds are no longer visible. (A) A synform-antiform pair defining an Isoclinal to tight fold in area 5 (the direction of view is SSW). Note how greater the granite accumulation is in the hinge zones as opposed to the limbs of the isoclinal fold. (B) and (C) synform-antiform pair defining chevron-type folds with sharp hinges and relatively straight limbs in area 4. The direction of view for (B) is NNE and SSW for (C).*

These aforementioned folds outcrop predominantly in areas 4 and 5 (Fig. 4.1) as synform-antiform pairs in the form of tight folds (Fig. 5.13A) and chevron-type folds with sharp hinges (Fig. 5.13B, C). The hinges of both fold types close either towards the SE (to ESE) direction or towards the NW (to WNW) direction; a direction subparallel to the trend of the S_1 foliation and trending direction of the Malmesbury banding in the lit-par-lit zone.

In the northern section of the study area, three antiformal fold structures outcrop prominently (Figs. 5.14, 5.15, 5.16). The entire Malmesbury outcrop in the northern-most portion of the study area appears to form part of a larger-scale regional fold. The fold closure can be seen in area 11 (Figs. 4.1, 5.14) of the mapped area. The fold in its entirety is not inherently obvious upon initial viewing as only the NE dipping limb is dominantly exposed whereas the other roughly SW dipping limb is largely submerged (into the ocean) (Fig. 5.14). From the measured bedding readings, the fold is classified as a gently plunging (20°), moderately inclined (57°) tight fold (interlimb angle of 28°).

***Figure 5.14**: Outcrop photograph of a fairly large scale antiformal fold structure exposed in the northern portion of the study area (i.e. area 11). The SW-dipping limb is largely submerged, whereas the NE dipping limb remains well exposed. The direction of view is to the WNW.*

In area 10 of the mapped area (Fig. 4.1), the country rock has been intruded by the microgranite along the limbs and hinge of a fairly large (approximately 30 m laterally) antiformal fold structure to define an isoclinal to tightly folded pattern (Fig. 5.15). The folded pattern is a continuation of the fold in area 11 (Fig. 5.14) and represents the hinge of the area 11 fold. The original folded bedding structure, before the granite intrusion, is no longer apparent but the microgranite limbs, however, trend in a direction sub-parallel to the regional foliation. The fold is non-cylindrical with the limbs oriented WNW-ESE and the hinge assuming a NNW-SSE orientation (Figs. 4.1, 5.15). The fact that the microgranite is primarily localized along the limbs of the fold suggests that it primarily used the folded S_0 beds (in this portion of the study area) for its propagation.

Neighbouring the folded microgranite in area 10 is the northern coarse-grained porphyritic granite sheet (Fig. 5.15). This sheet is defined by large K-feldspar megacrysts which are, in general, largely randomly oriented but do show some form of alignment parallel to sub-parallel with the contact between itself and the country rock. This is illustrated by the mineral lineation data in Figure 5.15B. The overall impression is that the megacrysts are largely aligned parallel/sub-parallel to the coarse-grained porphyritic granite-country rock contact, with only a minority being oriented obliquely to that contact (Fig. 5.15B). The observation of preferential alignment diminishes rapidly away from the contact.

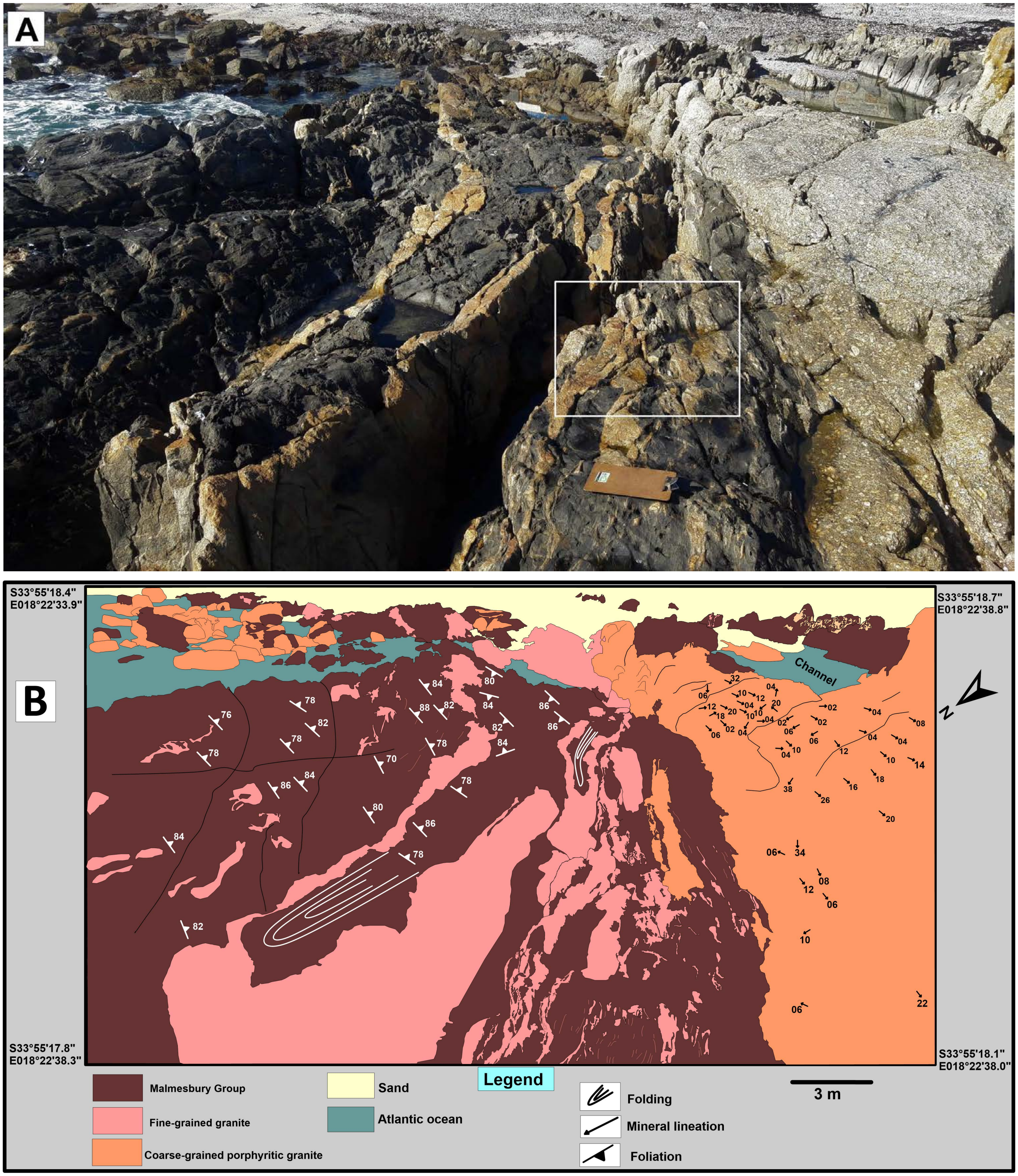

Figure 5.15: *(A) Tight to isoclinal folding of the Malmesbury Group in the northern portion of the study area; the picture was taken looking towards the ESE direction. The fine-grained granite/microgranite (pink) toward the left/bottom centre appears folded in both the photo and drawing representation (the closure is to the left of the clipboard in (A) and above "Malmesbury Group" in the legend in (B)). (B) Corresponding geological map of (A) showing the orientation of the S_1 foliation planes and K-feldspar mineral lineation data from the adjacent northern coarse-grained porphyritic granite sheet (peach). The foliation planes are WNW-ESE- to NW-SE-trending and steeply dipping to the NE or SW. The K-feldspars are largely aligned parallel/sub-parallel to the coarse-grained porphyritic granite-Malmesbury contact. In parts where the coarse-grained porphyritic granite and the microgranite are in contact (white square in A), the contact is transitional instead of sharp.*

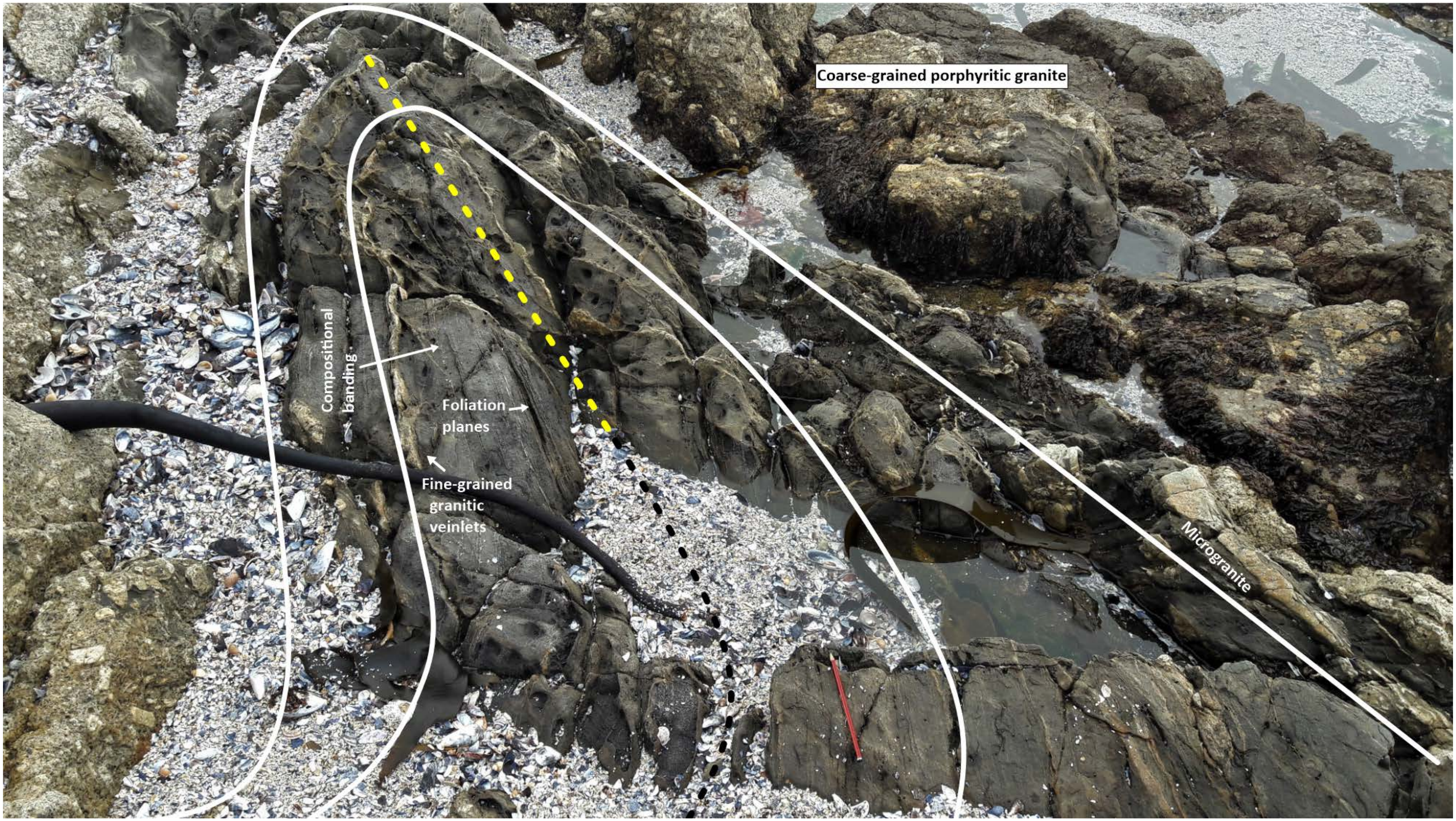

Figure 5.16: *Antiformal fold structure, closing towards the WNW direction, exposed in the northern portion of the study area at area 9. This folded structure is non-cylindrical as evident from the varying orientation of the compositional banding (S_0) exposed at the hinge area (yellow-dashed line) compared to that in the limbs in the bottom portion of the Figure (black dashed line). Various fine-grained granitic veinlets and microgranites follow the foliation (S_1) and bedding (S_0) planes for their propagation much more readily compared to the adjacent coarse-grained porphyritic granite which cuts across the country rock in a few places. The direction of view is NW*.

The third antiformal structure, outcropping in area 9 of the mapped area (Fig. 4.1), is another example of a folded country rock body where the original bedding structure is still intact (Fig. 5.16). In this fold, sub-vertical bedding is tightly folded to define an antiformal structure that closes towards the WNW direction. Just as was the case with the folded bedding in the southern portion of the study area (Fig. 5.11) and the microgranite fold in area 10 (Fig. 5.15), this fold is also non-cylindrical. This is evident from the trend of the bedding being dominantly oriented in a WNW-ESE direction (towards the hinge; yellow dashed line) from an initial NNW-SSE direction (towards the limbs; black dashed line) (Fig. 5.16). The fold is classified as a horizontal (plunge = 8°), moderately inclined (52°) tight fold (interlimb angle of 28°).

A comparison of the axial surface and fold hinge orientation of the various F_1 fold structures located in area 2 (Figs. 4.1, 5.11), area 9 (Figs. 4.1, 5.16) and area 11 (Figs. 4.1, 5.14) are given in Figure 5.17. The antiformal fold structures of areas 9 and 11 have similar NW-SE trending axial surfaces (i.e. 224/52 for area 9; 230/57 for area 11) and gently inclined fold hinges that plunge to the NW (i.e. fold hinge trend & plunge of 308/08 for area 9 and 306/20 for area 11) (Fig. 5.17). The antiform located in area 2 has a differently orientated fold hinge, relative to the antiforms of areas 9 and 11 respectively, and moderately plunges to the SE (i.e. 116/40-trend/plunge). Its axial surface also varies in orientation and dip relative to the folds in areas 9 and 11, and is instead WNW-ESE orientated with a steeply inclined dip (i.e. 189/71) (Fig. 5.17).

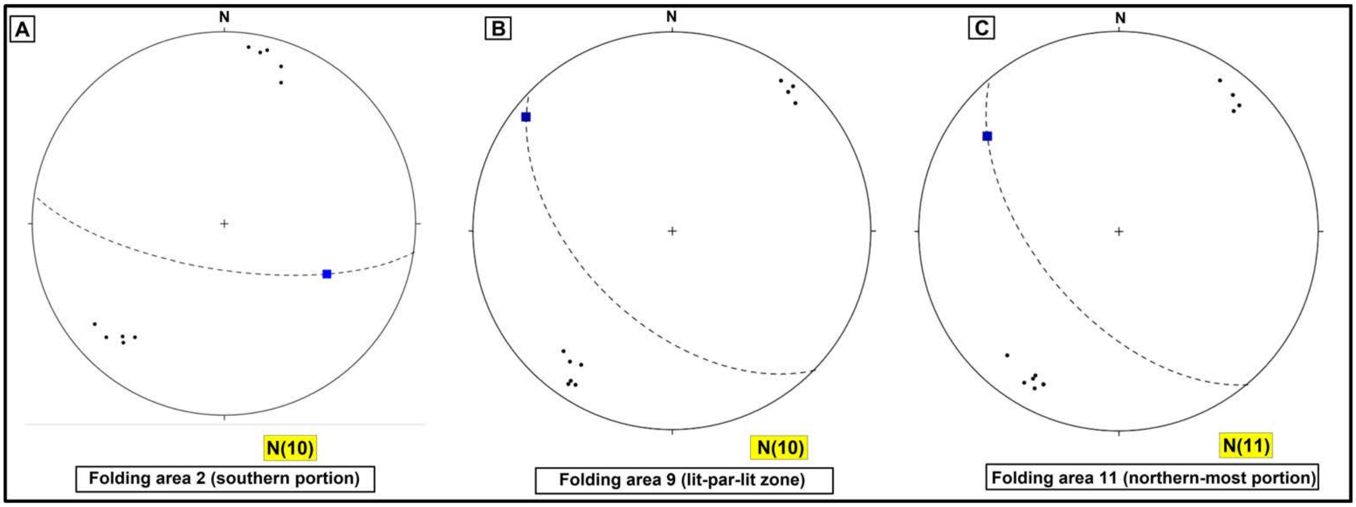

Figure 5.17: *Lower hemisphere equal-area projections of the plunge and plunge direction of the fold hinge (blue square) and the associated dip direction and dip of the axial surface (dashed black line) as determined from the bedding orientation readings taken from the folded bed limbs at area 2 (A), area 9 (B) and area 11 (C).*

5.3 Shear sense indicators in the lit-par-lit zone

Shear zones are defined as high strain zones where the distributed deformation usually contains a rotation component, reflecting lateral displacement of wall rock segments relative to each other (Passchier & Trouw, 2005). Shear zones separate less strained or unstrained portions of the lithosphere and are the deeper counterparts to upper crustal faults and fault zones in thrust, extensional and strike-slip settings alike (Fossen & Cavalcante, 2017). Shear zones can be developed in rocks of any original composition and fabric and occur at almost any scale (from a few mm to very large kilometre wide structures) (Mawer, 1992; Fossen, 2010).

The direction of movement in shear zones is important for the reconstruction of the tectonic history or evolution in an area, but most important is the sense of displacement which can either be dextral or sinistral, normal or reverse (Passchier & Trouw, 2005). Typical shear sense indicators include: tiling of objects, shear band cleavage/foliation (including C/S fabrics), mantled porphyroclasts (grain-tail complexes), mineral fish (disrupted grains), quarter structures, lattice preferred orientation and deformed sigmoidal and *en échelon* vein arrays at dilation sites (Mawer, 1992; Passchier & Trouw, 2005). The shear sense indicators observed in the lit-par-lit zone of the study area are in the form of:

(i) **Grain-tail complexes** defined either by: (a) K-feldspar megacrysts lodged or embedded within the country rocks, and (b) hornfels xenoliths within a metamudstone host. The origin (magmatic or *in-situ* growth) of the K-feldspar megacrysts is discussed later on in the thesis.

(ii) ***En échelon* vein arrays (tension gash veins)** developed within the country rock

(iii) **Shear band foliations** within the country rock

Sense of shear indicators are best observed in XZ sections cut perpendicular to the foliation plane and parallel to the stretching lineation (Passchier & Trouw, 2005). In the study area, however, most of the shear sense indicators were studied based on what was visible on outcrop surfaces. This was due to several reasons including: (i) most of the ideal shear sense indicators lie on flat surfaces which cannot be easily sampled, (ii) the Sea Point contact outcrop is a heritage site, therefore, all the samples that were extracted were restricted to specific sites (gullies and jointed surfaces) to not adversely affect the visual quality of the outcrop, and (iii) some of the structures (e.g. shear band foliations and S_2 crenulation cleavage) that could have potentially been sampled were purposely left preserved due to their rarity in the outcrop. As a consequence, the orientations in which some of the shear sense indicators were viewed may not be ideal and this could be the reason why some sites give contradicting results (sinistral as opposed to dominantly dextral, for example) especially for grain-tail complexes and shear band foliations. Additionally, the study area underwent bulk shortening, in which case one would expect conjugates of opposing shear sense (e.g. Tourigny & Schwerdtner, 1991; Little et al., 2013).

5.3.1 Grain-tail complexes: K-feldspars and hornfels xenoliths

Grain-tail complexes form as material recrystallizes or precipitates in the flow field exerted by a large grain (phenocrysts or porphyroblasts sitting within a finer-grained matrix) (van der Pluijm & Marshak, 2004). These grains may have tails of material with compositions and/or grain shape and sizes that differ from the matrix and, during deformation, the grains act as rigid bodies, making it possible to determine the sense of displacement from the tails (Mawer, 1992; van der Pluijm & Marshak, 2004; Passchier & Trouw, 2005). Grain-tail complexes are usually used to infer the sense of shear in mylonites, where they occur as porphyroclasts.

Three types of grain-tail complexes are recognized in the study area based on the shape of their tails (or 'wings') and their relationship with the shear-zone foliation. They include **ϕ-type**, **σ-type**, and **δ-type**. ϕ-type grain-tail complexes occur in the study area for both the K-feldspar grains and hornfels xenoliths, however, their tails show no evidence of stair-stepping relative to the foliation reference plane (Fig. 5.18) and thus cannot be used to accurately decipher shear sense. For this reason, they will not be described further.

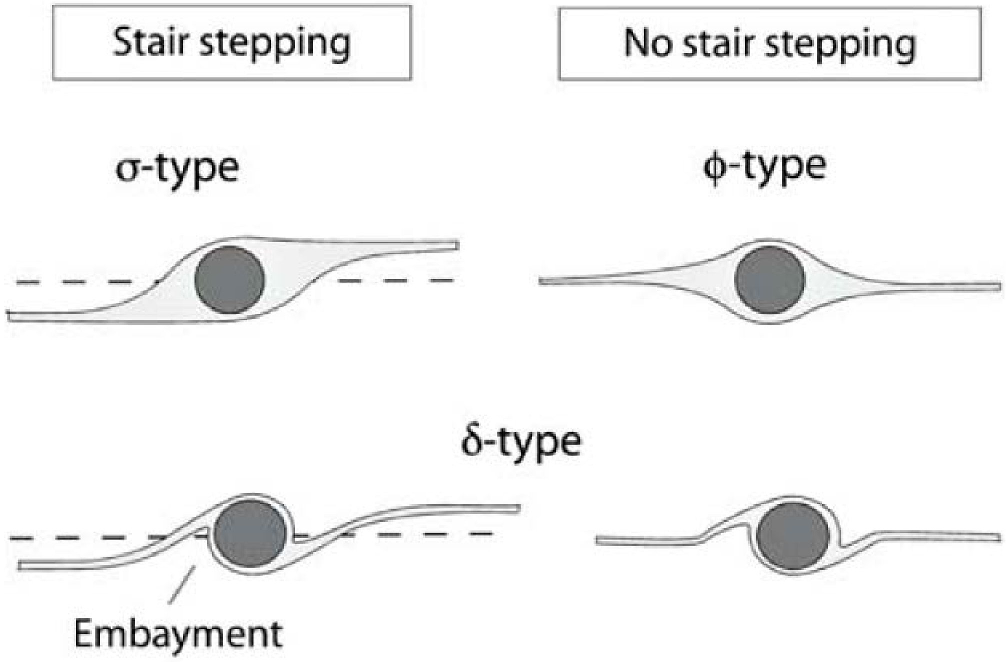

__Figure 5.18__: The three types of grain-tail complexes and their use as shear sense indicators (modified after Passchier & Trouw, 2005). A dextral sense of shear is inferred for all grain-tail complexes to the left of the figure under the heading 'stair-stepping'. The circles shaded in grey are used to indicate a large single grain sitting within a finer matrix and the dashed lines, running through the centre of the grain, are used to indicate the foliation reference plane.

σ-type grain-tail complexes are characterized by their wedge-shaped tails which do not cross the foliation reference plane when tracing the tail away from the grain whereas δ–type complexes have thinner, more curved tails that cross-cut the reference plane when their tails are traced away from the grain (Fig. 5.18) (van der Pluijm & Marshak, 2004). Both σ- and δ-types have asymmetric tail geometries produced by non-coaxial deformation (Fossen, 2010). They can both be used as shear sense indicators using their internal asymmetry and the stair-stepping geometry of their tails since the tails 'step up' (on either side of the reference line; Fig. 5.18) in the direction of displacement of the upper block (Passchier & Trouw, 2005).

For the K-feldspar grains, all the grain-tail complex types are defined by euhedral to subhedral K-feldspar megacrysts connected by thin fine-grained granitic material (which define the tails) and are all embedded within the country rock (Figs. 5.19). Where clearly defined, the tails extend in the direction of the foliation within the host rock (Fig. 5.19A, C, E). From the σ-type and δ-type grain-tail complexes observed, the sense of shear is predominantly dextral, top to the NW–WNW, shear (Fig. 5.19A, B, D, E), although there are a minor amount of grains which show an opposite shear sense, i.e. sinistral, top to the SE–SSE, shear (Fig. 5.19C).

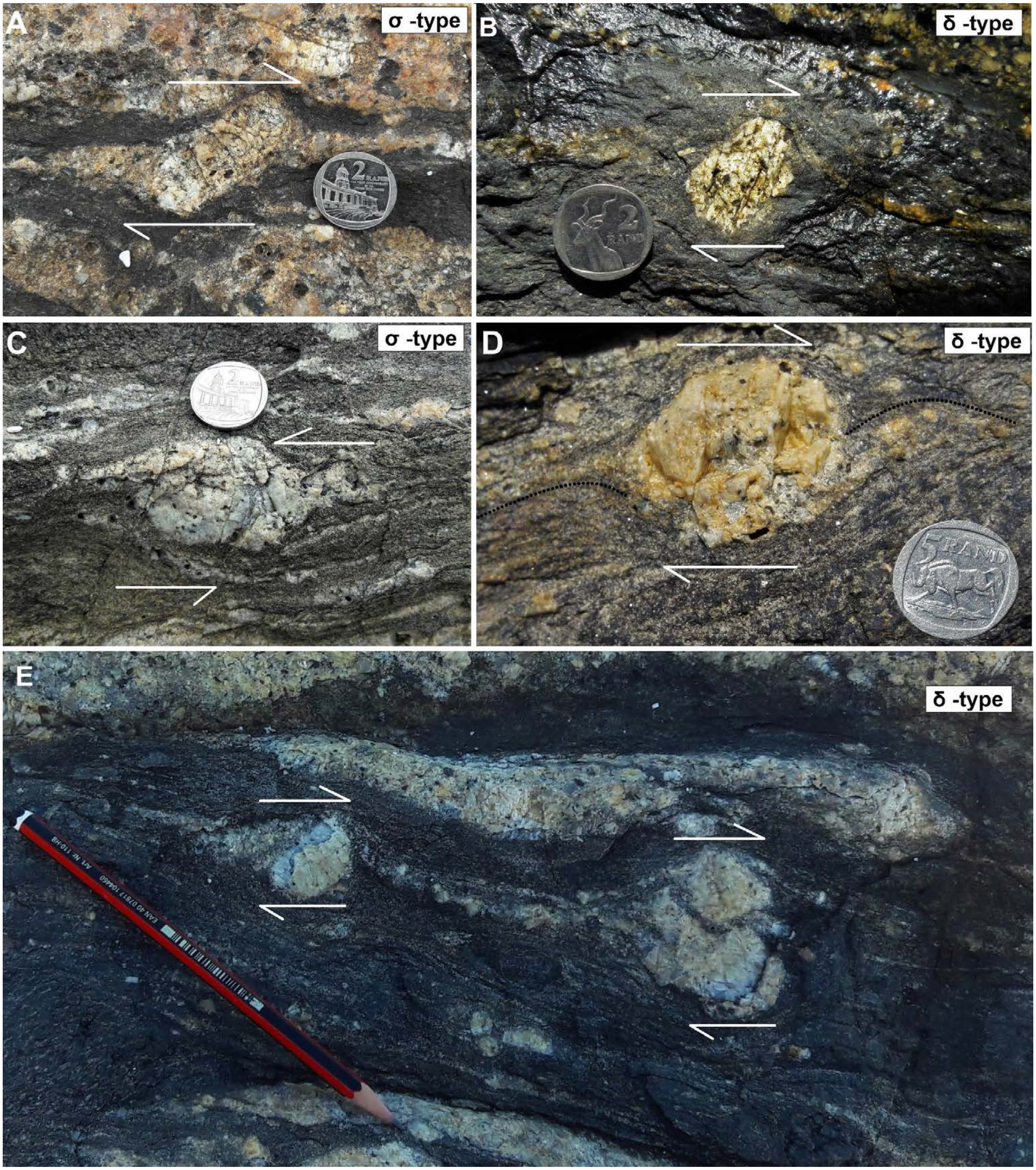

Figure 5.19*: Grain-tail complexes of the σ- and δ- type characterized by subhedral K-feldspar grains lodged within a country rock host at various locations in the lit-par-lit zone. For both types, a dextral, top to the NW, sense of shear predominates (A, B, D & E) but there are a few cases that show a sinistral, top the SE, opposite shear (C). Trails of feldspathic material, emanating from the tips of the K-feldspar grains, extend in a direction roughly sub-parallel to the main foliation. All of the megacrysts occur on horizontal/sub-horizontal surfaces.*

With regards to the hornfels xenoliths, only grain tail complexes of the σ-type are recognized. Most of the hornfels xenoliths are commonly rimmed by fine-grained feldspathic granitic material and their grain-tail geometry implies a dextral, top to the NW, shear sense (Fig. 5.20B) or dextral, top to the SE, shear (Fig. 5.20A).

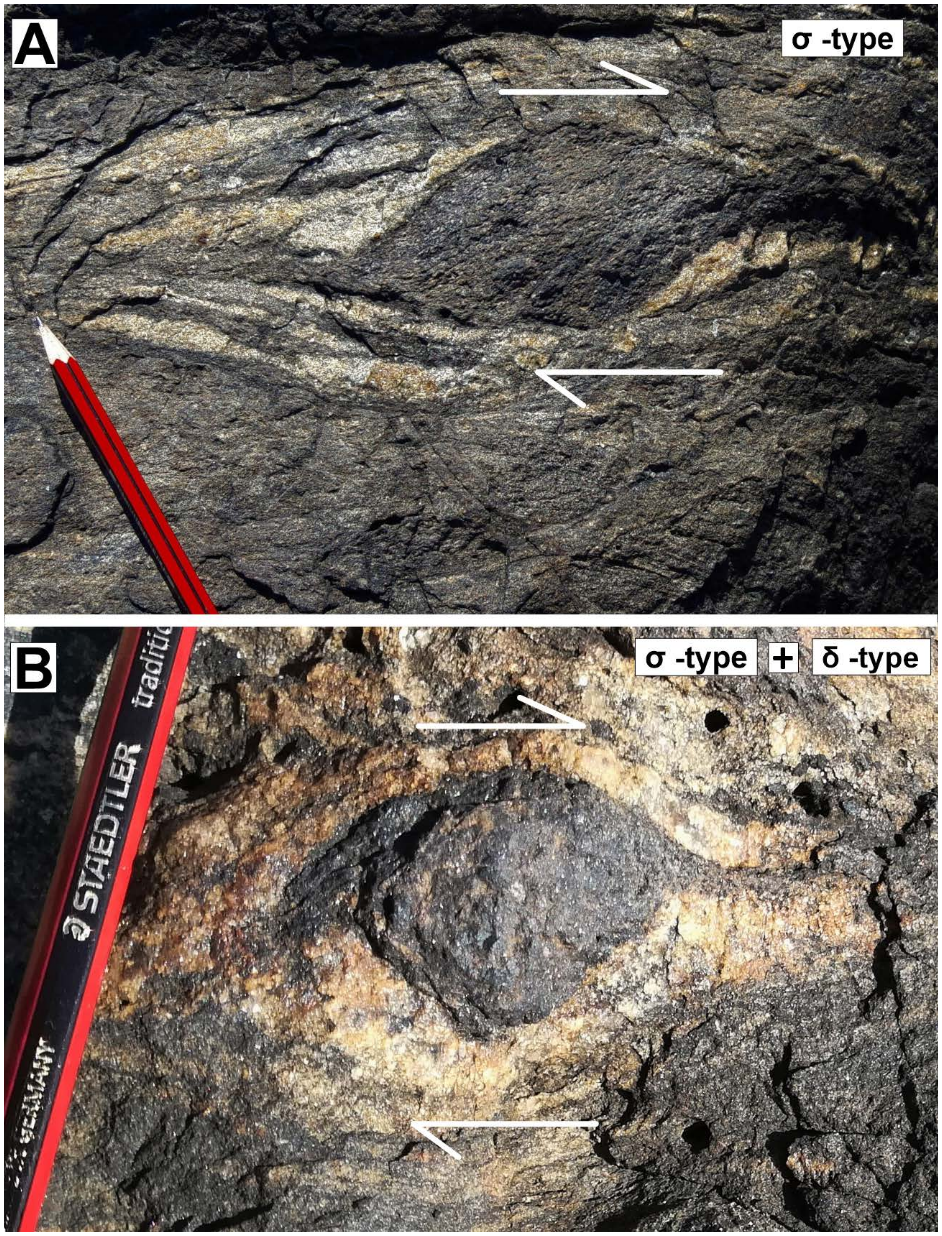

Figure 5.20*: σ-type Malmesbury Group hornfels xenoliths sitting within a more biotite-rich metamudstone host in the lit-par-lit zone. Hornfels xenolith in (B) has characteristics of a σ-clast and part δ. A dextral, top to the SE, shear is interpreted for (A) whereas (B) indicates dextral, top to the NW, shear. All of the hornfels xenoliths occur on horizontal/sub-horizontal surfaces.*

5.3.2 *En échelon* vein arrays (tension gash veins) at dilation sites

Dilation sites are voids in a rock originally filled with fluid (Passchier & Trouw, 2005). They commonly include veins, strain shadows, fringes and microboudins. In brittle fault zones and some ductile shear zones, extension features with curved geometries known as ‘tension gashes’ develop in sets of veins that are arranged *en échelon* (Passchier & Trouw, 2005). They are useful as shear sense indicators because during non-coaxial deformation, the older central part of the vein will rotate just like any material line in the bulk flow and the younger outer parts will rotate less explaining the curved shape of tension gash veins (Passchier & Trouw, 2005).

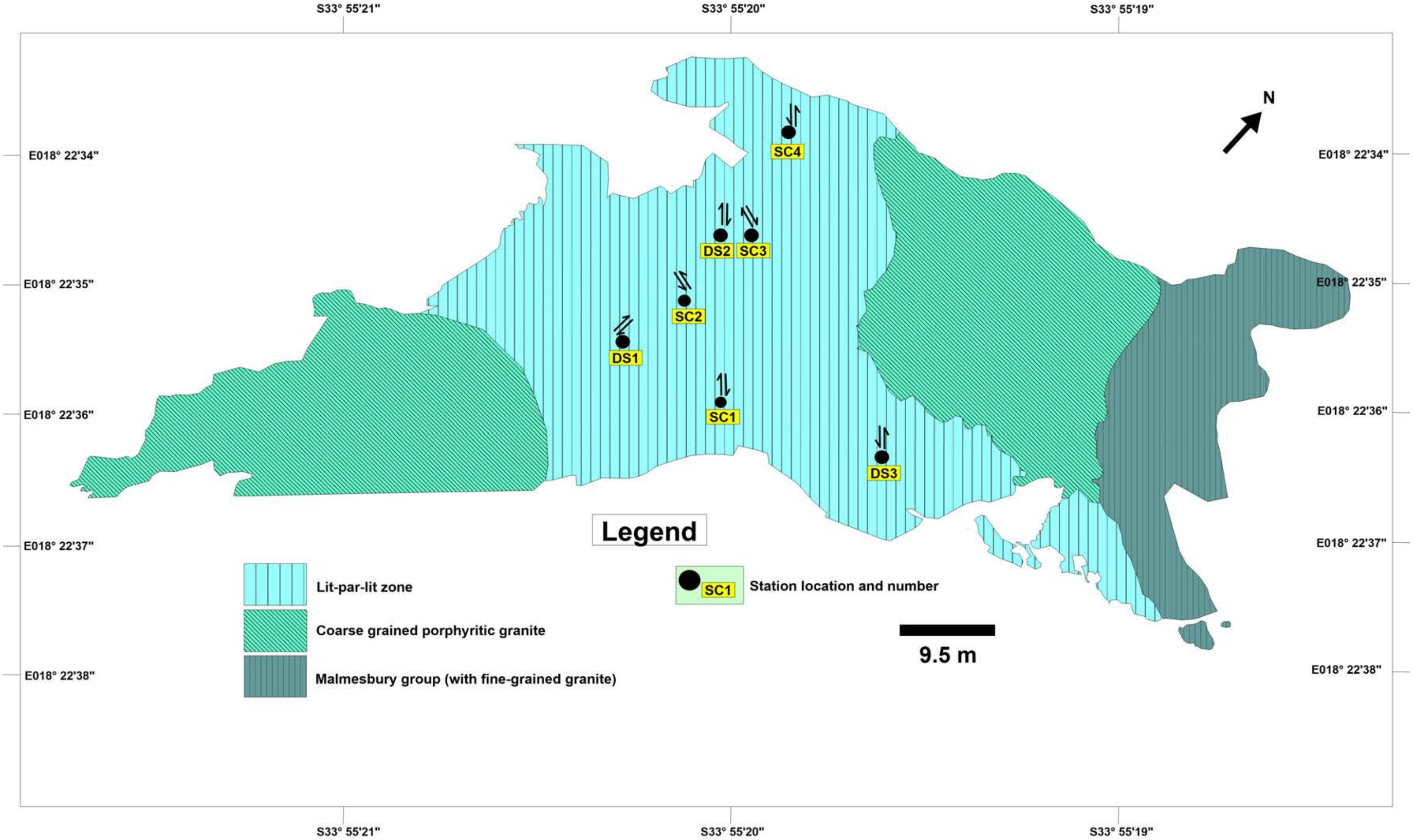

***Figure 5.21**: Simplified geological map of the Sea Point contact (the rest of the coarse-grained porphyritic granite further south is also excluded for the same reason as stated in Fig. 5.1). The map shows the locations of suitable shear sense indicators in the study area. Stations SC1 to SC4 are the locations that show evidence of C/S fabrics and DS1 to DS3 are dilation sites (DS) with well-developed tension gash veins. The stations for grain-tail complexes are excluded due to their common occurrence within the lit-par- lit zone. The sense of shear at each station is drawn to orientation.*

Two characteristic shapes namely, an S-shape and Z-shape, are inferred from the tension gash veins developed during progressive non-coaxial deformation. Z-shaped tension gash veins indicate a dextral shear sense whereas S-shaped tension gash veins imply a sinistral shear sense (Passchier & Trouw, 2005). Prime examples of dilation sites with well-developed S- and Z-shaped tension gash veins are shown in Figure 5.22. All these examples are located within the lit-par-lit zone (i.e. stations DS1-DS3; Fig. 5.21).

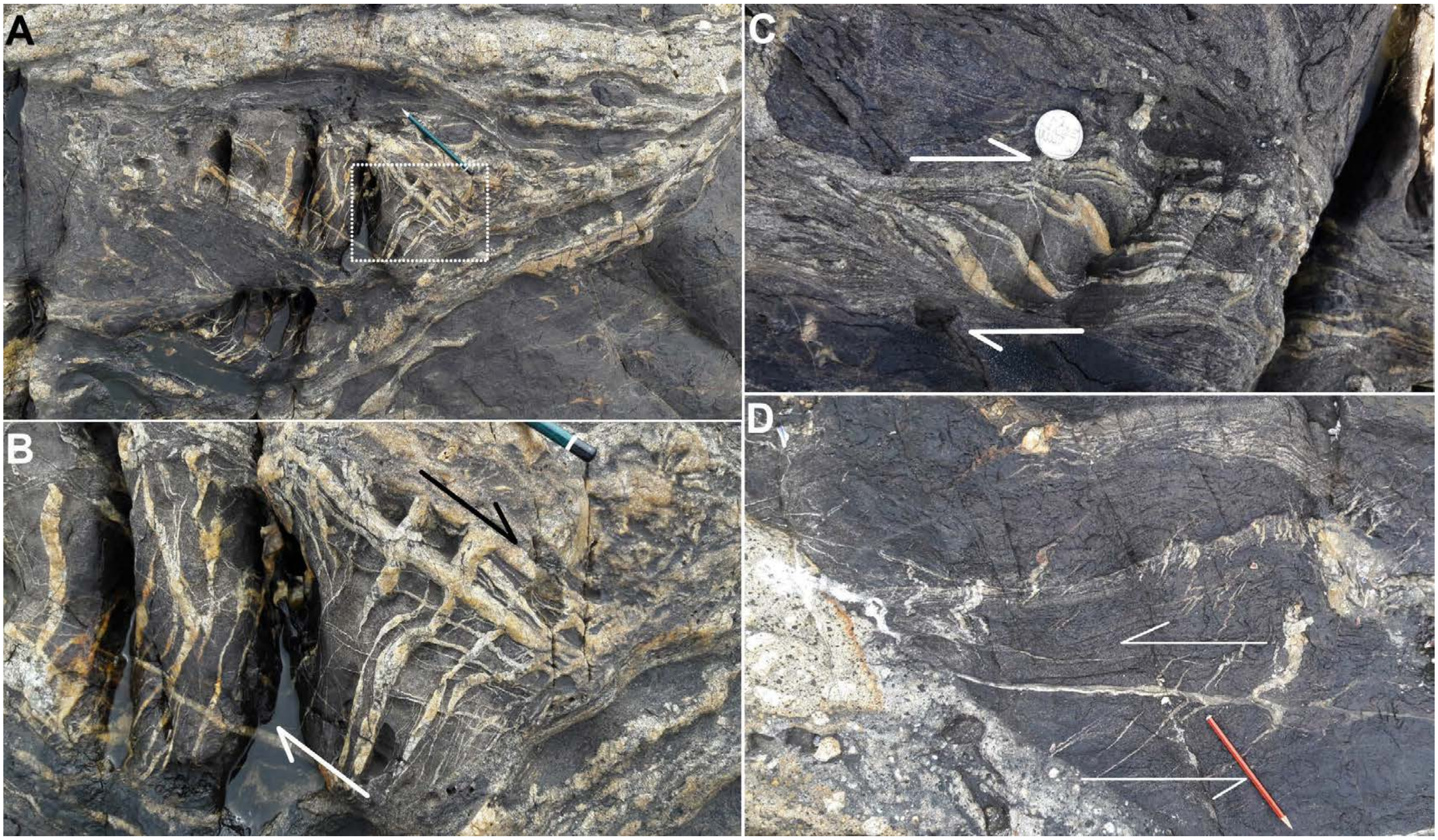

Figure 5.22: *En échelon tension gash veins in the lit-par-lit zone. (A) A metasiltstone xenolith with well-developed tension gashes occurring within a metamudstone host, which, is in turn, rimmed by a fine-grained semi porphyritic hybrid granite. (B) Close-up view of the small portion in (A) demarcated by the white rectangle; the z-shaped tension gashes indicate a dextral, top the N, sense of movement. (C) A smaller metasiltstone xenolith, compared to (A), which is also enveloped within a metamudstone host; the z-shaped tension gashes suggest a dextral, top the NW, shear sense. (D) Metamudstone with compositional layering in contact with a medium-grained porphyritic hybrid granite phase (bottom left). The S-shaped tension gashes suggest a sinistral, top the SE, shear. All examples occur on sub-horizontal surfaces.*

Figure 5.22A shows a metasiltstone xenolith within a metamudstone host at station DS1 (Fig. 5.21). The xenolith is cross-cut by various quartzofeldspathic tension gash veins which are perpendicular to the orientation of the main principal foliation as well as the orientation of the adjacent hybrid granite banding (top portion of Fig. 5.22A) surrounding the metamudstone. The Z-shaped orientation or geometry of the *en échelon* arranged tension gashes suggests a dextral sense of shear (Fig. 5.22A, B), more specifically, dextral, top to the N, shear. These Z-shaped *en échelon* tension gash veins are cross-cut by another generation of predominantly planar tension gash veins trending N to NNW (Fig. 5.22A, B). These cross-cutting tension gash veins are likely to be 'feather veins' which form part of a continuous planar vein growing over or cutting through the series of *en echelon* tension gashes (Passchier & Trouw, 2005).

Another set of en-echelon Z-shaped tension gash veins (Fig. 5.22C) are located at station DS2 (Fig. 5.21). As is the case in station DS1, the tension gashes in DS2 are also developed within a metasiltstone host that is surrounded by a metamudstone host except that the metasiltstone, in this case, is boudinaged and planar veins are absent (Fig. 5.22C). Their orientation suggests a dextral, top to the NW, shear sense and they are also oblique to the main principal foliation. Figure 5.22D shows the vein arrays at station DS3 (Fig. 5.21). The tension gashes developed at DS3 are of two types: (1) one set of gashes are thin and propagate outward at an oblique angle along bedding surfaces (mid- and top-portions of Fig. 5.22D), and (2) the other set is larger and propagates outward along the main stem and tip of a planar vein (bottom-right to the bottom-central portion of Fig. 5.22D) lying subparallel to the compositional layering. Both have an S-shaped geometry implying a sinistral, top to the SE, shear, which is an opposite sense of shear to what is observed at DS1 and DS2 (Fig. 5.21).

5.3.3 Shear band foliation

Apart from the occurrence of S_0, S_1 and S_2, field and petrographic studies revealed evidence of a third foliation plane that shows all the characteristics of an extensional shear band foliation (Passchier & Trouw, 2005). Just like the crenulation cleavage, however, this shear band foliation is not a prevalent feature across the Malmesbury Group outcrops in the study area. A shear band foliation structure is defined as a mica-preferred orientation or compositional layering that is transected at low angles (15–35°) by sets of subparallel minor shear zones known as 'shear bands'

(Passchier & Trouw 2005). It is acknowledged that although the examples in Figures 5.25A and C show shear zones they are not strictly C/S fabrics because the original angle of the subparallel shear zones is close to 90 degrees (varying between 84–88°). Because they resemble C/S fabrics, however, they are described as such.

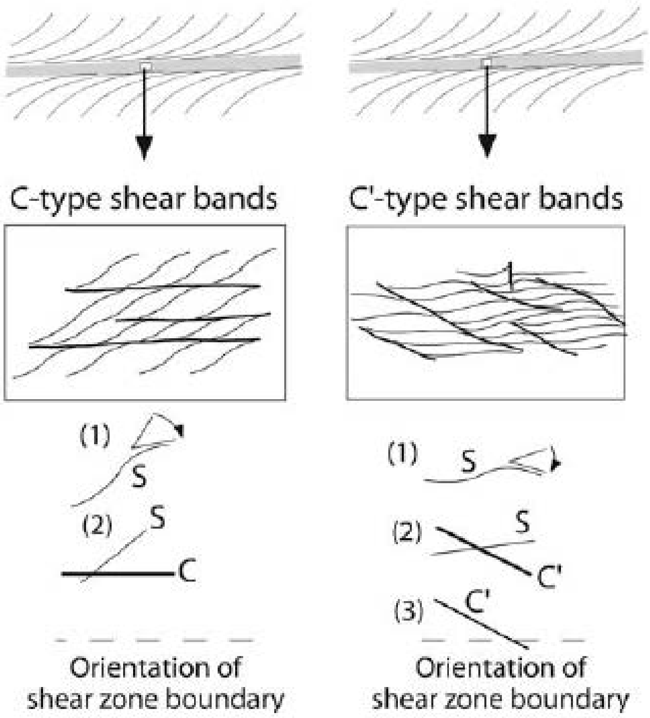

Figure 5.23: The two types of foliation pairs, C- and C'-type, that are characterized by foliation curvature relative to the shear plane and their differences in geometry (after Passchier & Trouw, 2005). All examples involve dextral shear. C-type shear bands are parallel to shear zone boundaries and are relatively straight and continuous whereas the C'-type shear band foliation is oblique to shear zone boundaries and the older foliation.

In a C/S or C’/S fabric, the shear bands are called C-type shear bands, with the “C” standing for “cisaillement”, the French word for shear and the foliation planes are called S- (for schistosity) foliations (Passchier & Trouw, 2005; Fossen, 2010). Two types of shear band foliation are distinguished, namely C-type and C'-type (Fig. 5.23). In both a C/S and C’/S fabric, the sense of rotation of the foliation (S) from the margin into the shear zone (C) is generally a safe shear sense indicator because as the foliation curves into and out of the C (or C’) -type shear band, the sense of deflection shown by the curving foliation reflects the sense of shear of the entire shear zone (Fig. 5.23; Fossen, 2010).

In the study area, only C/S fabrics are observed at both the outcrop (Fig. 5.25, 5.26) and thin section scale (Fig. 5.24). In thin section, the shear band foliation (C) is defined by a preferential alignment of biotite grains (0.15-1.25 cm) that trend in a direction perpendicular to the main S_1 foliation (S) (Fig. 5.24). The alignment of biotite grains in this shear band foliation, however, is not as strong or continuous compared to S_1 and the shear band boundaries show spacing that is 0.25-0.4 mm wide (Fig. 5.24B). The main foliation is transected and deflected at the shear band boundaries and indicates a sinistral sense of movement (Fig. 5.24B).

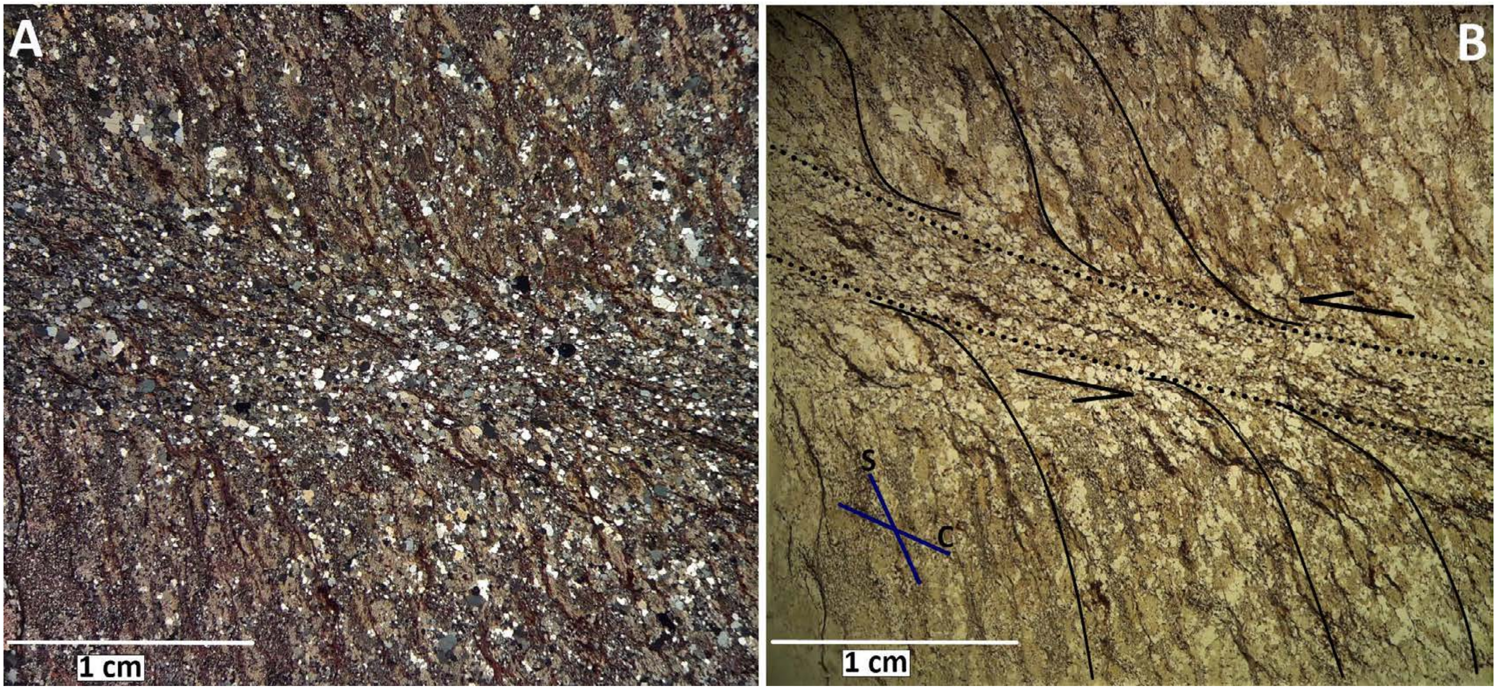

Figure 5.24: Thin section photomicrographs, in cross polars and plane-polarized light, highlighting the development of a C/S fabric in sample SP14. (A) & (B) The shear band foliation (C) is defined by the alignment of Bt grains (seen more clearly in B) which are not as elongate and continuous compared to those defining the alignment of the main foliation (S). The main foliation is transected and deflected at the shear band boundaries to indicate a sinistral shear sense.

At the outcrop scale, all C/S fabrics identified are located in the lit-par-lit zone at stations SC1–SC4 (Fig. 5.21). The C/S fabrics developed at stations SC1 (Fig. 5.25A, B) and SC4 (Fig. 5.25C, D) have internal planes (or S-surfaces) that are defined by compositional banding. These are transected by relatively planar and E-W trending (e.g. 004/88, 004/84) C-type shear bands to define a dextral, top to the NW, shear sense (Fig. 5.25B) at station SC1 and a sinistral, top to the SE, shear sense at station SC4 (Fig. 5.25D). This is inferred from the S-foliations that show evidence of progressively verging over in the direction of shearing as deformation proceeded (Fig. 5.25B, D).

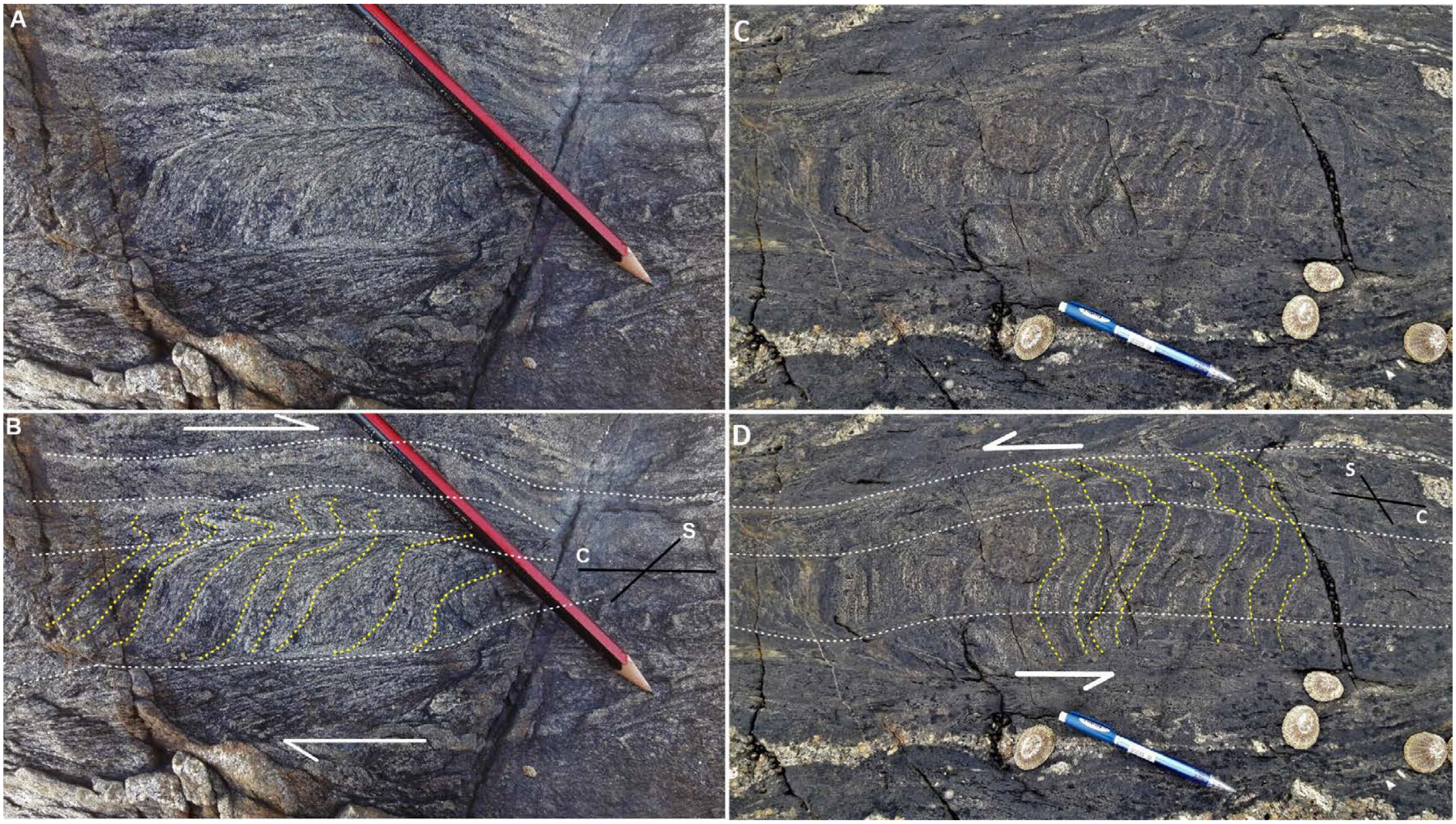

Figure 5.25: Subhorizontal surfaces showing evidence of a C/S fabric at stations SC1 (A) and SC4 (C) respectively. (B) and (D) are annotated and close-up views of (A) and (C) respectively. Displacements along shear zones curve the foliation (S) into the regularly spaced shear planes (C) to define a dextral, top to the NW, shear sense for SC1 and sinistral, top to the SE, shear for SC4. The degree of curvature or folding of (S) is much tighter for the C/S fabric at (A) and (B) than it is for (C) and (D). At station SC1, the relatively straight and continuous C-type shear bands (white dashed lines in B) appear to be a younger set of shear bands that overprinted an older set that has a more gentle inclination (bottom-left and bottom-central portion of B).

At station SC2 (Fig. 5.26C, D) and SC3 (Fig. 5.26A, B), the internal S-surfaces are instead defined by quartzofeldspathic veins/veinlets intruded along an older S_1 foliation surface. At station SC2, these veins are transected by a shallow dipping, WNW-ESE-trending (e.g. 026/02, 020/02) shear bands (C), whereas for station SC3, the shear bands are not sufficiently exposed for accurate orientation measurement. Both C/S fabrics, at stations SC2 and SC3, are developed on sub-vertical surfaces. Along these surfaces, the quartzofeldspathic vein material (0.5-1 cm) are folded (or crenulated) into discrete planes or shear zones across which the earlier foliation and veins are displaced (Fig. 5.26B, D). Based on the sigmoidal geometry or asymmetry of the quartzofeldspathic veins between the shear zones (or bands), a dextral, top to the WNW, sense of shear is inferred for station SC3, whereas station SC2 indicates a sinistral, top the ESE shear (Fig. 5.26B, D).

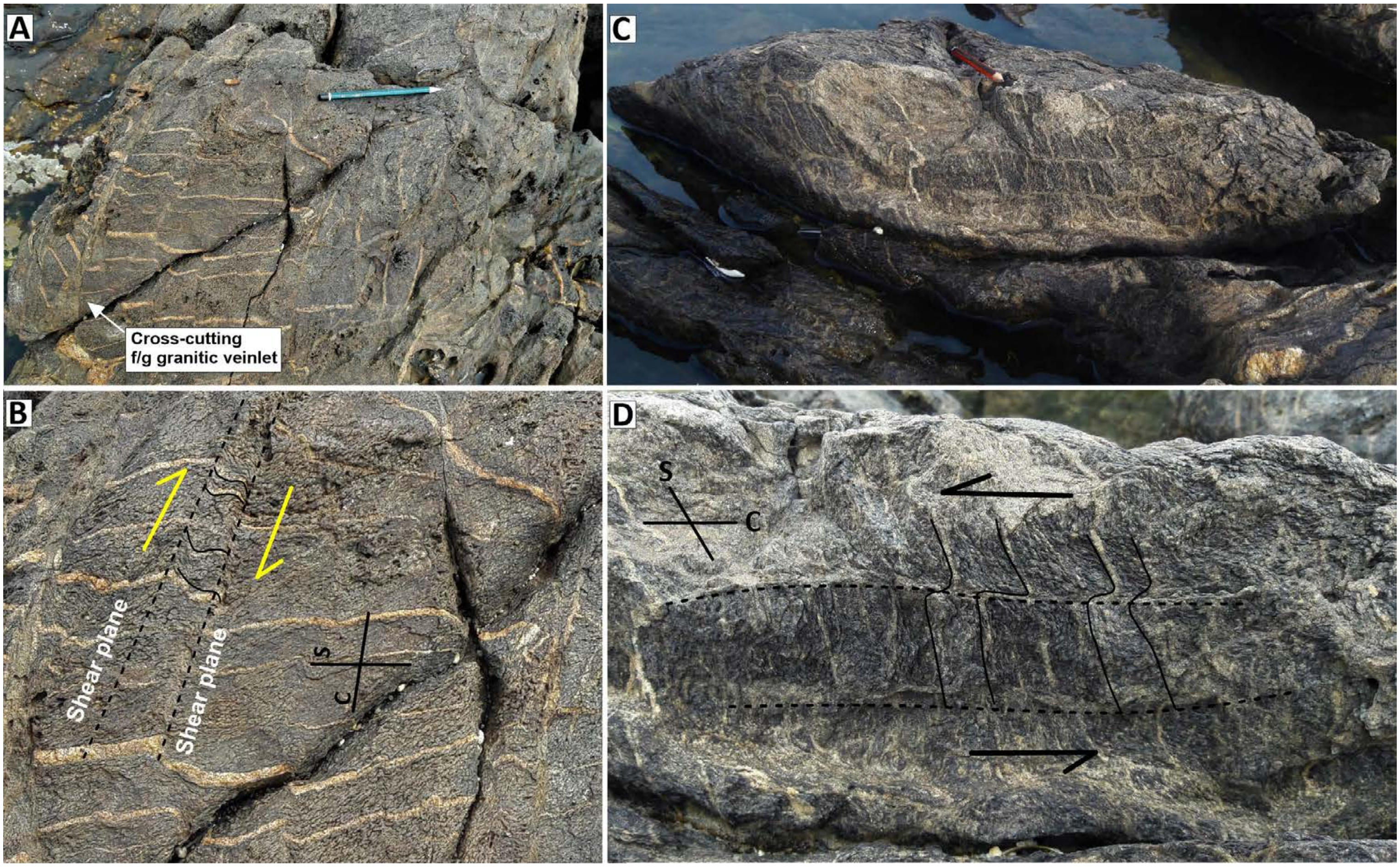

Figure 5.26: *Sub-vertical surfaces showing evidence of a C/S fabric at stations SC3 (A) and SC2 (C) respectively. (B) and (D) are annotated and close-up views of (A) and (C) respectively. S-surfaces are defined by quartzofeldspathic veins (intruded along older S_1 foliation surfaces) transected by shallow dipping shear bands (C). Deflection of (S) at the shear zone boundaries indicates a dextral, top the WNW, sense of movement for station SC3 and sinistral, top to the ESE, shear for station SC2. The direction of view for stations SC2 and SC3 are west and south respectively*.

5.4 Porphyritic S-type granite

5.4.1 Shape preferred orientation (SPO) of K-feldspar megacrysts

A total of 513 K-feldspar megacrysts across 11 stations (SPO 1-SPO 11; Fig. 5.29) spanning the main porphyritic coarse-grained granite in the south, through the lit-par-lit zone and, lastly, within the northern porphyritic coarse-grained granite sheet, were analysed and measured in terms of their relative orientation. Utilizing the SPO method involved measuring the trend and plunge (i.e. lineation) of the long axes of the megacrysts situated on two or three mutually perpendicular surfaces exposed in the study area (e.g. Han et al., 2014). The lineation data from each respective surface, at a particular station, were averaged to yield a mean vector (i.e. one for the top, east/west facing- and north/south facing-surface). The number of mean vectors per station could amount to two or three depending upon the number of surfaces present. The aforementioned mean vectors, at each station, were fitted by a great circle on an equal area lower-hemisphere plot to yield the magmatic foliation defined by the megacrysts (Fig. 5.27B).

Examples of the surfaces identified in the study area are shown in Figure 5.27 (for three mutually perpendicular surfaces) and Figure 5.28 (for two mutually perpendicular surfaces). The legend supplied in Figure 5.27B applies to all the stereonets (supplied in each figure) within section 5.4. In general, the K-feldspar megacrysts on each respective surface, across most of the stations, are relatively well aligned, with the only difference, among them, coming in the form of their plunge angle. The only stations where megacryst alignment is not apparent is on the east-facing surface (shown in red) of station SPO 4 and the south-facing surface (shown in pink) of station SPO 5 (Fig. 5.29). The inferred foliation plane is consistently steeply dipping across each station with the only variant being the direction of dip.

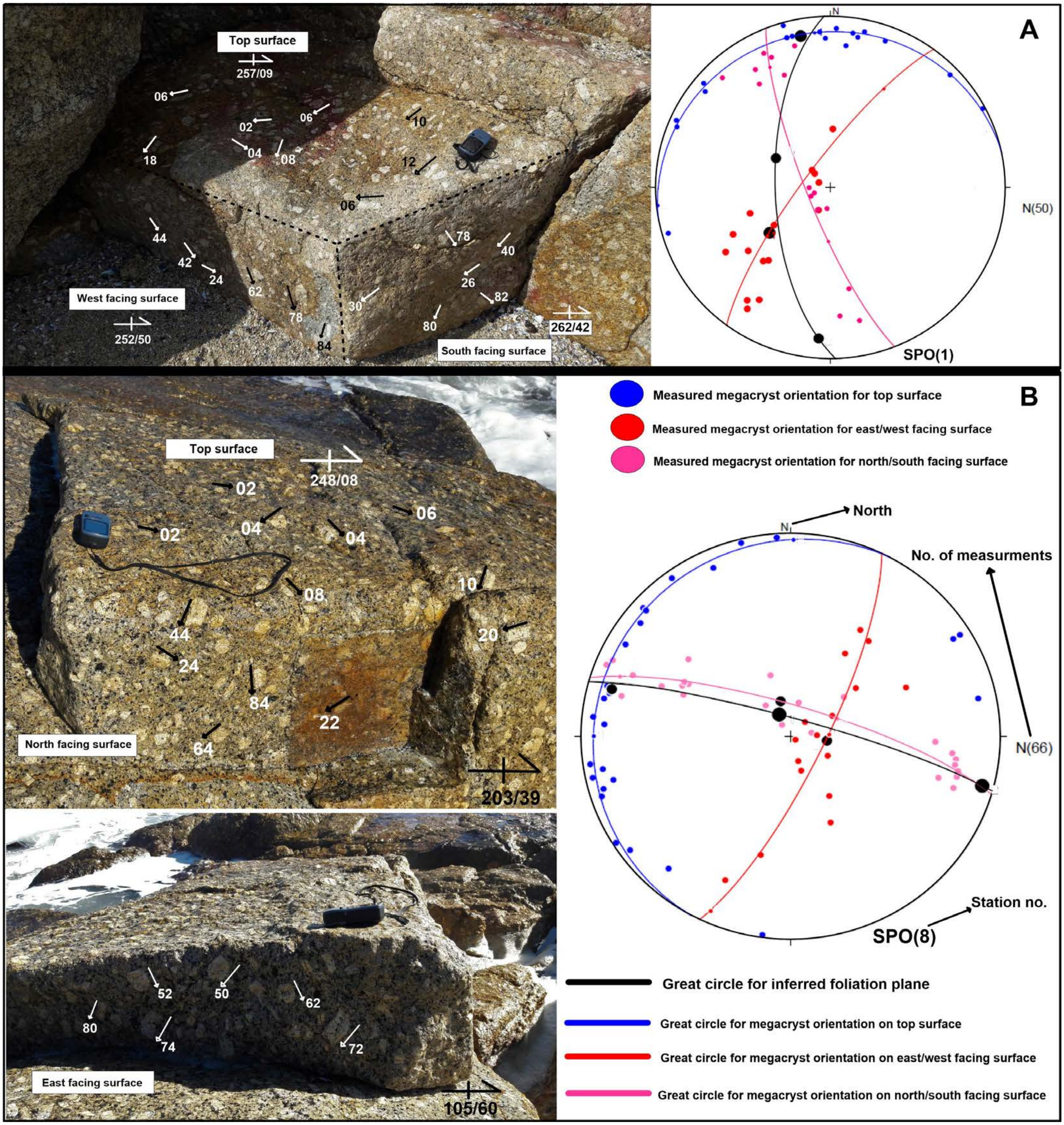

***Figure 5.27**: Examples of three mutually perpendicular surfaces observed and their associated equal-area lower hemisphere projections that show the preferred orientation of the K-feldspar megacrysts on each respective surface and the inferred magmatic foliation plane per station. The mean vector for each respective surface per station is also supplied in each photograph. (A) An outcrop with three (top, west and south-facing) mutually perpendicular surfaces occurring in the main porphyritic granite phase to the south (station SPO 1; Fig. 5.29). (B) An outcrop with three (top, north and east-facing) mutually perpendicular surfaces occurring in the portion of the main granite phase that occurs adjacent to the lit-par-lit zone when approaching the zone from the south (station SPO 8; Fig. 5.29).*

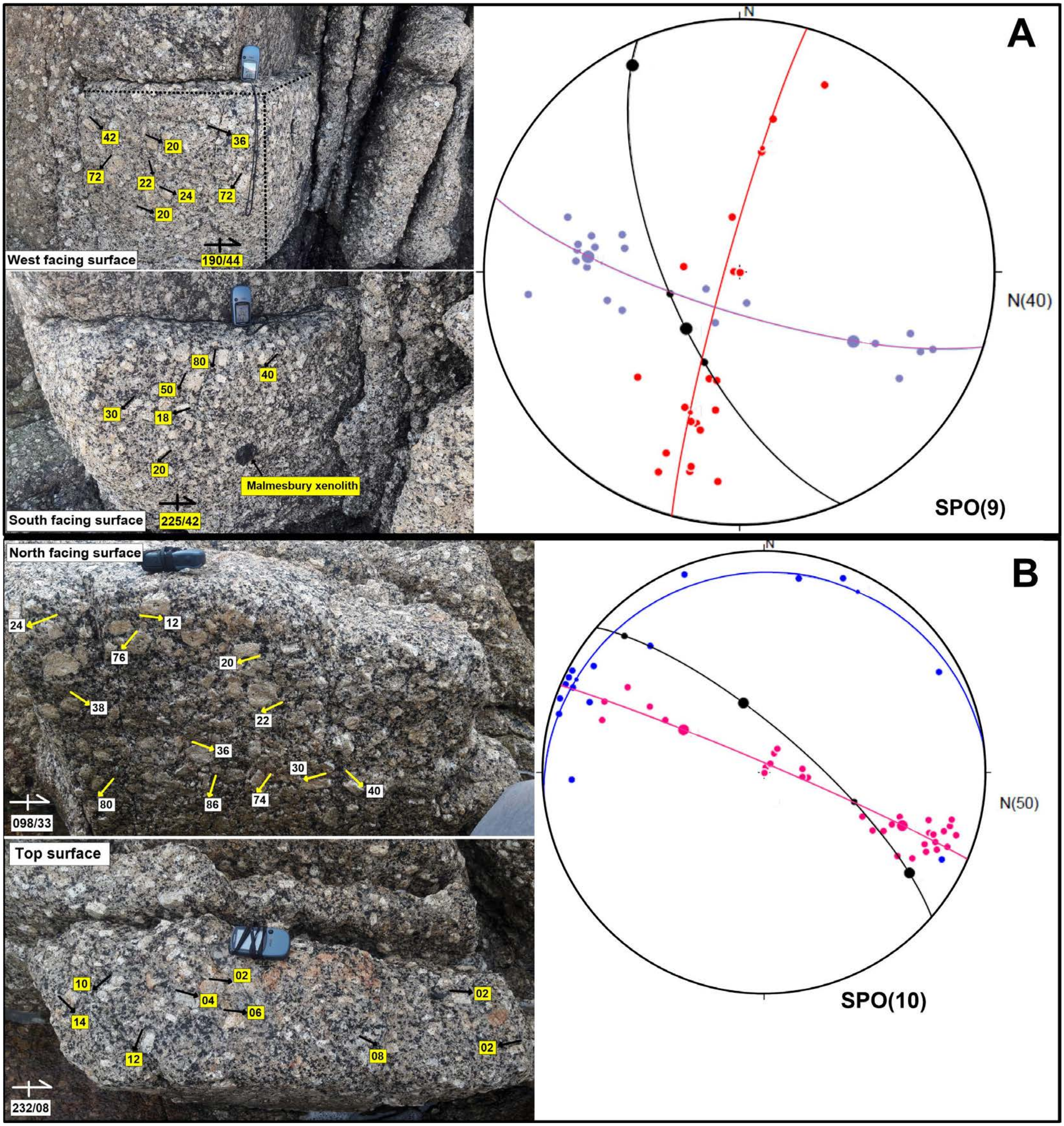

***Figure 5.28**: Examples of two mutually perpendicular surfaces observed and their associated equal-area lower hemisphere projections that show the preferred orientation of the K-feldspar megacrysts on each respective surface and the inferred magmatic foliation plane per station. The mean vector for each respective surface per station is also supplied. (A) An outcrop with two (west and south-facing) mutually perpendicular surfaces occurring in the lit-par-lit zone (station SPO 9; Fig. 5.29). (B) A surface with two (top and north-facing) mutually perpendicular surfaces occurring in the coarse-grained porphyritic granite sheet to the north (station SPO 10; Fig. 5.29).*

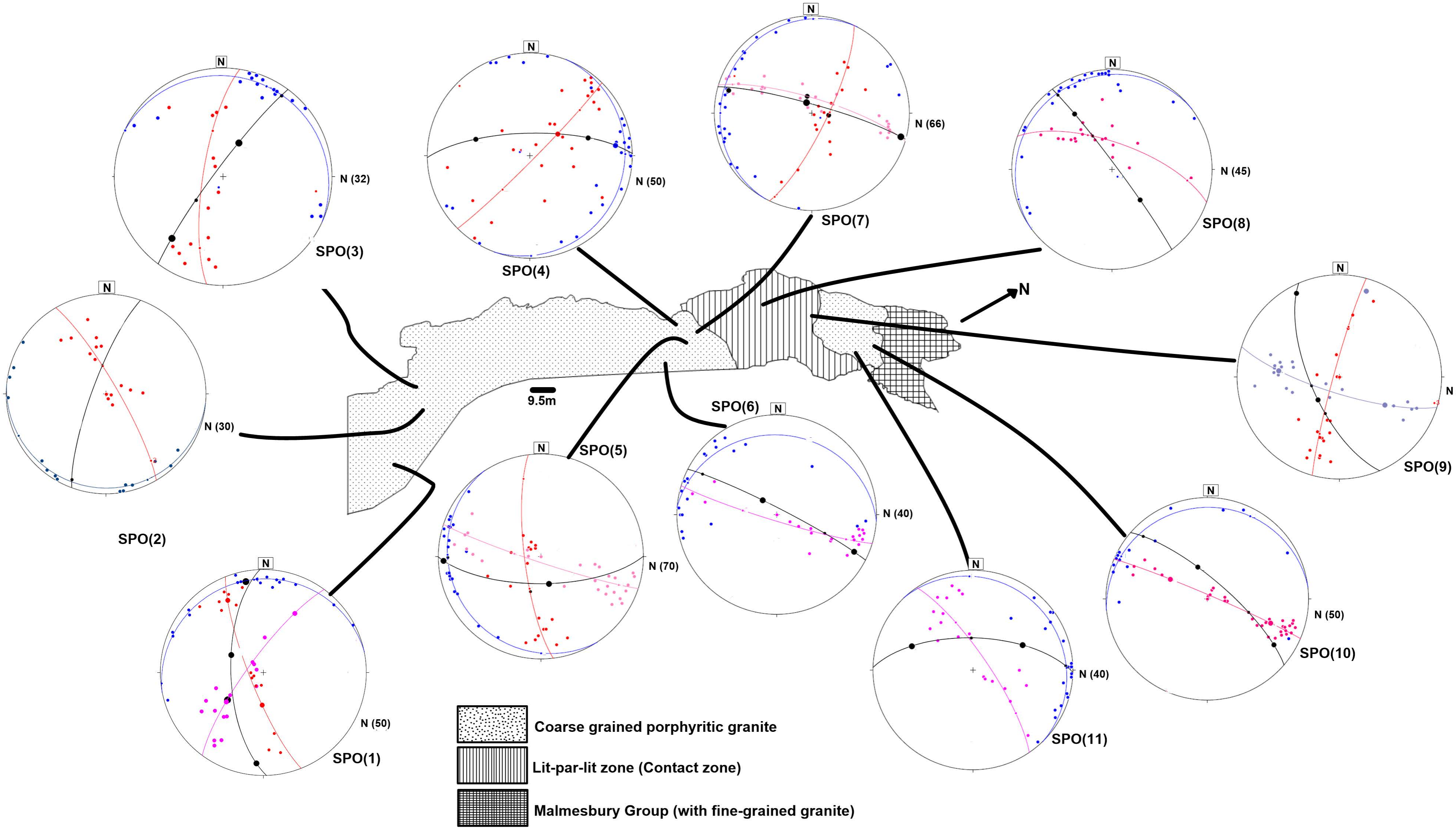

***Figure 5.29**: Simplified map of the Sea Point contact depicting all the station locations used for SPO analysis and their associated preferred K-feldspar megacryst orientations and resultant magmatic foliation plane (Fig. 5.27B); both are displayed on equal-area lower hemisphere projections. Note how the inferred magmatic foliation plane (black solid line in each stereonet) is consistent when approaching the lit-par-lit zone, from either the south or north, by being dominantly E-W through WNW-ESE trending. It, however, differs when heading towards the main granitic phase at the southern end, where it varies between NNE-SSW- and NNW-SSE-trending.*

At the southernmost station, the megacryst orientation is NNW-SSE (SPO 1; Fig. 5.29). As one approaches the lit-par-lit zone from the southern end, the orientation of the megacrysts assume a NNE-SSW (SPO 2) trend heading towards a more NE-SW trend (SPO 3). The trend then becomes E-W adjacent to the lit-par-lit zone (SPO 4 and SPO 5) with slight variations towards WNW-ESE (SPO 6 and SPO 7) and NW-SE (SPO 8 and SPO 9) (Fig. 5.29). When approaching the lit-par-lit zone from the northern end, a similar trend is observed, with the megacryst orientation varying from E-W-trending (SPO 11) towards WNW-ESE-trending (SPO 10) (Fig. 5.29). Overall, the orientation of the megacrysts is fairly consistent approaching the lit-par-lit zone, within it and to the north and largely corresponds (or is generally concordant) with the orientation of the original bedding (S_0) and principal S_1 foliation planes within the lit-par-lit zone as discussed in sections 5.2.1 and 5.2.2 respectively.

6 Geochemistry

6.1 Introduction

This chapter describes the major-, trace- and isotope-geochemistry of the various S-type granitic rocks and Malmesbury Group metasediments outcropping in the study area. A total of 25 samples, of which 19 samples are granites from the S-type Peninsula Pluton and 6 are metasedimentary rocks from the Malmesbury Group, were analysed for determination of their major and trace element composition. In addition, the Sr-Nd isotopic composition of 7 samples (6 granites and 1 metasedimentary sample) has been analysed. For a comparative study with previous work done on the Peninsula Pluton, supplementary geochemical data from Villaros et al. (2009a) and Farina et al. (2012) were utilized, and for previous studies on the Tygerberg Formation of the Malmesbury Group, data from Frimmel et al. (2013) and unpublished data were used. Samples of Frimmel et al. (2013) and the unpublished data are lithologically more variable and cover a much larger area (Bloubergstrand to Sea Point in the case of the unpublished data and Robben island in the case of the Frimmel et al., 2013 data) relative to those from the study area.

The granites in the study area are compositionally variable (as mentioned in the Lithological descriptions chapter). For simplification purposes, the hybrid granite phases are all treated as a group and are compared to the microgranite and main coarse-grained porphyritic granite in terms of composition. Cr_2O_3 concentrations (for all lithologies) are unreliable due to milling in a Cr-steel mill and are therefore excluded from this report.

6.2 Major element composition of the granites

The major element compositions of 19 granite samples are presented in Table 6.2. The observed outcrop/field variability shown by the granites is also reflected by the major element composition (summarized in Table 6.1) when the entire granite dataset is considered. This is shown by their SiO_2 (69.66 –76.27 wt. %), Al_2O_3 (12.92–15.68 wt. %), FeO^{tot} (0.66 –2.96 wt. %), CaO (0.16 –1.51 wt. %), TiO_2 (0.06 – 0.4 wt. %) and MgO (0 – 0.92 wt. %) contents which are all highly variable (Table 6.1). Conversely, K_2O and Na_2O (4.39 –5.99 wt. % & 2.42–3.55 wt. % respectively) are less variable (Table 6.1).

***Table 6.1**: Statistical summary of the major element composition of the various granite phases of the study area*

Major elements	**Composition range (wt. %) for entire granite dataset**	**Average composition (wt. %) for hybrid phases**	**σ**	**Average composition (wt. %) for main coarse-grained porphyritic granites**	**σ**	**Average composition (wt. %) for microgranites**	**σ**
SiO_2	69.66 – 76.27	71.78	1.65	72.69	2.09	74.83	1.27
Al_2O_3	12.92 – 15.68	14.24	0.69	13.51	0.81	13.46	0.53
TiO_2	0.66 – 0.40	0.29	0.10	0.30	0.08	0.08	0.03
MgO	0.00^b – 0.92	0.64	0.24	0.56	0.24	0.08	0.09
FeO^{tot}	0.66 – 2.96	2.23	0.55	2.30	0.52	0.90	0.30
CaO	0.16 – 1.51	0.78	0.32	0.80	0.08	0.27	0.09
K_2O	4.39 – 5.99	5.08	0.56	4.81	0.19	5.15	0.30
Na_2O	2.42 – 3.55	2.91	0.23	2.89	0.078	3.32	0.20
MnO	0.01 – 0.05	0.03	0.009	0.05	0.007	0.01	0.006
P_2O_5	0.08 – 0.21	0.18	0.02	0.19	0.02	0.15	0.06
Mg#	0.00^b – 24.80	21.90	4.57	18.90	3.36	6.70	6.13

Superscript b = below the detection limit; this applies to all the geochemistry data tables in this chapter.

When the granites are viewed as separate phases (on account of their mineralogy and field occurrence) the microgranites are more silica-rich (average of 74.83 wt. %) compared to the hybrid phases (average SiO_2 = 71.78 wt. %) and main coarse-grained porphyritic granites (average SiO_2 = 72.69 wt. %) respectively (Table 6.1). Moreover, the microgranites have, on average, low CaO contents (0.27 wt. %), low TiO_2 (0.08 wt. %) and a low Mg# (6.67) (Table 6.1). The hybrid phases and main coarse-grained granites have higher averages of Mg#, CaO and TiO_2 (hybrid phases: Mg# = 21.90; CaO = 0.78 wt. %; TiO_2 = 0.29 wt. %; main phase: Mg# = 18.90; CaO = 0.80 wt. %; TiO_2 = 0.30 wt. %) (Table 6.1).

Table 6.2: *Whole-rock major, trace and rare-earth element (REE) geochemistry of the various granite phases of the study area.*

Granite type	**Microgranites**			**Main c/g granites**		**Hybrid granites**													**Aplite**
Sample	**SP3**	**SP19**	**SP38**	**SP7**	**SP18**	**SP6**	**SP11**	**SP21**	**SP30**	**SP31**	**SP32**	**SP33**	**SP34**	**SP35**	**SP40**	**SP42A**	**SP42B**	**SP43A**	**SP15**
Major elements (Wt. %)																			
SiO_2	73.89	74.32	76.27	71.21	74.16	71.17	72.62	69.66	74.77	70.04	71.39	72.7	71.22	70.67	73.26	71.67	73.11	70.91	75.14
Al_2O_3	13.99	13.45	12.94	14.08	12.94	15.05	14.00	15.68	13.33	14.26	14.22	13.64	14.04	14.56	13.76	14.28	13.81	14.50	12.92
TiO_2	0.07	0.12	0.06	0.36	0.24	0.33	0.23	0.27	0.13	0.36	0.40	0.31	0.39	0.33	0.19	0.27	0.19	0.40	0.10
MgO	0.07	0.17	0.00^b	0.73	0.39	0.76	0.58	0.65	0.24	0.72	0.80	0.56	0.84	0.80	0.43	0.61	0.42	0.92	0.09
FeOt	0.81	1.24	0.66	2.70	1.97	2.30	1.97	1.99	1.24	2.43	2.65	2.21	2.86	2.67	1.74	2.29	1.79	2.96	1.13
CaO	0.33	0.31	0.16	0.86	0.74	0.71	0.57	0.64	0.27	1.51	1.08	0.77	1.05	0.71	0.62	0.64	0.61	0.92	0.28
K_2O	5.48	4.91	5.06	4.94	4.67	5.99	5.09	5.88	5.53	5.37	4.46	5.06	4.46	5.23	4.39	5.04	5.00	4.48	5.96
Na_2O	3.55	3.22	3.18	2.83	2.94	2.42	3.03	3.11	2.74	2.66	2.92	2.85	2.83	2.78	3.24	3.10	3.25	2.87	2.91
MnO	0.01	0.02	0.01	0.05	0.04	0.04	0.03	0.03	0.02	0.04	0.04	0.03	0.04	0.04	0.03	0.04	0.03	0.04	0.01
P_2O_5	0.20	0.16	0.08	0.20	0.17	0.18	0.16	0.17	0.13	0.19	0.19	0.19	0.20	0.21	0.17	0.18	0.18	0.21	0.14
L.O.I.	0.80	1.16	0.77	1.08	0.83	1.05	1.16	1.22	1.06	1.30	0.96	0.83	1.02	1.16	1.07	1.00	0.81	1.29	0.70
Sum	**99.33**	**99.28**	**99.29**	**99.37**	**99.36**	**100.29**	**99.70**	**99.55**	**99.65**	**99.20**	**99.45**	**99.43**	**99.31**	**99.40**	**99.14**	**99.42**	**99.45**	**99.88**	**99.56**
Mg#	8.95	12.06	0.00^b	21.28	16.53	24.84	22.75	24.62	16.22	22.86	23.19	20.22	22.70	23.74	19.82	21.03	19.00	23.71	7.38
A/CNK	1.13	1.20	1.18	1.22	1.15	1.28	1.21	1.24	1.21	1.10	1.23	1.18	1.23	1.23	1.23	1.22	1.13	1.29	1.10
Trace elements (ppm)																			
Sc	9.00	8.81	8.13	11.49	9.35	12.24	10.33	10.06	7.51	11.34	11.47	10.40	11.33	10.72	8.61	10.24	8.90	10.99	7.91
V	31.30	42.60	29.22	55.50	48.63	52.68	46.70	47.78	41.80	57.70	59.65	46.15	60.75	58.16	46.71	49.10	45.60	64.85	36.84
Co	0.87	1.97	0.81	5.37	3.02	5.10	3.40	3.92	1.74	5.54	5.44	4.08	5.25	5.53	2.23	3.47	2.90	5.22	1.70
Ni	10.60	12.95	11.15	16.65	18.05	21.35	15.40	14.40	12.45	18.85	16.90	17.25	17.75	16.45	14.60	14.00	14.55	19.20	11.30
Cu	28.60	10.07	43.30	23.37	236.20	14.73	14.08	22.56	11.87	15.00	25.92	30.05	16.68	1860	10.14	22.78	46.00	18.32	25.10
Zn	15.35	15.80	8.17	60.65	38.80	45.35	35.80	35.05	17.20	48.20	50.80	41.80	57.30	54.20	30.05	44.10	31.35	58.50	15.05
Rb	163	164	268	255	257	220	183	200	160	254	220	208	223	233	164	205	190	229	295
Ba	158	156	97.15	329	66.20	753	367	765	228	488	289	227	261	434	195	293	285	370	53.55
Sr	53.90	53.20	26.52	79.40	38.48	112	80.15	122	63.90	97.35	91.00	68.25	79.40	85.30	67.50	75.20	68.60	106	25.49
Cs	10.59	8.37	19.96	14.68	22.34	9.54	8.93	8.15	6.20	15.30	15.45	9.71	16.46	17.98	10.59	14.05	13.95	14.78	11.40
Zr	23.37	48.16	31.49	149	94.65	137	83.15	109.25	29.73	132	150	132	159	133	79.95	117	95.05	175	20.49
Nb	7.33	9.08	7.78	15.37	12.65	12.43	10.72	11.15	5.54	12.87	14.93	13.69	15.18	13.73	9.30	14.96	11.85	17.18	8.30

Granite type	**Microgranites**			**Main c/g granites**		**Hybrid granites**													**Aplite**
Sample	**SP3**	**SP19**	**SP38**	**SP7**	**SP18**	**SP6**	**SP11**	**SP21**	**SP30**	**SP31**	**SP32**	**SP33**	**SP34**	**SP35**	**SP40**	**SP42A**	**SP42B**	**SP43A**	**SP15**
Trace elements continued																			
Y	6.12	14.67	11.73	29.33	25.40	27.83	21.42	23.93	12.53	26.82	29.37	30.99	33.33	26.74	20.47	25.25	23.51	30.44	13.21
Ta	1.33	1.37	1.11	1.43	1.53	1.17	1.18	0.89	0.54	1.37	1.53	1.37	1.26	1.51	0.97	1.49	1.44	1.38	0.97
Hf	1.06	2.11	1.55	4.82	3.28	4.32	2.98	3.37	1.31	4.02	4.89	4.39	4.96	4.61	2.80	3.99	3.54	5.29	1.06
Pb	28.23	24.57	12.82	26.01	22.22	36.21	29.94	36.45	28.43	27.29	25.26	29.05	24.34	28.48	23.23	28.76	28.19	25.27	25.40
Th	1.18	5.16	3.53	13.00	9.34	12.04	9.40	10.07	4.15	10.65	13.19	11.88	14.01	11.64	7.86	11.09	9.11	14.53	3.52
U	3.71	3.83	4.38	4.78	3.65	3.81	6.50	4.87	3.95	4.31	3.40	4.95	5.35	3.74	5.84	3.75	3.79	5.57	5.38
Mo	18.18	25.40	16.64	17.66	22.45	14.19	19.95	15.58	22.75	20.33	17.62	15.24	18.23	20.58	22.61	18.81	20.56	21.31	23.27
Rare earth elements (ppm)																			
La	2.76	7.60	3.69	27.28	15.90	24.62	16.54	21.98	6.21	24.30	27.74	21.86	28.42	24.58	13.88	20.14	15.79	32.49	3.84
Ce	5.83	15.99	8.30	56.60	33.56	51.50	35.10	44.33	13.30	49.53	57.75	46.59	59.61	51.39	28.74	42.55	33.44	66.36	8.27
Pr	0.63	1.83	1.03	6.43	3.96	5.93	4.05	5.20	1.43	5.77	6.81	5.37	6.99	5.83	3.38	4.85	3.95	7.73	0.94
Nd	2.83	7.03	3.19	23.49	14.19	21.93	14.42	18.32	4.88	20.69	25.43	20.06	25.79	22.57	11.91	17.25	14.46	28.61	3.23
Sm	0.78	1.79	0.90	5.25	3.58	4.82	3.56	4.28	1.30	4.91	5.21	4.74	5.81	4.83	2.65	4.28	3.43	6.32	1.09
Eu	0.39	0.46	0.18	0.84	0.38	1.26	0.82	1.38	0.60	1.05	0.90	0.69	0.89	0.88	0.53	0.69	0.63	0.93	0.17
Gd	0.67	1.93	1.30	5.20	3.42	4.68	3.61	3.63	1.49	4.43	4.80	4.84	5.46	4.69	2.75	4.20	3.37	5.72	1.14
Tb	0.16	0.42	0.29	0.84	0.62	0.78	0.57	0.64	0.31	0.75	0.82	0.90	0.94	0.77	0.46	0.69	0.61	0.90	0.27
Dy	0.98	2.59	1.85	5.47	4.14	4.98	3.80	4.33	2.08	4.66	5.51	5.62	5.84	5.07	3.54	4.47	4.19	5.75	2.01
Ho	0.21	0.50	0.39	0.99	0.90	1.00	0.75	0.91	0.41	0.84	1.01	1.07	1.17	0.95	0.73	0.89	0.81	1.03	0.44
Er	0.62	1.33	1.12	2.79	2.61	2.94	2.23	2.66	1.35	2.70	3.00	2.73	3.26	2.52	1.92	2.59	2.41	3.00	1.39
Tm	0.09	0.23	0.20	0.37	0.39	0.42	0.35	0.39	0.22	0.36	0.41	0.40	0.45	0.35	0.33	0.40	0.35	0.39	0.19
Yb	0.89	1.35	1.46	2.45	2.69	2.59	2.31	2.33	1.41	2.63	2.87	2.30	2.98	2.14	2.08	2.43	2.04	2.51	1.57
Lu	0.11	0.20	0.25	0.34	0.38	0.37	0.36	0.37	0.21	0.36	0.40	0.34	0.43	0.30	0.31	0.32	0.35	0.35	0.21
∑REE	**16.95**	**43.25**	**24.15**	**138.34**	**86.72**	**127.82**	**88.47**	**110.75**	**35.20**	**122.98**	**142.66**	**117.51**	**148.04**	**126.87**	**73.21**	**105.75**	**85.83**	**162.09**	**24.76**
Average crust (Rudnick & Gao, 2003) normalised ratios (subscript C = crust)																			
$(La/Sm)_C$	0.69	0.83	0.80	1.01	0.87	1.00	0.91	1.00	0.93	0.97	1.04	0.90	0.95	0.99	1.02	0.92	0.90	1.00	0.69
$(Eu/Eu^*)_C$	1.86	0.85	0.57	0.56	0.38	0.92	0.79	1.21	1.49	0.78	0.62	0.50	0.55	0.64	0.68	0.56	0.64	0.53	0.53
$(Ce/Ce^*)_C$	1.02	0.99	0.98	0.98	0.97	0.98	0.99	0.95	1.03	0.96	0.97	0.99	0.97	0.99	0.97	0.99	0.97	0.96	1.00
$(Gd/Yb)_C$	0.39	0.73	0.46	1.09	0.65	0.93	0.80	0.80	0.54	0.86	0.86	1.08	0.94	1.13	0.68	0.89	0.85	1.17	0.37
$(La/Yb)_C$	0.29	0.53	0.24	1.06	0.56	0.90	0.68	0.90	0.42	0.88	0.92	0.90	0.91	1.09	0.63	0.79	0.74	1.23	0.23
$(La/Lu)_C$	0.38	0.57	0.22	1.20	0.63	1.00	0.69	0.89	0.44	1.01	1.04	0.96	0.99	1.23	0.67	0.94	0.68	1.39	0.27
$(Gd/Lu)_C$	0.49	0.78	0.42	1.24	0.73	1.03	0.81	0.80	0.58	1.00	0.97	1.15	1.03	1.27	0.72	1.06	0.78	1.33	0.44
$(Ce/Yb)_C$	0.29	0.52	0.25	1.02	0.55	0.88	0.67	0.84	0.42	0.83	0.89	0.90	0.88	1.06	0.61	0.77	0.72	1.17	0.23
$(Ce/Sm)_C$	0.68	0.81	0.84	0.98	0.85	0.97	0.89	0.94	0.93	0.91	1.01	0.89	0.93	0.97	0.98	0.90	0.88	0.95	0.69

All the granite phases plot within the granite field on the total alkalis vs. SiO_2 plot (after Middlemost, 1994) (Fig. 6.1A) and they all classify as mozongranites on the QAP classification diagram using the granite mesonorm (after Streckeisen, 1976) (Fig. 6.1B). Figure 6.1C, D and E are the Frost et al. (2001) geochemical classification schemes for granitic rocks based upon the three variables of (i) Fe-number [(or Fe* (in wt.%) = FeO^{tot}/ (FeO^{tot} + MgO)], (ii) the modified alkali-lime index [(or MALI (in wt. %) = $Na_2O + K_2O - CaO$)], and (iii) aluminium saturation index [(or ASI (molar) = Al/Ca x 1.67P + Na + K].

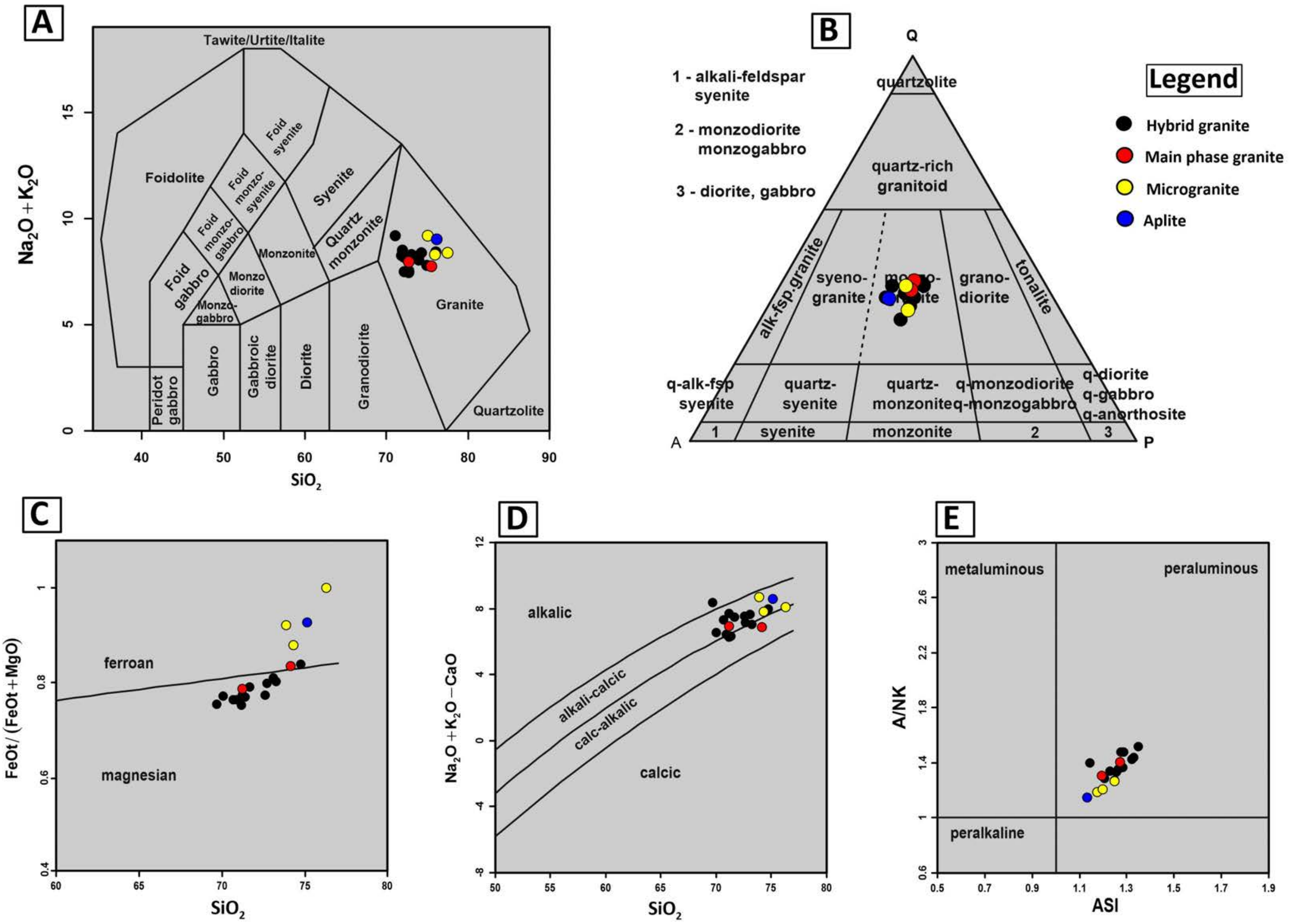

Figure 6.1: *Major element classification plots for the various granite phases of the study area. (A) The total alkali (Na_2O + K_2O) versus silica (SiO_2) classification diagram (after Middlemost, 1994). (B) The QAP classification using the granite mesonorm (after Streckeisen, 1976). (C), (D) & (E) are the Frost et al. (2001) geochemical classification diagrams for granitic rocks using the chemical parameters of Fe-number [(Fe* = FeOt/(FeOt + MgO)] vs. SiO_2, modified alkali-lime index (Na_2O + $K_2O - CaO$) vs. SiO_2, and A/NK (Al_2O_3/Na_2O + K_2O) vs. the aluminium saturation index [Al/Ca x 1.67P + Na + K (mol.)] respectively. Legend supplied applies to all figures in sections 6.1 and 6.2.*

Using the Fe* chemical parameter (Fig. 6.1C), the microgranites (average Fe* value = 0.93) and the aplitic sample (Fe* value = 0.93) plot entirely within the ferroan field. The majority of the hybrid granites (average Fe* value = 0.78) and a single coarse-grained porphyritic phase (sample SP7) plot within the magnesian field, whereas sample SP30 (fine-grained hybrid) and SP18 (main coarse-grained porphyritic granite) plot very close to the Fe*−index boundary line and slightly within the ferroan field (Fig. 6.1C). The granites further classify mostly into the alkali-calcic series (Fig. 6.1D) based on MALI apart from three samples (two hybrids and one main phase granite) which plot within either the alkalic or calc-alkalic fields respectively (Fig. 6.1D). Moreover, the granites are all exclusively peraluminous based on their A/NK (Al_2O_3/ (Na_2O + K_2O) vs. ASI values (Fig. 6.1E).

Figure 6.2 shows a series of bivariate plots for Al, Ca, Ti, P, Mg#, A/CNK, Si, K and Na (all as element atomic values) against the atomic Fe + Mg index/parameter referred to as maficity (which is defined as moles of Fe and Mg per 100 g of rock or magma by Clemens et al., 2011). Maficity is an ideal parameter in bivariate plots for granitic rocks because it is easier to relate mineralogical and chemical influences on magma composition (i.e. it allows data trends to be interpreted for any addition of ferromagnesian material) and hence potential source differences when it is utilized (Clemens et al., 2011).

There are two overall trends displayed by the major element compositions of the granites when plotted against maficity:

(i) An increase in the Al, Ca, Ti, P, Mg# and A/CNK values as a function of increasing maficity (Fig. 6.2A–F). The trends are fairly consistent and coherent for most of the major elements under this category, with Ti and P (in particular) showing exceptionally well-defined positive linear trends as a function of increasing maficity.

(ii) A decrease in the Si, K and Na values with increasing maficity (Fig. 6.2G-I). Of the three major element compositions under this category, the trend shown by Si is a well-defined linear trend, whereas Na and K show scattered weak negative trends as a function of increasing maficity.

From a viewpoint of the individual granite phases, the microgranites (and the single aplitic phase) plot towards low maficity values for all major element compositions and the selected geochemical parameters (Mg# and A/CNK) (Fig. 6.2). The main coarse-grained porphyritic granite and hybrid phases, which both have higher feldspar megacryst and biotite content, plot towards higher maficity values (Fig. 6.2).

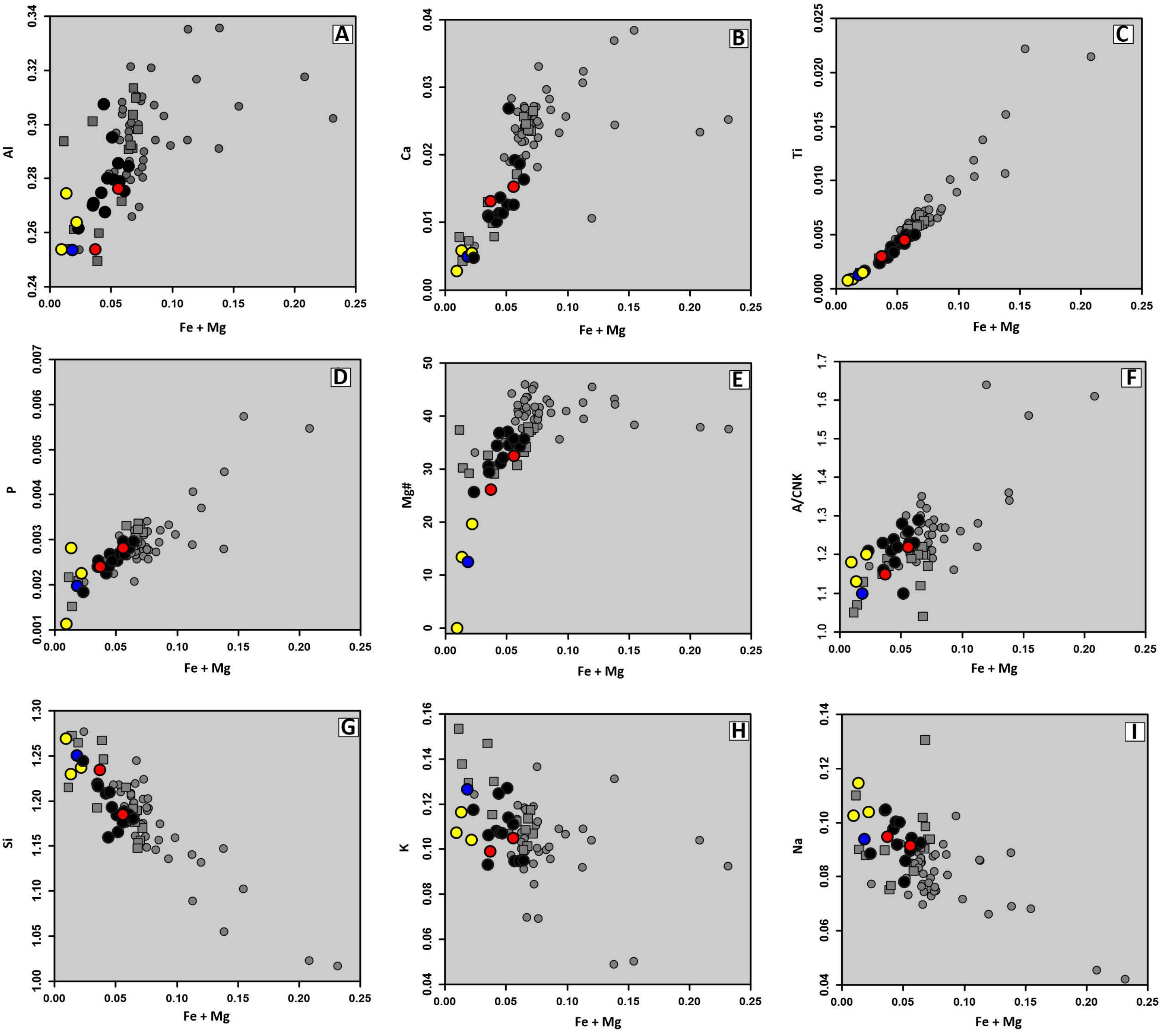

***Figure 6.2**: Select major elements (all as element atomic values) vs. maficity (Mg + Fe) plots for the various granite phases of the study area. The data for Villaros et al. (2009a) (grey circles) and Farina et al. (2012) (grey squares) are shown for reference.*

6.3 Trace element composition of the granites

The trace element composition of the granites in the study area vary in abundance as reflected by the variation in concentration shown by the trace elements forming part of either the large ion lithophile elements (LILE), high field strength elements (HFSE) or rare earth elements (REE) of the dataset (Table 6.3). When the different granite types are highlighted individually (Table 6.3), the microgranites and the single aplite show notably lower average concentrations or abundances in LILE (particularly Ba, Sr and Rb), REE, Y and some of the HFSE such as Zr, Th, Nb and Hf compared to the hybrid- and main coarse-grained porphyritic-granites.

***Table 6.3**: Statistical summary of selected trace element compositions of the various granite phases of the study area*

Trace element group	Trace element	Composition range (ppm) for the entire granite dataset	Avg. composition (ppm) for hybrid phases	σ	Avg. composition (ppm) for main coarse-grained porphyritic granites	σ	Avg. composition (ppm) for microgranites	σ
LILE	Ba	53.55 – 764.50	381.15	187.42	197.55	185.76	137.08	34.61
	Rb	160.20 – 295.00	206.82	27.29	255.98	0.95	98.42	60.09
	Sr	25.49 – 121.55	85.90	18.62	58.94	28.94	44.54	15.61
	Cs	6.20 – 22.34	12.39	3.69	18.51	5.41	12.97	6.51
HFSE	Zr	20.49 – 175.10	117.84	38.74	121.90	38.54	34.34	12.64
	Th	1.18 – 14.53	10.74	2.76	11.17	2.59	3.29	2.00
	Nb	5.45 – 17.18	12.57	3.02	14.01	1.93	8.06	0.91
	Hf	1.06 – 5.29	3.88	1.08	4.05	1.09	1.57	0.52
	U	3.40 – 6.50	4.60	0.98	4.21	0.80	3.97	0.36
	Ta	0.54 –1.53	1.24	0.29	1.48	0.07	1.27	0.14
LREE	La	2.76 – 32.49	21.42	6.99	21.59	8.05	4.68	2.57
	Ce	5.83 – 66.36	44.63	14.27	45.08	16.29	10.04	5.30
	Nd	2.38 – 28.61	18.95	6.45	18.84	6.58	4.20	2.49
	Pr	0.63 –7.73	5.17	1.68	5.20	1.75	1.16	0.61
	Sm	0.78 – 6.32	4.32	1.33	4.42	1.18	1.15	0.55
HREE	Eu	0.17 – 1.38	0.86	0.25	0.61	0.33	0.34	0.15
	Y	6.12 – 33.33	25.59	5.45	27.37	2.78	10.84	4.35
	Gd	0.67 – 5.72	4.13	1.15	4.31	1.26	1.30	0.63
	Tb	0.16 – 0.94	0.70	0.18	0.73	0.15	0.29	0.13
	Dy	0.98 – 5.84	4.60	1.06	4.80	0.94	1.80	0.81
	Ho	0.21 – 1.17	0.89	0.19	0.95	0.06	0.37	0.15
	Er	0.62 – 3.26	2.56	0.51	2.70	0.12	1.02	0.37
	Tm	0.09 – 0.45	0.37	0.06	0.38	0.01	0.17	0.07
	Yb	0.89 – 2.98	2.35	0.40	2.57	0.17	1.23	0.30
	Lu	0.11 – 0.43	0.34	0.06	0.36	0.03	0.19	0.07

Figures 6.3 and 6.4 show a series of maficity plots plotted for selected LILE, HFSE, LREE and HREE. Trace elements that show linear trends are plotted together in Figure 6.3 and those that show some scatter in their trend are shown separately in Figure 6.4. The LREE (La, Ce and Sm; Fig. 6.3A-C), as well as the HFSE (Zr, Nb, and Th; Fig. 6.3D-E), show very good linear positive trends as a function of increasing maficity similar to those linear trends displayed by Ti, Mg# and P against maficity in Figure 6.3. The same is true for the HREE (Y, Dy and Yb; Fig. 6.3G-I) although they do show minor scatter in their trends.

In contrast, elements such as Eu, Sr, Ba and Rb show overall weakly defined positive trends, as a function of maficity, due to the observed large scatter they show (Fig. 6.4A-D). The trends that these elements show are defined by very steep gradients or rapid increasing upward trends (especially for Eu) which reach their peak at low to intermediate values of maficity instead of showing a more direct positive relationship with increasing maficity as shown by the various trace elements in Figure 6.3.

Figure 6.5A and B are the REE plot and the multi-element spider plot for the granites of the study area respectively; both are normalized to the average crustal values of Rudnick and Gao (2003). With regards to the REE plot, the micrograbites and the single aplite phase sample plot at values well below one (Fig. 6.5A) reflecting their low concentrations in both the LREE and HREE (as mentioned previously). The hybrid phases and the main coarse-grained granites plot at values close to and slightly above 1 (Fig. 6.5A).

The LREE pattern for the microgranites is initially slightly negative sloping to Nd but peaks again at Sm (Fig. 6.5A). This (positive peak) gives the LREE pattern an overall slightly positive sloping trend (Fig. 6.5A); an observation also reflected by the $(La/Sm)_C$ ratios (ranging from 0.69-0.83; an average of 0.77), below one. For the LREE pattern of the aplite sample [$(La/Sm)_C$ ratio of 0.68)], the same general effect (initial slightly negative slope and positive peaks at Sm) is seen. The HREE pattern for the microgranites (and the single aplite sample) is generally positive, with $(Gd/Lu)_C$ ratios ranging from 0.42-0.78 (0.44 for aplite) with an average of 0.56. The only significant peaks shown by the microgranites and the aplite are at Yb (apart from SP 19) and Tb (apart from SP3) (Fig. 6.5A). The two microgranites show moderate to strongly negative europium anomalies [$(Eu/Eu^*)_C$ = 0-57-0.85)] while sample SP3 shows a prominent positive anomaly [$(Eu/Eu^*)_C$ = 1.85)]. The aplite phase has a strong negative europium anomaly as reflected by its [$(Eu/Eu^*)_C$] value of 0.53.

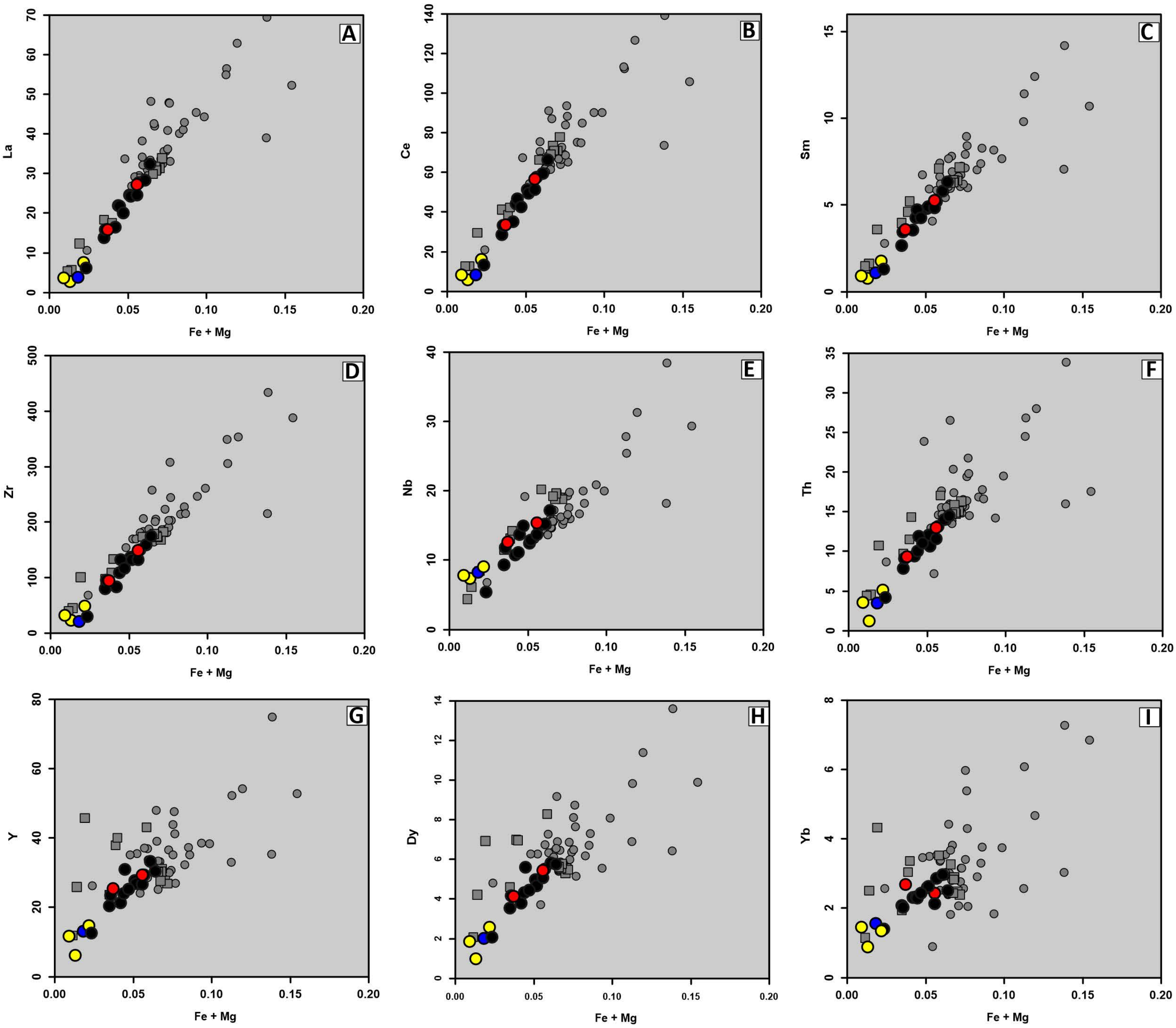

__Figure 6.3__: Select REE and HFSE vs. maficity plots for the various granite phases of the study area. The data for Villaros et al. (2009a) (grey circles) and Farina et al. (2012) (grey squares) are shown for reference.

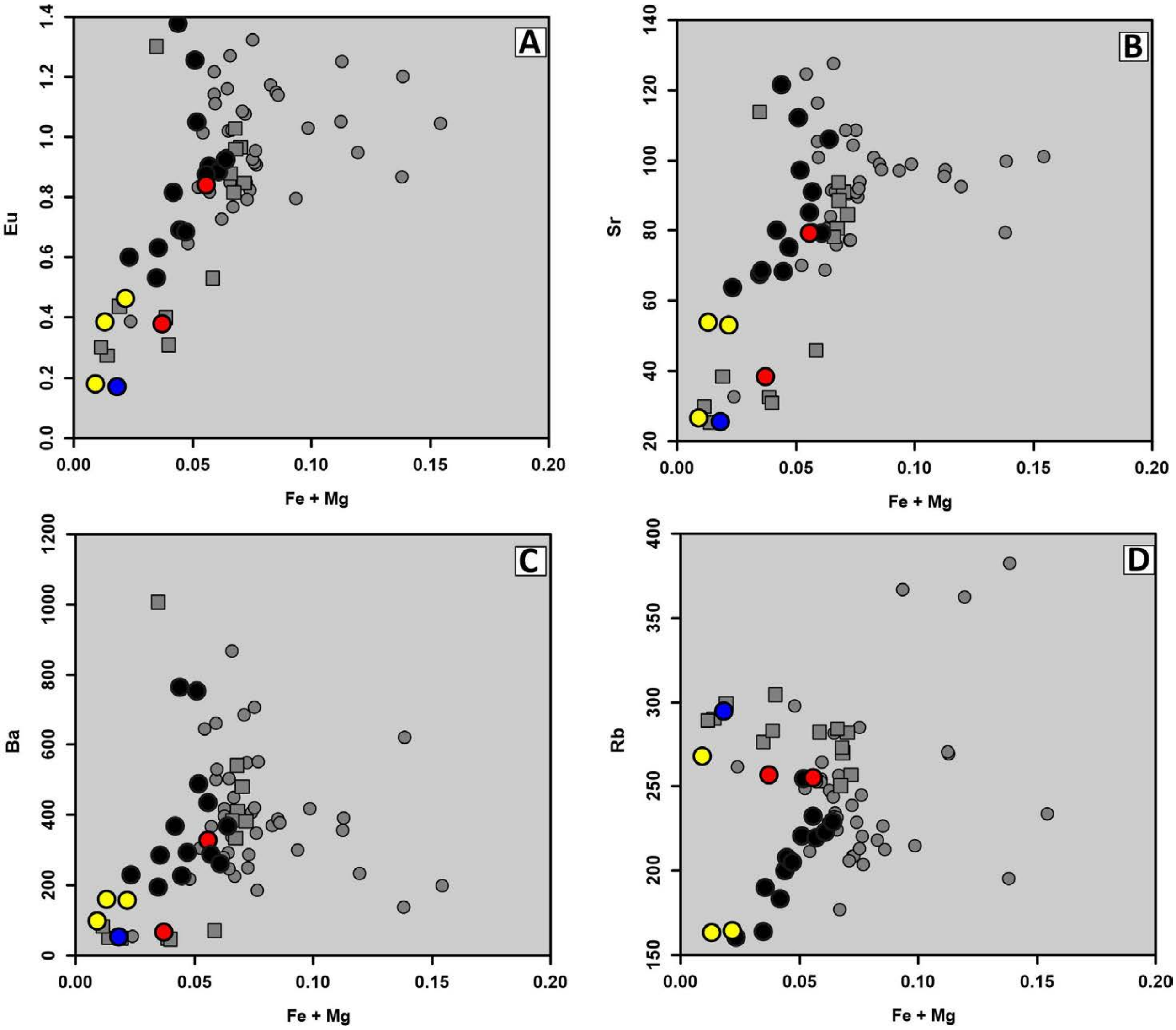

***Figure 6.4**: Select LILE vs. maficity plots for the various granite phases of the study area. The elements of Sr, Ba, Rb and Eu show a larger scatter in their trends as a function of maficity. The data for Villaros et al. (2009a) (grey circles) and Farina et al. (2012) (grey squares) are shown for reference.*

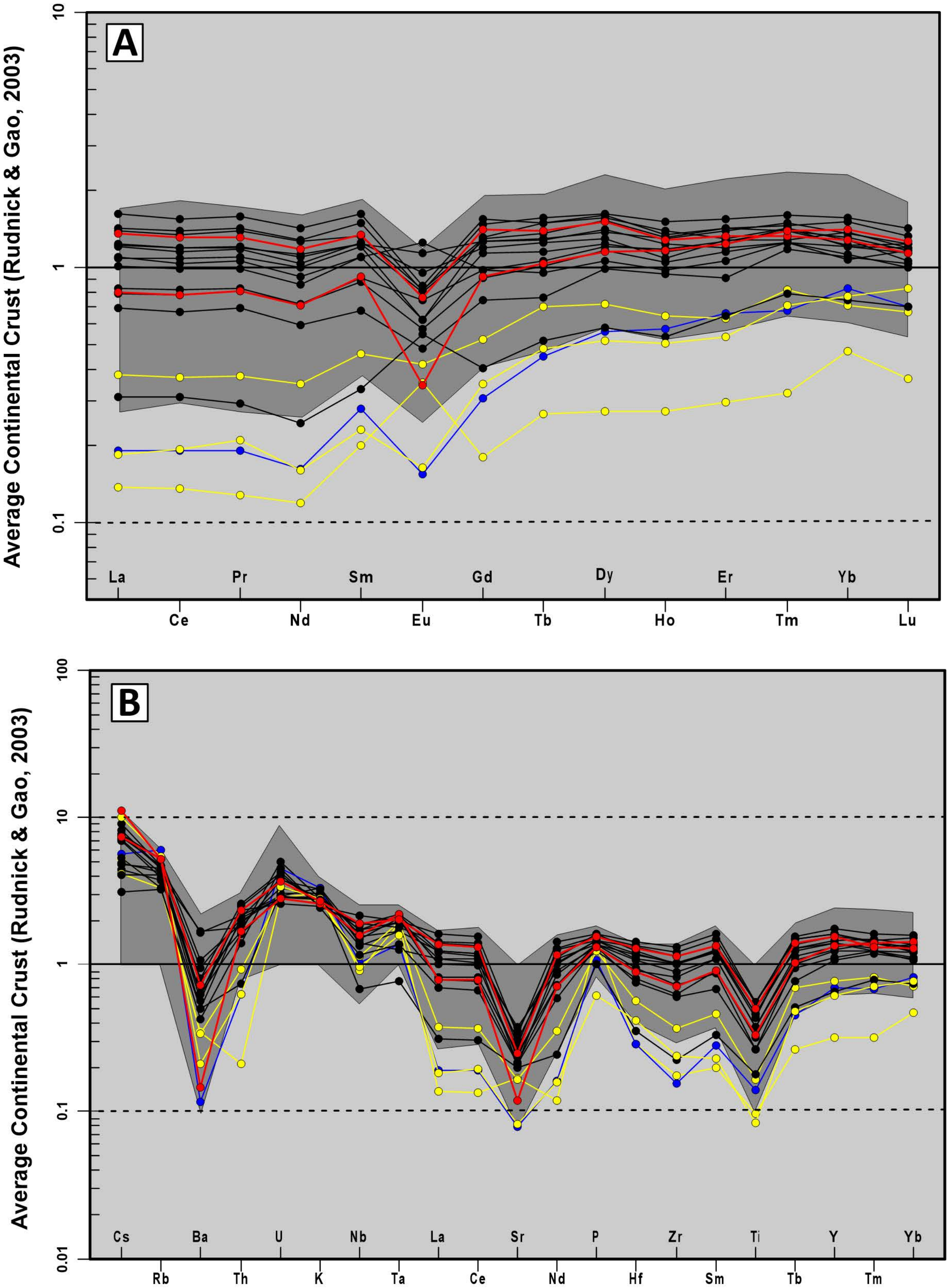

Figure 6.5*: Rare earth element (A) and multi-element spider (B) plots for the various granite phases of the study area. Both plots are normalized to the average continental crust values of Rudnick and Gao (2003). Only data from Farina et al. (2012) (dark-grey field) is used for reference due to the incomplete trace element dataset of Villaros et al. (2009a).*

Similar LREE and HREE patterns as described for the microgranites and aplite are also shown by the main coarse-grained granite and the hybrid granites (Fig. 6.5A); the latter two granite-types plot at an elevated position as a result of their higher REE concentrations which are similar to that of the average crust. Similarities in concentrations to the average crust is evident from the fairly flat LREE [(hybrid $(La/Sm)_C$ = 0.90-1.05 (average = 0.96); main phase $(La/Sm)_C$ = 0.87-1.01 (average = 0.94)] and HREE [(hybrid phase $(Gd/Lu)_C$ = 0.58-1.33 (average = 0.96); main phase $(Gd/Lu)_C$ = 0.73-1.24 (average = 0.98)] patterns the hybrid- and main coarse-grained-granites yield. Sample SP30, a fine-grained non-porphyritic hybrid phase (Fig. 6.5A; black line pattern fourth from bottom), deviates away from the rest of the hybrid granites by having lower LREE and HREE concentrations. The two main coarse-grained porphyritic granites show a moderate to strongly negative europium anomaly [$(Eu/Eu^*)_C$ = 0.38-0.56)], whereas most hybrid phases show minor to moderately negative europium anomalies [$(Eu/Eu^*)_C$ = 0.50-0.92)]. Samples SP21 and SP30 [$(Eu/Eu^*)_C$ = 1.21 and 1.49 respectively] show a positive europium anomaly.

On the spider diagram in Figure 6.5B, all the granite types of the study area show similar and consistent trace element patterns of depletion and enrichment with the microgranites and the aplite phase having, on average, lower REE and HFSE concentrations compared to the hybrid granite phases and the main coarse-grained porphyritic granites. When normalized to the average crust, the granites show enrichments in the HFSE of Th, U and P, and the LILE Cs and Rb. The troughs are typified by depletions in the LILE of Sr and Ba, and the HFSE Hf, Zr, Nb and Ti.

6.4 Major element composition of the Malmesbury Group metasedimentary rocks

The major element contents of the six Malmesbury Group metasedimentary rocks are presented in Table 6.4. The samples have average values of TiO_2 (0.79 wt. %), MnO (0.09 wt. %) and P_2O_5 (0.19 wt. %) that closely match or compare with the average composition of the average crust as calculated by Rudnick and Gao (2003). In contrast, the average CaO (0.60 wt. %) and MgO (2.81 wt. %) contents of the metasedimentary samples show a significant depletion compared to the average crust (CaO avg. = 6.51 wt. %; MgO avg. = 4.66 wt. %), whereas the composition of major oxides such as FeO^{tot} (avg. 5.78 wt. %) and Na_2O (avg. 2.16 wt. %) only show slight to minor depletions relative to the average crust (FeO^{tot} = 6.71 wt. %; Na_2O = 3.07 wt. %). The metasedimentary samples show enrichments in K_2O (avg. 4.07 wt. %), SiO_2 (avg. 63.59 wt. %) and Al_2O_3 (avg. 16.44 wt. %) relative to average crust values of K_2O (1.81 wt. %), SiO_2 (60.6 wt. %) and Al_2O_3 (15.90 wt. %).

Figure 6.6 is a geochemical classification plot by Herron (1988) which uses the three chemical parameters of SiO_2/Al_2O_3, Fe_2O_3/K_2O and the Ca content to differentiate between sandstone and shale. In terrigenous sands and shales, the SiO_2/Al_2O_3 ratio separates Si-rich quartz arenites from Al-rich shales, the Fe_2O_3/K_2O ratio separates lithic sands (litharenites and sublitharenites) from feldspathic sands (arkoses and subarkoses) and the Ca content is used to differentiate non-calcareous from calcareous sandstones and shales and to separate siliciclastic from carbonate rocks (Herron, 1988). All the samples in the study area classify as shales but plot near the wacke boundary, with SP1 and SP44, in particular plotting on the boundary separating shale and wacke (Fig. 6.6).

***Table 6.4**: Whole-rock major, trace and rare-earth (REE) geochemistry of the Malmesbury metasedimentary rocks of the study area*

Sample	**SP1**	**SP2**	**SP8**	**SP16**	**SP41**	**SP44**
Rock type	Metamudstone	Metamudstone	Metamudstone	Metamudstone	Metamudstone	Interlayered metamudstone-metasiltstone
Major elements (wt. %)						
SiO_2	65.32	63.21	62.74	63.23	61.82	65.21
Al_2O_3	16.2	16.7	16.45	16.44	17.13	15.72
TiO_2	0.8	0.78	0.80	0.80	0.79	0.75
MgO	2.37	2.89	2.95	3.00	2.94	2.69
FeOt	4.93	6.00	5.91	6.07	6.38	5.38
CaO	0.59	0.51	0.62	0.52	0.56	0.78
K_2O	3.87	3.99	4.44	4.42	4.06	3.64
Na_2O	2.26	2.01	1.99	1.84	2.32	2.51
MnO	0.09	0.08	0.10	0.09	0.11	0.08
P_2O_5	0.23	0.18	0.19	0.18	0.18	0.18
L.O.I.	2.34	2.46	2.76	2.61	2.63	2.07
Sum	**99.58**	**99.50**	**99.64**	**99.89**	**99.65**	**99.63**
Trace elements (ppm)						
Sc	18.82	21.12	20.39	20.05	20.84	18.02
V	103	124	123	120	130	110
Co	11.48	19.82	15.69	15.08	16.16	12.48
Ni	37.15	42.85	43.25	48.60	46.80	39.05
Cu	13.55	33.15	43.70	38.55	50.40	24.72
Zn	95.30	117	113	109	114	108
Rb	163	163	296	297	259	147
Sr	85.80	76.95	74.25	84.20	73.40	107.00
Ba	505	495	515	567	469	482
Cs	17.24	22.48	26.36	28.23	34.32	13.84
Zr	307	171	183	184	180	229
Nb	19.87	19.53	18.18	19.03	18.35	17.65
Y	35.07	31.83	33.63	32.92	33.05	29.69
Ta	2.01	1.15	1.13	1.17	1.08	1.07
Hf	9.09	5.09	5.52	5.44	5.47	6.69
Pb	28.26	22.21	24.62	20.56	18.98	34.61
Th	16.05	15.55	15.74	15.90	16.02	14.98
U	4.96	3.21	4.08	3.68	3.47	3.06
Mo	9.25	8.38	9.73	7.51	7.51	6.77

Sample	**SP1**	**SP2**	**SP8**	**SP16**	**SP41**	**SP44**
Rock type	Metamudstone	Metamudstone	Metamudstone	Metamudstone	Metamudstone	Interlayered metamudstone-metasiltstone
Rare earth elements (ppm)						
La	45.72	43.69	44.29	43.70	44.37	41.27
Ce	95.17	87.89	89.05	88.35	88.83	82.78
Pr	10.79	10.14	10.07	10.11	10.03	9.60
Nd	40.02	37.20	37.10	37.60	37.53	34.68
Sm	8.06	7.48	7.46	7.53	7.74	6.97
Eu	1.53	1.35	1.46	1.37	1.22	1.33
Gd	7.24	6.50	6.82	6.96	6.65	6.11
Tb	1.02	0.94	1.03	0.97	0.99	0.89
Dy	6.51	6.07	6.30	6.02	6.32	5.60
Ho	1.30	1.19	1.17	1.23	1.22	1.14
Er	3.76	3.52	3.44	3.49	3.57	3.16
Tm	0.54	0.48	0.48	0.48	0.49	0.44
Yb	3.30	3.26	3.15	3.37	3.30	3.05
Lu	0.54	0.48	0.50	0.55	0.48	0.48
∑REE	**225.50**	**210.19**	**212.32**	**211.73**	**212.74**	**197.50**
Average crust (Rudnick & Gao, 2003) normalised ratios (subscript C = crust)						
$(La/Sm)_C$	1.11	1.14	1.16	1.13	1.12	1.15
$(Eu/Eu^*)_C$	0.69	0.67	0.70	0.66	0.59	0.70
$(Ce/Ce^*)_C$	0.99	0.96	0.97	0.97	0.97	0.96
$(Gd/Yb)_C$	1.13	1.02	1.11	1.06	1.04	1.03
$(La/Yb)_C$	1.32	1.27	1.34	1.23	1.28	1.29
$(La/Lu)_C$	1.27	1.37	1.33	1.20	1.38	1.29
$(Gd/Lu)_C$	1.09	1.10	1.11	1.04	1.12	1.04
$(Ce/Yb)_C$	1.27	1.19	1.25	1.16	1.19	1.20
$(Ce/Sm)_C$	1.07	1.07	1.08	1.06	1.04	1.08

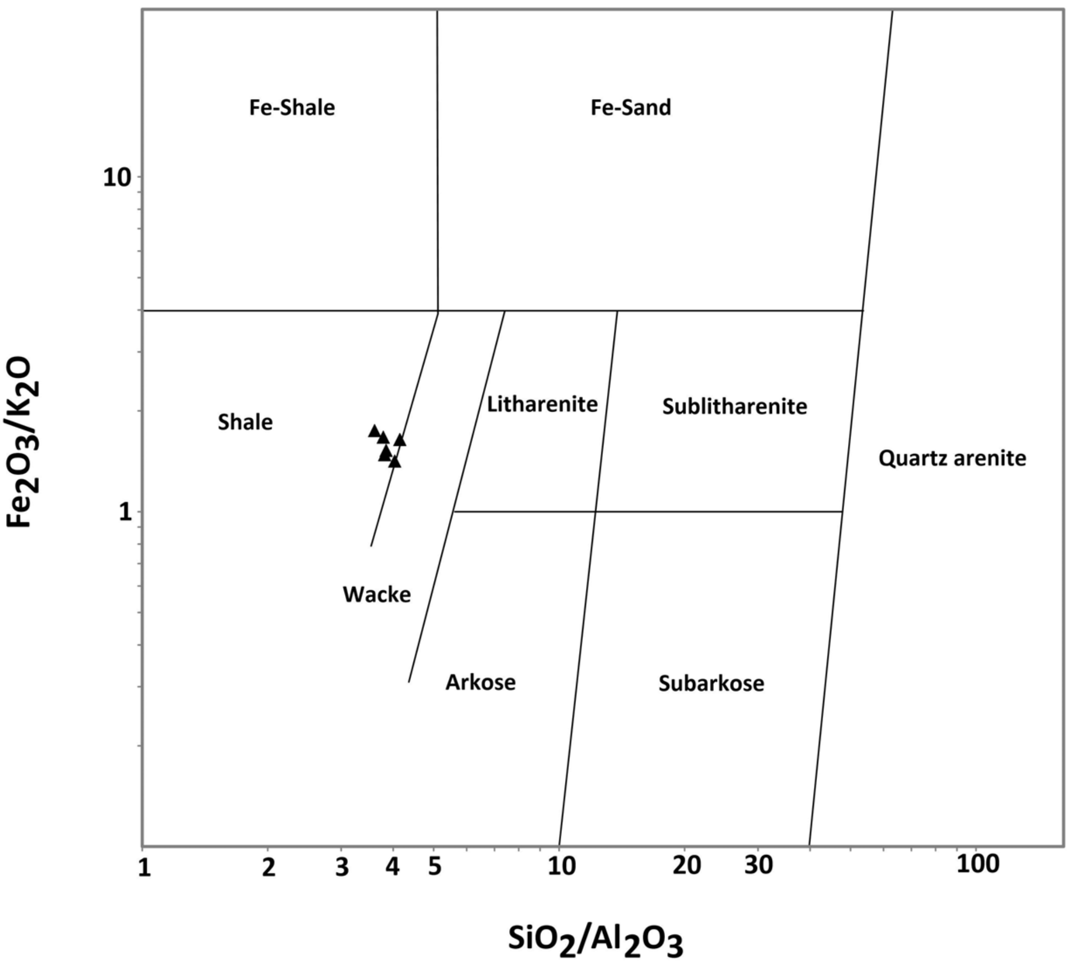

***Figure 6.6**: Geochemical classification of the metasedimentary rocks of the study area using the log (SiO_2/Al_2O_3) vs. log (Fe_2O_3/K_2O) diagram (after Herron, 1988). Black triangles represent samples from the study area in all figures of section 6.4 and 6.5.*

6.4.1 Weathering and weathering indices

Major-element chemistry of sedimentary rocks is best employed to determine the extent of weathering of the source terrain (Potter et al., 2005). A major process of chemical weathering is the transformation of feldspar to clay minerals and the subsequent loss (due to high mobility) of the K^+, Na^+ and Ca^{2+} cations (Fedo et al., 1995). One of the most useful indices derived to quantify chemical weathering effects is the chemical index of alteration (CIA) after Nesbitt and Young (1982) (Fig. 6.7). It represents a ratio of predominantly immobile Al_2O_3 to the mobile cations Na^+, K^+ and Ca^{2+} and is defined as CIA = ($Al_2O_3/Al_2O_3 + Na_2O + K_2O + CaO^*$) × 100 (where molar proportions or ratios are used to emphasize mineralogical relationships and CaO* is the amount of Ca incorporated into the silicate fraction of the rock). CIA values of < 60 indicate essentially minimal to no weathering, CIA values falling between 60 and 80 indicate intermediate levels of weathering and those >90 indicate extensive conversion of feldspar and hence intense weathering (Fedo et al., 1995; Potter et al., 2005). The CIA values for the metasedimentary samples in the study area fall in the range of 62.36 and 66.13, indicating intermediate weathering (Fig. 6.7). This is consistent with the CIA values derived from the reference geochemical data of Frimmel et al. (2013) (CIA value range: 56.61-76.87) and the unpublished dataset (CIA value range: 53.73-76.16) (Fig. 6.7) suggesting that the Malmesbury Group metasedimentary rocks of the Tygerberg Formation were essentially all affected by low to intermediate degrees of chemical weathering.

To obtain information about weathering trends, post-depositional alteration effects (e.g. K-metasomatism) and possible source-rock composition (provenance), the chemical compositions of sedimentary rocks can be plotted as molar proportions within Al_2O_3, CaO^*+ Na_2O, K_2O (A-CN-K) compositional space or A-CN-K ternary plots (Nesbitt & Young, 1984; Fedo et al., 1995) (Fig. 6.7). Potential source rocks, such as fresh or unweathered basalts, have CIA values between 30 and 45, whereas fresh granites and granodiorites have CIA values between 45 and 55 (Nesbitt & Young, 1984; Fedo et al., 1995) (Fig. 6.7). Thus provenance information may be obtained by extrapolating a plotted point from a sample towards the CN axis of the diagram parallel to the A-CN axis. Weathering products derived from feldspar (plagioclase and K-feldspars which both have CIA values of 50), such as kaolinite, has a CIA value of 100 and represents the highest degree of weathering, whereas Illite and smectite have values between 75 and 90 and muscovite is at 75 (Fig. 6.7). Weathering information can be obtained by observing where samples plot relative to the plotting position of these weathering products, for example, the transformation of feldspar to illite will cause a sample's composition to plot closer to the A-K join and the illite composition in the A-CN-K plot.

All of the samples of the study area plot as a cluster along the intermediate part of the granite and rhyolite weathering line and have a general steep trend directed towards illite-muscovite compositions (Fig. 6.7). The supplementary data also show similar trends to the Malmesbury samples from the study area, with trends tending towards illite-muscovite compositions. They are, however, not confined within one weathering line for one of the potential source rocks as they show overlap by plotting between the predicted weathering trends of granodiorite, granite and rhyolite compositions (Fig. 6.7).

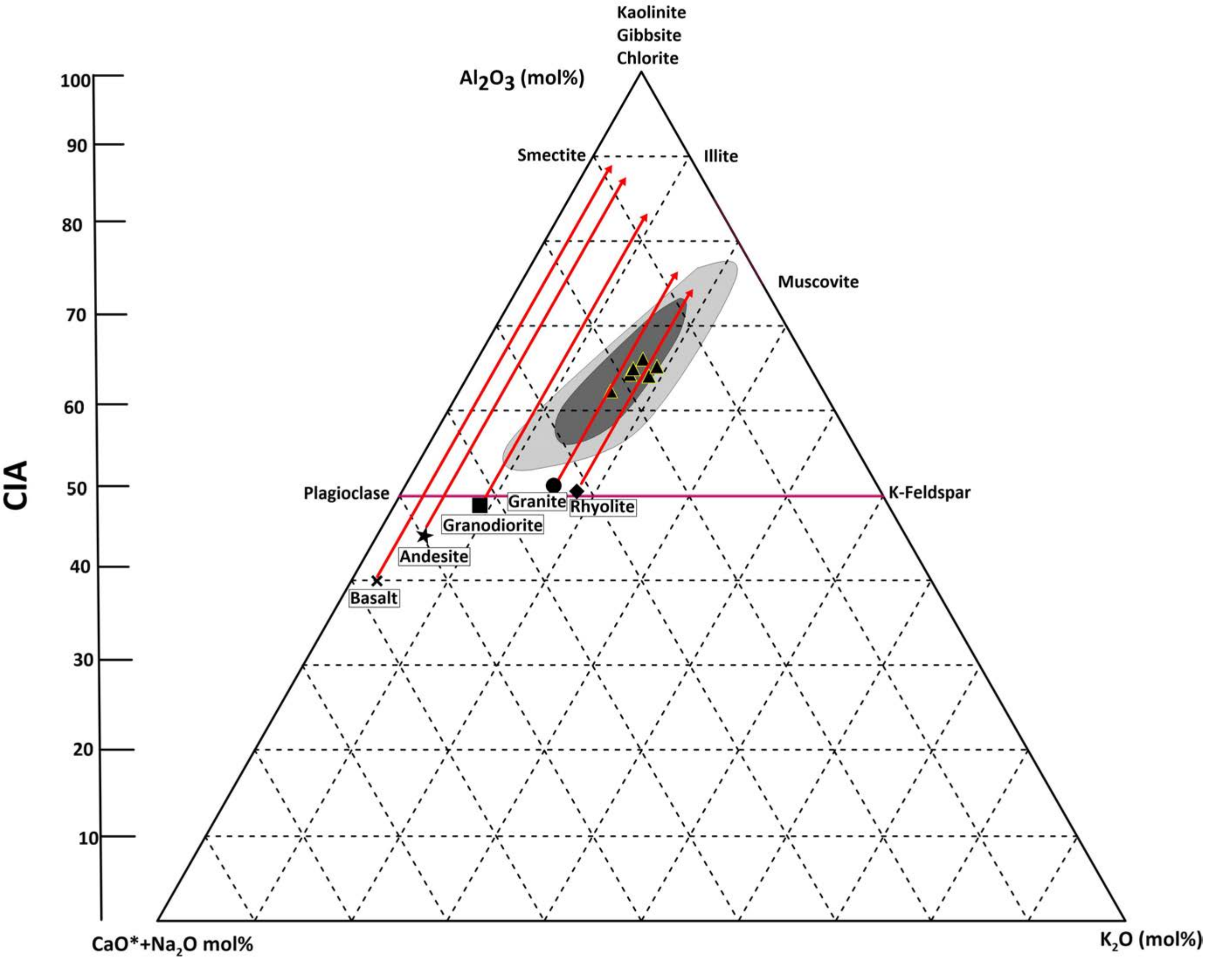

Figure 6.7*: A-CN-K and CIA ternary diagram (after Nesbitt & Young, 1984; Fedo et al., 1995) showing the weathering trend for the metasedimentary rocks of the study area. Solid red arrows represent the predicted weathering trend for typical igneous rocks after Cox et al. (1979). The fields for the unpublished data (light-grey field) and Frimmel et al. (2013) (dark-grey field) are shown for reference.*

6.5 Trace element composition of the Malmesbury Group metasedimentary rocks

6.5.1 Provenance

Figure 6.8A and B are the REE and spider plot for the Malmesbury metasedimentary rocks in the study area respectively; both are normalized to average crustal values of Rudnick and Gao (2003). The REE in sedimentary rocks are important because they are not fractionated from each other by most sedimentary processes and are largely insoluble (or remain unaffected) under most geological conditions and post-depositional processes (Potter et al., 2005). This makes them particularly useful as provenance parameters.

The metasedimentary samples in the study area are relatively enriched in the REE compared to the average continental crust normalized concentrations of the REE as evidenced by the LREE and HREE patterns all plotting above 1 (Fig. 6.8A). The samples are characterized by relatively flat to gently negative sloping REE patterns [$(La/Lu)_C$ = 1.20-1.38) relative to average continental crust (Fig. 6.8A) With both $(La/Sm)_C$ and $(Gd/Lu)_C$ ratios falling between the range of 1 and 2, this indicates little fractionation within the LREE and HREE, respectively. The samples show moderately negative europium anomalies [$(Eu/Eu^*)_C$ = 0.59-0.70)].

The spider plot in Figure 6.8B shows that the trace element contents of the metasedimentary rocks of the study area are largely enriched relative to average continental crust trace element abundances. The samples show consistent negative anomalies or depletions in the LILE Sr (strongest negative anomaly to values lower than the average crust), K and Ba, and the HFSE Hf, Ti and Ta (Fig. 6.8B). Moreover, the samples show enrichments in the HFSE of Th and U and the LILE Cs and Rb (Fig. 6.8B).

Figure 6.8C is the Th/Sc vs. Zr/Sc bivariate plot after McLennan et al. (1993). The Th/Sc ratio is a good indicator of sedimentary provenance, because Th and Sc are relatively insoluble during geological processes such as weathering and diagenesis, and thus are transported almost exclusively by terrigenous detritus (McLennan et al., 1993; Potter et al., 2005). This makes them useful because they reflect the chemistry of their sources and can be utilized to detect mixing processes and the effect of sediment recycling in sediments (McLennan et al., 1993; Potter et al., 2005). The ratio Zr/Sc is a useful index of zircon enrichment since Zr is strongly enriched in zircon, whereas Sc is not enriched but generally preserves a signature of the provenance (McLennan et al., 1993).

The samples have a narrow Th/Sc variation (0.74-0.85) and a Zr/Sc variation that is relatively more variable (8.10-16.29). On the Th/Sc- Zr/Sc diagram (Fig. 6.8C) the samples in the study area show a general direct proportionality or positive correlation, with the samples plotting slightly away from the magmatic compositional variation trend of rocks, between the andesite and granite compositional range, towards Th-rich compositions (and Zr-rich compositions in the case of sample SP1). In general, the samples show minimal evidence of sedimentary recycling (or reworking) as shown by the relatively low Zr/Sc ratios indicating that geochemical variation was dominated by the composition of the source materials (which were intermediate to felsic as shown by the samples plotting between average andesite and granite compositions) (Cullers, 1994). However, a degree of sediment recycling or reworking cannot be disregarded, as evident from the plotting positions of supplementary data on the same diagram (Fig. 6.8C), with some of the data points from the supplementary dataset overlapping with the sedimentary recycling line.

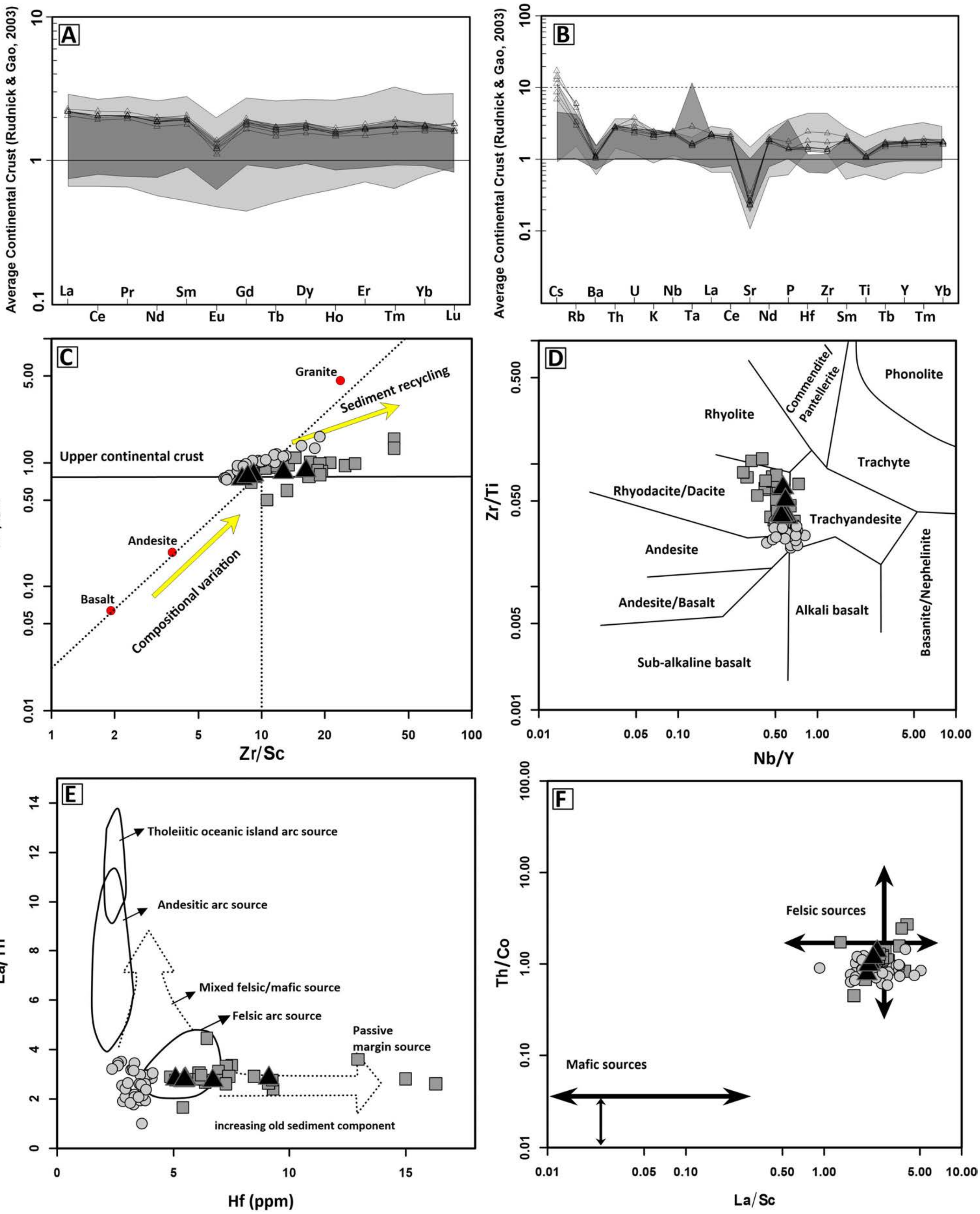

***Figure 6.8**: Various provenance and degree of weathering plots for the metasedimentary rocks of the study area. (A) REE plot and (B) multi−element spider plot both normalised using values for the average crust from Rudnick and Gao (2003); the fields for the unpublished data (light-grey field) and Frimmel et al. (2013) (dark-grey field) are shown for reference. (C) Th/Sc vs. Zr/Sc plot (after McLennan et al., 1993) for determination of the general provenance type, composition, sedimentary recycling, sedimentary sorting, and upper crustal input. Th/Sc > 0.79 (solid-line) reflects provenance of samples from the upper continental crust. (D) Zr/Ti vs. Nb/Y plot (after Winchester & Floyd, 1976) for determination of the average composition of the provenances to the metasedimentary rocks of the study area. (E) Hf – La/Th diagram (after Floyd & Leveridge, 1987) with the various fields indicative of the compositions of sedimentary rocks deposited in different tectonic settings. (F) Th/Co vs. La/Sc (after Cullers, 2002) for provenance discrimination. The length of the horizontal and vertical arrows on the diagram indicate the typical extent of the range of felsic and mafic samples respectively. The data for the unpublished dataset (grey squares) and Frimmel et al. (2013) (grey circles) are shown for reference.*

Figure 6.8D is the Zr/Ti vs. Nb/Y plot after Winchester and Floyd (1976) that is used to determine the average composition of the provenances to the Malmesbury Group metasedimentary rocks of the study area. The Nb/Y ratio is useful in discerning the alkalinity of magmatic and volcanic rocks due to Nb being enriched relative to Y in alkaline rocks, whereas the Zr/Ti ratio indicates the degree of differentiation (Winchester & Floyd, 1976). The samples in the study area all plot within the rhyodacite / dacite fields as a fairly tight cluster but very close to the trachyandesite boundary (Fig. 6.8D). This reflects their high silica content (61.82-65.32 wt. %) and suggests a felsic provenance for the samples.

Further evidence supporting a felsic provenance comes in the form of the Hf vs. La/Th plot (after Floyd & Leveridge, 1987; Fig. 6.8E) and Th/Co vs. La/Sc diagrams (after Cullers, 2002; Fig. 6.8F). The La/Th ratios and Hf contents are sensitive indices of the source composition of clastic rocks and this led Floyd and Leveridge (1987) to develop the La/Th vs. Hf ratio diagram to differentiate whether sediments had a contribution from an arc system source (i.e. tholeiitic, andesitic and felsic sources). All the samples in the study area plot within the felsic arc source whereas samples from Frimmel et al. (2013) plot in the felsic–mafic mixed source field (and some within the felsic arc source) and samples from the unpublished data predominantly plot within the felsic arc field but have a minor influence from passive margin components (Fig. 6.8E).

Using the Th/Co and La/Sc ratios, Cullers (2002) developed a diagram that can be used to discriminate sediments derived from mafic sources from those of felsic composition (Fig. 6.8F). Values of Th/Co > 0.3 (Sea Point Malmesbury Th/Co = 1.7) and La/Sc > 0.7 (Sea Point Malmesbury La/Sc = 2.21) are characteristic of sediments from felsic sources, whereas La/Sc < 0.4 is related to mafic sources (Cullers, 2002). All samples in the study area, along with the supplementary data, plot or fall within the felsic field or domain (Fig. 6.8F).

6.5.2 Tectonic setting

The immobile trace elements of La, Ce, Nd, Th, Zr, Nb, Y, Sc and Co and their ratios (e.g. Th, La-Th-Sc, Ti/Zr-La/Sc, La/Y-Sc/Cr, Th-Sc-Zr/10 and Th-Co-Zr/10) are useful in tectonic setting/environment and provenance discrimination (Bhatia & Crook, 1986). Figure 6.9 shows two ternary plots (Fig. 6.9B, C) and a single bivariate plot (Fig. 6.9A) which utilize the ratios of La, Th, Sc and Zr after Bhatia and Crook (1986). The metasedimentary samples in the study area, as well as the vast majority of the supplementary data, all plot within the field of continental island arc in the La/Sc vs. Ti/Zr (Fig. 6.9A), Th–La–Sc (Fig. 6.9B) and Th-La-Zr/10 diagrams (Fig. 6.9C).

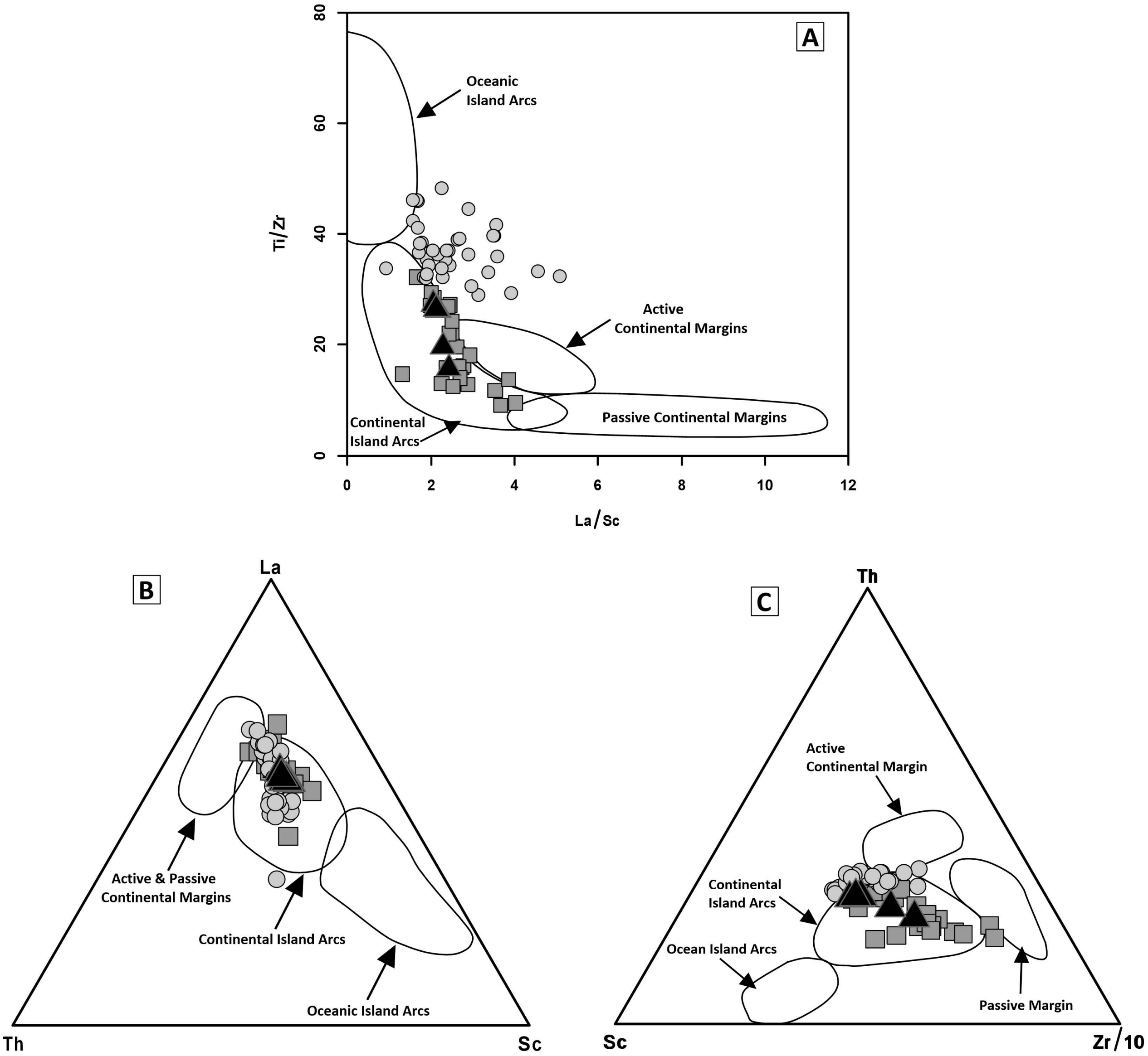

***Figure 6.9**: Trace element tectonic discrimination diagrams for the metasedimentary rocks of the study area. (A) A plot of La/Sc vs. Ti/Zr (after Bhatia & Crook, 1986). (B) La-Th-Sc ternary plot (after Bhatia & Crook, 1986) (C) Th–Sc–Zr/10 ternary plot (after Bhatia & Crook, 1986). The data for the unpublished dataset (grey squares) and Frimmel et al. (2013) (grey circles) are shown for reference.*

6.6 Sr and Nd radiogenic isotope geochemistry

Seven samples were selected for whole-rock samarium-neodymium (Sm-Nd) and rubidium-strontium (Rb-Sr) analyses. The results are presented in Tables 6.5 (Sm-Nd) and 6.6 (Rb-Sr). For this study, the single- and two-stage Nd model ages were calculated using a Sm decay constant of 6.54×10^{-12} year^{-1} (Lugmair & Marti, 1978) and the depleted mantle values of DePaolo (1981) (Table 6.5). The initial $^{87}Sr/^{86}Sr$ (Sr_I) ratios were calculated using a Rb decay constant of 1.42×10^{-11} year^{-1} (Steiger & Jäger, 1977) (Table 6.6). For the granites, the initial Sr and Nd isotopes were calculated using the derived 540 ± 4 Ma emplacement age for the Peninsula Pluton by Scheepers and Armstrong (2002). The error for the Sr_I, Initial $^{143}Nd/^{144}Nd$ (Nd_I) and ε_{Ndt} (epsilon Nd) yielded by the granites were calculated considering the uncertainty on the Sm/Nd, Rb/Sr and the emplacement age. For the metasedimentary sample, initial Sr and Nd isotopes were calculated using the 560 Ma age of deposition for the Tygerberg Formation by Armstrong et al. (1998). This age was presented only as a short conference abstract without supporting data or indication of uncertainties. Error calculations were, thus, not performed for the metasedimentary sample.

The granites (particularly the microgranites) yield highly anomalous/radiogenic values for some of the calculated Nd and initial Sr isotopes. The highly radiogenic values can be due to three things: (i) weathering (the granites at the Sea Point contact are variably weathered and fresh samples are hard to come by there), (ii) hydrothermal activity (seen from the sericitisation of feldspars and extensive cordierite alteration in both the country rock and granites; section 4.1), and (iii) the S-type granites of the CGS were derived from melting of Malmesbury Group sediments or their high-grade equivalents at depth (Stevens et al., 2007; Villaros et al., 2009b; Harris & Vogeli, 2010). These metasedimentary rocks are, in turn, postulated to have been derived from erosion of Namaquan gneisses (Frimmel et al., 2013), which are known to be highly radiogenic with high initial Sr isotope ratios. This may have been translated to the Malmesbury Group and, in turn, to the CGS granites.

6.6.1 Sr and Nd isotope geochemistry results for the granite phases

The granite phases have Sm/Nd ratios that vary between 0.22 and 0.32, with the two microgranite samples having the highest Sm/Nd ratios (SP3 = 0.32; SP38 = 0.28) compared to the hybrid granite phases and the main coarse-grained porphyritic granite respectively (i.e. Sm/Nd ratios between 0.22-0.24) (Table 6.5). Initial $^{143}Nd/^{144}Nd$ (Nd_I) ratios for the granites show a narrow range, varying between 0.512149 and 0.512351. The SP3 microgranite sample has a much lower ε_{Ndt} value (-8.04) compared to the rest of the granites, which have ε_{Ndt} values varying from -5.75 to -4.52 (Table 6.5). T_{CHUR} model ages for the granites range from 1.255 – 2.764 Ga, with sample SP3 having a T_{CHUR} model age of -4.849 Ga (Table 6.5).

The single-stage Sm-Nd model ages (T_{DM}) for the granites vary from 2.055 Ga (SP7) to 3.699 Ga (SP38), with sample SP3 having a far higher T_{DM} value of 24.651 Ga (Table 6.5). Two-stage depleted-mantle Nd model ages (T_{2DM}), calculated after Liew and Hofmann (1988), constrain the isotopic ages of the various granite phases better (Table 6.5). The T_{2DM} ages, that are yielded, are far less variable and vary between 1.59 and 1.84 Ga (Table 6.5). As is the case with a single-stage Nd model age, the two-stage Nd model age is an age at which the isotopic composition of the sample was identical to that of a model reservoir [(chondritic uniform reservoir (CHUR) or depleted mantle (DM)]. The difference is that T_{2DM} compensates for the effects of possible secondary Sm/Nd fractionation as a result of processes such as partial melting, fractional crystallisation, magma mixing or alteration (Liew & Hofmann, 1988; Champion, 2013). The fact that the T_{2DM} model ages give better ages than the T_{DM} ages shows that the Sea Point contact has been affected by certain secondary processes (as previously mentioned in section 6.6). T_{2DM} models are calculated using the measured $^{147}Sm/^{144}Nd$ ratio back to the magmatic age of the rock and an assumed (and not the measured) $^{147}Sm/^{144}Nd$ ratio for calculating the sample evolution curve before the crystallisation age (Champion, 2013). An assumed $^{147}Sm/^{144}Nd$ ratio of 0.12, equivalent to average upper continental crust values (cc), after Liew and Hofmann (1988) has been used for this study.

The granite phases show highly variable Rb/Sr ratios which vary between 2.16 and 10.10, with the highest value within this range (10.10) coming from sample SP38 (microgranite) (Table 6.6). Without SP38, the granite phases show a much more narrow Rb/Sr variation (2.16 – 3.52). The Sr_I ratios show a large range by varying between 0.717350 and 0.739350 (Table 6.6).

6.6.2 Sr and Nd isotope geochemistry results for the metasedimentary sample (SP16)

Sample (SP16) has a Sm/Nd ratio value of 0.20, a Nd_I value of 0.511985, a low ε_{Ndt} value of -7.84, T_{CHUR} model age of 1.441 Ga and a T_{DM} age of 2.071 Ga (Table 6.5). The Rb/Sr ratio value for the sample is 3.52 and the Sr_I value is 0.728103 (Table 6.6).

***Table 6.5**: Whole−rock Sm-Nd isotopic data for the S-type Peninsula Pluton granites and the single Malmesbury Group metasedimentary rock of the study area*

Sample	**Rock type**	**Sm (ppm)**	**Nd (ppm)**	**Sm/Nd**	**±1σ**	**$^{147}Sm/^{144}Nd$**	**$(^{143}Nd/^{144}Nd)_0$**	**±2σ internal**	**Nd I**	**±2σ**	**ε $Nd_{(t)}$**	**±1σ**	**Age (Ma)**	**T_{CHUR} (Ga)**	**T_{DM} (Ga)**	**T_{2DM} (Ga)**
SP3	Microgranite	0.78	2.38	0.33	0.11	0.20856	0.512268	14	0.511531	250	-8.04	4.8	540	-4.839	24.651	1.836
SP7	Main c/g porphyritic granite	5.25	23.49	0.22	0.02	0.14315	0.512197	11	0.511690	50	-4.92	0.9	540	1.255	2.055	1.592
SP31	M/g porphyritic hybrid granite	4.91	20.69	0.24	0.0008	0.15184	0.512187	15	0.511650	6	-5.70	0.01	540	1.528	2.365	1.653
SP33	F/g porphyritic hybrid granite	4.74	20.07	0.24	0.02	0.15138	0.512235	15	0.511699	49	-4.74	0.86	540	1.354	2.232	1.578
SP38	Microgranite	0.90	3.19	0.28	0.005	0.18099	0.512351	14	0.511711	16	-4.51	0.2	540	2.764	3.699	1.560
SP43A	C/g porphyritic hybrid granite	6.32	28.61	0.22	0.003	0.14149	0.512149	24	0.511648	10	-5.74	0.1	540	1.349	2.108	1.656
SP16	Metamudstone	7.53	37.60	0.20		0.12818	0.511985	9	0.511515		-7.84		560	1.441	2.071	1.836

−**ε $Nd_{(t)}$** = $((^{143}Nd/^{144}Nd_{(i)}/^{143}Nd/^{144}Nd_{(CHUR,\ t)})-1) \times 10000$

−**T_{DM}** = $1/(\lambda) \times \ln(1+ (^{143}Nd/^{144}Nd_{(0)} - {}^{143}Nd/^{144}Nd_{(DM)}/^{147}Sm/^{144}Nd - {}^{147}Sm/^{144}Nd_{(DM)})) \times 0{,}000000001$ (after DePaolo, 1981)

where $(^{143}Nd/^{144}Nd)_{DM} = 0.51351$, $(^{147}Sm/^{144}Nd)_{DM} = 0.2136$

−**T_{2DM}** = $1/(\lambda) \times \ln(1+ (^{143}Nd/^{144}Nd)_0 - (e^{\lambda t}-1)\{(^{147}Sm/^{144}Nd - {}^{147}Sm/^{144}Nd)_{cc}\{-(^{143}Nd/^{144}Nd)_{DM}/^{147}Sm/^{144}Nd)_{cc} - (^{147}Sm/^{144}Nd)_{DM}$ (after Liew & Hofmann, 1988)

where $(^{143}Nd/^{144}Nd)_{DM} = 0.51351$, $(^{147}Sm/^{144}Nd)_{DM} = 0.2136$, $(^{147}Sm/^{144}Nd)_{cc} = 0.12$

−**T_{CHUR}** = $1/(\lambda) \times \ln(1+ (^{143}Nd/^{144}Nd_{(0)} - {}^{143}Nd/^{144}Nd_{(CHUR,\ t)})/^{147}Sm/^{144}Nd - {}^{14}7Sm/^{144}Nd_{(CHUR,\ t)}) \times 10^9$ (after DePaolo, 1981)

where $(^{143}Nd/^{144}Nd)_{(CHUR,\ t)} = 0.512638$, $(^{147}Sm/^{144}Nd)_{(CHUR,\ t)} = 0.1967$

***Table 6.6**: Whole−rock Rb-Sr isotopic data for the S-type Peninsula Pluton granites and the single Malmesbury Group metasedimentary rock of the study area*

Sample	**Rock type**	**Rb (ppm)**	**Sr (ppm)**	**Rb/Sr**	**±1σ**	**$(^{87}Sr/^{86}Sr)_0$**	**±2σ internal**	**$^{87}Rb/^{86}Sr$**	**Sr I**	**±2σ**	**Age (Ma)**
SP3	Microgranite	163	53.9	3.03	0.03	0.789025	13	8.045136	0.727098	1100	540
SP7	Main c/g porphyritic granite	255	79.4	3.22	0.01	0.788324	13	8.540814	0.722582	700	540
SP31	M/g porphyritic hybrid granite	254	97.4	2.61	0.02	0.770782	13	6.941448	0.717350	800	540
SP33	F/g porphyritic hybrid granite	208	68.3	3.04	0.07	0.784699	18	8.075778	0.722536	600	540
SP38	Microgranite	268	26.5	10.10	0.19	0.945818	22	26.822917	0.739350	5400	540
SP43A	C/g porphyritic hybrid granite	229	106.2	2.16	0.01	0.764947	16	5.729142	0.720847	530	540
SP16	Metamudstone	297	84.2	3.52		0.802792	13	9.355237	0.728103		560

7 U-Pb geochronology

7.1 Introduction

Three samples from the various granite lithologies at the Sea Point contact were dated. Samples SP19 is a microgranite that outcrops in the northern end of the study area, whereas samples SP33 (fine-grained porphyritic granite) and SP43A (coarse-grained porphyritic granite) form part of the hybrid granites in the main contact zone (Fig. 4.1). A description of the morphology (as revealed by cathodoluminescence (CL) images) and the resultant U-Pb ages from the zircon grains in all three granite samples are described in this chapter.

7.2 Zircon descriptions

The zircons from all three samples generally show similar zonation patterns and crystal shapes, however, certain forms (or populations) tend to predominate in one sample over the other. Most of the zircon grains vary from euhedral and prismatic to subhedral. Elongate, narrow and tabular to needle-shaped zircon forms also occur along with rare anhedral zircon grains. The zircon grains have typical sizes ranging from 85–330 µm in length (with typical length-width ratios of 2:1 to 5:1), with the more elongate zircon grains varying from 215–550 µm in length (with length-width ratios up to 8:1). A summary of the textures each zircon population shows is provided below:

1. Oscillatory zoned euhedral to subhedral zircons

This zircon population is the most commonly occurring across all three samples but is more prevalent in sample SP33. Oscillatory zoned zircon grains are characterised by narrow and fine-scale cyclic variations (or zonation) which are continuous from the core to the rim (Fig. 7.1A, B, C, E, F, M, N). Some have larger-scale oscillatory zones (with wider cyclic variations) that alternate with narrow oscillatory bands found in the cores (Fig. 7.1D). The truncation of oscillatory zoned core structures, indicating resorption (Gagnevin et al., 2010), also occurs. This feature occurs in some of the oscillatory zoned grains of sample SP43A (e.g. Fig. 7.1O, P).

Other features shown by the oscillatory zoned zircon grains is that they either have:

(i) Low luminescent (CL-dark) oscillatory zoned cores surrounded by high- (CL-bright) to intermediate-luminescent (i.e. light-grey to medium-grey CL responses) rims (Fig. 7.1B, F, G, L, M), or
(ii) high luminescent oscillatory zoned cores and low to intermediate luminescent rims (Fig. 7.1C, H, J, K).

Furthermore, some of the cores of these oscillatory zoned zircon grains show characteristics associated with inherited zircons. This inherited character can be recognised by sub-rounded zircon cores surrounded by oscillatory zoning; the subrounded characteristic indicates either partial dissolution within the melt or mechanical abrasion during sedimentary transport before its incorporation in the melt (e.g. Paterson et al., 1992; Corfu et al., 2003). These sub-rounded cores may show narrow to broad zonation patterns (Fig. 7.1E, F, H, L), or they may have relics of primary textures (growth zoning) left preserved (Fig. 7.1J), or they may be completely unzoned (Fig. 7.1G, I).

2. Zircon grains with a homogenous, unzoned core surrounded by a zoned rim

This zircon population tends to take on elongated to partly-elongated prismatic shapes and is more prevalent in sample SP43A. These zircons are characterized by large homogenous and unzoned equant-euhedral cores surrounded by much finer oscillatory-zoned rims (Fig. 7.2 A-D).

3. Elongate zircon grains

This zircon population is more common in sample SP43A but is consistently present in samples SP33 and SP19 as well. These grains tend to show the following properties:

(i) Oscillatory zonation from the core to the rim (Fig. 7.2F)
(ii) Broadly zoned core surrounded by a narrow oscillatory zoned rim (Fig. 7.2 E)
(iii) Simple broad parallel twinning in which zonation bands are either thin and well-defined (Fig. 7.2G, H), or broad and faint (Fig. 7.2I)
(iv) Unzoned to weakly zoned low luminescent cores and high luminescent rims (Fig. 7.2J)
(v) Unzoned to weakly zoned high luminescent cores and low luminescent rims (Fig. 7.2K)

(vi) Unzoned equant cores, which are locally truncated by CL-dark structureless lobate zircon portions, surrounded by thin oscillatory zoned rims (e.g. Fig. 7.2L)

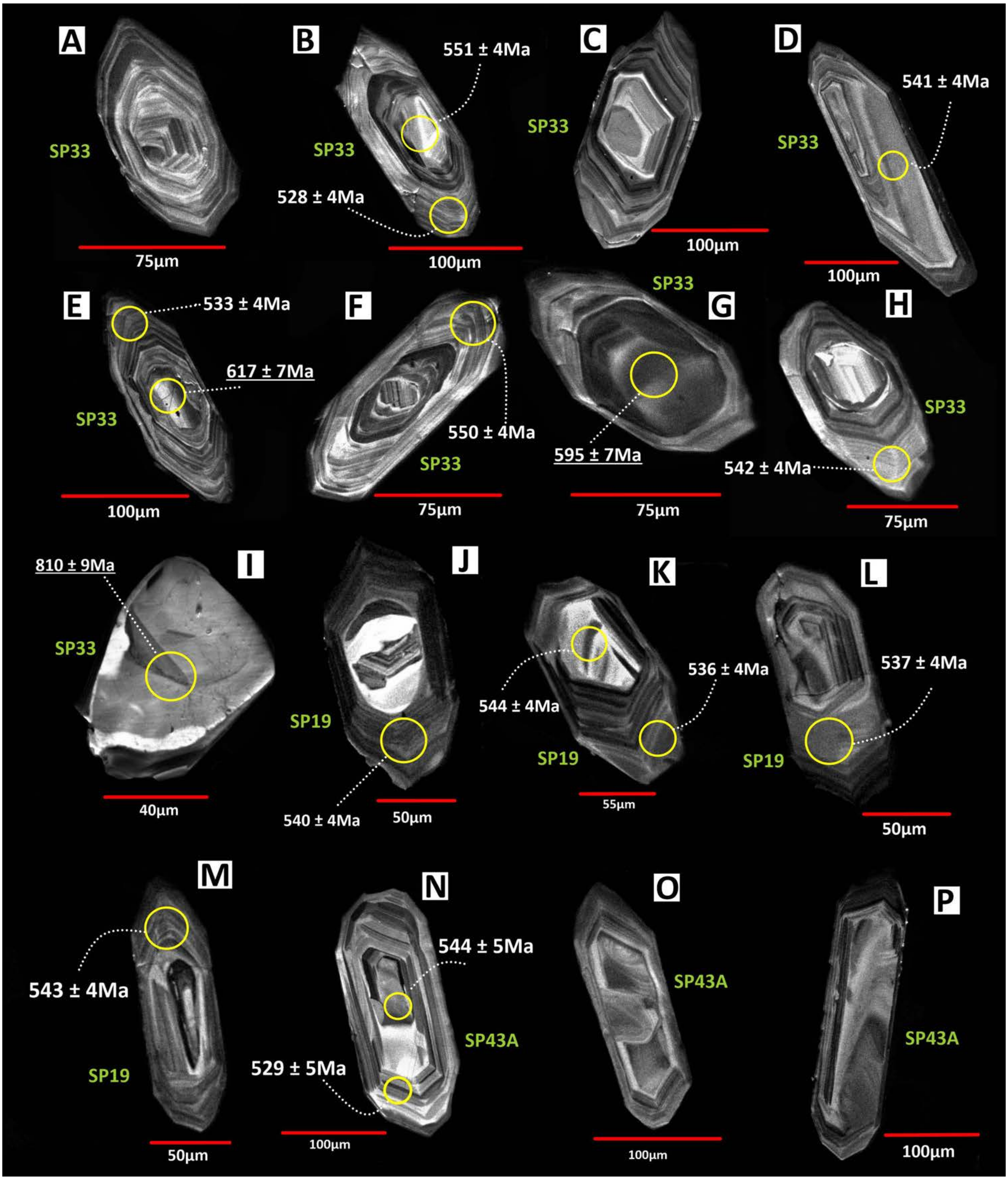

***Figure 7.1**: CL images of oscillatory zoned zircons and their associated internal structures and textures. The yellow circles indicate the locations of LA-ICP-MS (Laser Ablation Inductively Coupled Plasma Mass Spectrometry) analysis and resultant spot ages are reported as ^{206}Pb/^{238}U ages with 2σ uncertainties. Underlined ages were not included in age regressions. Textures are described in the text.*

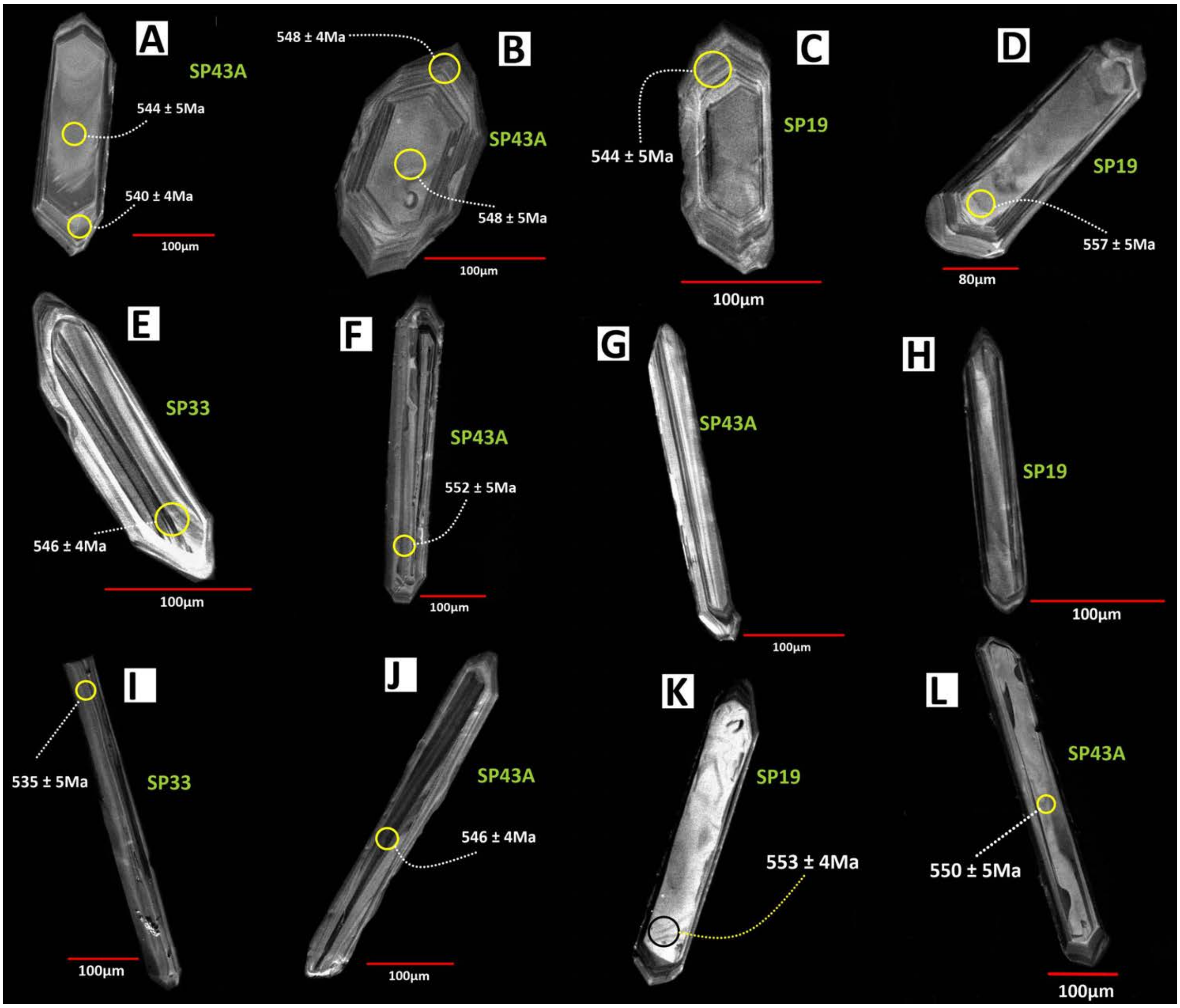

Figure 7.2: *CL images of zircon grains with unzoned cores (A-D) and those which are elongate (E-L) The yellow circles [(and the one black circle; e.g. (K)] indicate the locations of LA-ICP-MS analysis and resultant spot ages are reported as* $^{206}Pb/^{238}U$ *ages with 2σ uncertainties. Textures are described in the text.*

4. Unzoned zircon grains

The unzoned to weakly zoned zircon population is more common in sample SP43A but a few do occur in sample SP33 as well. They tend to have a weak luminescence and are uniformly unzoned to weakly zoned throughout the entire zircon grain (Fig. 7.3A-C).

5. Irregularly zoned zircon grains

This zircon population have alternating CL-dark and CL-bright zones arranged in irregular, non-planar patterns that generally have no preferred structure. The zonation patterns are typically broadly banded and strongly developed (Figs. 7.3D-F) or weakly developed with narrower bands (Fig. 7.3G-I). This zircon population is more prevalent in sample SP19 but occurs fairly consistently in samples SP33 and SP43A.

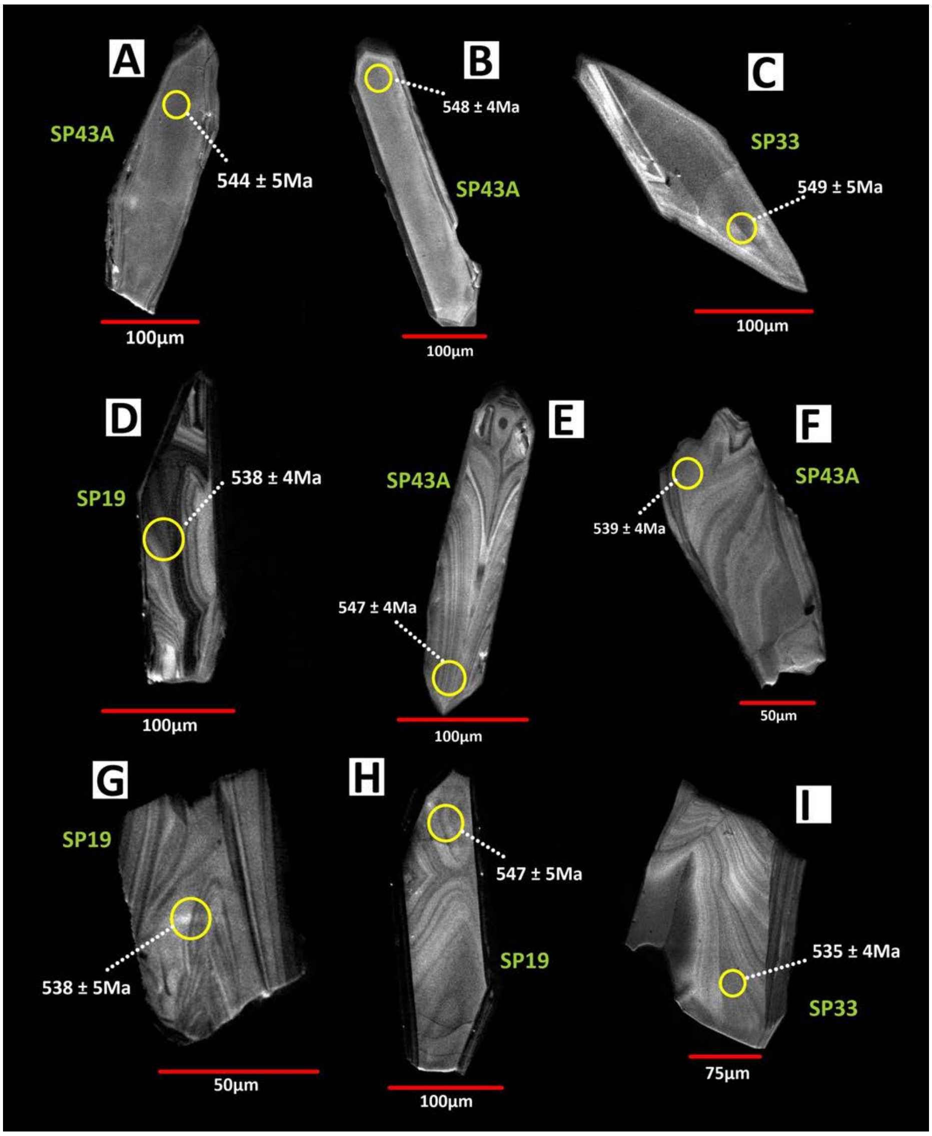

Figure 7.3*: CL images of zircon grains that are completely unzoned (A-C) and those which are irregularly zoned (D-I). The zircon grains all have Th/U < 0.1. The yellow circles indicate the locations of LA-ICP-MS analysis and resultant spot ages are reported as ^{206}Pb/^{238}U ages with 2σ uncertainties. Textures are described in the text.*

Zircons with weak zonation and fairly homogeneous textures throughout the extent of the grain and those with irregular zonation patterns (referred to as convoluted zoning or “flow zones” or “flow domains”) are all features interpreted to be metamorphic in origin (Hoskin & Schaltegger, 2003; Rubatto, 2017). The CGS granites were derived by partial melting of the high-grade equivalents of the Malmesbury Group (e.g. Harris & Vogeli, 2010; Villaros et al., 2012) which were metamorphosed shortly before melting occurred during regional deformation (Rowe et al., 2010). So it is possible that the granites incorporated/inherited some of the metamorphic zircons into the melt. The grains are, however, likely magmatic as a separate weighted mean age done for them (not shown) is identical within error to the weighted mean age calculated for zircons (in each sample) which do not have the same features (also not shown).

7.3 U-Pb ages

Tables 7.1, 7.2 and 7.3 present the U–Th–Pb isotopic analyses performed on a total of 77 zircon grains spanning across the three selected granite samples (i.e. SP19, SP33 and SP43A). All ages calculated/derived based on either the $^{207}Pb/^{206}Pb$ or $^{206}Pb/^{238}U$ isotopic ratios, yield ages of less than 1500 Ma. Therefore based on the recommendations of Spencer et al. (2016) and Burnham (2018), $^{206}Pb/^{238}U$ ages are reported for the zircon grains of this study as they are all <1500 Ma.

Uncertainties on individual analyses in data tables are reported at the 2σ level and mean ages for pooled U/Pb analyses are quoted at the 95% confidence interval. All the analyses are plotted on concordia diagrams (i.e. Wetherill plots; Figs. 7.4, 7.5, 7.6) which were generated using *Isoplot v. 4.15* (Ludwig, 2012). For this study, any dates with greater than 5% discordancy are not considered in determining the weighted mean $^{206}Pb/^{238}U$ age.

7.3.1 Microgranite (Sample SP19)

A total of 26 U-Th-Pb analyses on zircon grains from sample SP19 were done. All but one of the analyses (i.e. SP19-5; Table 7.1) passed the <5% discordancy filter test. All the analyses (both concordant and discordant) are plotted on a concordia diagram where they define a fairly tight cluster at ages of 530-550 Ma, with a few outliers at ages >550 Ma (Fig. 7.4).

Of the 25 analyses (after exclusion of SP19-5), five spots (i.e. SP19-3, SP19-4, SP19-7, SP19-8 & SP19-18 which fall outside the cluster range on Fig. 7.4) yielded inherited $^{206}Pb/^{238}U$ ages ranging from 557-599 Ma. They have uranium (U) concentrations and Th/U ratios ranging between 264-339 ppm (avg. 288 ppm) and 0.09-0.25 (avg. 0.15) respectively. These ages are interpreted as inherited because the Malmesbury Group metasedimentary rocks contain detrital zircons with apparent spot ages as young as 560 Ma (Armstrong et al., 1998). Therefore any $^{206}Pb/^{238}U$ age, in Table 7.1, that exceeds or is within an error of this age is classified as inherited. The same reasoning applies for zircons of samples SP33 (Table 7.2) and SP43A (Table 7.3).

The remaining 20 analyses have U concentrations and Th/U ratios varying from 196-858 ppm (avg. = 419 ppm) and 0.04-0.29 (avg. 0.11; with 9 analyses having a Th/ U ratio < 0.1) respectively. Their $^{206}Pb/^{238}U$ ages vary from 528-555 Ma. They yield a weighted mean

$^{206}Pb/^{238}U$ age of 540.7 ± 3.8 Ma (MSWD = 3.6; Fig. 7.4). This age is taken as the crystallisation age of the microgranite.

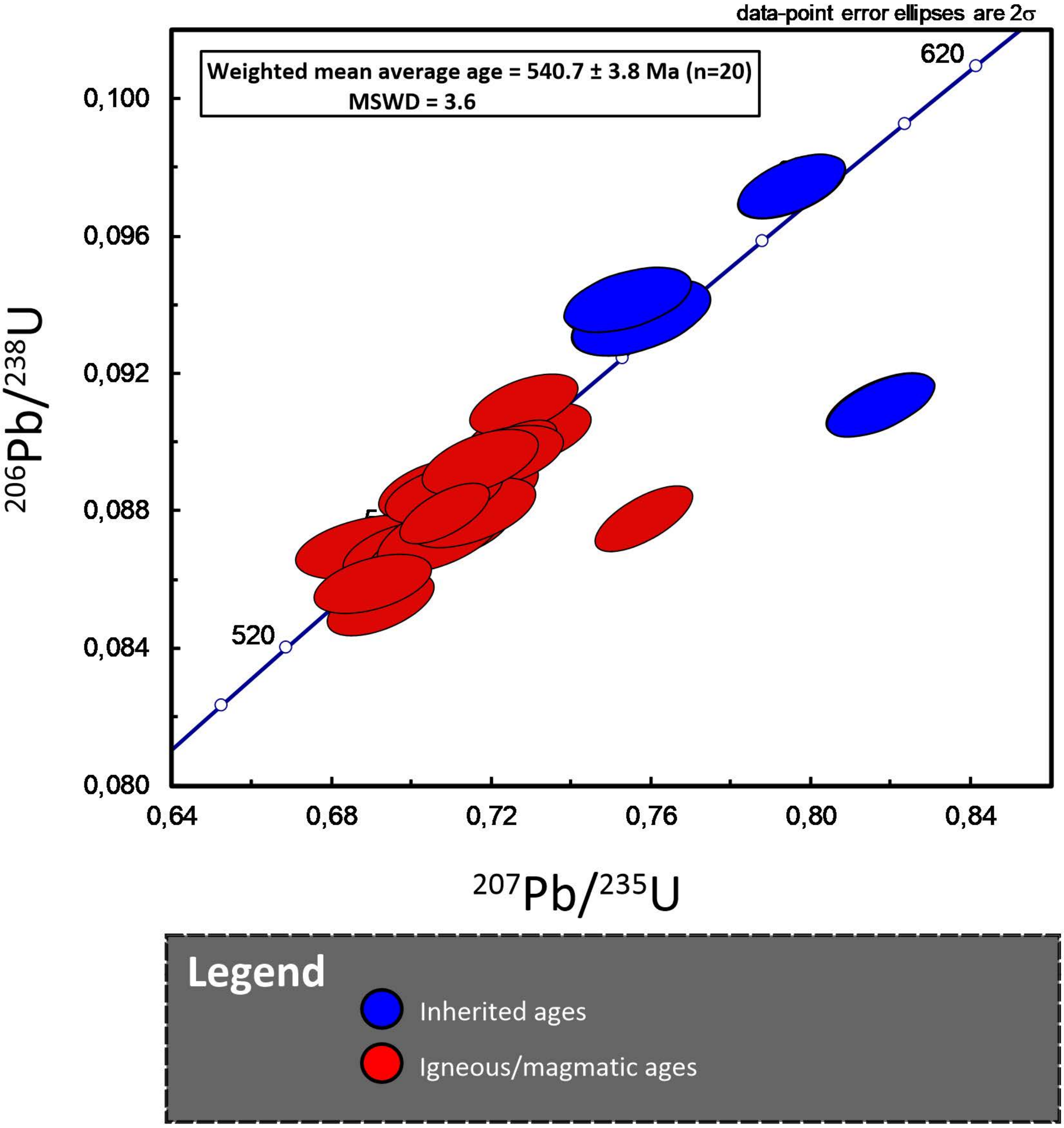

***Figure 7.4**: U-Pb concordia diagram of inherited and igneous ages of zircon grains from sample SP19. Data-point error ellipses are plotted at 2σ. The reported mean weighted average age is for igneous ages. Legend applies to all U-Pb concordia diagrams plotted in section 7.3.*

__Table 7.1:__ LA-ICP-MS U-Pb geochronological data for zircons of sample SP19

				Data for Wetherill plot [a]					**Dates (Ma)**						**Concordance (%)** [b]
	^{206}Pb meas. (CPS)	U (ppm)[c]	Th/U	^{207}Pb/^{235}U	2 s	^{206}Pb/^{238}U	2 s	rho	^{207}Pb/^{206}Pb	2 s	^{206}Pb/^{238}U	2 s	^{207}Pb/^{235}U	2 s	
Samples															
SP19 - 1	252000	539	0.04	0.695	0.008	0.0870	0.0006	0.62	525	25	538	4	536	5	100
SP19 - 2	149600	327	0.08	0.689	0.015	0.0870	0.0008	0.41	507	46	538	5	532	9	101
SP19 - 3	**142000**	**285**	**0.13**	**0.757**	**0.014**	**0.0936**	**0.0009**	**0.51**	**556**	**41**	**577**	**5**	**572**	**8**	**101**
SP19 - 4	**144100**	**273**	**0.11**	**0.795**	**0.011**	**0.0975**	**0.0007**	**0.55**	**569**	**31**	**599**	**4**	**594**	**6**	**101**
SP19 - 5	**325000**	**677**	**0.07**	**0.817**	**0.011**	**0.0911**	**0.0008**	**0.61**	**773**	**27**	**562**	**4**	**606**	**6**	**93**
SP19 - 6	395000	858	0.10	0.692	0.008	0.0857	0.0006	0.65	550	24	530	4	534	5	99
SP19 - 7	**134900**	**281**	**0.25**	**0.729**	**0.013**	**0.0902**	**0.0008**	**0.49**	**553**	**37**	**557**	**5**	**556**	**8**	**100**
SP19 - 8	**133000**	**264**	**0.17**	**0.754**	**0.013**	**0.0941**	**0.0008**	**0.47**	**534**	**41**	**580**	**5**	**571**	**7**	**102**
SP19 - 9	154600	321	0.09	0.705	0.011	0.0887	0.0007	0.52	527	33	548	4	542	7	101
SP19 - 10	236800	520	0.08	0.692	0.010	0.0854	0.0007	0.58	551	30	528	4	534	6	99
SP19 - 11	186300	397	0.09	0.758	0.010	0.0878	0.0008	0.68	692	31	543	5	573	6	95
SP19 - 12	161100	343	0.11	0.695	0.010	0.0869	0.0007	0.54	529	33	537	4	536	6	100
SP19 - 13	233000	493	0.08	0.714	0.009	0.0874	0.0006	0.58	574	26	540	4	547	5	99
SP19 - 14	198300	423	0.07	0.717	0.012	0.0886	0.0008	0.53	554	37	547	5	549	7	100
SP19 - 15	128900	268	0.29	0.713	0.011	0.0881	0.0007	0.51	549	35	544	4	547	6	100
SP19 - 16	226900	481	0.09	0.699	0.009	0.0867	0.0007	0.58	543	26	536	4	538	5	100
SP19 - 17	264500	581	0.05	0.707	0.013	0.0873	0.0009	0.55	556	37	540	5	543	8	99
SP19 - 18	**166400**	**339**	**0.09**	**0.728**	**0.011**	**0.0911**	**0.0007**	**0.53**	**528**	**33**	**562**	**4**	**555**	**6**	**101**
SP19 - 19	287000	597	0.21	0.725	0.009	0.0898	0.0007	0.60	549	26	555	4	554	5	100
SP19 - 21	95300	196	0.15	0.722	0.013	0.0896	0.0008	0.47	560	37	553	4	552	8	100
SP19 - 22	189000	409	0.12	0.715	0.013	0.0880	0.0008	0.53	557	36	544	5	548	8	99
SP19 - 23	151700	325	0.13	0.692	0.011	0.0853	0.0007	0.55	556	34	528	4	534	7	99
SP19 - 24	134100	289	0.12	0.690	0.012	0.0859	0.0007	0.47	534	35	531	4	533	7	100
SP19 - 25	123700	259	0.07	0.708	0.012	0.0885	0.0007	0.48	529	36	547	4	544	7	101
SP19 - 26	147500	301	0.10	0.717	0.012	0.0895	0.0008	0.52	535	37	552	5	549	7	101
SP19 - 27	212100	454	0.11	0.708	0.009	0.0880	0.0007	0.64	545	30	543	4	544	5	100

Samples in bold represent analyses not used in igneous age regressions. **a**: Data not corrected for common Pb; **b**: Concordance calculated as: (^{206}Pb-^{238}U date/^{207}Pb-^{235}U date)*100 and (^{206}Pb-^{238}U date/^{207}Pb-^{206}Pb date)*100. **c**: estimated by comparison with GJ1 zircon reference material.

Table 7.2: *LA-ICP-MS U-Pb geochronological data for zircons of sample SP33*

				Data for Wetherill plot [a]					**Dates (Ma)**						**Concordance (%)** [b]
	^{206}Pb meas. (CPS)	U (ppm)[c]	Th/U	^{207}Pb/^{235}U	2 s	^{206}Pb/^{238}U	2 s	rho	^{207}Pb/^{206}Pb	2 s	^{206}Pb/^{238}U	2 s	^{207}Pb/^{235}U	2 s	
Samples															
SP33 - 1	**247700**	**491**	**0.08**	**0.805**	**0.019**	**0.0967**	**0.0012**	**0.53**	**618**	**43**	**595**	**7**	**600**	**11**	**99**
SP33 - 2	120500	247	0.08	0.712	0.011	0.0891	0.0008	0.55	529	37	550	4	546	7	101
SP33 - 3	176000	363	0.13	0.713	0.010	0.0893	0.0007	0.57	532	33	551	4	547	6	101
SP33 - 4	310000	666	0.07	0.693	0.009	0.0854	0.0007	0.61	559	28	528	4	535	5	99
SP33 - 5	**355200**	**681**	**0.13**	**0.929**	**0.019**	**0.1004**	**0.0012**	**0.58**	**844**	**40**	**617**	**7**	**667**	**10**	**92**
SP33 - 6	378300	797	0.11	0.696	0.007	0.0863	0.0006	0.75	548	21	533	4	536	4	99
SP33 - 7	310500	664	0.02	0.680	0.007	0.0843	0.0006	0.69	547	21	522	4	527	4	99
SP33 - 8	118300	236	0.10	0.700	0.012	0.0883	0.0007	0.47	518	38	546	4	539	7	101
SP33 - 9	217200	439	0.11	0.713	0.009	0.0891	0.0007	0.58	531	28	550	4	547	5	101
SP33 - 10	137600	290	0.10	0.689	0.011	0.0860	0.0007	0.50	532	35	532	4	532	7	100
SP33 - 11	162700	332	0.11	0.704	0.009	0.0877	0.0006	0.55	538	31	542	4	541	5	100
SP33 - 12	125400	265	0.19	0.691	0.011	0.0858	0.0007	0.51	549	37	531	4	533	7	100
SP33 - 13	87100	188	0.43	0.696	0.014	0.0852	0.0008	0.45	582	48	527	5	536	8	98
SP33 - 14	112800	234	0.09	0.704	0.012	0.0881	0.0007	0.45	527	35	544	4	541	7	101
SP33 - 15	156300	327	0.05	0.709	0.011	0.0873	0.0007	0.50	565	33	539	4	544	7	99
SP33 - 16	164500	352	0.32	0.706	0.013	0.0878	0.0008	0.51	549	41	543	5	542	8	100
SP33 - 17	160000	337	0.01	0.716	0.014	0.0889	0.0009	0.52	541	41	549	5	548	8	100
SP33 - 18	**52200**	**73**	**0.12**	**1.250**	**0.035**	**0.1338**	**0.0016**	**0.43**	**866**	**58**	**810**	**9**	**823**	**16**	**98**
SP33 - 19	237700	500	0.12	0.689	0.008	0.0867	0.0007	0.62	514	27	536	4	532	5	101
SP33 - 20	184700	384	0.07	0.711	0.009	0.0875	0.0006	0.61	567	27	541	4	546	5	99
SP33 - 21	150900	306	0.07	0.710	0.010	0.0882	0.0007	0.58	541	30	545	4	545	6	100
SP33 - 22	208400	448	0.01	0.698	0.010	0.0860	0.0007	0.57	562	33	532	4	538	6	99
SP33 - 23	198300	411	0.09	0.693	0.009	0.0868	0.0006	0.56	528	28	537	4	535	5	100
SP33 - 24	117900	252	0.09	0.718	0.016	0.0887	0.0009	0.46	560	48	548	5	549	9	100
SP33 - 25	213800	462	0.15	0.703	0.012	0.0865	0.0008	0.53	552	37	535	5	541	7	99
SP33 - 26	132200	278	0.07	0.696	0.010	0.0866	0.0007	0.52	547	33	535	4	536	6	100

Samples in bold represent analyses not used in igneous age regressions. **a**: Data not corrected for common Pb; **b**: Concordance calculated as: (^{206}Pb-^{238}U date/^{207}Pb-^{235}U date)*100 and (^{206}Pb-^{238}U date/^{207}Pb-^{206}Pb date)*100. **c**: estimated by comparison with GJ1 zircon reference material.

***Table 7.3:** LA-ICP-MS U-Pb geochronological data for zircons of sample SP43A*

				Data for Wetherill plot[a]					**Dates (Ma)**						**Concordance (%)**[b]
	^{206}Pb meas. (CPS)	U (ppm)[c]	Th/U	^{207}Pb/^{235}U	2 s	^{206}Pb/^{238}U	2 s	rho	^{207}Pb/^{206}Pb	2 s	^{206}Pb/^{238}U	2 s	^{207}Pb/^{235}U	2 s	
Samples															
SP43A - 1	150400	313	0.07	0.724	0.012	0.0894	0.0008	0.57	552	37	552	5	553	7	100
SP43A - 2	135200	287	0.09	0.707	0.012	0.0881	0.0008	0.53	532	37	544	5	543	7	100
SP43A - 3	107400	221	0.11	0.720	0.013	0.0898	0.0008	0.52	534	38	554	5	551	8	101
SP43A - 4	**168800**	**352**	**0.05**	**0.738**	**0.013**	**0.0902**	**0.0009**	**0.56**	**575**	**35**	**557**	**5**	**561**	**8**	**99**
SP43A - 5	177100	370	0.08	0.717	0.013	0.0891	0.0009	0.53	541	38	550	5	549	8	100
SP43A - 6	128700	276	0.09	0.709	0.014	0.0870	0.0008	0.45	567	44	538	5	544	8	99
SP43A - 7	190000	410	0.15	0.715	0.011	0.0883	0.0007	0.52	553	34	546	4	548	6	100
SP43A - 8	145300	313	0.10	0.678	0.010	0.0845	0.0007	0.58	541	34	523	4	525	6	99
SP43A - 9	202400	424	0.07	0.711	0.010	0.0887	0.0007	0.58	535	30	548	4	545	6	100
SP43A - 10	120700	257	0.09	0.712	0.014	0.0888	0.0008	0.47	549	41	548	5	546	8	100
SP43A - 11	170100	347	0.09	0.710	0.009	0.0887	0.0007	0.57	530	29	548	4	545	5	101
SP43A - 12	113900	237	0.06	0.705	0.011	0.0878	0.0007	0.50	543	35	543	4	542	7	100
SP43A - 13	171300	361	0.09	0.702	0.009	0.0872	0.0006	0.57	538	29	539	4	540	5	100
SP43A - 14	91500	188	0.19	0.726	0.014	0.0910	0.0009	0.51	526	42	561	5	554	8	101
SP43A - 15	309000	647	0.07	0.710	0.009	0.0879	0.0007	0.63	554	26	543	4	545	5	100
SP43A - 17	138300	287	0.10	0.702	0.010	0.0883	0.0007	0.53	522	33	545	4	540	6	101
SP43A - 18	**292100**	**604**	**0.08**	**0.707**	**0.008**	**0.0879**	**0.0007**	**0.67**	**545**	**23**	**543**	**4**	**543**	**5**	**100**
SP43A - 19	157800	326	0.07	0.710	0.010	0.0886	0.0007	0.55	540	32	547	4	545	6	100
SP43A - 20	169100	366	0.06	0.712	0.013	0.0880	0.0008	0.50	549	37	544	5	546	8	100
SP43A - 21	205400	430	0.08	0.707	0.009	0.0874	0.0007	0.62	556	28	540	4	543	5	100
SP43A - 22	142900	300	0.08	0.701	0.010	0.0871	0.0007	0.55	544	34	539	4	539	6	100
SP43A - 23	258000	551	0.03	0.705	0.009	0.0877	0.0007	0.61	548	28	542	4	542	5	100
SP43A - 24	199000	425	0.11	0.698	0.010	0.0873	0.0007	0.57	528	30	539	4	537	6	100
SP43A - 25	138400	295	0.13	0.700	0.013	0.0880	0.0008	0.46	515	42	544	5	539	8	101
SP43A - 26	192500	420	0.11	0.694	0.012	0.0856	0.0008	0.53	559	34	529	5	535	7	99

Samples in bold represent analyses not used in igneous age regressions. **a**: Data not corrected for common Pb; **b**: Concordance calculated as: (^{206}Pb-^{238}U date/^{207}Pb-^{235}U date)*100 and (^{206}Pb–^{238}U date/^{207}Pb-^{206}Pb date)*100. **c**: estimated by comparison with GJ1 zircon reference material.

7.3.2 Fine-grained porphyritic hybrid granite (Sample SP33)

A total of 26 U-Th-Pb analyses on zircon grains from sample SP33 were done (Table 7.2). All of the analyses, except for one (i.e. spot SP33-5; Fig. 7.1E, Table 7.2), passed the <5% discordancy filter test. All the analyses (both concordant and discordant) are plotted on a concordia diagram (Fig. 7.5) where they define a relatively large spread of ages. The majority of the analyses show a tight grouping of ages from 530-550 Ma (Fig. 7.5B), with the outlier analyses spread out over a wide age range from 600-800 Ma (Fig. 7.5A). Out of the remaining 25 analyses (after the exclusion of spot SP33-5), two spots, SP33-1 and SP33-18 (outlier analyses on Fig. 7.5A) yield inherited ages varying from 595-810 Ma. Spots SP33-1 and SP33-18 have U concentrations and Th/U ratios between 73-285 ppm and 0.08-0.12, respectively.

The remaining 23 analyses have U concentrations and Th/U ratios varying from 188-797 ppm (avg. 382 ppm; a lower U avg. compared to the non-inherited zircon grains in the microgranite), and 0.01-0.43 (avg. 0.11; comparable with the Th/U ratio of the microgranite). They yield a weighted mean $^{206}Pb/^{238}U$ age of 538.7 ± 3.6 Ma (MSWD = 4; Fig. 7.5A), interpreted to be the crystallization/emplacement age.

7.3.3 Coarse-grained porphyritic hybrid granite (Sample SP43-A)

A total of 25 U-Th-Pb analyses on zircon grains from sample SP43A were done (Table 7.3). All of the zircon analyses from sample SP43A (discordancy between 99-101%) pass the <5% concordancy test. The resulting analyses are plotted on a concordia diagram, where they define a fairly narrow spread when compared to samples SP19 and SP33, varying between 520-570 Ma. The majority of the analysis form a tight cluster at ages 530-555 Ma and there are two outlier sets, one with a set of analyses with ages of less than 530 Ma and the other with a set of analyses greater than or approximately equal to 560 Ma (Fig. 7.6). Out of the 25 analyses, two spots from the cores of SP43A-4 and SP43A-14 yield inherited ages. These two inherited spots have $^{206}Pb/^{238}U$ ages ranging from 557-561 Ma, with U concentrations and Th/U ratios between 188-352 ppm and 0.05-0.12 respectively.

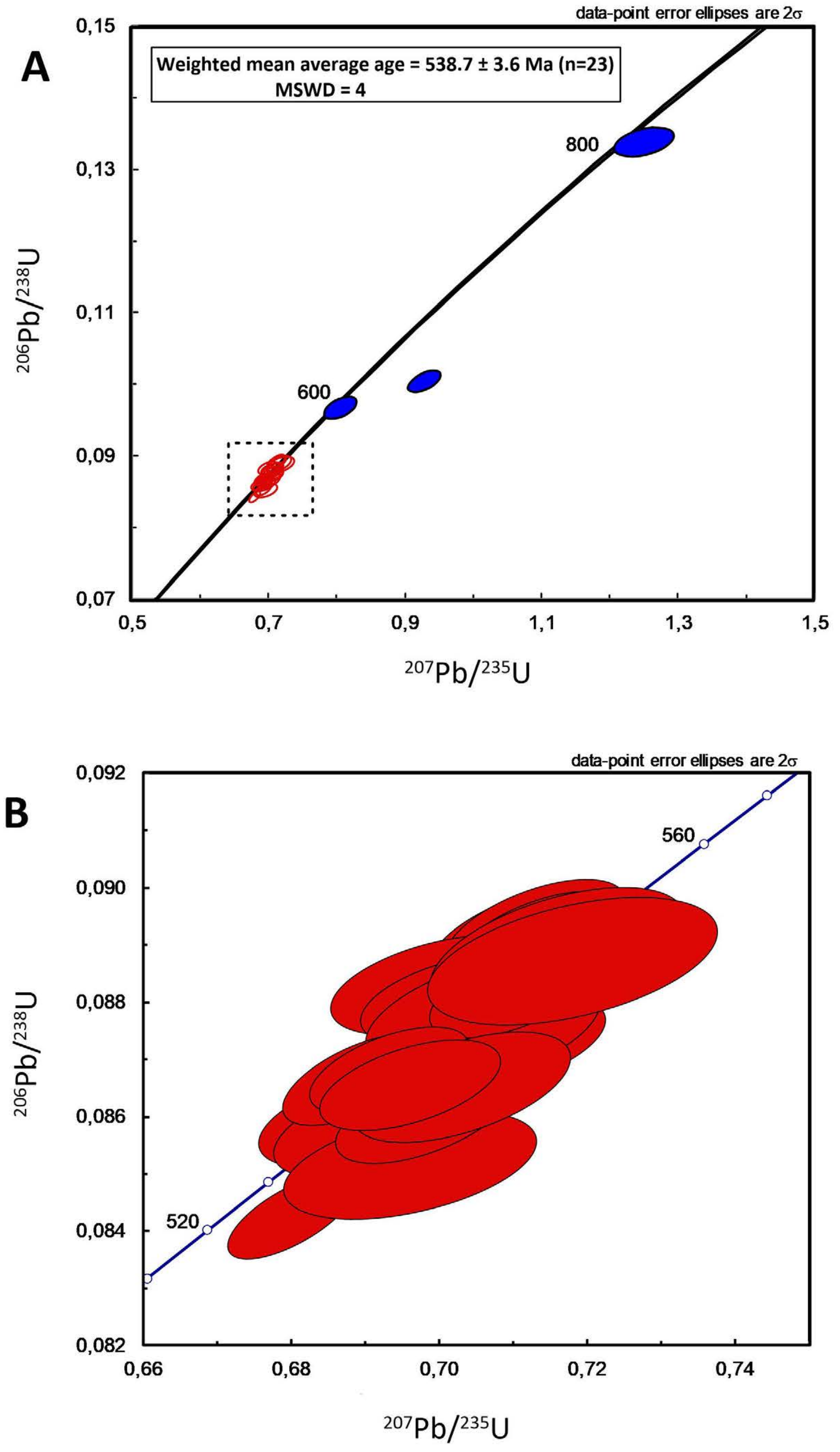

***Figure 7.5**: (A) U-Pb concordia diagram of inherited and igneous ages of zircon grains from sample SP33. (B) A separate U-Pb concordia diagram zoomed in on all the concordant spots demarcated by a dashed rectangle in (A). Data-point error ellipses are plotted at 2σ. The reported mean weighted average age in (A) is for igneous ages.*

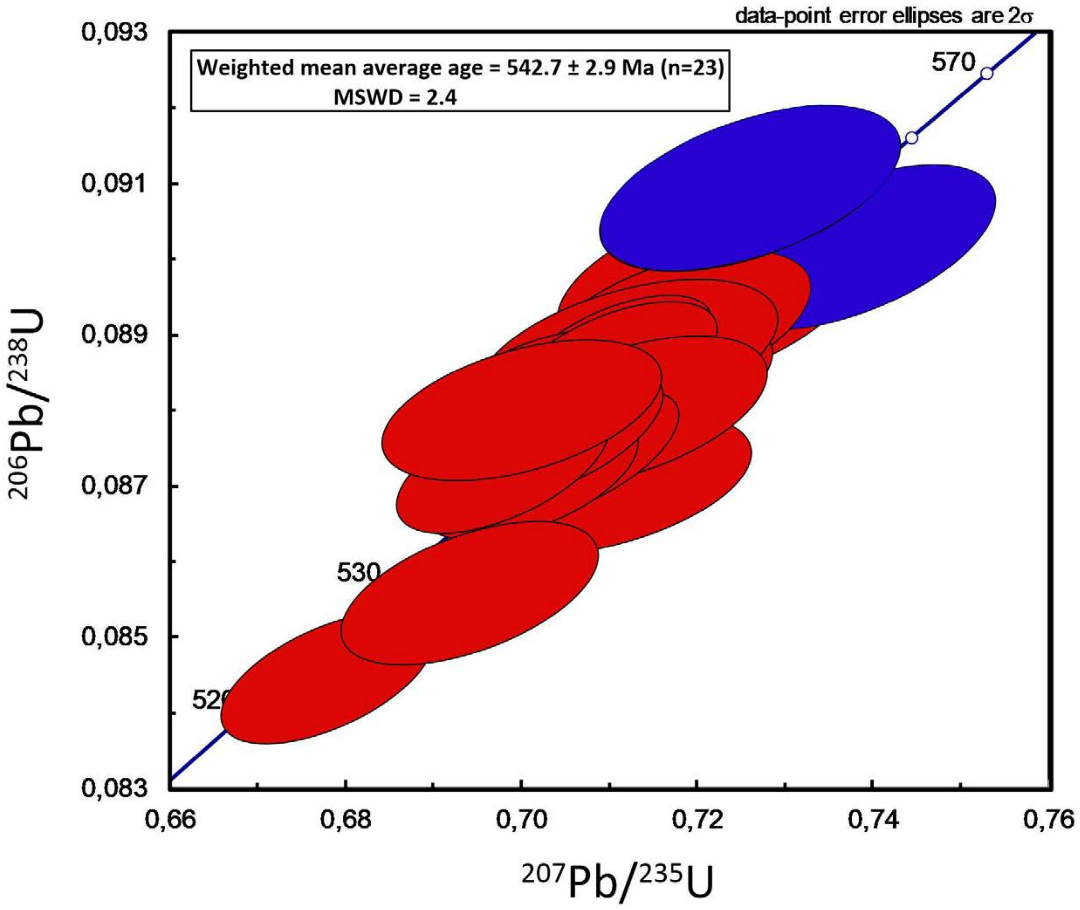

Figure 7.6*: U-Pb concordia diagram of inherited and igneous ages of zircon grains from sample SP43A. Data-point error ellipses are plotted at 2σ. The reported mean weighted average age is for igneous ages.*

The remaining 23 analyses, with non-inherited characteristics, have U concentrations varying from 237-647 ppm (avg. 368 ppm; lower avg. U concentrations than the non-inherited zircon grains in both the microgranite and fine-grained porphyritic hybrid phase). They have Th/U ratios between 0.03-0.15 (avg. 0.09; lower avg. Th/U compared to the zircon grains in both the microgranite and fine-grained porphyritic hybrid phase). The 23 analyses yield a weighted mean ^{206}Pb/^{238}U age of 542.7 ± 2.9 Ma (MSWD = 2.4; Fig. 7.6), interpreted to be the crystallization/emplacement age.

8 Discussion

8.1 Geochemistry of the S-type granites

8.1.1 Introduction

Peraluminous S-type granitic rocks, such as the granites of the Peninsula Pluton, typically display a wide compositional range (Collins, 1996; Chappell et al., 2000; Stevens et al., 2007; Villaros, 2010). They are interpreted to have been formed by the partial melting of aluminous clastic sedimentary sources in the continental crust such as metapelites or metaspsamites (Chappell & White, 1974; Clemens & Benn, 2010). The temperature and nature of melting depend on the composition of the source rock, the H_2O content, and the particular pressure-temperature-time (*P*-*T*-*t*) path of that portion of the crust (Brown, 2013). The peraluminous, S-type granites of the CGS are interpreted to be the products of incongruent fluid-absent melting of biotite in a metasedimentary source near the base of the crust (Stevens et al., 2007; Villaros et al., 2009b).

The nature of partial melting reactions involved in the genesis of such granites, under fluid absent conditions at 800°C or above, is well known, through experimental studies of metasediment and migmatite sources (e.g. Sawyer, 1991; Montel & Vielzuf, 1997; Brown, 2001; Johnson et al., 2001; Clemens, 2003; Stevens et al., 2007). The reactions generally involve the breakdown of biotite in the presence of quartz and feldspar to form solid peritectic mineral phases (e.g. Villaros, 2010):

1. Bt + Qtz + Pl + Sil = melt + Grt + Ilm ± Kfs: in metapelites
2. Bt + Qtz + Pl = melt + Grt + Opx + Ilm ± Kfs: in metapsammites

The composition of the melt produced (by the reactions) is often difficult to analyse due to its rare occurrence in natural rocks (i.e. the melt often occurs as inclusions in minerals) (Maas et al., 2001). As a result, experimental studies are needed to determine the composition of the melt produced. According to the experimental melt studies of metasediment sources (undertaken by the various authors as previously mentioned), the melt produced from any sediment composition is leucocratic, a finding corroborated by Stevens et al. (2007) during their investigation of the origin of the major element geochemical diversity in the S-type CGS using appropriate experimental melt compositions.

As is well known, granites of the upper crust (which range from leucogranitic to granodioritic) tend to show a substantial variation in major and trace element contents over various scales ranging from centimetres to hundreds of meters (Garcia-Arias, 2018). This observation contradicts experimental melt studies which predict strictly leucocratic compositions for these rock types. This has led to many different processes/mechanisms being proposed to account for the substantial geochemical variation exhibited by S-type granites which are discussed extensively by Clemens and Stevens (2012). Some of them include:

(i) Source inheritance models: (a) restite unmixing (White & Chappel, 1977) and (b) peritectic assemblage entrainment (e.g. Stevens et al., 2007; Clemens et al., 2011; Clemens & Stevens et al., 2012)
(ii) Magma mixing (e.g. Collins, 1996; Barbarin, 2005)
(iii) Fractional crystallization (e.g. Breaks & Moore, 1992; Foden et al., 2002)
(iv) Crustal contamination (i.e. assimilation) (e.g. Jung et al., 1999; Clarke & Carruzo, 2007).

The petrogenetic model of the S-type granites of the CGS as well as their likely source has already been established through the findings and contributions of various authors (e.g. Harris et al., 1997; Stevens et al., 2007; Villaros et al., 2009a, b; Villaros, 2010; Harris & Vogeli, 2010). Therefore, for this study, only processes of geochemical variation at a localized scale (i.e. applicable to the Sea Point contact) will be described. These were identified mostly through outcrop evidence and include the fractional crystallization of K-feldspar, crustal assimilation of the granite by the country rock (also considered an emplacement mechanism) and filter pressing. Certain geochemical trends presented in chapter 6 support the main process for geochemical variation in the S-type granites of the CGS, i.e. the co−entrainment of peritectic and accessory phases (Stevens et al., 2007; Villaros et al., 2009a), having occurred in the study area. These trends will, however, only be briefly described as they will not contribute to the entrainment model overall nor will they add anything to what is already known.

8.1.2 Source characterization

The likely source for the S-type granites of the CGS pluton is considered to be a high-grade equivalent of the Malmesbury Group metasediments (e.g. Harris et al., 1997; Stevens et al., 2007; Harris & Vogeli, 2010). This is because oxygen isotope compositions of garnet in the S-type Peninsula Pluton are consistent with the partial melting of a metapelitic source with an oxygen isotope composition similar to that of the Malmesbury Group exposed on the surface (Harris & Vogeli, 2010).

ε_{Ndt} and initial Sr values (Tables 6.5, 6.6) are plotted against each other, along with the positions of the various mantle and continental isotopic reservoirs, for the discrimination of likely sources for the granites of the study area (Fig. 8.1). The granite phases all plot close to the trend that delineates an upper-crust reservoir giving further proof of a crustal origin for the granites. This is because their initial Sr ratios are greater than 0.706 (they vary between 0.7171350 – 0.739350) and their ε_{Ndt} values are negative (varying between -5.75 and -8.04); these values indicate that the granites were derived from a crustal source that was enriched over time (Rollinson, 1993). Samples SP38 and SP3 (micrograinites) have large uncertainties for the initial Sr and ε_{Ndt} values respectively (Fig. 8.1). Their values are, therefore, not reliable. The more appropriate and representative range would be 0.717350 – 0.722582 for the initial Sr and -5.75 to -4.75 for ε_{Ndt}. These values are from samples SP7, SP33 and SP43A which yield smaller uncertainties.

The granites show enrichments in Th, U, P, Cs, Rb and K, and are typified by depletions in Sr, Ba, Hf, Zr, Nb and Ti relative to the average crust (Fig. 6.5B). All of these trends suggest that the crustal source of the granite melts was radiogenic (as suggested by enrichments in the radioactive elements of Th and U) and fairly feldspathic (as suggested by enrichments in Cs, Rb and K). Depletions in Sr and Ba can be explained by the fractionation of plagioclase and/or retention of plagioclase in the source area during melting (Rollinson, 1993). Nb and Ti partition into Ti-rich phases (e.g. titanite, titanomagnetite, rutile and ilmenite), P into apatite and Zr and Hf into zircon (Winter, 2010). Thus the depletion of these elements suggests the retention of such phases in the source region or accumulation in restite.

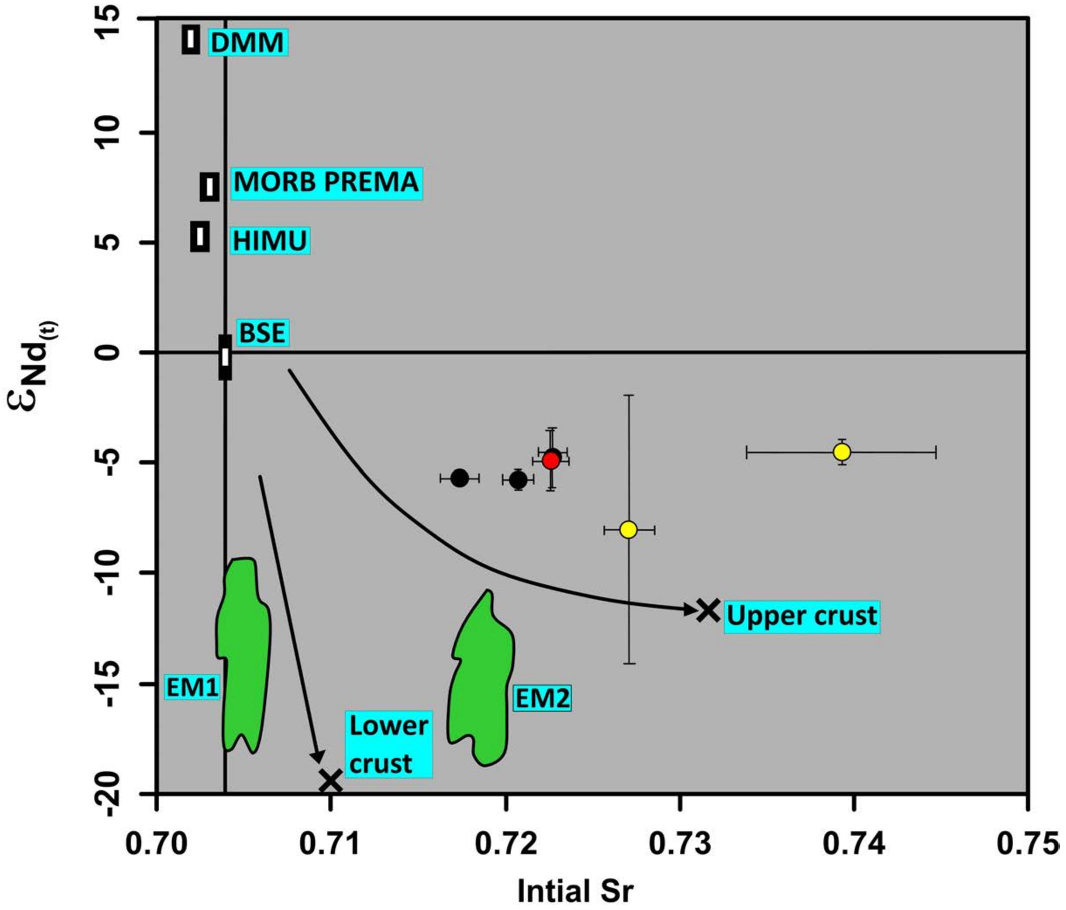

Figure 8.1: *$\varepsilon_{Nd(t)}$ vs. initial Sr [($^{87}Sr/^{86}Sr)_I$]; yellow circles: micrograntes, red circle: main phase granite and black circles: hybrid granites. The upper crust curve (Harris et al., 1986) and a theoretical lower crustal curve (Othman et al., 1984) are indicated for reference along with the positions of the main oceanic mantle reservoirs of Zindler and Hart (1986) which are: BSE = bulk silicate earth, EMI and EMII = enriched mantle I and II, HIMU= high mantle U/Pb ratio, PREMA = frequently observed prevalent mantle composition. The mantle source of MORB (mid-oceanic ridge basalts) and the mantle end-members DMM (depleted end member MORB-mantle component) and PREMA are from Zindler and Hart (1986). Error bars for $\varepsilon_{Nd(t)}$ are plotted for the two hybrid granites furthest left but are all smaller than the plot symbols.*

8.1.3 Mechanisms/processes for geochemical variation

8.1.3.1 Co−entrainment of peritectic and accessory phases

The consensus by Stevens et al. (2007) and Villaros et al. (2009a) is that the chemical variability shown by the granites of the CGS is inherited from the source. The granites of the study area, which themselves exhibit a wide range of compositions (i.e. ranging from fine-grained leucocratic to coarse-grained porphyritic), match some of the geochemical trends cited to be the evidence behind the co-entrainment peritectic model. Simplified evidence for the model is as follows:

(i) An increase in the Al, Ca, Ti, P, Mg# and A/CNK values as a function of increasing maficity (Fig. 6.2A–F).

These major elements are concentrated or occur predominantly in the phases forming part of the peritectic assemblage (following the breakdown of biotite).

The positive trends are interpreted to indicate the increase in maficity of the magma due to the entrainment of Fe- and Mg-rich peritectic phases such as garnet, cordierite and/or orthopyroxene (Stevens et al., 2007; Clemens & Stevens, 2012). The increase in Ti and Ca, as a function of maficity, is as a consequence of the presence of ilmenite and plagioclase respectively (Stevens et al., 2007; Garcia-Arias, 2018). For the S-type granitic rocks of the CGS, the magma entrained the peritectic assemblage in proportions that range from 0 (pure melts; leucogranites) to approximately 30 mol. % (granodiorites) (Stevens et al., 2007).

(ii) A decrease in the Si, K and Na values with increasing maficity (Fig. 6.2G–I). These major elements are concentrated in the minerals/phases that are the major reactants in the partial melting reactions. The entrainment of the peritectic mineral assemblage dilutes those elements present mainly in the melt (Si, K, Na) and enriches the magma in those elements present mainly in the mineral assemblage (Fe, Mg, Ti, Ca), producing the observed compositional trends (i.e. negative correlations) (Garcia-Arias & Stevens, 2017) as seen in Figure 6.2G-I.

(iii) The less defined to poor positive trends shown by Rb, Sr, Ba and Eu as a function of maficity (Fig. 6.4). These trace elements are also concentrated in the mineral phases that are reactants in partial melting reactions (Villaros et al., 2009a). The variations/scatter shown by these elements reflects (a) the variations in source mineralogy and trace element composition, and (b) is as a consequence of the consumption of the reactant phases to form the melt or magma.

(iv) The well-defined positive linear trends shown by the LREE (Fig. 6.3A-C) and the HFSE (Fig. 6.3D-E) as a function of increasing maficity. Monazite primarily concentrates LREE whereas zircon concentrates HFSE (as well as the REE of Y and Yb) into its structure (Villaros et al., 2009a). In addition to their small crystal sizes and their availability at the sites of melting, Villaros et al. (2009a) concluded that the positive linear trends shown by the HFSE and LREE as a function of increasing maficity reflect the co-entrainment of zircon and monazite along with the peritectic mineral assemblage. In essence, the low REE and HFSE compositions of the leucogranites mean their melts left the source with variable proportions of entrained peritectic phases (close to zero percent) but before the melt has dissolved any zircon and monazite accessory minerals (Villaros et al., 2009a).

8.1.3.2 Fractional crystallization

For the granites phases of the study area, the observed well-defined linear negative trend of FeOt, TiO_2, MgO, P_2O_5 and CaO with increasing silica content (Fig. E1A, B, C, E, F; Appendix E) could be indicative of the crystallisation of plagioclase (concentrates Ca), biotite (concentrates Fe, Ti and Mg depending on the type of biotite) and accessory apatite (concentrates P) from a parental magma. The variation of Na_2O and K_2O relative to SiO_2 show a larger scatter (Fig. E1G, H). They instead show a better trend when modelled against maficity (Fig. 6.2H, I). Against maficity, they show weak negative trends. Other than the reason given in section 8.1.3.1, the weak trends could be because these two elements are associated with alkali-feldspar (or K-feldspar) (e.g. Winter, 2010). Therefore, their weak negative trends against maficity, as opposed to the neat positive linear trends shown by Fe, Ti, Al, Ca and Mg (against maficity), suggests a fractionation of alkali feldspar.

Other clues that support the idea of the fractionation of a feldspar mineral can be found from REE and spider plots plotted in Fig. 8.3A and B. On these plots, the granites of the study area are normalized relative to the average trace element composition of the coarse-grained porphyritic granites of the Peninsula Pluton from Farina et al. (2012). Despite belonging to the same pluton, the granites of the study area, apart from, SP18 (main coarse-grained porphyritic granite) and SP33 (fine-grained porphyritic hybrid granite), show positive Eu anomalies [$(Eu/Eu^*)_{Farina}$ = 1.01 – 3.53; Avg. 1.54)] and a moderate enrichment in HREE, particularly for the main coarse-grained porphyritic and hybrid granite phases, relative to the average granite composition from Farina et al. (2012) (Fig. 8.3A). Moreover, the granites of the study area also show slight to moderate enrichments (and positive anomalies) in Sr and K, whereas Ba is enriched for samples SP21, SP6, SP31 and SP35 (medium- and coarse-grained porphyritic hybrid granites) (Fig. 8.3B). All of these observations suggest that feldspar fractionation may have caused some variation in the granites of the study area.

Eu, Rb, Sr and Ba can be used to assess the crystallization of K-feldspar and plagioclase. This is because Ba concentrates strongly in K-feldspar and Sr commonly substitutes for Ca in plagioclase, and, to a lesser extent, for K in K-feldspar (Winter, 2010). Eu^{2+} can substitute for Ca and Sr in plagioclase, whereas Rb behaves similarly to K (due to having the same radius and valence as K) and can thus concentrate in K-feldspar (in place of K) (Winter, 2010). Moreover, Rb, Sr, Ba and Eu are also compatible with regard to the pyroxenes, amphiboles and biotite (Rollinson, 1993; Cao et al., 2018), although to a variable, and mostly lesser extent. Therefore the validity of the linear negative trends of FeOt, TiO_2, MgO, CaO and P_2O_5 with increasing silica content, which is suggestive of the crystallization of biotite, as mentioned previously, can be assessed using Rb, Sr, Ba and Eu. Pyroxenes and amphiboles are not assessed because they are not observed petrographically.

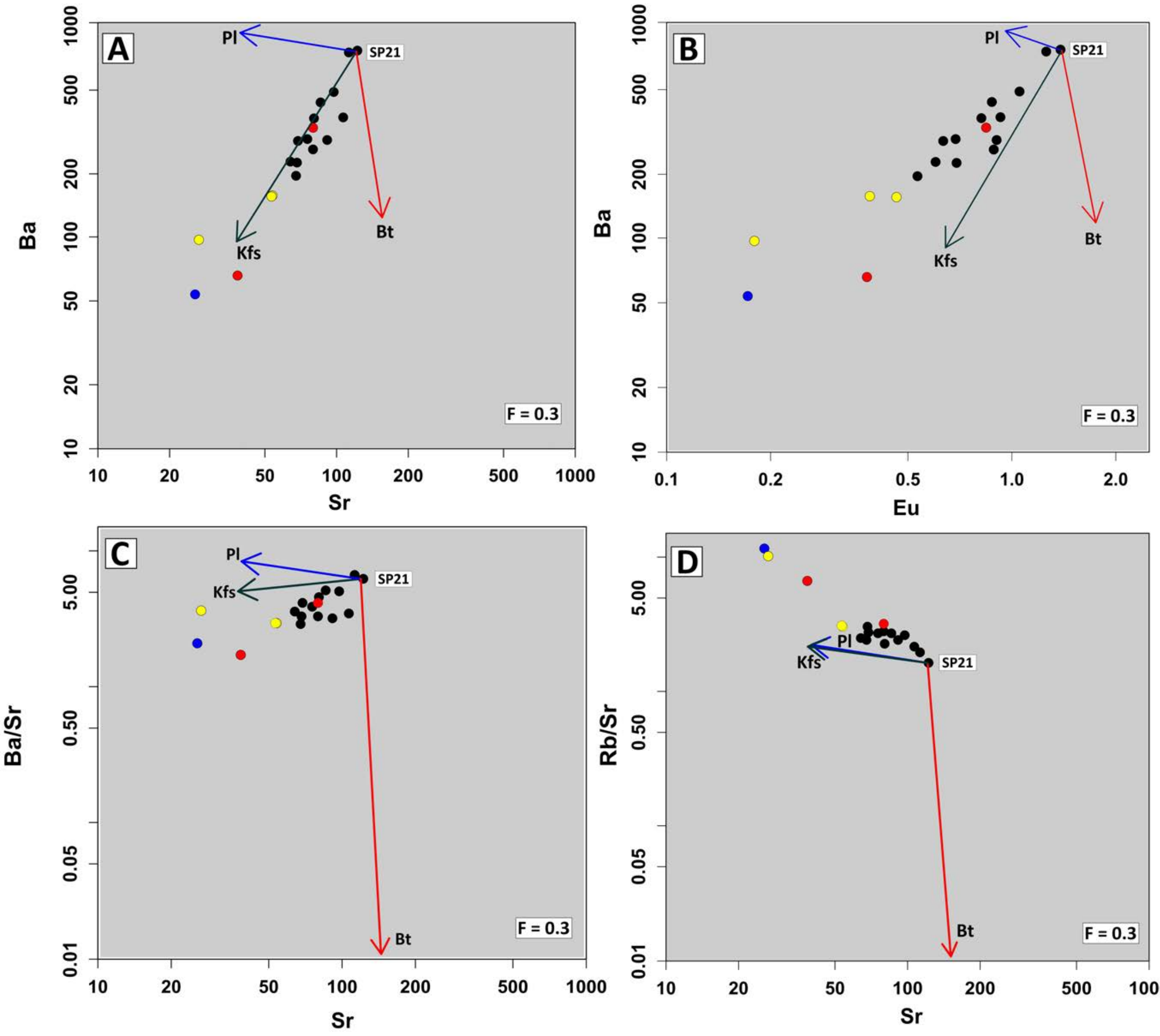

***Figure 8.2**: Binary log-log diagrams of (A) Ba vs. Sr, (B) Ba vs. Eu, (C) Ba/Sr vs. Sr, and (D) Rb/Sr vs. Sr (After Cao et al., 2018) modelled at 30% fractional crystallization. The diagrams illustrate which fractionation trend, K-feldspar (Kfs; green arrow), plagioclase (Pl; blue arrow) and biotite (Bt; red arrow), had the most control in causing geochemical variation in the granites of the study area (yellow circles: microgranites; red circles: main coarse-grained porphyritic granite; black circles: hybrid granites; blue circle: aplite). The assumed parent magma composition is represented by the least fractionated sample in the form of SP21 (a medium-to coarse-grained porphyritic hybrid granite).*

Fractionation vectors plotted on log-log-diagrams of Ba vs. Sr, Ba vs. Eu, Ba/Sr vs. Sr, and Rb/Sr vs. Sr (after Cao et al., 2018) (Fig. 8.2) were used to assess the fractionation of feldspar in the study area. All the fractional crystallization trends are modelled from the assumed parent magma composition represented by the least fractionated sample (i.e. low SiO_2 wt. % and high wt. % MgO & FeOt) in the form of SP21 (a medium- to coarse-grained porphyritic hybrid granite) (Fig. 8.2). The partition coefficients of the various trace elements (i.e. Rb, Sr, Ba and Eu) for a particular major mineral phase (i.e. K-feldspar, plagioclase or biotite) in felsic rocks are from Rollinson (1993).

The diagrams of Ba/Sr vs. Sr, Ba vs. Eu, and Ba/Sr vs. Sr (Fig. 8.2A, B, C) show that the majority of the samples follow the fractionation vector trend for K-feldspar (Kfs) as opposed to plagioclase and biotite, whereas the Rb/Sr vs Sr plot (Fig. 8.2D) cannot clearly distinguish the fraction of K-feldspar from plagioclase (Pl). The diagrams reveal that, in general, the granite phases that have a higher Kfs phenocrystic content, particularly the medium- to coarse-grained porphyritic hybrid phases and one of the main coarse-grained porphyritic granites, progress/evolve towards samples with a low Kfs content (i.e. microgranite and aplite phases). This subsequently proves that the crystallization of Kfs played some role in causing the geochemical variation in the granites of the study area.

The crystallization of Kfs as a control on the geochemical/compositional variation, however, is likely to have been of a secondary role that superimposed itself onto the primary process of peritectic assemblage entrainment (e.g. Clemens, 2010; Clemens et al., 2017). It likely took place at levels close to the emplacement site, causing a secondary compositional trend or variation after the granitic magma entrained ferromagnesian material inherited from a metasedimentary source material. This interpretation implies that the leucocratic compositions or rocks (microgranites and aplites) of the study area should show some geochemical difference that reflects feldspar fractionation relative to other leucocratic compositions/melts that have been interpreted as almost pure anatectic melts. This is confirmed by the positive Eu anomalies and slight to moderate enrichments (and anomalies) in Cs, K and Sr relative to average leucocratic compositions of Farina et al. (2012) (Fig. E2; Appendix E3).

8.1.3.3 Crustal assimilation and filter pressing

Assimilation is the incorporation of chemical components from the host rock to the ascending magma (Clemens & Stevens, 2012). It is a process that forms when magma creates space for itself by melting its way upwards through the host rock during intrusion. In the study area, there are a few outcrop and microscopical textural features that are indicative of the assimilation process:

(i) The common presence of metasedimentary xenoliths. Stoped blocks can become partly disintegrated and assimilated by the intruding magma (Lackey et al., 2006; Clarke, 2007).

(ii) Gradational contacts between the country rock and the hybrid granites in the lit-par-lit zone (Figs. 4.22, 4.23). The contact is primarily gradational because minerals that have a similar size and texture to those occurring in the country rock are incorporated into the granite phases (and vice-versa). This is indicative of an assimilation process to some capacity. For example, the hybrid granites, particularly the medium-grained porphyritic phase, tend to incorporate biotite crystals, similar in size, shape and texture to those found occurring in the country rock (Fig. 4.23B, D). This could also explain why the medium-grained hybrid granites in the lit-par-lit zone show variations in terms of biotite content, with some portions of the granite being biotite-rich, while other portions are relatively biotite-poor. The country rock itself incorporates certain minerals from the surrounding granite. These are interpreted to be from the granite on account of their large sizes. The mineral constituents include phenocrysts of K-feldspar, plagioclase, quartz, and biotite. As a result, certain portions of the country rock in the lit-par-lit zone appear more feldspathic and porphyritic (Fig. 4.22) than the usual appearance of the country rock (e.g. Figs. 4.4, 4.6).

Filter pressing is a mechanism that involves the segregation of melt fractions from a crystal mush (melt plus crystals) during crystallization (e.g. Petford & Koenders, 2003; Weinberg et al., 2015; Berger et al., 2017; Garibaldi et al., 2018). In such a situation, a certain fraction of a melt in a crystal-laden magma can be segregated or forced out by tectonic compression and moved into fractures or other free spaces, leaving the crystals behind. Outcrop evidence suggests that the main contact zone of the study area is consistent with melt accumulation and escape as suggested by the K-feldspar megacrysts embedded or mantled by the country rock (Figs. 4.25; 5.19) (the mechanism of how they became embedded is described later on in the thesis). As granite emplacement in the study area is interpreted to be late-syntectonic (section 8.5), the magma (melt plus crystals) underwent deformation and the melt fraction was more easily mobilized and driven out, compared to the crystal fraction, leaving the K-feldspar megacrysts behind. This process may have affected the composition of the crystallizing granites in the lit-par-lit zone and thus causing a variation in their chemistry.

Multiple tests were done to test for assimilation including:

(i) Plotting REE and spider diagrams to assess any element depletions and enrichments in the granites of the study area relative to the main coarse-grained porphyritic granite from elsewhere in the Peninsula Pluton (e.g. Farina et al., 2012 dataset) and Malmesbury Group metasedimentary rocks of the Tygerberg Formation further away from the contact (e.g. Frimmel et al., 2013 dataset)

(ii) Assessing the Rb-Sr and Sm-Nd isotope data for the granites of the study area

(iii) Plotting diagrams of compatible element vs. silica where both the Malmesbury Group rocks and granites are plotted to assess whether trends off a main "differentiation" trend in the granites toward the Malmesbury Group occurs which may suggest assimilation of the country rock.

For assimilation, none of the tests yielded the desired results to support outcrop evidence of assimilation. On spider plots normalized to the average trace element compositions of coarse-grained granites from Farina et al. (2012) and metasiltstones (ideal country rock composition before contact metamorphism) from Frimmel et al. (2013), slight to moderate enrichments in Ba, K, Sr, Pb, Cs and U (with the latter two enriched relative to the metasiltstone lithologies) might initially suggest an enrichment in crustal material relative to the aforementioned lithologies (Fig. 8.3B, D). This is because the upper crust is felsic (hence enrichments in Cs, Ba, K and Sr which are associated with feldspars) and radiogenic (hence enrichments in U) relative to the lower crust (Petford et al., 2000; Rudnick & Gao, 2003). This, however, is misleading because fractionation will have a far greater effect on compositional variation than limited, localised assimilation induced by thin granite sills as is the case in the study area. The chemical variation seen, therefore, particularly with regard to LILE, is likely due to feldspar fractionation (both plagioclase and alkali) as previously described.

Assimilation of crustal material by a magma can push up the initial Sr ratio and lower the ε_{Ndt} value (e.g. DePaolo, 1981; Janoušek et al., 2016). Because the granites of the CGS are derived by crustal melting the effect is masked by their crustal origin to begin with. Moreover, as previously mentioned in chapter 6, the microgranite has high initial Sr ratios (e.g. 0.739350 yielded by sample SP38) likely due to weathering and, possibly, hydrothermal effects. Although it could be possible that the values may be due to assimilation, the fine-grained nature of the microgranite tends to argue for rapid cooling (upon initial contact with the cold country rock) and little time for assimilation. Lastly, compatible element vs. silica showed no deviation of granites towards compositions of the Malmesbury Group; they are, therefore, not shown.

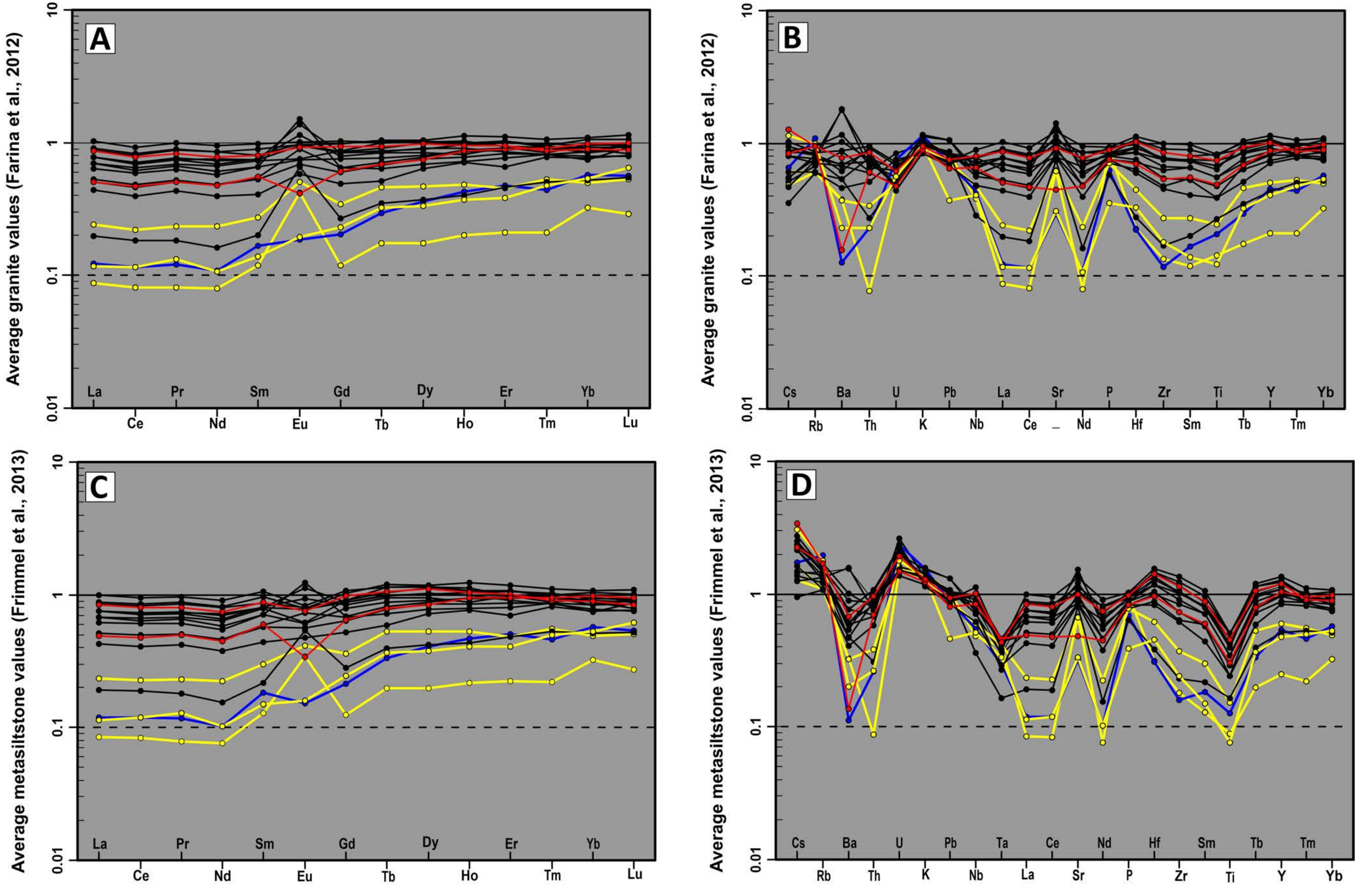

***Figure 8.3**: Rare earth element (A, C) and multi-element spider (B, D) plots for the various granite phases of the study area. (A) and (B) are normalized to the average trace element composition of the main coarse-grained porphyritic granites of the Peninsula Pluton From Farina et al. (2012) and (C) and (D) are normalized to average metasiltstone trace element composition from Frimmel et al. (2013). Black trends: Hybrid granites; red trends: Main coarse-grained porphyritic granites; yellow trends: Microgranites; blue trend: Aplite.*

The filter-pressing mechanism can be assessed, but not necessarily be proven, by use of a Pearce element ratio (PER) diagram first developed by Pearce (1968). PER diagrams are designed to test hypotheses relating to the compositions of samples of a rock suite (Nicholls & Gordon, 1994). In a PER diagram, the numerators are typically an element (or combination of elements) that participate in crystal fractionation of the minerals in the magma, whereas the element or elements in their denominators, must be conserved (i.e. they do not change during the fractionation process in order for the system change to be accurately portrayed) (Nicholls & Russell, 2016).

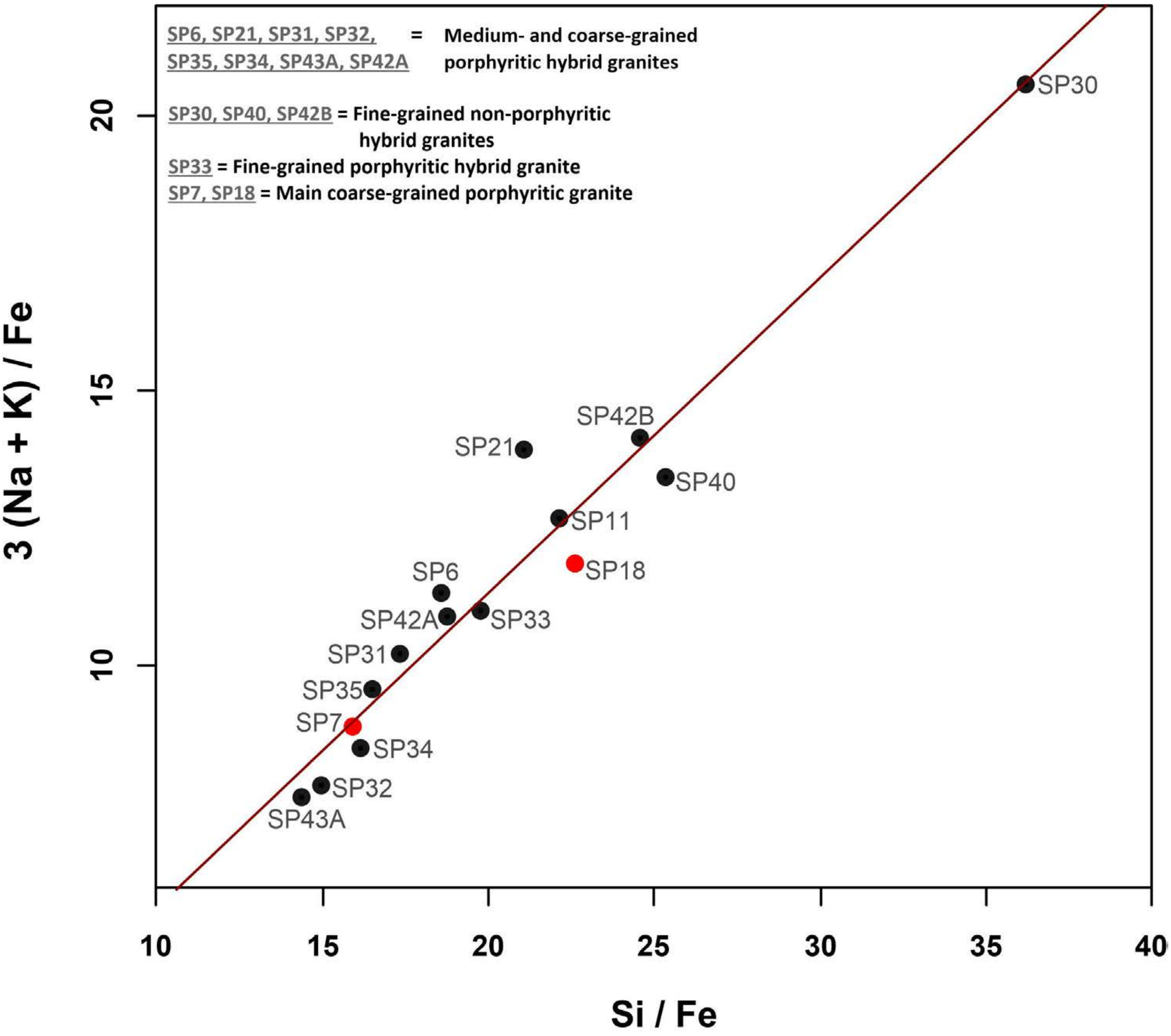

Figure 8.4*: Plot of 3(Na + K)/Fe versus Si/Fe. The model line/linear trend (with a slope of 1) represents the compositional variation caused by the fractionation of K- or alkali-feldspar. The scatter is quite substantial for some samples (e.g. samples SP21, SP18 and SP40) and falls off the main trend suggesting that an external mechanism, outside of alkali-feldspar fractionation, is causing geochemical variation.*

Since it was determined that the fractionation of K-feldspar megacrysts may be influencing the K content of the granite phases (section 8.1.3.2), differences in terms of Na and K were tested between the various medium- and coarse-grained porphyritic hybrid granites, the main coarse-grained porphyritic granite and fine-grained non-porphyritic hybrid granite (Fig. 8.4). This was done to test how the "stranding" of the Kfs megacrysts in the country rock may possibly be influencing their chemistry by the filter-pressing mechanism. Fe was selected as a denominator as it would not partition into the embedded K-feldspar megacrysts (Fig. 8.4).

The linear trend, in this case, represents the compositional variation caused by K-feldspar fractionation (Fig. 8.4). Any deviation off the linear trend suggests (but does not prove) that an external mechanism may be influencing compositional variation off the trend. The scatter is quite substantial for some samples (e.g. samples SP21, SP18 and SP40) and falls off the main trend (Fig. 8.4). This may be due to either filter pressing or even assimilation of the country rock. It is, however, acknowledged, that the mobile nature of Na and K may also have affected the ratios to some extent.

Overall, the available data (for this thesis) does not allow any whole-rock geochemical variability, which may be due to assimilation or filter pressing, to be detected and proven definitively despite the outcrop evidence of their occurrence. More in-depth studies, including mineral chemistry, software computational modelling and experimental studies (e.g. Erdmann et al., 2007; Garcia-Arias & Stevens, 2017) need to be done to test these mechanisms more rigorously.

8.1.3.4 Aplite petrogenesis

The representative aplite sample (SP15) has the same geochemical characteristics as the microgranites. Relative to the main coarse-grained porphyritic granite (in the study area as well as on a regional scale) and the hybrid granites, the aplite sample is also depleted in the LILE, HFSE, LREE, most HREE and it has low CaO (0.28 wt. %), TiO_2 (0.10 wt. %) and Mg# (7.38) contents. Thus, based on the main petrogenetic model for the suite, it could be classified as a relatively pure leucocratic melt phase. Alternatively, the aplites may be interpreted as late-stage magmatic fractionates largely due to their close association with the main coarse-grained porphyritic phase. In the outcrop, the aplites occur as variably sized dykes within the main coarse-grained porphyritic granite phase at the southern end of the study area (Fig.

4.14). The aplites cooled quickly, as evident from their fine grain size (Fig. 4.14B). Their contact with the coarse-grained porphyritic granite is sharp locally (but is elsewhere more gradational) indicating that the latter was largely crystallised during the crystallisation of the aplitic phase. However, the aplites were still at a sufficiently high temperature to prevent the development of an extensive chilled margin. The late silicate melt, interpreted to be a product of extensive crystal fractionation of the melt associated with the main coarse-grained porphyritic phase, which gave rise to the aplites is likely to have escaped along a network of fractures (e.g. Winter, 2010), developed within the main coarse-grained porphyritic granite, as dykes. This is because, unlike the microgranite and hybrid granite phases (in the lit-par-lit zone) which made use of the existing bedding and foliation structures of the country rock for their propagation, no such favourable pathways or textural anisotropies existed in the main coarse-grained granite. This prevented extensive linear dyke-like intrusions but gave rise, rather, to more irregularly shaped aplitic masses in the porphyritic granite. Alternatively, the coarse-grained granite could have represented the still partially molten granite (the crystal mush) that prevented the fracture propagation of the aplite (e.g. Miller et al, 2011).

8.2 Geochemistry of the Malmesbury Group metasedimentary rocks

8.2.1 Introduction

This section will aim to interpret (and subsequently constrain) the sedimentary provenance and tectonic setting of the Malmesbury Group metasedimentary samples of the study area using their geochemistry. The derived interpretations will be compared to findings on past work done on the geochemistry and tectonic evolution of the Malmesbury Group (and the western Saldania belt in the greater context).

8.2.2 Sediment provenance and tectonic setting

The Malmesbury Group metasedimentary samples are relatively enriched in the REE and trace elements of Cs, Rb, Th, U, K, Nb, Ta relative to the average continental crust values of Rudnick and Gao (2003) (Fig. 6.8B). In addition to their relatively high SiO_2 (Avg. 63.59 wt. %) and K_2O (Avg. 4.07 wt. %) and low MgO (Avg. 2.81 wt. %), relative to the average crust, these trace element enrichments are suggestive of an upper crustal origin for the metasedimentary samples. This is because the upper crust is enriched in felsic minerals (hence enrichments in Rb and Cs which preferentially concentrate in felsic minerals such as K-feldspar), heat-producing radioactive elements (hence the enrichments in U and Th) and the LREE (Petford et al., 2000; Rudnick & Gao, 2003). The samples show moderate to strongly negative europium anomalies [$(Eu/Eu^*)_C$ = 0.59-0.70)]. This, together with the low average CaO (0.60 wt. %) content of the samples (relative to the average crust CaO concentration of 6.51 wt. %), and depletions in Sr, K and Ba (relative to the average crust; Fig. 6.8B), suggests that the source material the metasedimentary samples were derived from was plagioclase-poor. Figures 6.8C–F confirms an overall upper continental felsic provenance for the metasedimentary samples as previously described.

Sm-Nd and Rb-Sr isotope geochemistry were only performed on one sample. Despite this, sample SP16 is deemed as a suitable proxy to account for the Sm-Nd and Rb-Sr isotope characteristics of the rest of the metasedimentary rocks of the study area. This is because the results obtained for sample SP16 are consistent with those of Buggisch et al. (2010) and Frimmel et al. (2013) from the Malmesbury Group samples (of the Tygerberg Formation) they analysed (Appendix E1). The ε_{Ndt} value of SP16 (-7.84) is also negative as is the case with ε_{Ndt}

values from Frimmel et al. (2013) [(ε_{Ndt} values between −8.0 and −3.2)] and Buggisch et al. (2010) [(ε_{Ndt} values between −13.4 and −11.0)], although values from Buggisch et al. (2010) are far more negative in general. Although there is no Rb-Sr isotope data for Buggisch et al. (2010), the initial Sr value of SP16 (0.728103) is consistent with the lower range of initial Sr values from Frimmel et al. (2013) (0.72735-0.73098; Fig. 8.5B). The initial Sr values from Frimmel et al. (2013) do, in general, show a large spread from 0.72735-0.76446.

The low ε_{Ndt} value (-7.84) and the fairly high initial Sr value (0.728103) sample SP16 produced supports the interpretation of a felsic upper continental crustal source (Fig. 8.5B). The 2.07 Ga T_{DM} age relative to the depleted mantle at the time of sediment deposition (560 Ma) (Fig. 8.5A) indicates the involvement of Paleoproterozoic crustal sources in the formation of the metasedimentary rocks of the study area (i.e. they were derived from the provenance of reworked Paleoproterozoic crust).

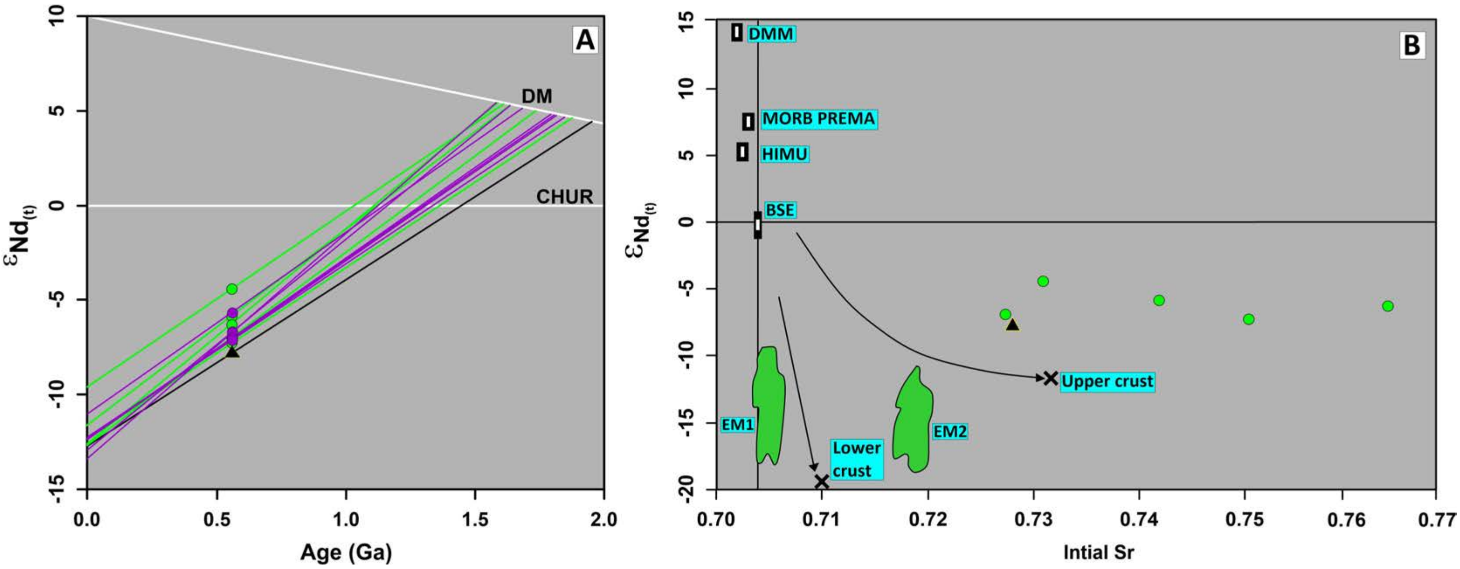

***Figure 8.5**: Whole-rock isotope plots for the various Malmesbury Group samples (black triangle: Tygerberg Formation metasedimentary sample of the study area; green- and purple-circles: Tygerberg Formation metasedimentary samples from Frimmel et al., 2013 and Bugisch et al., 2010 respectively. (A) εNd(t) vs. age (Ga) plot. (B) εNd(t) vs. initial Sr [(^{87}Sr/^{86}Sr)I]. The upper crust curve (Harris et al., 1986) and a theoretical lower crustal curve (Othman et al., 1984) are indicated for reference in (B). The positions of the main oceanic mantle reservoirs of Zindler and Hart (1986) shown in (B) are: BSE = bulk silicate earth, EMI and EMII = enriched mantle I and II, HIMU= high mantle U/Pb ratio, PREMA = frequently observed prevalent mantle composition. The mantle source of MORB (mid-oceanic ridge basalts) and the mantle end-members DMM (depleted end member MORB-mantle component) and PREMA are from Zindler and Hart (1986). Data from Buggisch et al., (2010) is not plotted (in B) due to the absence of Rb-Sr isotope geochemistry data in their dataset.*

Geochemically, the likely source rocks, which eroded and weathered to form the metasedimentary rocks of the study area, are likely to have been rhyodacites/dacites (Fig. 6.8D). These source rocks were plagioclase-poor (as previously mentioned) and minimally to moderately weathered as suggested by the relatively low Zr/Sc ratios (McLennan et al., 1993; Fig. 6.8C) and low to moderate CIA values produced by the samples of the study area. The fairly low intensity of weathering indicates that the geochemical variation of the metasedimentary rocks was mostly dominated by the composition of the source materials as opposed to any subsequent sediment recycling or reworking and compositional maturing of the sediments before lithification. According to age data from Frimmel et al. (2013), however, the likely source rocks for the metasedimentary samples are ortho- and para-gneisses of the Namaqua Metamorphic Province. A greywacke of the Porterville Formation (Table 1.1) yield $^{206}Pb/^{238}U$ ages of Cryogenian age (750 Ma) to Namaquan age (1.05 –1.15 Ga), whereas the maximum age of the Tygerberg and Morreesburg Formations (Table 1.1) is constrained at 564 ± 3 Ma and 557 ± 6 Ma respectively (Frimmel et al., 2013). The differences in the age spectra of these Malmesbury Group formations relate to the much more prominent input of late-Mesoproterozoic and early Neoproterozoic zircons. This likely reflects the proximity of the Namaqua-age (1200–950 Ma) metamorphic hinterland to the immediate east of the Saldania Belt (e.g. Rozendaal et al., 1999; Kisters et al., 2018).

With regards to the tectonic position of the provenance area, all the Malmesbury Group metasedimentary samples plot in the continental island arc field using the plots of La/Sc vs. Ti/Zr, La-Th-Sc and Th–Sc–Zr/10 after Bhatia and Crook (1986) (Fig. 6.9). However, the tectonic regime of the Tygerberg Formation (and the western Saldania belt in the greater context) is interpreted to be an active continental margin (e.g. Belcher, 2003; Rowe et al., 2010; Frimmel et al., 2013; Kisters & Belcher, 2018). A reason for this incorrect tectonic classification, as highlighted by Bock et al. (2000) and Kutterolf et al. (2008), is that using bulk-rock geochemistry is problematic for discrimination between active continental margins and island arc provenances.

The active continental margin, in question, is related to the convergence of the Rio de la Plata and Kalahari Cratons during Gondwana assembly (Villaros et al., 2009b). Frimmel et al. (2013) suggest a back-arc position relative to the Dionisio Cuchilla-Pelotas arc (now located in Brazil and Uruguay) for the depo-basin in which the Malmesbury Group was deposited. The main suture between the Kalahari and Rio de la Plata cratons is interpreted by Frimmel et al. (2013) to be west of the Dionisio Cuchilla-Pelotas arc, possibly along the Major Gercino-Sierra Balena Lineament within southeastern South America. Kisters and Belcher (2018), however, argue that the western Saldania belt is instead representative of a section through a fore-arc region situated along the western margin of the Kalahari Craton (Kisters & Belcher, 2018). In this fore-arc region, the Malmesbury Group (encompassing the Tygerberg Formation, large parts of the eastern Boland Subgroup and the upper parts of the central Swartland complex) represents the relics of a fore-arc basin fill of late-Neoproterozoic to Cambrian age (Kisters & Belcher, 2018). This basin sits on top of an accretionary prism where the lower, structurally complex, Swartland complex was once situated (Kisters & Belcher, 2018). The sinistral transpressive strains of the Malmesbury fore-arc agree with the oblique closure of the Adamastor Ocean (or proto-Atlantic ocean), which existed between South America and southern Africa, during the late Neoproterozoic (Kisters & Belcher, 2018).

Important information about the depth extent of the Malmesbury Group can be obtained from the CGS; this is because the thickness of the Malmesbury Group is poorly constrained (Kisters, 2016). Using a foliated metamafic xenolith (a possible high-grade equivalent of the Malmesbury Group metasediments and likely source for the granites of the CGS) found at the Darling Batholith of the CGS, Villaros et al. (2009b) were able to constrain the possible pressure-temperature (P-T) conditions at the source region for the CGS plutons. The xenolith records regional granulite facies metamorphism, of ~850 °C and 10 kbars (depths over 25 km), before the intrusion by the CGS granites and can be considered as minimum conditions for partial melting of the source (Villaros et al., 2009b). Inherited $^{206}Pb/^{238}U$ ages obtained from the zircon grains of three granite samples have ages of 557 ± 5 and 599 ± 4 Ma in sample SP19, 599 ± 7 and 810 ± 9 Ma in sample SP33 and 557 ± 5 and 561 ± 5 Ma in sample SP43A (see U-Pb geochronology chapter 7); these ages correspond closely to ages of inherited zircon cores found in the Peninsula Pluton granite by Villaros et al. (2012). These results, therefore, point to Pan-African aged Malmesbury-type material at depth (i.e. in the anatectic source region of the magmas at > 25 km depths) (e.g. Kisters et al., 2018).

8.3 Metamorphism of the country rock

8.3.1 Introduction

Owing to the sub-greenschist facies metamorphism of the Malmesbury Group rocks and their poor exposure, there has been limited research on the metamorphism of the Malmesbury Group (Belcher, 2003). Furthermore, the knowledge of the temperature of the Peninsula Pluton granite (at the time of intrusion) and the surrounding (country rock) areas upon intrusion is also limited, hindering thermal modelling (e.g. Wheeler et al., 2004). Other limiting factors, in the case of the study area, is the occurrence of alteration and the absence of petrogenetic modelling (from bulk-rock analyses) and mineral compositional data. The presence of the former means that reaction textures, especially those involving cordierite, cannot easily be observed petrographically and the absence of the latter (analytical data and modelling) means that metamorphic P-T conditions can only be estimated.

This section will, therefore, mention standard reactions, from literature, that are expected to take place in average pelites during a progressive increase in temperature without a significant change in pressure (e.g. as in contact aureoles). These reactions will then be compared to the stable assemblage of the metapelites in the study area to delineate any variations or similarities the assemblage shows when compared to average or “true” pelites undergoing contact metamorphism. Any conclusions drawn from this section should, however, remain tentative until further metamorphic studies are undertaken.

8.3.2 Reactions expected for low-grade pelitic rocks undergoing contact metamorphism

Pelitic rocks are very fine-grained (typically <2µm) mature clastic sedimentary rocks derived from the weathering and erosion of the continental crust (Winter, 2010). Their mineralogical composition is dominated by fine Al-K-rich phyllosilicates, in the form of clay minerals (i.e. montmorillonite, kaolinite, or smectite), fine white micas (sericite or phengite) and chlorite (Bucher & Frey, 2002; Winter, 2010). Fine quartz, feldspars (albite and K-feldspar), iron oxides and hydroxides, zeolites, carbonates, sulphides, and organic matter are the other common constituents in pelitic rocks (Bucher & Frey, 2002; Winter, 2010). The geochemical characteristics that distinguish pelites from other common rocks are high Al_2O_3 and K_2O (and usually SiO_2) and low CaO. These characteristics reflect the high clay and mica content of the original sediment and lead to the dominance of muscovite and quartz throughout the low- and medium-grade range of metamorphism (Winter, 2010).

In contact metamorphic environments, the heat source that drives further metamorphism of low-grade pelitic rocks is typically magma that intrudes the upper crust from depth (Bucher & Grapes, 2011). As a result, thermal contact aureoles are typically developed around magma bodies. The maximum temperature to which the low-grade rocks can be heated depends on several factors, including the composition of the magma, the size of the magma body and the temperature of the country rock (Bucher & Grapes, 2011). For example, the intrusion of large amounts of hot and dry mafic magma from the mantle may result in extensive high-temperature (900 –1000°C) contact aureoles, whereas shallow-level H_2O-saturated granitic & granitoid magmas (i.e. “wet” magma) rarely exceeds 650°C (Bucher & Grapes, 2011). In contrast, Winter (2010) estimates the intrusion temperature of H_2O-saturated granite magma to be between 700 and 800°C.

The chemical composition of pelites can be represented by the K_2O-FeO-MgO-Al_2O_3-SiO_2-H_2O (KFMASH) system as it accounts for 95% or more of their composition (Winter, 2010; Spear et al., 2017). The KFMASH system involves six chemical components, three of which (H_2O-SiO_2-K_2O) can be assumed to be in excess in rocks with quartz and muscovite or K-feldspar, and that, during the reaction, liberate H in the form of a hydrous fluid or silicate melt (Spear et al., 2017). The major mineralogical differences that distinguish low-pressure pelites from higher pressure types are the occurrences of andalusite and/or cordierite in the former. In general, Al-rich pelites contain andalusite-bearing assemblages over a wide range of temperatures (from below 400° to > 600°C) at very low pressures (as low as 0.2 GPa) whereas at higher temperatures cordierite is the characteristic mineral of low-pressure pelites (Bucher & Grapes, 2011). This is because cordierite has a relatively high molar volume, placing it at the low pressure-high temperature side of reactions (Winter, 2010).

The metapelites of the study area contain a stable mineral assemblage of Crd + Bt + Kfs + Qtz + Pl (the latter represents the non-KFMASH components of Na_2O and CaO). Primary muscovite is rare to absent and is instead present within an assemblage involved in the replacement of cordierite (Appendix B1; Fig. B1G, H). Primary chlorite is also not present in the assemblage; it is largely a retrograde phase replacing biotite. Contrary to the prograde path of “normal” or average low-grade pelitic sedimentary rocks, andalusite is absent from the final assemblage. Its absence possibly alludes to the lack of sufficient Al_2O_3 content in the metapelites of the study area to crystallize andalusite during progressive metamorphism. Instead, the distinctive mineral phases related to thermal metamorphism are biotite and cordierite. The characteristic assemblage of the metapelites of the study area is similar to the assemblage described by Pattison and Harte (1997) for pelites in the lower and upper cordierite zones in the Ballachulish thermal aureole located in the West coast of Scotland. Therefore all reactions that summarize what is happening in the aureole of the Sea Point contact will be a direct reference to their findings. Zone III, the chlorite-absent zone in the lower cordierite zone of the Ballachulish thermal aureole, contains the assemblage Ms + Qtz + Crd + Bt. The model reaction (550 – 560°C), given by Pattison and Harte (1997), that accounts for the production of cordierite and biotite at the expense of chlorite is:

$$\text{Ms} + \text{Chl} + \text{Qtz} = \text{Crd} + \text{Bt} + H_2O \ (1)$$

Assemblage IVb of the upper cordierite zone, an upgrade of zone III, of the Ballachulish thermal aureole is muscovite-free and typified by the assemblage Bt + Crd + Kfs + Qtz. Pattison and Harte (1997) interpret the model reaction (at ca. 620°C) that accounts for the production of K-feldspar and cordierite at the expense of muscovite to be:

$$\text{Ms} + \text{Bt} + \text{Qtz} = \text{Crd} + \text{Kfs} + H_2O \ (2)$$

Overall, the distribution of mineral assemblages in the thermal aureole of the study area is consistent with the sequential crossing of reactions (1) and (2). The absence of primary chlorite in the study area can be explained by reaction (1), whereas the absence of muscovite can be explained by both reactions. Reaction (2), however, consumes biotite but petrographic evidence of biotite consumption was not observed due to limited evidence of reaction textures.

Although it cannot be said with certainty whether biotite in the study area is of contact or regional metamorphic origin without a larger regional study aimed at determining the extent of the thermal aureole, some clues support a contact origin. For example, if reaction (1), which takes place at temperature conditions of 550 – 560°C, is envisaged to be the reaction responsible for biotite formation in the study area, that would suggest that at the point of biotite formation, the grade is already higher than in any of the Malmesbury Groups rocks outside the contact aureole. Regionally, the Malmesbury Group rocks (outside the contact zone) are interpreted to reflect lower or sub greenschist facies conditions (i.e. 250°C to 350°C) (e.g. Scheepers, 1995; Rozendaal et al., 1999; Belcher & Kisters, 2003), with the metagreywackes and metapelites of the Malmesbury Group lithologies comprised predominantly of quartz, feldspar (albite and microcline), muscovite and minor chlorite (Belcher, 2003). This, therefore, provides supporting evidence of a contact origin for the biotite grains due to their absence in the rocks of the Malmesbury Group outside of the contact aureole. Only isolated biotite-feldspar schist outcrops, north of the town of Malmesbury (Fig. 2.3A) and classified under the Swartland complex, are cited by Belcher (2003) as the only lithologies in the western Saldania belt containing biotite (outside of the contact aureole). These isolated outcrops place the aforementioned schists within a slightly higher grade of metamorphism compared to the other metapelitic schists of the Swartland complex (Belcher, 2003). Lastly, if biotite (which defines the S_1 foliation) is formed at the same time as cordierite (Fig. 5.10; section 5.2.4), it belongs to the peak assemblage, also in a structural sense, and hence is intrusion-related.

8.4 Structural interpretation of the country rock

8.4.1 Introduction

This section will provide an interpretation of the deformation history of the Malmesbury Group country rock in the study area based on the orientation data (Appendix C) measured from the various fold and foliation structures described in the Structural geology chapter. The characterization of the deformation history will provide an overview of the structural setting of the area which, will, in turn, help to constrain the time of granite emplacement relative to deformation as well establishing the extent of the role played by the structure of the country rock in accommodating granite emplacement. The deformation of the country rock related to the granite intrusion itself is described in the granite emplacement section.

8.4.2 Deformation

The bedding planes (S_0) of the Malmesbury Group country rock in the study area are moderate to steeply dipping (55° – 88°), trend NW-SE in the northern portion of the study area, are E-W to WNW-ESE trending in the lit-par-lit zone and trend WNW-ESE (with minor variation towards E-W) in the southern portion of the study area (section 5.2.1). The bedding planes are suggestive of a horizontal, principal compressional type differential strain to have produced their orientation during the first deformation event (D_1). The horizontal compressional strain was directed NE-SW (Fig. 8.6) and produced various WNW-ESE- to NW-SE- oriented tight- to isoclinal- and chevron-type F_1 folds outcropping at various localities in the study area (Figs. 5.11–5.16). The F_1 folds are associated with an axial planar S_1 foliation that dips either to the NE or SW (Fig. 8.6). The orientation of the S_1 foliation planes is subparallel to the S_0 bedding planes on fold limbs of tight to isoclinal folds.

None of the stereonets plotted show more than a single maximum (Fig. 8.6), making it problematic to extract further data from the plots (e.g. interpretation of the overall structural regime of the study area). The plots do, however, show that the fold axis/hinge corresponds to σ_3 (Fig. 8.6). Fold hinges that are orientated parallel to the regional stretch are common in transpressional settings (Fossen, 2010). The NW plunging fold axis of all the bedding in the study area (Fig. 8.6A) is similar in orientation to the fold axes obtained from the folds of areas 9 and 11 (Fig. 5.17B, C) albeit more inclined.

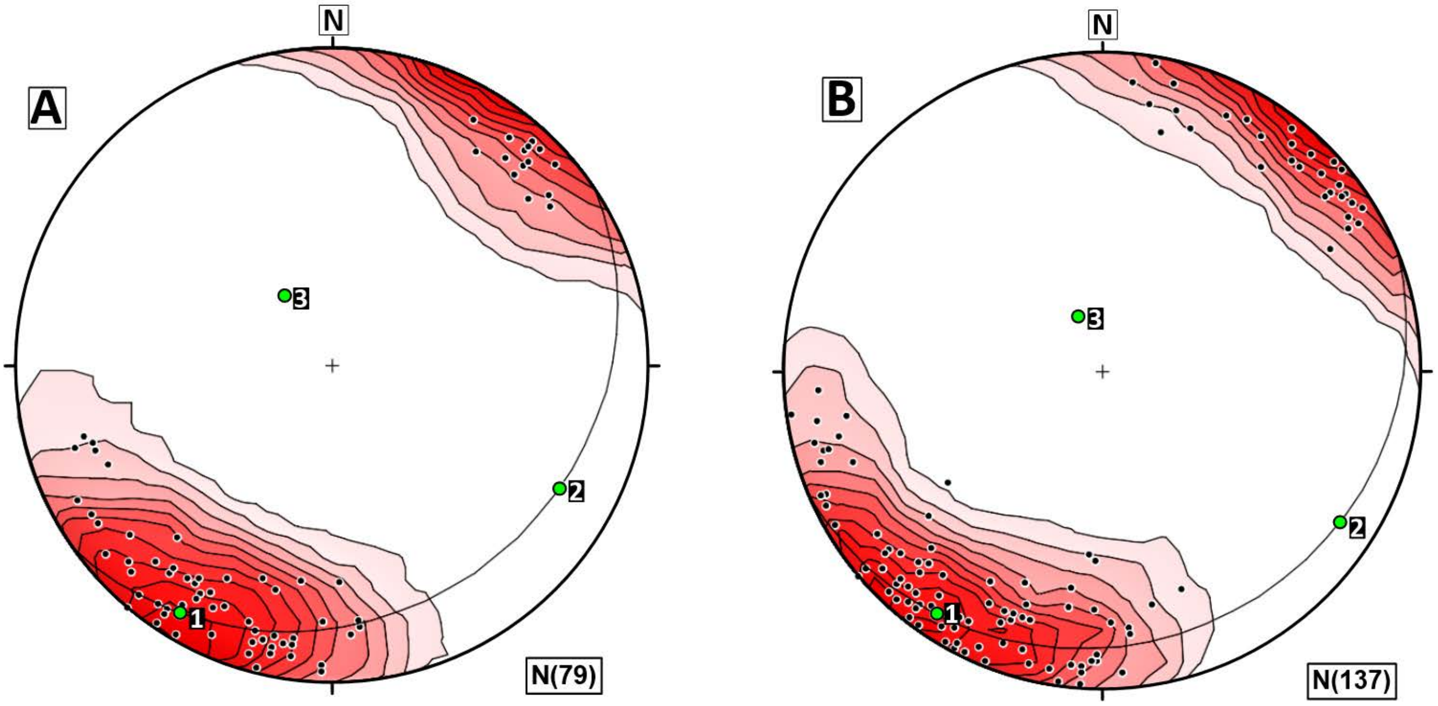

***Figure 8.6**: Lower hemisphere equal-area projections of bedding (A) and S_1 foliation poles (B). The poles (black dots with white borders) are cumulative totals for the respective bedding (A) and S_1 foliation (B) readings taken. The contours (shown in different shades of red) indicate clustering ("density") of orientation in space and the green dots and the great circle (solid black line) are the software's (Stereonet 10) statistical best-fit pole girdle (shown by the numbers 1 and 2 which correspond to σ_1 and σ_2 respectively) and the pole to that girdle (shown by the number 3 corresponding to σ_3), which is the best estimate of the fold axis; all of this information applies to all stereoplots in section 8.4. Two fold limbs as separate maxima are not observed implying that these are single clusters. The occurrence of isoclinal folding can explain this.*

The overall structural regime of the western Saldania belt is explained by Kisters and Belcher (2018). At the onset of the Saldanian orogeny, the Malmesbury fore-arc basin experienced a NE-SW shortening strain (Kisters & Belcher, 2018). The non-coaxial or transcurrent component of the strain (D_1) was accommodated by regional scale, NW-trending strike-slip faults in the form of the Colenso and Piketberg-Wellington faults (Kisters & Belcher, 2018). The coaxial component of the strain was accommodated by various N-NW trending folds (Kisters & Belcher, 2018). This explains the occurrence of both folding and shearing in the study area. This pattern of orogen-parallel transcurrent shear zones bordering or enveloping folded domains is characteristic of obliquely convergent margins (Kisters & Belcher, 2018).

The crenulation cleavage (S_2) is shallowly inclined (average dip angle of 11°), suggestive of a vertical compressional type differential (Fig. 8.7). Such a vertical compressional strain (σ_1) was oriented WNW-ESE (Fig. 8.7), signifying a change in the principal strain orientation from dominantly NE-SW (during D_1) to WNW-ESE (during D_2) with time during the Saldanian orogeny. S_2 is, however, spaced and localized implying that D_2 is not likely to have caused a large degree of interference folding of both bedding (S_0) and the axial planar S_1 foliation in the study area.

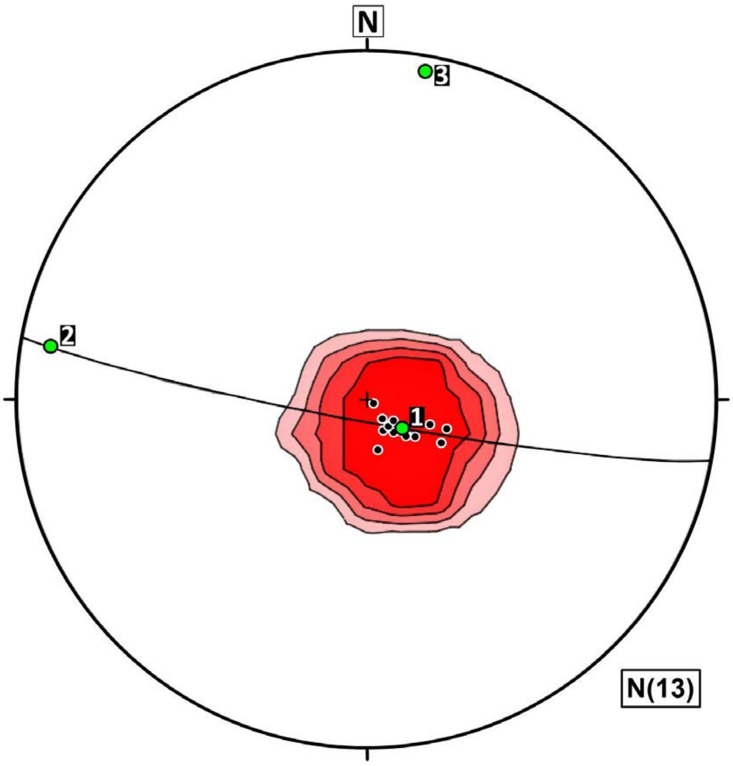

Figure 8.7*: Lower hemisphere equal-area projection for S_2 cleavage orientation (as contoured poles) measured at the northern portion of the study area.*

8.5 Granite emplacement

8.5.1 Introduction

This section of the thesis will discuss the timing of the granite intrusions in the study area relative to deformation, their depth of emplacement and the method by which they got emplaced. For the latter, outcrop observations, rock block samples, petrographic studies and geochronological data were used as a means of deciphering or delineating which emplacement mechanisms are likely to have played a role in the emplacement of the granites.

8.5.2 Depth of emplacement

Granitic plutons are considerably large igneous bodies and their formation and the associated deformation of the host rocks must be mechanically compatible on the long term with the average lithospheric strain rate (Petford et al., 2000; Menand, 2011). The depth of emplacement of these large igneous bodies plays a significant role in solving issues related to granite accommodation in the crust. The emplacement of a pluton in the shallow upper crust will be facilitated by the presence of the near free surface, whereas the emplacement of deeper plutons in the lowermost parts of the crust will benefit from ductile flow, either from the mantle or the ductile crust or even both (Menand, 2011).

Armstrong et al. (1998) provide the only estimate of the depth of intrusion based on contact metamorphic assemblages in the aureole of the Peninsula Granite exposed at Sea Point. They estimate the emplacement depth to be ~ 8 to 10 km. This interpretation corresponds to the consensus by other researchers (e.g. Scheepers, 1995; Rozendaal et al., 1999; Belcher & Kisters, 2003) who interpret that the CGS granites were emplaced at shallow crustal levels. This is because the lower greenschist facies of the Malmesbury Group, a metamorphic grade obtained before CGS granite intrusion, indicates upper crustal levels of metamorphism. The CGS intrusions then intruded at that level as indicated by the low grade of the country rocks they intruded.

8.5.3 Granite emplacement relative to regional deformation

Outcrop and microscopic evidence point to a late (syn-) to post-tectonic emplacement relative to D_1 whereas a timing of emplacement relative to D_2 could not be established due to its weakly developed nature. Evidence for a late syn-tectonic emplacement relative to D_1 include:

(i) Syn-emplacement thermal contact metamorphic features of the country rock: (a) the syn-tectonic growth of cordierite porphyroblasts in the aureole relative to D_1 (see section 5.2.4; Fig. 5.10) and (b) growth of preferentially oriented contact metamorphic biotite grains (section 8.3.2) which form the pervasive S_1 fabric in the country rocks of the study area. This implies that at the time of granite intrusion the biotite grains could have grown while the NE-SW directed strain field associated with D_1 was active resulting in them obtaining a preferred WNW-ESE to NW-SE orientation.

(ii) The boudinage of various granitic phases (Fig. 4.24C, E). These features consistently indicate NE-SW shortening and WNW-ESE extension. The orientation of shortening corresponds to the principal orientation of the compressive stress component (σ_1) associated with the first deformation phase (D_1). This, therefore, suggests that the boudinaged features associated with the granite formed while D_1 was active (i.e. they are post-crystallization or solid-state structures).

(iii) Sheared or rotated megacrysts of K-feldspar, embedded in the country rock, during non-coaxial (rotational) deformation/shearing (Fig. 5.19). The sheared K-feldspar grains can be used to infer the timing of granite emplacement provided that an igneous origin for the K-feldspar megacrysts is interpreted.

The reason why a late syn- to post-tectonic emplacement relative to D_1 is also postulated, despite the reasons given above, is because all the granite phases of the study area lack evidence of a tectonic fabric. The absence of a tectonic fabric, however, may also mean that the crystallization of the granites was fairly rapid or there was a degree of pre-emplacement crystallization (meaning they were rheologically strong, to begin with) as suggested by the high megacrystic content of some of the granitic pulses (e.g. Farina et al., 2012). Once fully crystallized, they were able to behave in a competent manner meaning that as deformation (regional shortening) continued, the bedding and folds in the Malmesbury Group metasedimentary rocks draped/wrapped around the competent granite (e.g. Brun et al., 1990; Paterson et al., 1998; McFadden et al., 2010; Fernández et al., 2019). This could serve to explain the common occurrence of non-cylindrical folds and the varying bedding and foliation orientation in the lit-par-lit zone (sections 5.2.1 and 5.2.2). An example of this can also be seen at the thin section- and rock block sample-scale (Figs. 8.8, 8.9), where the S_1 foliation (in the metamudstone bands) is deflected around the various phenocrysts of the porphyritic medium- and coarse-grained granites in the lit-par-lit zone.

Many models of syn-tectonic granite emplacement consider the development of dilatant sites in relation to shear zones in strike-slip systems (e.g. Hutton et al., 1990; D'Lemos et al., 1992; Hutton & Reavy, 1992; McCaffrey, 1992; Neves et al., 1996; Holdsworth et al., 1999; Passchier et al., 2005; Kratinová et al., 2007) or in extensional settings (e.g. Clemens & Mawer, 1992; Díaz-Alvarado et al., 2012) as important space-making processes that provide favourable pathways for magma transportation. On a regional scale, two NW-trending, near-vertical strike-slip fault zones, associated with the main deformation event (D_1), are recognized; they are the Colenso and Piketberg-Wellington fault zones (Hartnady et al., 1974; Theron et al., 1992; Kisters et al., 2002; Belcher, 2003; Frimmel et al., 2011, 2013). The Colenso fault is far more prominent and better exposed (can be traced 180 km along its strike), whereas the Piketberg-Wellington fault is poorly exposed and its actual location and trace are not well known (Kisters & Belcher, 2018).

By performing a kinematic analysis of shear zones in granite fabrics of the CGS coupled with published geochronological data, Kisters et al. (2002) were able to constrain the kinematic history of the Colenso fault. The U-Pb zircon ages from granites of the Darling Batholith, emplaced during sinistral strike-slip movement along the Colenso fault, point to deformation along the fault zone between 545 and 525 Ma (Kisters et al., 2002). Northwest of the Darling Batholith, fault rocks related to the Colenso fault zone are developed in the Cape Columbine granite and Vredenburg monzogranite. Shear sense indicators in these younger, 540 – 520 Ma, granites mainly point to dextral kinematics, suggesting a late-stage reversal of shear along the Colenso fault (Kisters et al., 2002).

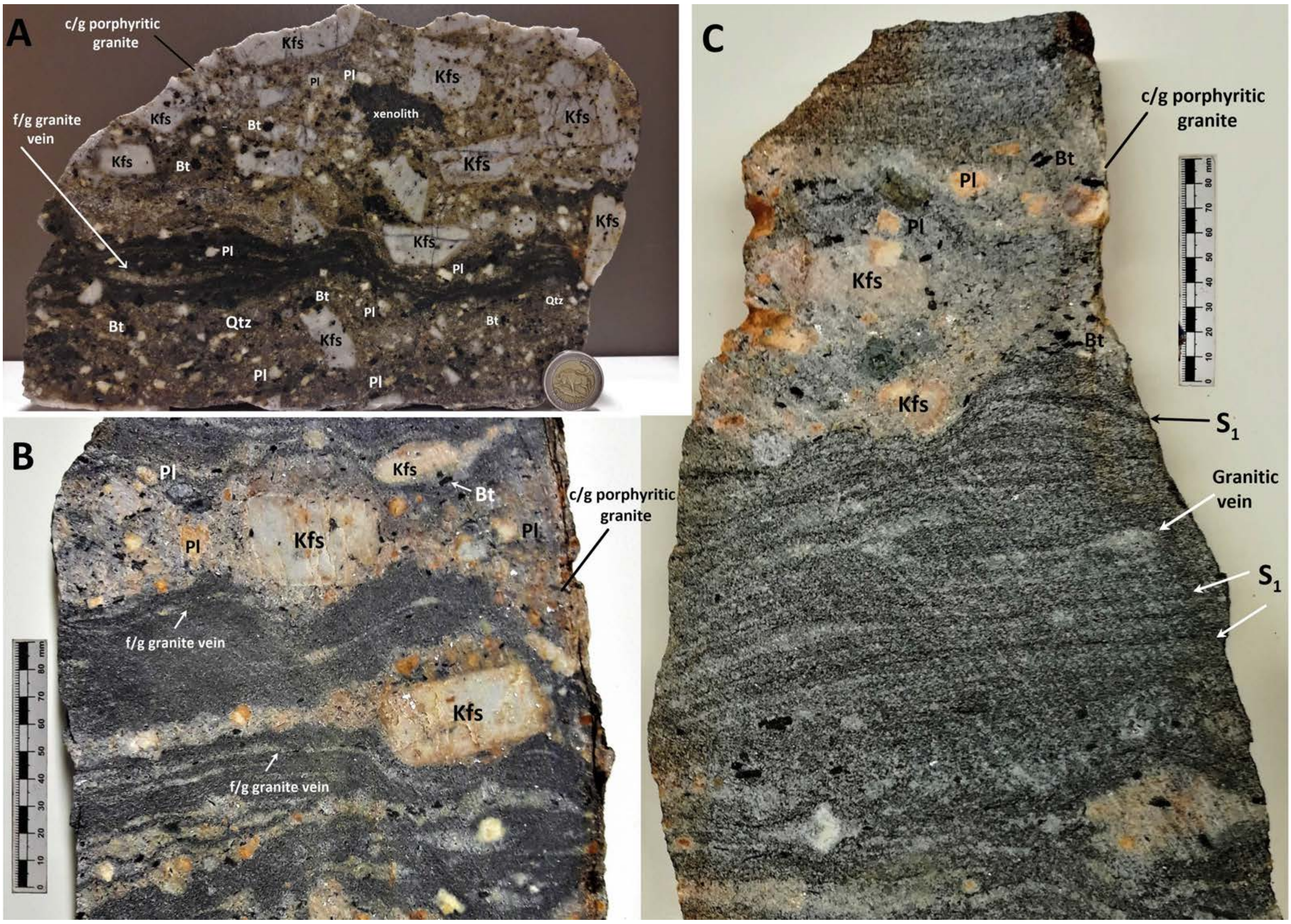

Figure 8.8: *Rock block photographs of samples SP5 (A), SP43D (B) and SP43B (C) showing the contact relationships between various fine-, medium- and coarse-grained porphyritic granite pulses and the metamudstone country rock. All the granite pulses are intruded sub-parallel to the S_1 foliation planes (which are more evident in C) of the metamudstone. In areas where the metamudstone is in contact with porphyritic medium- and coarse-grained granite pulses, the metamudstone bands and the S_1 foliation is deflected around the competent granite during regional shortening (A & C). For (B) later intruded fine-grained granitic veinlets are also deflected/wrap around the K-feldspar megacrysts of the voluminous granite pulses.*

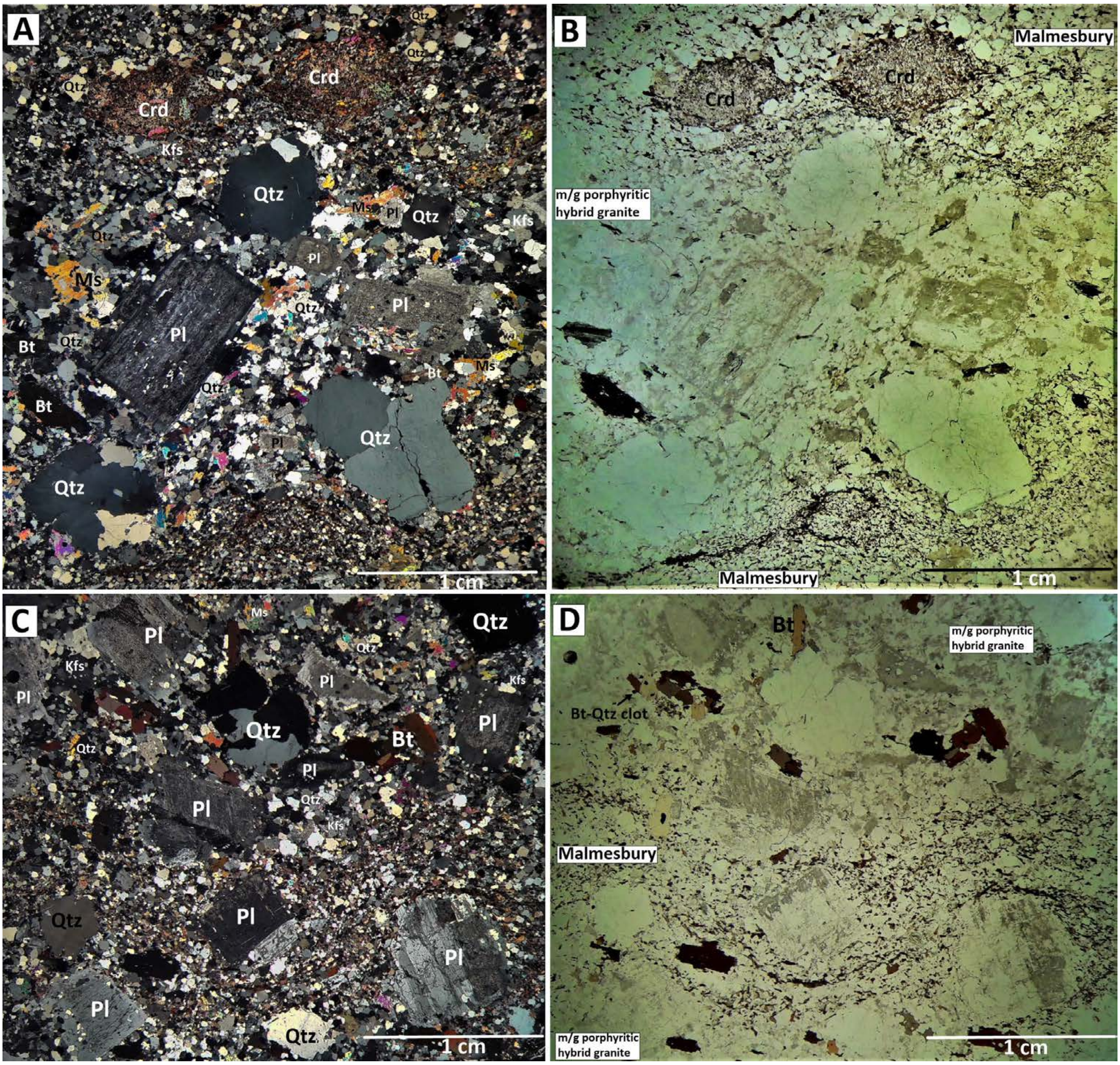

***Figure 8.9**: Thin section photomicrographs, in cross-polars and plane-polarized light, highlighting the contact relationships between the various porphyritic hybrid granitic phases and the biotite-rich metamudstone bands. (A) – (D) Medium-grained porphyritic hybrid granite intrusions that are intruded subparallel to the metamudstone [(i.e. foliation planes; more apparent in (A) & (B))]. They show no immediate signs of deformation apart from the undulose extinction shown by the quartz grains (both phenocrystic and matrix quartz; e.g. bottom left of A). The porphyritic granite intrusions are competent and the shortening of weaker metamudstone around the competent granites, during progressive shortening, causes foliation deflection (B, C).*

The ^{206}Pb/^{238}U emplacement ages from the selected granite phases vary between 538.7 ± 3.6 Ma and 542.7 ± 2.9 Ma. These emplacement ages correspond to an intrusion during the time (i.e. at ~540 Ma) when the Colenso fault, a large-scale shear zone, made a switch from sinistral movement to dextral movement (Kisters et al., 2002), an ideal scenario for magma transportation and emplacement. Unlike the Darling Batholith/Pluton, however, the Peninsula Pluton does not intrude into the Colenso fault but rather in the pure-shear dominated region outside the fault. Given the limited extent of the Sea Point contact outcrop (170 m × 60 m), the difficulty in distinguishing regional strains and strains related to emplacement and how they interfere and the lack of a controlling shear zone (and local dilational jogs) in facilitating granite emplacement, the following paragraphs will detail how granite emplacement, relative to regional shortening, was possible.

The various granite sheets are intruded sub-parallel to the favourably inclined pre-existing country rock anisotropies (S_0 and S_1) implying an intrusion more or less normal (i.e. high angles) to regional shortening (σ_1). They, therefore, classify as inclined sills/sheets, an observation supported by the K-feldspar megacryst-defined magmatic foliation plane which is consistently steeply dipping across each station (Fig. 5.29). The emplacement of sheet-like intrusions is governed mostly by the interaction of the following factors: (1) the orientation and magnitude of the regional and/or local stress fields (Ferre et al., 2012), (2) pre-existing anisotropies (bedding and foliation) and their orientation (Lucas & St. Onge, 1995; Holdsworth et al., 1999; Sibson, 2003; Kisters et al., 2009), and (3) the melt pressure that drives sheet and fracture propagation (Gudmundsson, 2011).

According to Lucas and St. Onge (1995), sheet intrusions can be emplaced at high angles to σ_1 when the difference in tensile strength normal and parallel to the bedding and foliation anisotropy of the country rock is larger than the regional differential stress ($\sigma_1 - \sigma_3$, with $\sigma_1 \geq \sigma_2 \geq \sigma_3$) at the time of emplacement. These conditions of low differential stress could have been prevalent in the study area, explaining how the granitic sheets were able to preferentially propagate along the various bedding and foliation planes of the country rock more or less normal to regional shortening.

Theoretical, experimental and outcrop studies (e.g. Lister & Kerr, 1991; Lucas & St. Onge, 1995; Dahm, 2000; Mériaux & Lister, 2002; Gudmundsson, 2011; Ferre et al., 2012) have detailed the dynamics and direction of propagation of inclined melt transfer structures/fractures. They found that it depends on: (1) the buoyancy (i.e. density contrasts between host rocks and magmas), (2) the external deviatoric stress field (including the stresses induced by the fractures themselves at their tip), (3) an upward-decreasing pressure gradient and (4) the melt pressure, which may assist in pushing the country rocks aside, hence creating additional room, but must be equal to lithostatic pressure to keep the pathway open and must be sufficiently high that it exceeds the sum of σ_1 and the tensile strength of the rock (T_1) parallel to σ_1 (i.e. $P_{Melt} > \sigma_1 + T_1$). The mechanism of sheet propagation that is relevant to the study area is described in more detail in section 8.6, as it has important implications on the origin of the K-feldspar megacrysts embedded in the country rock.

8.5.4 Proposed granite emplacement mechanisms for the study area

8.5.4.1 Incremental emplacement of magma bodies: clues from the relationship of the various granite phases to each other and the country rock

Past geochemical and outcrop studies on the Peninsula Pluton of the CGS reveals an incremental construction for the Peninsula Pluton by rapid emplacement of successive magma pulses whose isotopic composition is directly inherited from the source (Harris & Vogeli, 2010; Villaros et al., 2012; Farina et al., 2012). Villaros et al. (2012) were able to prove that, within individual samples, the hafnium isotope values ($\varepsilon_{Hf,\,t}$) of inherited zircon cores (ages between 1200 and 570 Ma) show a similar range to that derived from magmatic zircon when both are recalculated to the magmatic age or emplacement age of the Peninsula Pluton (i.e. 540 Ma; $\varepsilon_{Hf,t}$ of inherited zircon: -15.2 to + 1.7; $\varepsilon_{Hf,t}$ of magmatic zircon: -8.6 to +1.5). This was interpreted to imply that the homogenisation of Hf isotopic variation in the magma, acquired through a dissolution of the entrained zircon via mechanical mixing and/or diffusion within the granite, was particularly inefficient (Villaros et al., 2012). The lack of homogenization, therefore, argues for the assembly of the pluton through numerous small magma batches that undergo rapid cooling from their intrusion temperature to the temperature at which most of the magmatic zircon had crystallized (> 80% by 700°C) (Villaros et al., 2012). This is supported by findings from Harris and Vogeli (2010). They suggest that the variable oxygen isotope compositions ($\delta^{18}O$) of garnet (ranging from 10.0 to 11.4‰) in the S-type Peninsula Pluton are consistent with the partial melting of a metapelitic source, with an oxygen isotope composition similar to that of the Malmesbury Group exposed on the surface, to produce magma batches characterized by slightly different $\delta^{18}O$ values. The magma batches were subsequently mixed and partly homogenized before and/or during the emplacement process, resulting in a narrower spread of quartz $\delta^{18}O$ (13.2 to 14.0‰) values (Harris & Vogeli, 2010).

The Sea Point contact appears to be an ideal setting that presents outcrop evidence to back up the interpretation of an incremental construction for the Peninsula Pluton as suggested by the isotopic evidence described above. This is because the outcrop exposes a variety of granite phases at a more localized scale compared to the rest of the Peninsula Pluton. These granitic phases are not always in direct contact with each other but, whenever they are, the contacts are generally transitional and rarely sharp (e.g. Figs. 4.24A, F, 4.29). The process behind the build-up of an igneous body by successive intrusions is described by Annen (2011), where individual intrusions are envisaged as sills because that is a geometry often observed in nature. The timing of pluton construction can either be rapid, with construction taking place by intrusions in close succession (i.e. tens of thousands of years) (e.g. Wiebe & Collins, 1998; Miller & Paterson, 2001a) or by an amalgamation of discrete increments over a longer period (i.e. millions of years) (e.g. Coleman et al., 2004; Glazner et al., 2004).

The process (as described by Annen, 2011) is summarized as follows: the first emplaced sills are in contact with cold country rock and as a result, they cool and solidify rapidly (i.e. magma quenching). In the earliest stage of the igneous body growth, each successive sill (unless the time interval between intrusions is very small) crystallises before the next one is emplaced. When cooling down and crystallising, the sills transfer their sensible and latent heat to the country rock that progressively heats up. Given enough time, the sills thermally equilibrate with their surroundings at progressively higher temperatures.

When the process is explained with regards to the setting of the study area, the microgranite phases to the north and south of the study area (Fig. 4.1), as well as the less voluminous fine-grained non-porphyritic hybrid phases in the lit-par-lit zone (Fig. 4.24C, D) correspond with earlier emplaced sheets which solidified rapidly. This is due to their fine-grained nature and the localized chilled contacts they show with the country rock (the latter more commonly observed in the contact areas between the microgranite and country rock at the northern end of the study area). The successive sheets that thermally equilibrated with the surrounding country rock at progressively higher temperatures (following the rapid solidification of the earlier emplaced microgranites) correspond to the various coarser-grained and porphyritic phases in the study area. These include the hybrid phases in the lit-par-lit zone in the form of the fine-grained porphyritic granites, medium- and coarse-grained porphyritic granites and the main coarse-grained porphyritic granite at the southern end. Their coarse grain-sizes and lack of chilled margins with the country rock suggests that the time interval between their successive emplacements was not too long (e.g. Annen, 2011). This prevented the country rock from completely cooling down between each magma injection and explains why there is a distinct lack of chilled margins and sharp contacts between the country rocks and the granites in the lit-par-lit zone. The contacts between the aforementioned coarse-porphyritic phases and the country rock in the lit-par-lit zone are instead gradational (e.g. Figs. 4.22, 4.23).

The lack of sharp contacts between the various granite phases could be explained as follows: (1) As the intrusions proceed, following on from the early emplaced magma pulses, temperatures continue to increase and an increasing volume of melt is present in the system as the extent of melt present in the newly intruded sills increases and older sills re-melt. This is likely to destroy original sharp contacts as a result (Annen, 2011). (2) Depending on the balance between heat input from magma replenishment and heat loss to the surroundings, relatively melt-rich zones may expand far beyond the dimensions of individual sills precluding the development of sharp contacts between successive batches (Farina et al., 2012). (3) Additionally, sharp contacts may never have existed due to the intrusion of new magma batches into a partly molten magma chamber (Farina et al., 2012).

The U-Pb zircon geochronology analysis performed on selected granite samples, for determination of their emplacement ages, yield ages between 542.7 ± 2.9 Ma and 538.7 ± 3.6 Ma. All the derived ages for the granitic rocks of the study area, as well as those by Scheepers and Armstrong (2002) (e.g. 540 ± 4 Ma) for the Peninsula Pluton, are identical within error. The ages, therefore, suggest that the different phases/batches were emplaced either at the same time or in rapid sequence. In the case of the former, one may argue that the age disproves the existence of different batches, however, a case for the latter is more likely to apply in the study area because of the lack of chill margins (i.e. the intrusions were rapid between each magma pulse, preventing the country rock from completely cooling down between each magma injection as explained above).

8.5.4.2 Additional space making processes/mechanisms – ductile host rock deformation to accommodate magma during incremental assembly

There are three different types of accommodation structures associated with the emplacement of an intrusion. The first two have already been discussed in section 8.5.3. They are in the form of tectonically driven structures that are utilized and/ or reactivated during magma emplacement and favourably oriented pre-existing country rock structures. The third type consists of localized structures that develop in the country rock in response to magma intrusion so that the incoming extra volume of magma can be accommodated either laterally or vertically within the host rocks (e.g. Spacapan et al., 2017; Guldstrand, 2018; Magee et al., 2018; Wilson et al., 2019). In this case, deformation is driven purely by magma emplacement.

Of particular interest in the study area is the apparent ductile behaviour of some country rock portions in the lit-par-lit zone (Fig. 4.30). Other features which support the interpretation of a fairly ductile behaviour of the country rock are boudinage structures of granitic material (Figs. 4.24C, E, 4.30) and ptygmatic folds of quartzofeldspathic injections in the country rock and some xenoliths (Figs. 4.28B). The granitic material and the quartzofeldspathic veins were the competent layers in this case. Competent (viscous) layers tend to boudinage/fracture or buckle (fold) under layer-parallel extension or shortening relative to the surrounding host rock (the Malmesbury Group country rock in this case) which deforms in a ductile or plastic fashion (Fossen, 2010).

The lower greenschist facies of metamorphism of the Malmesbury Group country rock before granite intrusion suggests the host rocks were not at a depth great enough to start exhibiting plastic/ductile behaviour. Therefore, with the depth of burial not likely to be the primary reason for the apparent ductility of the country rock, other factors have to be considered. These include properties related to the granite phases such as their temperature and rheology (i.e. viscosity and strength) at the time of emplacement. Furthermore, the rheology of the country rock also has to be considered as rock mineralogy/composition (amongst other factors e.g. pressure, temperature, strain history, pore-fluid pressures & chemical activities; Passchier & Trouw, 2005) can have a profound influence on a rock's ability to deform in a ductile manner (e.g. Fossen, 2010).

At the emplacement level, the influx of magma is likely to lead to complex transient changes in the rheology of the country rock that reflect the dramatic changes in viscosity during the crystallization of a magmatic body (Miller & Paterson, 2001b). For example, the emplacement of igneous bodies introduces important rheological heterogeneities in the crust and can thermally weaken the surrounding country rocks (Davidson et al., 1992, 1994; Tommasi et al., 1994). This, therefore, suggests that most of the apparent ductile behaviour in the country rock of the study area was, in large part, caused by the heat of the intruding granite and its viscosity (i.e. a property that governs its capacity to behave as a solid).

With regards to the viscosity, the coarse grain sizes of the megacrystic phases of the study area (i.e. main coarse-grained porphyritic phase and medium- and coarse-grained porphyritic hybrid phases), suggest that the magma generating these phases underwent a degree of pre-emplacement crystallization, with crystallinity up to 50 % at the emplacement level (Farina et al., 2012). According to Miller et al. (2011), igneous material with ~45 to ~60% crystal load are termed magma mushes and are rheologically stronger but not as mobile compared to crystal-poor magmas. According to Yoshinobu et al. (2009), high-strength, crystal-melt mushes are capable of transmitting deviatoric stresses, which can drive both elastic and plastic deformation of host rock and xenoliths. This would explain the localization of ductile/plastic behaviour of the country rock in the lit-par-lit zone as opposed to areas outside of it (e.g. the northern end of the study area characterized by the microgranite intrusion). The numerous crystal-rich and megacrystic phases in the lit-par-lit zone could essentially behave as hot, high strength materials capable of deforming the country rock in a ductile manner.

Out of the two Malmesbury Group lithologies, which make up the compositional variation of the country rock in the study area, the metamudstone had the greater capacity to behave in a ductile fashion whereas the metasiltstone was relatively competent. This is because the metamudstones are the ones that commonly show ductile behaviour (e.g. elongation and a characteristic wavy appearance) (e.g. Fig. 4.30). This is supported by observations from various high-level magmatic systems, where intrusions preferentially exploit horizons of shale/mudrock lithologies that easily behave in a non-brittle fashion (e.g. Schofield et al., 2010, 2012; Magee et al., 2018). This implies that ductile deformation may be achieved, at least partially, around some large plutonic bodies even in the upper crust (Schofield et al., 2012).

Based on outcrop evidence and the details outlined above (as well as in section 8.5.3), the following can be concluded: (ii) the fine-grained hybrid phases in the lit-par-lit zone and the microgranites utilized discontinuities in the intruded rocks without any need to create extra room, and (iii) as the magma pulses intruding became more voluminous and porphyritic, the magma ductiley deformed the country rock to make space for itself. This observation indicates a certain degree of ductile flow of the host material to accommodate emplacement owing to highly viscous magma flow (e.g. Hutton, 1982).

8.5.4.3 Magmatic stoping: clues from rotated xenoliths in the lit-par-lit zone

If the country rocks are sufficiently brittle, the blocks of the roof over a rising pluton could become dislodged, fall, and sink through the magma in a process referred to as stoping (Winter, 2010). The stoping process is most efficient in the brittle upper crust where large temperature gradients between upper crustal rocks and intruding magma are expected (Žák et al., 2006). Some of the features that are generally attributed to the magmatic stoping process include: (i) the presence of xenoliths that have been enclosed by magma, (ii) mixed populations of xenoliths, (iii) stepped intrusive contacts, and (iv) the geochemical evidence of magma contamination (e.g. Cruden & Weinberg, 2018). Although magma stoping is an effective emplacement mechanism in shallow crustal levels, it cannot make the original room for the pluton where there was none before (Winter, 2010). This implies that stoping is a secondary or small-scale emplacement process that acts in conjunction with a primary process of emplacement.

In the study area, variably sized country rock xenoliths are enclosed within the various granitic phases (e.g. Fig. 4.27), suggesting a degree of stoping during the incremental emplacement of the granitic magma bodies. Therefore, apart from utilizing open spaces created along structural weaknesses in country rock for propagation, the granite phases appear to have created additional room for their propagation and subsequent emplacement through stoping during the final stages of emplacement. This interpretation is supported by observations from various granitoid plutons (e.g. Marsh, 1982; Hutton, 1996; Tikoff et al., 1999; Acocella, 2002; Bartley et al., 2012) where granitic felsic material appears to first infiltrate along pre-existing weaknesses in its host rocks as elongate “fingers” of magma which will eventually connect, given enough infiltration, resulting in the process of stoping.

An additional indicator of stoping in the study area comes in the form of rotated xenoliths. Some of the xenoliths, particularly in the lit-par-lit zone, have S_0 bedding and S_1 foliation planes that have a different orientation relative to the main Malmesbury Group S_0 and S_1 planes (Figs. 4.2, 4.29). The differently oriented S_0 and S_1 planes imply that the country rock bodies were dislodged and subsequently carried along with the magma where they become rotated and/or translated during magma transit (Paterson et al., 2008).

8.6 The origin of K-feldspar megacrysts

8.6.1 Introduction

The origin of K-feldspar megacrysts has been a subject of continued debate, with long-standing arguments being about which process, subsolidus or magmatic, has the most profound influence on their formation (Gualda, 2019). Some of the arguments in support of a magmatic origin (i.e. growth of K-feldspar when the igneous system was still largely molten at the pre-emplacement level) include the following (as described by Paterson et al., 2005; Vernon & Paterson, 2008):

(i) Euhedral-equant shapes
(ii) Simple and Carlsbad twinning
(iii) Concentrically arranged mineral inclusions parallel to crystallographic planes
(iv) Oscillatory & normal geochemical zoning
(v) Megacryst-rich clusters and their systematic distribution and orientation within plutonic suites (features attributed to movement and segregation while the magma was still sufficiently liquid to flow).

However, a pure magmatic origin has been contradicted by various phase equilibria experiments and natural examples of crystallization and partial melting (e.g. Winkler & Schultes, 1982; Whitney, 1988; Johnson & Rutherford, 1989). These experiments indicate that K-feldspar saturates late in the crystallization sequence of calc-alkaline, felsic magma leaving little space (< 50% melt) to grow large, euhedral megacrysts (Johnson & Glazner, 2010; Glazner & Johnson, 2013). This apparent contradiction has led to the debate and the subsequent derivation of various hypotheses aimed at determining the factors responsible for K-feldspar megacryst growth. Such hypotheses, which are based on experimental, textural, and geochemical observation, are summarized by Chambers (2020) as follows: (1) they owe their large sizes to slow nucleation rates and faster crystal growth rates compared to other matrix minerals (e.g. quartz, plagioclase, biotite) (Fenn, 1977; Vernon, 2018; Gualda, 2019); (2) they grew to large sizes due to prolonged growth (Memeti et al., 2014; Holness et al., 2018) via crystal transfer or mixing into different magma batches (Gagnevin et al., 2005; Paterson et al., 2016); (3) they texturally coarsened during late-stage crystallization at low melt percentages due to thermal cycling (Higgins, 1999; Johnson & Glazner, 2010; Glazner & Johnson, 2013); and/or (4) they represent metasomatically coarsened crystals that formed as low as 400 °C due to fluid fluxing during incremental pluton growth (Glazner & Johnson, 2013).

Based on the occurrence of K-feldspar megacrysts within the country rock (Fig. 4.25A, B) relative to those forming part of the porphyritic granite phases (Figs. 4.10, 4.11), an argument can be made for contrasting origins of the K-feldspar megacrysts in the study area. Using outcrop and petrographic evidence, this section will aim to prove whether there are any contrasting origins (i.e. magmatic or in-situ crystallization) for the K-feldspar megacrysts based on the lithology they occur within.

8.6.2 The origin of K-feldspar megacrysts in the porphyritic granite phases

The K-feldspar grains that occur within the porphyritic granite phases have all the characteristics that are suggestive of an igneous origin, as previously mentioned. These include dominantly euhedral forms (indicating that they grow freely in liquid) with a tabular shape or habit, simple twins and concentric geochemical zonation (Figs. 4.10B, C, 4.11). The best way the occurrence of the latter is recognized in the study area (due to extensive exsolution) is by crystallographically aligned mineral inclusions (defined by biotite grains and plagioclase as well quartz) parallel to crystallographic planes (Figs. 4.10A, C, 4.11B). These aligned inclusions indicate that the K-feldspar megacrysts grew while surrounded by melt, allowing the inclusions to periodically attach themselves to the faces of the growing crystals (Moore & Sisson, 2008). Considering that the K-feldspar megacrysts have large sizes (2.5-10 cm in length) and show concentric zoning, they are likely to have grown to their sizes due to prolonged growth as a result of repeated replenishment of magma bodies by fresh granitic melt, that maintained temperatures above the solidus for extended periods, providing components necessary for K-feldspar growth (Moore & Sisson, 2008). This corresponds to the interpreted primary mechanism of emplacement for the granite phases in the study area (i.e. incremental emplacement of magma bodies). The zoning in the megacrysts, therefore, represents compositional changes within the magma (or pluton) with time caused by fluctuations in growth conditions during solidification (Holness et al., 2018); this also applies to the zoning features shown by the plagioclase phenocrysts (e.g. Fig. 4.12A, B).

Furthermore, the location of the derived K-feldspar saturation boundary for the Peninsula Pluton, experimentally derived by Farina et al. (2012), yields temperatures of ≤ 750°C. At this temperature, the magma contains about 50 vol. % of crystals (Farina et al., 2012), a value that matches with experimental evidence indicating that when K-feldspar begins to crystallize in granites, the magma typically contains 60 –70 % liquid (Clemens & Wall, 1981; Vernon & Paterson, 2008; Holness et al., 2018). This proves that abundant melt is still present at the stage where K-feldspar starts to crystallize, allowing sufficient space for the megacrysts to grow (Vernon, 1986).

8.6.3 K-feldspar megacrysts in the country rocks – a case for an igneous/magmatic origin

Most of the K-feldspar megacrysts occurring in the country rocks have similar characteristics that are suggestive of an igneous origin such as euhedral shapes with tabular habits and crystallographically aligned mineral inclusions. If an igneous origin for the K-feldspar megacrysts in the country rock is envisaged, a possible mechanism that could explain how they ended up being embedded in the country rock is when a dyke/fracture (or inclined sheet) is modelled as a buoyancy-driven structure of finite volume relative to a surrounding host rock that behaves as an elastic solid (Weertman, 1971a). This process was also described and modelled by Kisters et al. (2009), from the much better exposed Damara Belt in Namibia.

For a dyke or an inclined sheet to form and propagate, the magmatic overpressure (p_o - driving pressure) must be sufficiently high to overcome the tensile strength of the host rock (T_0) and the normal stress or minimal principal stress (σ_3) on the magma-filled fracture (Gudmundsson, 2011). The conditions for dyke initiation from a fluid source are:

$$p_l + p_e = \sigma_3 + T_0$$

where p_l is the lithostatic stress at the rupture site in the walls of the magma chamber and p_e is the excess pressure (i.e. magma pressure in excess of the lithostatic/overburden pressure) (Gudmundsson, 2011).

Lithostatic stress, where the principal stresses are equal (i.e. $\sigma_1 + \sigma_2 + \sigma_3$), is usually used as a reference state of stress for magma chambers. In instances where the lithostatic equilibrium of a magma chamber is disturbed during external and/or internal loading (i.e. when forces, stresses, pressures, or displacements are applied to a magma chamber), deviation from lithostatic stress is expected (Gudmundsson, 2011). For a host rock that behaves as an elastic material, as the earth's upper crust generally does during external and/or internal loading, the host rock responds immediately to pressure changes in the chamber (Gudmundsson, 2011). Once the excess pressure reaches the tensile strength of the host rock, the magma chamber ruptures and injects dykes, inclined sheets, or sills.

The Weertman models for buoyancy-driven ascending dykes/fractures, in a host rock that behaves as an elastic solid, were first introduced by Weertman (1971a, b, 1973). In Weertman models, the volume of fluid contained in the fracture is conserved during propagation by assuming that the fractures pinch themselves close at the tail while they propagate (Rivalta et al., 2015). The dimension of the cracks must, however, be large enough to make surface tension effects associated with the magma unimportant, but small relative to the thickness of the crust (Weertman, 1971a; Rivalta et al., 2015). Once the vertically oriented fractures/dykes are formed, the driving force for fracture filling would be the pressure difference between the opening fracture and the surrounding rock (Sleep, 1988). It is during this stage that the surrounding magma and its constituents (e.g. K-feldspar megacrysts in the case of the study area) flow into the new opening as a result of the pressure contrast (Fig. 8.10A). The Weertman model predicts that as magma rises into a vertical, slowly moving fracture, the low density of the magma compared to the host rock means that the pressure in the fracture falls less rapidly than in the surrounding denser rock. Given this density contrast between melt and host rocks, for any equal change in depth (h) along the fracture, there will be a greater change in lithostatic pressure (P_{lith}) in the host rocks compared with the pressure in the melt-filled inclined fracture (P_{melt}) (Kisters et al., 2009). As a consequence the melt pressure exceeds the lithostatic pressure at the tip (or head) of the fracture and the tip will balloon outward (Melosh, 2011) (Fig. 8.10B).

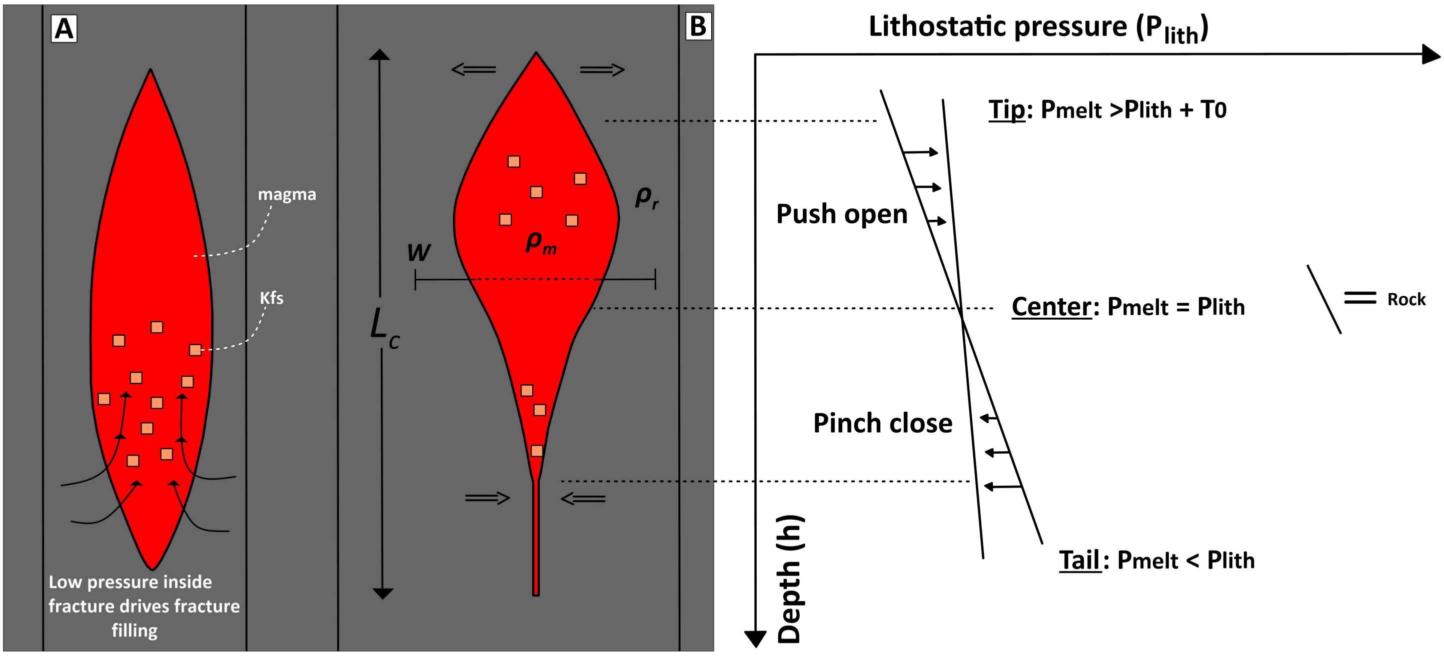

***Figure 8.10**: Model for a Weertman buoyancy-driven fracture/dyke (modified after Melosh, 2011). Based on the predictions of the Weertman models, vertically oriented magma-filled fractures of constant volume can "self-propagate," once they reach a critical length (L_c) (also called the buoyancy length). The relation between the critical fracture length (Lc) and width (w) is $L_c = \sqrt{Ew/\Delta\rho gh}$, where E is Young's modulus and $\Delta\rho gh$ is the buoyancy pressure or pressure drop (Melosh, 2011). In $\Delta\rho gh$, $\Delta\rho = \rho r - \rho m$ (the difference between host-rock density, ρr, and magma density, ρm), g is the acceleration due to gravity and h is the depth. (A) An idealized fracture opening. Once a fracture is formed, the driving force for fracture filling would be the pressure difference between the opening fracture and the surrounding rock (shown in dark grey). It is during this stage that the surrounding magma and its constituents (e.g. K-feldspar megacrysts) flow into the new opening as a result of the pressure contrast. (B) A rising magma filled fracture, with a characteristic bulbous head and a tapered tail, driven by buoyancy differences between magma and the surrounding rock. Given this density contrast between melt and host rocks, for any equal change in depth (h) along the fracture, there will be a greater change in lithostatic pressure (P_{lith}) in the wall rocks compared with the pressure in the melt-filled inclined fracture (P_{melt}). As a result, P_{melt} at the tip of the propagating fracture will exceed the sum of the P_{lith} and the tensile (T_0) strength of the host rock enabling the P_{melt} to part the bedding/foliation planes of the host rock. At the tail of the fracture, $P_{melt} < P_{lith}$ and so P_{lith} will close the melt-filled fracture. At the centre of the fracture, $P_{melt} = P_{lith}$ and so the fracture remains open.*

However, as the tip of the fracture balloons and the fracture continuously lengthens, the tail of the fracture grows narrower and pinches off due to the elastic reaction of the surrounding rock and because the pressure in the rock exceeds the pressure in the dyke tail (Fig. 8.10B) (Melosh, 2011). In the case of the study area, some of the K-feldspar megacrysts get dragged upward with the propagating magma head as magma is forced out of the tail (Fig. 8.10B). The magma in the fracture tail, however, cannot be "squeezed" or pinched out in its entirety because of the very large viscous resistance as the fracture thins (Stevenson, 1982). Therefore, some fraction of melt/magma will become "trapped" within the tail as a result. Included in this "trapped" magma fraction is the K-feldspar megacrysts which are left embedded in the country rock as the base/tail of the dyke is continually sealed off or closes. This would serve to explain the observation of why some of the K-feldspar grains embedded in the country rock occur with trails and/or tails of quartzofeldspathic granitic material (i.e. they are not completely isolated by themselves) (e.g. Fig. 4.25B).

8.6.4 K-feldspar megacrysts in the country rocks – a case for late-stage growth

There is an argument that can be made against the proposed mechanism that explains the apparent inclusion or "entrapment" of K-feldspars in the country rock. From a theoretical standpoint, the subject of dyke propagation is complex, involving fluid and fracture mechanics, solid deformation, and thermodynamic aspects of magma solidification (Taisne et al., 2011). Therefore any model for dyke propagation, such as the Weertman buoyancy-driven dyke ascent model in section 8.6.3, has to ignore or simplify some of the processes that can affect dyke ascent and intrusion (Buck et al., 2006). Among some of the processes ignored or simplified during modelling, as pointed out by Lister & Kerr (1991) and Buck et al. (2006) are:

(i) The pressure and flux of magma coming out of a source region

(ii) The viscous resistance to magma flow along the body of the dyke and into the tip region (e.g. what is the maximum crystal content of the magma allowed to flow in the fracture openings before it becomes too viscous and unable to flow through the country rock?)

(iii) Elastic stresses in the lithosphere

(iv) The crustal strength or lithostatic force (e.g. could the confining pressure applied by the column of overlying rock allow for the formation of large/wide enough fracture openings that can accommodate a crystal-rich/megacrystic magma?)

(v) The freezing or solidification of magma during ascent (related to how rapidly it crystallizes or the extent of undercooling)

(vi) Host rock softening due to heating by magma (e.g. can the country rock behave in a ductile enough fashion to facilitate or allow magma to squeeze and pass through it?)

Considering some of the limitations associated with dyke propagation mechanisms, an alternative explanation towards the occurrence of K-feldspar megacrysts in the country rock of the study area involves considering an *in situ* crystallization or late-stage growth of the K-feldspar megacrysts. As previously mentioned in section 8.6.1, experimental studies demonstrate that K-feldspar is typically the last major phase to crystallize and that most K-feldspar growth occurs after the magma crosses the rheologic lock-up threshold of ~50 % crystals (e.g. Whitney, 1988; Johnson & Rutherford, 1989). After a magma crosses this threshold, the relative motion of crystals becomes difficult and extrusion of the magma as lava is nearly impossible (Glazner & Johnson, 2013). Based on this, Johnson and Glazner (2010) propose that K-feldspar megacrysts grow to large sizes during the later stages of crystallization owing to the cycling of temperature during incremental emplacement, in the presence of a late-stage magmatic liquid. In this case, small K-feldspar crystals may partially or completely dissolve, along with the edges of larger crystals, which after multiple reheating and subsequent cooling events texturally coarsen (also known as Ostwald ripening) to become the megacrysts (Higgins, 1999; Johnson & Glazner, 2010). Furthermore, Glazner and Johnson (2013) suggest that K-feldspars megacrysts represent metasomatically coarsened crystals that formed as low as 400 °C due to fluid fluxing during incremental pluton growth.

More recently, Gualda (2019) argued against the textural coarsening process invoked to explain the large sizes of K-feldspar megacrysts. This was done by using rate equations developed in material sciences to investigate the viability of coarsening as an explanation for the growth of K-feldspar grains to megacrystic sizes. Using a range of rate constants calculated from suitable parameters for silicate magmatic systems, Gualda (2019) was able to show that: (i) diffusion rates are the main controls on the rate constant for coarsening in silicate melts and (ii) coarsening in silicate magmas cannot lead to crystals larger than tens of μm on timescales relevant for igneous processes. Gualda (2019) instead argues for the interplay between nucleation and growth rates in magmas as the likely origin of K-feldspar megacrysts.

Chambers et al. (2020) also argue against late-stage textural coarsening for K-feldspar megacrysts using dated zircon inclusions from the core and rim of one K-feldspar megacryst sampled from the Tuolumne Intrusive Complex, California, USA. The results showed that the core-to-rim age progression of zircon inclusions is indicative of megacryst growth in an igneous environment over at least 0.5 million years. The 0.5 million year age difference between the megacryst core and rim zircons supports the idea of continuous, extended growth in a long-lived magma body, or pulsed, rapid growth in multiple magma bodies, and/or a combination of these two end members, rather than sub-solidus K-feldspar coarsening and fast growth of the whole crystal (Chambers et al., 2020).

Despite all the factors that go against late-stage growth or in-situ crystallization of K-feldspar megacrysts, such processes having occurred at the Sea Point contact cannot be ruled out. This is because a more extensive study on mineralogical and textural data in conjunction with results from experimental and natural petrologic studies of granitic systems (e.g. Johnson &

Glazner, 2010; Glazner & Johnson, 2013) is needed to ascertain the occurrence of such a process. However, based on current evidence, such as the observation that the K-feldspar megacrysts occurring in the country rock show all of the textural characteristics that are indicators of an igneous origin (section 8.6.1), the conclusion is that the K-feldspar megacrysts in the country rock are of igneous origin until proven otherwise by further studies.

8.7 K-feldspar megacryst defined magmatic foliation: implications and conclusions

The consensus from the SPO study is that, overall, the orientation of the megacrysts are fairly consistent approaching the lit-par-lit zone, within it and to the north (Fig. 5.29). The orientation of the megacrysts largely corresponds (or is generally concordant) with the orientation of the bedding (S_0) and the S_1 foliation planes within the lit-par-lit zone. With aid from the numerous magma flow indicators (e.g. Figs. 4.28C, D, 4.29) the magma flow direction was to the WNW.

At station SPO (1), the most southerly station in the study area, the megacryst orientation is NNW-SSE (Fig. 5.29). This is consistent with what is observed as one heads further south, from Sea Point, into Bantry Bay, Clifton and Camps Bay where the megacryst orientation is dominantly NNW-SSE and N-S trending (Kumbe, 2017) (Appendix D2). The megacryst orientation changes from dominantly NNW-SSE and N-S trending (in Bantry Bay, Clifton and Camps Bay) towards WNW-ESE and E-W trending approaching the Sea Point contact (Fig. 5.29), which is located on the edge of the pluton (Fig. 2.3B). These observations suggest that the Peninsula Pluton is elongated in a general direction of NW-SE parallel to the structural trend of the Malmesbury Group bedding and foliation structures, and the strike of the Colenso fault. In other words, the orientation defined by the megacrysts is sub-parallel to external pluton contacts in general (e.g. Paterson et al., 1989). The overall alignment of the megacrysts with the country rock fabric thus reflects a magmatic type of lineation developed in a non-coaxial flow where crystals align themselves relative to the velocity gradient of magma flow due to the shear or drag between the magma and the host rock contact (Paterson et al., 1989; Winter, 2010). This, therefore, precludes the involvement of any primary or tectonic stresses in the alignment of the megacrysts.

9 Conclusions

9.1 Geochemistry summary

A summary of the geochemical and isotopic characteristics of the Peninsula S-type granite and the metasedimentary country rocks of the Malmesbury Group exposed at the Sea Point contact is as follows:

Granitic phases

(1) Based on the linear trends between the whole-rock major and trace elements of the granites vs. maficity, their initial Sr ratios (all greater than 0.706) and εNd(t) values (all negative), the granites of the study area are consistent with the currently proposed petrogenetic model for the Peninsula Pluton and the CGS in the broader context (e.g. Stevens et al., 2007; Villaros et al., 2009a; Harris & Vogeli, 2010); i.e., they are crustally derived and their chemical variability is controlled primarily by peritectic assemblage entrainment.

(2) Fractional crystallisation of K-feldspar, assessed using the diagrams of Ba/Sr vs. Sr, Ba vs. Eu, and Ba/Sr vs. Sr, is interpreted to have played a secondary, late-stage role which caused a secondary compositional trend or variation closer to the emplacement site. There is outcrop evidence in the lit-par-lit zone to suggest that assimilation (i.e. gradational contacts and the ductile behaviour of the country rock) the filter-pressing mechanism (K-feldspar entrapment in the country rock) may have caused geochemical variability at a localized scale. The extent to which they caused variation, however, could not be determined with the current whole-rock data and will need more rigorous testing.

Malmesbury Group metasedimentary rocks

(1) An upper crustal origin for the metasedimentary rocks in the study area is interpreted. This is supported by the low εNd (t) value (-7.84) and the fairly high initial Sr value (0.728103) sample SP16 produced. Geochemically, the likely source rocks, which eroded and weathered to form the metasedimentary rocks of the study area, are likely to have been rhyodacites/dacites which were fairly radiogenic and plagioclase poor. The actual source of metasedimentary rock, on a regional scale, is likely to have been the 950-1200 Ma ortho- and para-gneisses of the Namaqua Metamorphic Province based on the prominent input of late-Mesoproterozoic and early Neoproterozoic zircons in some of the Malmesbury Group formations (Frimmel et al., 2013).

(2) The fairly low intensity of weathering (CIA values of 62.36-66.13) indicates that the geochemical variation of the metasedimentary rocks was mostly dominated by the composition of the source materials as opposed to any subsequent sediment recycling or reworking and compositional maturing of the sediments before lithification.

9.2 Granite emplacement processes summary

A summary of the probable granite emplacement mechanisms and timing of emplacement relative to the deformation of the country rocks is as follows:

(1) Outcrop and petrographic evidence suggest a late-syn tectonic granite emplacement relative to the main deformation phase (D_1) associated with the NE-SW regional shortening of the Malmesbury fore-arc basin during the Saldanian orogeny. The evidence was in the form of: (i) boudinaged granite pulses which indicate NE-SW shortening and WNW-ESE extension, (ii) the syntectonic growth of the contact metamorphic minerals of cordierite and biotite and (iii) bedding and folds in the Malmesbury Group metasedimentary rocks draped/wrapped around the competent granite as deformation (regional shortening) continued.

(2) At the site of emplacement, the inclined/steep pre-existing planar anisotropies (folded bedding planes and foliations) in the country rock provided favourable paths along which the granitic magma could be injected (from their source) and propagate. The emplacement was concordant to the country rock structure, classifying the granites as inclined sills or sheets, and implying an intrusion more or less normal to regional shortening. Such a high angle intrusion can be achieved by assuming conditions of low differential stress i.e. when the difference in tensile strength normal and parallel to the bedding and foliation anisotropy of the country rock is larger than the regional differential stress ($\sigma_1 - \sigma_3$, with $\sigma_1 \geq \sigma_2 \geq \sigma_3$) at the time of emplacement (e.g. Lucas & St. Onge, 1995). Sheet propagation occurred through the balance of the following conditions: (i) density contrasts between host rocks and magmas, (ii) the pressure differential along the subvertical fractures/sheets, and (iii) the melt pressure equalling the lithostatic pressure to keep the magma pathways open and being sufficiently high such that it exceeds the sum of σ_1 and the tensile strength of the rock parallel to σ_1 (e.g. Lister & Kerr, 1991; Lucas & St. Onge, 1995; Dahm, 2000; Mériaux & Lister, 2002; Gudmundsson, 2011; Ferre et al., 2012).

(3) The granites were emplaced as incrementally assembled, repeated pulses of inclined granitic sills with partial solidification of each magma batch before subsequent injections and very limited mixing between magma batches (e.g. Farina et al., 2012). The crystallization ages of the dated granite samples are identical within error and vary between 538.7 ± 3.6 Ma and 542.7 ± 2.9 Ma. They therefore cannot prove which granite phase intruded first and which one proceeded. Based on field evidence, the microgranite and the fine-grained hybrid granites are interpreted to have intruded first based on their fine-grained nature (alluding to magma quenching). The various coarser-grained and porphyritic phases were next to intrude, with their coarse grain-sizes and lack of chilled margins with the country rock suggesting that the time interval between their successive emplacements was not too long, preventing the country rock from completely cooling down between each magma batch.

(5) Magma stoping is interpreted to be a secondary emplacement process whereas the occurrence of crustal assimilation, as an effective emplacement process, cannot be proven far beyond the textural evidence provided. The localized ductile behaviour of the metamudstone in the lit-par-lit zone suggests a degree of ductile flow of the host material to accommodate granite emplacement owing to highly viscous magma flow. In other words, as the magma pulses intruding become more voluminous, the porphyritic granitic phases pushed aside the country rock to make space for themselves particularly as the magma pulses intruding become more voluminous.

(7) The overall alignment of the K-feldspar megacrysts with the country rock fabric reflects a magmatic type of lineation developed in a non-coaxial flow. The megacrysts aligned themselves relative to the velocity gradient of magma flow due to the shear or drag between the magma and the host rock contact (e.g. Paterson et al., 1989; Winter, 2010).

(8) A possible mechanism that could explain how some K-feldspar megacrysts ended up being embedded in the country rock is when a dyke/fracture is modelled as a buoyancy-driven structure relative to a surrounding elastic host rock (Weertman, 1971a). The Weertman model predicts that if the average pressure in a magma-filled fracture and the surrounding rock is equal, the pressure in the fracture exceeds that of the enclosing rock at the top of the fracture, whereas the pressure in the rock exceeds the pressure at its tail. As a result, the fracture pinches itself close at the tail while the magma at the head pushes the host material open, allowing for further ascension. Some fraction of magma will become “trapped” as the fracture pinches itself close at the tail. Included in this “trapped” magma fraction, in the case of the study area, could be the K-feldspar megacrysts which are left embedded in the country rock as the base/tail of the fracture is continually sealed off.

9.3 Recommendations

- Geochemical study (e.g. electron microprobe) on the cordierite alteration types, in both the granites and metamudstones, to determine their origin (e.g. Ogiermann, 2002). This is because the cordierites in the granites are characterized specifically by one form of pinitization as opposed to the varying types in the metamudstones. This suggests that the pinitization of the cordierites in the country rocks is potentially due to several different and varied fluid flow events, including one potentially derived from the granites themselves.
- In-depth tests and analyses, other than whole-rock geochemical data, to determine the extent and validity of assimilation and the filter pressing mechanism

References

Abel, C. (1818). Narrative of a Journey in the Interior of China, in the Years 1816 and 1817.

Acocella, V. (2002). Space accommodation by roof lifting during pluton emplacement at Amiata (Italy). Terra Nova, 12, 149-155.

Allmendinger, R.W., Cardozo, N.C., Fisher, D. (2013). Structural Geology Algorithms: Vectors & Tensors. Cambridge University Press, 289.

Anderson, E. M. (1951). The Dynamics of Faulting and Dyke Formation with Applications to Britain, 2nd edition. Edinburgh: Oliver and Boyd.

Annen, C., Sparks, R. S. J. (2002). Effects of repetitive emplacement of basaltic intrusions on thermal evolution and melt generation in the crust. Earth and Planetary Science Letters, 203(3-4), 937-955.

Annen, C. (2011). Implications of incremental emplacement of magma bodies for magma differentiation, thermal aureole dimensions and plutonism–volcanism relationships. Tectonophysics, 500(1-4), 3-10.

Annen, C., Blundy, J. D., Leuthold, J., Sparks, R. S. J. (2015). Construction and evolution of igneous bodies: Towards an integrated perspective of crustal magmatism. Lithos, 230, 206-221.

Armstrong, R., de Wit, M. J., Reid, D., York, D., Zartman, R. (1998). Cape Town's Table Mountain reveals rapid Pan-African uplift of its basement rocks. Journal of African Earth Sciences, 27, 1A, 10.

Barbarin, B. (2005). Mafic magmatic enclaves and mafic rocks associated with some granitoids of the central Sierra Nevada batholith, California: nature, origin, and relations with the hosts. Lithos 80, 155–177.

Bartley, J. M., Glazner, A. F., Mahan, K. H. (2012). Formation of pluton roofs, floors, and walls by crack opening at Split Mountain, Sierra Nevada, California. Geosphere, 8 (5), 1086-1103.

Bea, F., Montero, P., Gonzalez-Lodeiro, F., Talavera, C. (2007). Zircon inheritance reveals exceptionally fast crustal magma generation processes in Central Iberia during the Cambro-Ordovician. Journal of Petrology 48, 2327–2339.

Belcher, R.W. (2003). Tectonostratigraphic evolution of the Swartland region and aspects of orogenic lode-gold mineralization in the Pan-African Saldania Belt, Western Cape, South Africa. PhD thesis, University of Stellenbosch, Stellenbosch, 330 pp.

Belcher, R.W., Kisters, A.F.M. (2003). Lithostratigraphic correlations in the western branch of the Pan-African Saldania belt, South Africa: the Malmesbury Group revisited. South African Journal of Geology 106, 327–342.

Belcher, R. W., Kisters, A. F.M. (2006). Progressive adjustments of ascent and emplacement controls during incremental construction of the 3.1 Ga Heerenveen batholith, South Africa. Journal of Structural Geology, 28(8), 1406-1421.

Berger, J., Lo, K., Diot, H., Triantafyllou, A., Plissart, G., Féménias, O. (2017). Deformation-driven differentiation during in situ crystallization of the 2.7Ga Iguilid mafic intrusion (West African Craton, Mauritania). Journal of Petrology, 58(4), 819–840.

Bhatia, M. R., Crook, K. A. (1986). Trace element characteristics of graywackes and tectonic setting discrimination of sedimentary basins. Contributions to Mineralogy and Petrology, 92(2), 181-193.

Bock, B., Bahlburg, H., Wörner, G., Zimmermann, U. (2000). Ordovician arcs and terranes in NW-Argentina and N-Chile? Geochemical and isotope evidence. Journal of Geology 108, 513-535.

Bowen, N.L. (1948). The granite problem and the method of multiple prejudices. Geological Society of America, 28, 79–90.

Breaks, F. W., Moore J. M. (1992). The Ghost Lake batholith, Superior Province of Northwestern Ontario - a fertile, S-type, peraluminous granite - rare-element pegmatite system. The Canadian Mineralogist (30), 835-875.

Brown, M. (1994). The generation, segregation, ascent and emplacement of granite magma: the migmatite-to-crustally-derived granite connection in thickened orogens. Earth-Science Reviews, 36(1-2), 83-130.

Brown, M., Pressley, R.A. (1999). Crustal melting in nature: Prosecuting source processes: Physics and Chemistry of the Earth 24, 305–316.

Brown, M. (2001). Crustal melting and granite magmatism: Key issues. Physics and Chemistry of the Earth, 26, 201–212.

Brown, M. (2010). The spatial and temporal patterning of the deep crust and implications for the process of melt extraction. Philosophical Transactions of the Royal Society: Mathematical, Physical and Engineering Sciences, 368(1910), 11-51.

Brown, M. (2013). Granite: From genesis to emplacement. Geological Society of America Bulletin, 125, 1079-1113.

Brun, J. P., Gapais, D., Cogne, J. P., Ledru, P., & Vigneresse, J. L. (1990). The Flamanville granite (northwest France): an unequivocal example of a syntectonically expanding pluton. Geological Journal, 25(3-4), 271-286.

Bucher, K., Frey, M. (2002). Petrogenesis of metamorphic rocks. Springer Science & Business Media.

Bucher, K., Grapes, R. (2011). Petrogenesis of metamorphic rocks. Springer Science & Business Media.

Buck, W. R., Einarsson, P., Brandsdóttir, B. (2006). Tectonic stress and magma chamber size as controls on dike propagation: Constraints from the 1975–1984 Krafla rifting episode. Journal of Geophysical Research: Solid Earth, 111(B12).

Buddington, A. (1959). Granite emplacement with special reference to North America. Geological Society of America, 70, 671.

Buggisch, W., Kleinschmidt, G., Krumm, S. (2010). Sedimentology, geochemistry and tectonic setting of the Neoproterozoic Malmesbury Group (Tygerberg Terrane) and its relation to neighbouring terranes, Saldania Fold Belt, South Africa. Neues Jahrbuch für Geologie und Paläontologie – Abhandlungen 257, 85-114.

Burchardt, S., Tanner, D., Krumbholz, M. (2012). The Slaufrudalur pluton, southeast Iceland—an example of shallow magma emplacement by coupled cauldron subsidence and magmatic stoping. Bulletin, 124(1-2), 213-227.

Burchardt, S., Troll, V. R., Schmeling, H., Koyi, H., Blythe, L. (2016). Erupted frothy xenoliths may explain lack of country-rock fragments in plutons. Scientific reports, 6, 34566.

Burchardt, S. (2018). Introduction to volcanic and igneous plumbing systems—Developing a discipline and common concepts. In Volcanic and Igneous Plumbing Systems (pp. 1-12). Elsevier.

Burg, J.P. (2017). Folds Retrieved from http://www.files.ethz.ch/structuralgeology/JPB/ files/English/8folds.pdf

Burnham, A. D. (2018). Zircon. Earth Systems and Environmental Sciences, 1-11.

Cao, H. W., Zhang, Y. H., Santosh, M., Li, G. M., Hollis, S. P., Zhang, L. K., Duan, Z. M. (2018). Petrogenesis and metallogenic implications of Cretaceous magmatism in Central Lhasa, Tibetan Plateau: A case study from the Lunggar Fe skarn deposit and perspective review. Geological Journal, 54(4), 2323-2346.

Cardozo, N., Allmendinger, R.W. (2013). Spherical projections with OSXStereonet. Computers & Geosciences 51, 193-205.

Chambers, M., Memeti, V., Eddy, M. P., Schoene, B. (2020). Half a million years of magmatic history recorded in a K-feldspar megacryst of the Tuolumne Intrusive Complex, California, USA. Geology, 48(4), 400-404.

Champion, D.C. (2013). Neodymium depleted mantle model age map of Australia: explanatory notes and user guide. Record 2013/44. Geoscience Australia: Canberra.

Chappell, B. W., White, A. J. (1974). Two contrasting granite types. Pacific Geology 8(2), 173-174.

Chappell, B.W., White, A.J.R., Williams, I.S., Wyborn, D. Wyborn, L.A.I. (2000). Lachlan Fold Belt granites revisited: High- and low-temperature granites and their implications: Australian Journal of Earth Sciences, v. 47, 123–138

Chemale, J.F., Scheepers, R., Gresse, P.G., Van Schmus, W.R. (2011). Geochronology and sources of late Neoproterozoic to Cambrian granites of the Saldania Belt. International Journal of Earth Sciences 100, 431-444.

Clarke, D. B., Carruzo S. (2007). Assimilation of country-rock ilmenite and rutile in the south mountain batholith, Nova Scotia, The Canadian Mineralogist. 45:31-42.

Clarke, D. B. (2007). Assimilation of xenocrysts in granitic magmas: principles, processes, proxies, and problems. The Canadian Mineralogist, 45(1), 5-30.

Clarke, D. B., Erdmann, S. (2008). Is stoping a volumetrically significant pluton emplacement process?: Comment. Geological Society of America Bulletin, 120(7-8), 1072-1074.

Clemens, J. D., Wall, V. J. (1981). Origin and crystallization of some peraluminous (S-type) granitic magmas. The Canadian Mineralogist, 19(1), 111-131.

Clemens, J.D., Mawer, C.K. (1992). Granitic magma transport by fracture propagation. Tectonophysics 204, 339–360.

Clemens, J.D. (2003). S-type granitic magmas—petrogenetic issues, models and evidence. Earth-Science Reviews 61, 1–18.

Clemens, J. D., Benn, K. (2010). Anatomy, emplacement and evolution of a shallow-level, post-tectonic laccolith: the Mt Disappointment pluton, SE Australia. Journal of the Geological Society, 167(5), 915-941.

Clemens, J. D., Stevens, G., Farina, F. (2011). The enigmatic sources of I-type granites: The peritectic connexion. Lithos 126 (3-4), 174-181.

Clemens, J. D. (2012). Granitic magmatism, from source to emplacement: a personal view. Applied Earth Science 121 (3), 107-136.

Clemens, J.D., Stevens, G. (2012). What controls chemical variation in granitic magmas? Lithos 134–135, 317–329.

Clemens, J.D., Stevens, G., Frei, D., Joseph, C.S.A. (2017). Origins of cryptic variation in the Ediacaran–Fortunian rhyolitic ignimbrites of the Saldanha Bay Volcanic Complex, Western Cape, South Africa. Contributions to Mineralogy and Petrology, 172, 99.

Coleman, D.S., Gray, W., Glazner, A.F. (2004). Rethinking the emplacement and evolution of zoned plutons: Geochronologic evidence for incremental assembly of the Tuolumne Intrusive Suite, California. Geology, 32, 433-436.

Collins, W.J. (1996). Lachlan Fold Belt granitoids: products of three-component mixing. Transactions of the Royal Society of Edinburgh: Earth Science (87), 171-179.

Corfu, F., Hanchar, J. M., Hoskin, P. W., Kinny, P. (2003). Atlas of zircon textures. Reviews in mineralogy and geochemistry, 53(1), 469-500.

Cruden, A. R., Weinberg, R. F. (2018). Mechanisms of magma transport and storage in the lower and middle crust—magma segregation, ascent and emplacement. In Volcanic and Igneous Plumbing Systems. Elsevier, pp. 13-53.

Cullers, R. L. (1994). The controls on the major and trace element variation of shales, siltstones, and sandstones of Pennsylvanian-Permian age from uplifted continental blocks in Colorado to platform sediment in Kansas, USA. Geochimica et Cosmochimica Acta, 58(22), 4955-4972.

Cullers, R. L. (2002). Implications of elemental concentrations for provenance, redox conditions, and metamorphic studies of shales and limestones near Pueblo, CO, USA. Chemical Geology, 191(4), 305-327.

Da Silva, L.C., Gresse, P.G., Scheepers, R., McNaughton, N.J., Hartmann, L.A., Fletcher, I. (2000) U-Pb and Sm-Nd age constraints on the timing and sources of the Pan-African Cape Granite Suite, South Africa. Journal of African Earth Science 30,795–815.

Dahm, T. (2000), Numerical simulations of the propagation path and the arrest of fluid-filled fractures in the Earth, Geophysical Journal International, 141, 623–638.

Darwin, C.R. (1844). Geological observations on the volcanic islands visited during the voyage of H.M.S. Beagle, together with some brief notices of the geology of Australia and the Cape of Good Hope. Being the second part of the geology of the voyage of the Beagle, under the command of Capt. Fitzroy, R.N. during the years 1832 to 1836. Smith Elder and Co, London.

Davidson, C., Hollister, L.S., Schmid, S.M. (1992). Role of melt in the formation of a deep-crustal compressive shear zone: the Maclaren Glacier metamorphic belt, south-central Alaska. Tectonics 11, 348– 359.

Davidson, C., Schmid, S.M., Hollister, L.S. (1994). Role of melt during deformation in the deep crust. Terra Nova 6, 133– 142.

Davis, G. H., Reynolds, S. J., Kluth, C. F. (2011). Structural geology of rocks and regions. John Wiley & Sons.

Deer, W.A., Howie, R.A., Zussman, J. (2013). An Introduction to the Rock-forming Minerals. Longman Group Limited, London, pp 696.

D'Lemos, R.S., Brown, M., Strachan, R.A. (1992). Granite magma generation, ascent and emplacement within a transpressional orogeny: Journal of the Geological Society of London, 149, 487–490.

DePaolo, D. (1981). A neodymium and strontium isotopic study of the Mesozoic calc-alkaline granitic batholiths of Sierra Nevada and Peninsular Ranges, California. Journal Geophysical Research 68, 470-488.

Díaz-Alvarado, J., Fernández, C., Díaz-Azpiroz, M., Castro, A., Moreno-Ventas, I. (2012). Fabric evidence for granodiorite emplacement with extensional shear zones in the Variscan Gredos massif (Spanish Central System). Journal of Structural Geology 42, 74-90.

Didier, J., Barbarin, B. (1991). The different types of enclaves in granites-Nomenclature. In Enclaves and granite petrology (pp. 19-23).

Elburg, M. A. (1996). Genetic significance of multiple enclave types in a peraluminous ignimbrite suite, Lachlan Fold Belt, Australia. Journal of Petrology, 37(6), 1385-1408.

Erdmann, S., London, D., Morgan, G. B., Clarke, D. B. (2007). The contamination of granitic magma by metasedimentary country-rock material: an experimental study. The Canadian Mineralogist, 45(1), 43-61.

Farina, F., Stevens, G., Villaros, A. (2012). Multi-batch, incremental assembly of a dynamic magma chamber: the case of the Peninsula pluton granite (Cape Granite Suite, South Africa). Contributions to Mineralogy and Petrology 106, 193-216.

Fedo, C. M., Wayne Nesbitt, H., Young, G. M. (1995). Unravelling the effects of potassium metasomatism in sedimentary rocks and paleosols, with implications for paleoweathering conditions and provenance. Geology, 23(10), 921-924.

Fenn, P.M. (1977). The nucleation and growth of alkali feldspars from hydrous melts: Canadian Mineralogist, 15, 135–161.

Fernández, R. D., Pascual, F. J. R., Parra, L. M. M. (2019). Re-folded structure of syn-orogenic granitoids (Padrón dome, NW Iberia): assessing rheological evolution of cooling continental crust in a collisional setting. Geoscience Frontiers, 10(2), 651-669.

Ferré, E. C., Galland, O., Montanari, D., Kalakay, T. J. (2012). Granite magma migration and emplacement along thrusts. International Journal of Earth Sciences, 101(7), 1673-1688.

Floyd, P. A., Leveridge, B. E. (1987). The tectonic environment of the Devonian Gramscatho basin, south Cornwall: framework mode and geochemical evidence from turbiditic sandstones. Journal of the Geological Society, 144(4), 531-542.

Foden J.D., Elburg M.A., Turner S.P., Sandiford M., O'Callaghan J., Mitchell S. (2002). Granite production in the Delamerian Orogen, South Australia. Journal of the Geological Society, 159, 557-575.

Fossen, H. (2010). *Structural Geology,* Cambridge University Press, New York.

Fossen, H., Cavalcante, G.C.G. (2017). Shear zones–A review. Earth Science Reviews, 171, 434–455.

Frimmel, H. E., Fölling, P. G. (2004). Late Vendian closure of the Adamastor Ocean: timing of tectonic inversion and syn-orogenic sedimentation in the Gariep Basin. Gondwana Research, 7(3), 685-699.

Frimmel, H. E. (2009). Trace element distribution in Neoproterozoic carbonates as a palaeoenvironmental indicator. Chemical Geology, 258(3-4), 338-353.

Frimmel, H.E., Basei, M.S., Gaucher, C. (2011). Neoproterozoic geodynamic evolution of SW-Gondwana: a southern African perspective. International Journal of Earth Sciences 100, 323-354.

Frimmel, H.E., Basei, M.A.S., Correa, V.X., Mbangula, N. (2013). A new lithostratigraphic subdivision and geodynamic model for the Pan-African western Saldania Belt, South Africa. Precambrian Research 231, 218-235.

Frost, B. R., Barnes, C. G., Collins, W. J., Arculus, R. J., Ellis, D. J., Frost, C. D. (2001). A geochemical classification for granitic rocks. Journal of Petrology 42 (11), 2033-2048.

Gagnevin, D., Daly, J.S., Waight, T.E., Morgan, D., Poli, G. (2005). Pb isotopic zoning of K-feldspar megacrysts determined by laser ablation multi-collector ICP-MS: Insights into granite petrogenesis. Geochimica et Cosmochimica Acta, 69, 1899–1915.

Gagnevin, D., Daly, J. S., Kronz, A. (2010). Zircon texture and chemical composition as a guide to magmatic processes and mixing in a granitic environment and coeval volcanic system. Contributions to Mineralogy and Petrology, 159(4), 579-596.

García -Arias, M., Stevens, G. (2017). Phase equilibrium modelling of granite magma petrogenesis: An evaluation of the magma compositions produced by crystal entrainment in the source. Lithos 277, 131-153.

García-Arias, M. (2018). Decoupled Ca and Fe+ Mg content of S-type granites: An investigation on the factors that control the Ca budget of S-type granites. Lithos, 318, 30-46.

Garibaldi, N., Tikoff, B., Schaen, A. J., Singer, B. S. (2018). Interpreting granitic fabrics in terms of rhyolitic melt segregation, accumulation, and escape via tectonic filter pressing in the Huemul pluton, Chile. Journal of Geophysical Research: Solid Earth, 123, 8548–8567.

Gary, M., McAfee, R., Jr., Wolf, C.F. (1972). Glossary of geology, 805 p. American Geological Institute, Washington, DC.

Glazner, A.F., Bartley, J.M., Coleman, D.S., Gray, W., Taylor, R.Z. (2004). Are plutons assembled over millions of years by amalgamation from small magma chambers? GSA Today 14, 4–11.

Glazner, A.F., Bartley, M. J. (2006). Is stoping a volumetrically significant pluton emplacement process? Geological Society of America Bulletin, v.118; no. 9/10; p. 1185-1195.

Glazner, A.F., Johnson, B.R. (2013). Late crystallization of K-feldspar and the paradox of megacrystic granites: Contributions to Mineralogy and Petrology, v. 166, p. 777–799.

Gresse, P.G., Theron, J.N. (1992). The geology of the Worcester area. Explanation sheet 3319 Worcester (1:250.000), Geological Survey of South Africa, 79 pp.

Gresse, P.G., Von Veh, M.W., Frimmel, H.E. (2006). Namibian (Neoproterozoic) to early Cambrian successions. In: Johnson, M.R., Anhaeusser, C.R., Thomas, R.J. (Eds.) The Geology of South Africa. Geological Society of South Africa, Pretoria, pp. 395-420.

Godfrey, J. D. (1954). The origin of ptygmatic structures. The Journal of Geology, 62(4), 375-387.

Gualda, G.A.R. (2019). On the origin of alkali feldspar megacrysts in granitoids: The case against textural coarsening. Contributions to Mineralogy and Petrology, 174, 88.

Gudmundsson, A. (2011). Magma chambers: Formation, local stresses, excess pressures, and compartments. Journal of Volcanology and Geothermal Research, 237, 19-41.

Guldstrand, F. (2018). Quantitative Laboratory Modelling of Host Rock Deformation due to the Intrusion of Magma.

Haakon, F. (2010). Structural geology. Cambridge University Press, New York, 1, 463.

Han, Y., Wang, Y., Zhao, G., Cao, Q. (2014). Syn-tectonic emplacement of the Late Mesozoic Laojunshan granite pluton in the eastern Qinling, central China: An integrated fabric and geochronological study. Journal of Structural Geology 68, 1-15.

Harris, N.B.W., Pearce, J.A., Tindle, A.G. (1986). Geochemical characteristics of collisional-zone magmatism. In: Coward, M.P., Reis, A.C. (Eds.), Collision Tectonics: Geological Society (London) Special Publication, vol. 19, pp. 57-81.

Harris, C., Faure, K., Diamond, R.E., Scheepers, R. (1997). Oxygen and hydrogen isotope geochemistry of S- and I-type granitoids: the Cape Granite Suite, South Africa. Chemical Geology 143, 95-114.

Harris, C., Vogeli, J. (2010). Oxygen isotope composition of garnet in the Peninsula granite, Cape Granite Suite, South Africa: constraints on melting and emplacement mechanisms. South African Journal of Geology 113(4), 385–396.

Hartnady, C.J.H., Newton, A.R., Theron, J.N. (1974). The stratigraphy and structure of the Malmesbury Group in the South-Western Cape. Bulletin of the Precambrian Research Unit 15, 193-213.

Herron, M.M. (1988). Geochemical classification of terrigenous sands and shales from core or log data. Journal of Sedimentary Petrology 58, 829-829.

Higgins, M. D. (1999). Origin of megacrysts in granitoids by textural coarsening: a crystal size distribution (CSD) study of microcline in the Cathedral Peak Granodiorite, Sierra Nevada, California. Geological Society, London, Special Publications, 168(1), 207-219.

Holdsworth, R.E., McErlean, M.A., Strachan, R.A. (1999). The influence of country rock structural architecture during pluton emplacement: The Loch Loyal syenites, Scotland. Journal of the Geological Society of London, 156, 163–175.

Holness, M.B., Clemens, J.D., Vernon, R.H. (2018). How deceptive are microstructures in granitic rocks? Answers from integrated physical theory, phase equilibrium, and direct observations. Contributions to Mineralogy and Petrology, 173, 62.

Horstwood, M.S.A., Košler, J., Gehrels, G., Jackson, S.E., McLean, N.M., Paton, C., Pearson, N.J., Sircombe, K., Sylvester, P., Vermeesch, P., Bowring, J.F., Condon, D.J., Schoene, B. (2016). Community-Derived Standards for LA-ICP-MS U-(Th-)-Pb Geochronology – Uncertainty Propagation, Age Interpretation and Data Reporting. Geostandards and Geoanalytical Research, 40, 3, 301–332.

Hoskin, P. W. O., Schaltegger, U. (2003). The composition of zircon and igneous and metamorphic petrogenesis. Reviews in mineralogy and geochemistry, 53(1), 27-62.

Hutton, D. H. W. (1982). A tectonic model for the emplacement of the Main Donegal Granite, NW Ireland. Journal of the Geological Society, 139(5), 615-631.

Hutton, D.H.W., Dempster, T.J., Brown, P.E., Decker, S.D. (1990). A new mechanism of granite emplacement: Intrusion in active extensional shear zones: Nature, v. 343, p. 452–455.

Hutton, D.H.W., Reavy, R.J. (1992). Strike-slip tectonics and granite petrogenesis. Tectonics, 11, 960–967.

Hutton, D. H. W. (1996). The 'space problem' in the emplacement of granite. Episodes, 19(4), 114-119.

Jackson, S.E., Pearson, N.J., Griffin, W.L., Belousova, E.A. (2004). The application of laser ablation-inductively coupled plasma-mass spectrometry to in situ U-Pb zircon geochronology. Chemical Geology, 211, 47–69.

Janoušek, V., Farrow, C. M., Erban, V. (2006). Interpretation of Whole-rock Geochemical Data in Igneous Geochemistry: Introducing Geochemical Data Toolkit (GCDkit). Journal of Petrology 47 (6), 1255-1259.

Janoušek, V., Moyen, J. F., Martin, H., Erban, V., Farrow, C. (2016). Geochemical modelling of igneous processes–principles and recipes in R language. Springer, Berlin, pp. 346.

Johnson, T.E., Hudson, N.F.C., Droop, G.T.R. (2001). Partial melting of the Inzie Head gneisses: The role of water and a petrogenetic grid in KFMASH applicable to anatectic pelitic migmatites: Journal of Metamorphic Geology 19, 99–118.

Johnson, B.R., Glazner, A.F. (2010). Formation of K-feldspar megacrysts in granodioritic plutons by thermal cycling and late-stage textural coarsening. Contributions to Mineral Petrology 159(5), 599–619.

Johnson, M.C., Rutherford, M.J. (1989). Experimentally determined conditions in the Fish Canyon Tuff, Colorado, magma chamber. Journal of Petrology, 30, 711–737.

Jung S., Hoernes S., Masberg P., Hoffer E. (1999). The petrogenesis of some migmatites and granites (central Damara Orogen, Namibia): Evidence for disequilibrium melting, wall-rock contamination and crystal fractionation. Journal of Petrology, 40, 1241-1269.

Kemp, A. I. S., Hawkesworth, C. J. (2003). Granitic Perspectives on the Generation and Secular Evolution of the Continental Crust. Treatise on Geochemistry, 349–410.

Kisters, A.F.M., Belcher, R.W., Scheepers, R., Rozendaal, A., Jordaan, L.S., Armstrong, R.A. (2002). Timing and kinematics of the Colenso Fault: The Early Palaeozoic shift from collisional to extensional tectonics in the Pan-African Saldania Belt South Africa. South African Journal of Geology 105, 257–270.

Kisters, A. F. M., Ward, R. A., Anthonissen, C. J., Vietze, M. E. (2009). Melt segregation and far-field melt transfer in the mid-crust. Journal of the Geological Society, 166(5), 905-918.

Kisters, A.F.M., Agenbach, C., Frei, D. (2015). The age and tectonic significance of the volcanic Bloubergstrand member in the Pan-African Saldania Belt, South Africa. South African Journal of Geology 118, 213–224.

Kisters, A.F.M. (2016). What lies beneath Table Mountain or all models are wrong, but some are useful. Stellenbosch University.

Kisters, A.F.M., Belcher, R.W. (2018). The stratigraphy and structure of the western Saldania belt, South Africa and geodynamic implications. In: Geology of Southwest Gondwana. Springer, Cham, pp. 387-410.

Kratinová, Z., Schulmann, K., Edel, J. B., Ježek, J., Schaltegger, U. (2007). Model of successive granite sheet emplacement in transtensional setting: Integrated microstructural and anisotropy of magnetic susceptibility study. Tectonics, 26(6).

Kumbe, D. (2017). Investigation of magmatic flow in the Peninsula Granite of the Cape Granite Suite, Saldania Belt, using megacryst orientation and imbrication. BSc Honours thesis (unpubl.), University of the Western Cape, 24 p.

Kutterolf, S., Diener, R., Schacht, U., Krawinkel, H. (2008). The provenance of the Carboniferous Hochwipfel Formation (Karawanken Mountains, Austria/Slovenia) geochemistry versus petrography. Sedimentary Geology 203, 246-266.

Lackey, J. S., Valley, J. W., Hinke, H. J. (2006). Deciphering the source and contamination history of peraluminous magmas using δ 18 O of accessory minerals: examples from garnet-bearing plutons of the Sierra Nevada batholith. Contributions to Mineralogy and Petrology, 151(1), 20-44.

Liew, T.C., Hofmann A.W. (1988). Precambrian crustal components, plutonic associations, plate environment of the Hercynian Fold Belt of central Europe: Indications from a Nd and Sr isotopic study. Contributions to Mineralogy and Petrology 98, 129-138.

Lister, J.R., Kerr, R.C. (1991) Fluid-mechanical models of crack propagation and their application to magma transport in dykes. Journal of Geophysical Research, 96.

Little, T.A., Hacker, B.R., Brownlee, S.J., Seward, G. (2013). Microstructures and quartz lattice-preferred orientations in the eclogite-bearing migmatitic gneisses of the D'Entrecasteaux Islands, Papua New Guinea. Geochemistry, Geophysics, Geosystems, 14, 2030–2062.

Lucas, S.B., St-Onge, M.R. (1995). Syn-tectonic magmatism and the development of compositional layering, Ungava Orogen (northern Quebec, Canada). Journal of Structural Geology, 17, 475–491.

Ludwig, K.R. (2012). Isoplot Version 3.75–4.15: a Geochronological Toolkit for Microsoft Excel. Berkeley Geochronological Center Special Publication, 5.

Lugmair, G. W., Marti, K. (1978). Lunar initial ^{143}Nd/^{144}Nd: differential evolution of the lunar crust and mantle. Earth and Planetary Science Letters, 39(3), 349-357.

Magee, C., Muirhead, J., Schofield, N., Walker, R. J., Galland, O., Holford, S., McCarthy, W. (2018). Structural signatures of igneous sheet intrusion propagation. Journal of Structural Geology, 125, 148-154.

Marsh, B. D. (1982). On the mechanics of igneous diapirism, stoping, and zone melting. American Journal of Science, 282.

Mawer, C. K. (1992). Kinematic indicators in shear zones. In: Bartholomew, M.J., Hyndman, D.W., Mogk, D.W., Mason, R. (Eds.) Basement Tectonics 8: Characterization and Comparison of Ancient and Mesozoic Continental Margins-Proceedings of the 8th International Conference on Basement Tectonics (Butte, Montana, 1988). Kluwer Academic Publishers, Dordrecht, Netherlands, 67-81pp.

McCaffrey, K.J.W. (1992). Igneous emplacement in a transpressive shear zone: Ox Mountains igneous complex. Journal of the Geological Society of London, 149, 221–235.

McFadden, R.R., Siddoway, C.S., Teyssier, C., Fanning, C.M. (2010). Cretaceous oblique extensional deformation and magma accumulation in the Fosdick Mountains migmatite-cored gneiss dome, West Antarctica. Tectonics, 29.

McKenzie, D. (1984). The generation and compaction of partially molten rocks. Journal of Petrology, 25, 713-765.

McLennan, S.M., Hemming, S., McDaniel, D.K., Hanson, G.N. (1993). Geochemical approaches to sedimentation, provenance, and tectonics. In: Johnsson, M.J., Basu, A. (eds.) Processes Controlling the Composition of Clastic Sediments. Geological Society of America (Special Paper) 284, Boulder, pp 21–40.

Melosh, H. J. (2011). Planetary surface processes (Vol. 13). Cambridge University Press.

Memeti, V., Paterson, S., Mundil, R., Paterson, S. R. Putirka, K. D. (2014). Day 4: magmatic evolution of the Tuolumne Intrusive Complex. Formation of the Sierra Nevada Batholith: Magmatic and Tectonic Processes and Their Tempos. Geological Society of America Field Guide, 34, 43-74.

Menand, T., de Saint-Blanquat, M., Annen, C. (2011). Emplacement of magma pulses and growth of magma bodies. Tectonophysics 500 (2011) 1–2.

Menand, T. (2011). Physical controls and depth of emplacement of igneous bodies: A review. Tectonophysics 500 (2011) 11–19.

Mériaux, C., Lister, J.R. (2002). Calculation of dike trajectories from volcanic centers. Journal of Geophysical Research, 107.

Middlemost, E. A. (1994). Naming materials in magma/igneous rock system. Earth-Science Reviews 37 (3-4), 215-224.

Míková, J., Denková, P. (2007). Modified chromatographic separation scheme for Sr and Nd isotope analysis in geological silicate samples. Journal of Geosciences, 52, 221–226.

Miller, R. B., Paterson, S. R. (1999). In defence of magmatic diapirs. Journal of Structural Geology, 21(8-9), 1161-1173.

Miller, R.B., Paterson, S.R. (2001a). Construction of mid-crustal sheeted plutons: Examples from the North Cascades, Washington: Geological Society of America Bulletin, v. 113, p. 1423-1442.

Miller, R. B., Paterson, S. R. (2001b). Influence of lithological heterogeneity, mechanical anisotropy, and magmatism on the rheology of an arc, North Cascades, Washington. Tectonophysics, 342(3-4), 351-370.

Miller, C.F., Furbish, D.J., Walker, B.A., Clairborne, L.L., Cotheas, G.C., Bleick, H.A., Miller, J.S. (2011). Growth of plutons by incremental emplacement of sheets in crystal-rich host: Evidence from Miocene intrusions of the Colorado River region, Nevada, USA. Tectonophysics 500, 65-77.

Milord, I., Sawyer, E. W. (2003). Schlieren formation in diatexite migmatite: examples from the St Malo migmatite terrane, France. Journal of Metamorphic Geology, 21(4), 347-362.

Montel, J.M., Vielzeuf, D. (1997). Partial melting of metagreywackes, 2: Compositions of minerals and melts: Contributions to Mineralogy and Petrology 128, 176–196.

Moore, J.G., Sisson, T.W. (2008). Igneous phenocrystic origin of K-feldspar megacrysts in granitic rocks from the Sierra Nevada batholith. Geosphere, 4, 387.

Nédélec, A., Bouchez, J. L. (2015). Granites: petrology, structure, geological setting, and metallogeny. OUP Oxford.

Nesbitt, H. W., Young, G. M. (1982). Early Proterozoic climates and plate motions inferred from major element chemistry of lutites. Nature, 299(5885), 715-717.

Nesbitt, H. W., Young, G. M. (1984). Prediction of some weathering trends of plutonic and volcanic rocks based on thermodynamic and kinetic considerations. Geochimica et Cosmochimica Acta, 48(7), 1523-1534.

Neves, S. P., Vauchez, A., Archanjo, C. J. (1996). Shear zone-controlled magma emplacement or magma-assisted nucleation of shear zones? Insights from northeast Brazil. Tectonophysics, 262(1-4), 349-364.

Nicholls, J., Gordon, T.M. (1994). Procedures for the calculation of axial ratios on Pearce element-ratio diagrams: Canadian Mineralogist, 32, 969–977.

Nicholls, J., Russell, J.K. (2016). Igneous Rock Associations 20. Pearce Element Ratio Diagrams: Linking Geochemical Data to Magmatic Processes. Geoscience Canada, 43, 133–146.

Ogiermann, J. C. (2002). Cordierite and its retrograde breakdown products as monitors of fluid-rock interaction during retrograde path metamorphism: case studies in the Schwarzwald and the Bayerische Wald (Variscan belt, Germany) (Doctoral dissertation).

Othman, D. B., Polvé, M., Allègre, C. J. (1984). Nd—Sr isotopic composition of granulites and constraints on the evolution of the lower continental crust. Nature, 307(5951), 510-515.

Passchier, C. W., Trouw, R. A. (2005). Microtectonics. Springer Science & Business Media, pp. 366.

Passchier, C. W., Zhang, J. S., Konopasek, J. (2005). Geometric aspects of synkinematic granite intrusion into a ductile shear zone—An example from the Yunmengshan core complex, northern China. Geological Society, London, Special Publications, 245(1), 65-80.

Paterson, B.A., Stephens, W.E., Rogers, G., Williams, I.S., Hinton, R.W., Herd, D.A. (1992). The nature of zircon inheritance in two granite plutons. Transactions of the Royal Society of Edinburgh: Earth Science 83, 459-471.

Paterson, S. R., Vernon, R. H., Tobisch, O. T. (1989). A review of criteria for the identification of magmatic and tectonic foliations in granitoids. Journal of Structural Geology, 11(3), 349–363.

Paterson, S. R., Fowler Jr, T. K., Miller, R. B. (1996). Pluton emplacement in arcs: a crustal-scale exchange. In The Third Hutton Symposium on the Origin of Granites and Related Rocks (Vol. 315, pp. 115-123). Geological Society of America.

Paterson, S.R., Fowler Jr., T.K., Schmidt, K.L., Yoshinobu, A.S., Yuan, E.S., Miller, R.B. (1998). Interpreting magmatic fabric patterns in plutons. Lithos 44, 53-82.

Paterson, S.R., Pignotta, G.S., Vernon, R.H. (2004). The significance of microgranitoid enclave shapes and orientations: Journal of Structural Geology, v. 26, p. 1465–1481.

Paterson, S.R., Vernon, R.H., Zak, J. (2005). Mechanical instabilities and physical accumulation of K-feldspar megacrysts in granitic magma, Tuolumne Batholith, California, USA. Journal of the Virtual Explorer 18, Electronic Edition, Paper 1 (ISSN 1441-8142).

Paterson, S. R., Pignotta, G. S., Farris, D., Memeti, V., Miller, R. B., Vernon, R. H., Žák, J. (2008). Is stoping a volumetrically significant pluton emplacement process?: Discussion. Geological Society of America Bulletin, 120(7-8), 1075-1079.

Paterson, S.R., Memeti, V., Mundil, R., Žák, J. (2016). Repeated, multiscale, magmatic erosion and recycling in an upper-crustal pluton: Implications for magma chamber dynamics and magma volume estimates. The American Mineralogist, 101, 2176–2198.

Pattison, D. R., Harte, B. (1997). The geology and evolution of the Ballachulish Igneous Complex and Aureole. Scottish Journal of Geology, 33(1), 1-29.

Paton, C., Hellstrom, J., Paul, B., Woodhead, J., Hergt, J. (2011). Iolite: freeware for the visualisation and processing of mass spectrometric data. Journal of Analytical Atomic Spectrometry, 26, 2508–2518.

Pearce, T.H. (1968). A contribution to the theory of variation diagrams: Contributions to Mineralogy and Petrology, 19, 142–157.

Petford, N. (1996). Dykes or diapirs. Transactions of the Royal Society of Edinburgh: Earth Sciences, 87(1-2), 105-114.

Petford, N., Cruden, A.R., McCaffrey, K.J.W., Vigneresse, J.L. (2000). Granite magma formation, transport and emplacement in the Earth's crust, Nature, Vol. 408, p. 669-673.

Petford, N., Koenders, M. A. (2003). Shear-induced pressure changes and seepage phenomena in a deforming porous layer-I. Geophysical Journal International, 171(2), 943–953.

Petrus, J.A., Kamber, B.S. (2012). VizualAge: A Novel Approach to Laser Ablation ICP-MS U-Pb Geochronology Data Reduction. Geostandards and Geoanalytical Research, 36, 247-270.

Pin, C., Briot, D., Bassin, C., Poitrasson, F. (1994). Concomitant separation of strontium and samarium–neodymium for isotopic analysis in silicate samples, based on specific extraction chromatography. Anal. Helvetica Chimica Acta, 298, 209–217.

Pin, C., Zalduegui, J.F.S. (1997). Sequential separation of light rare-earth elements, thorium and uranium by miniaturized extraction chromatography: application to isotopic analyses of silicate rocks. Anal. Helvetica Chimica Acta, 339, 79–89.

Potter, P. E., Maynard, J. B., Depetris, P. J. (2005). Mud and mudstones: Introduction and overview. Springer Science & Business Media, pp. 287.

Pyle, J. M., Spear, F. S., Rudnick, R. L., Mcdonough, W. F. (2001). Monazite–xenotime–garnet equilibrium in metapelites and a new monazite–garnet thermometer. Journal of Petrology, 42(11), 2083-2107.

Raith, M. M., Raase, P. R., Reinhardt, J. R. (2012). Guide to thin section microscopy. The University of Bonn, pp. 134.

Rivalta, E., Taisne, B., Bunger, A. P., Katz, R. F. (2015). A review of mechanical models of dike propagation: Schools of thought, results and future directions. Tectonophysics, 638, 1-42.

Rollinson, H. (1993). Using geochemical data: evaluation, presentation, interpretation. Edinburgh: Edinburgh Gate, pp 352.

Rosenberg, C.L. (2004). Shear zones and magma ascent: A model based on a review of the Tertiary magmatism in the Alps. Tectonics, 23.

Rowe, C.D., Backeberg, N.R., Van Rensburg, T., MacLennan, S.A., Faber, C., Curtis, C., Viglietti, P.A. (2010). Structural geology of Robben Island: implications for the tectonic environment of Saldanian deformation. South African Journal of Geology 113, 57–72.

Rozendaal, A., Gresse, P.G., Scheepers, R., Le Roux, J.P. (1999). Neoproterozoic to Early Cambrian crustal evolution of the Pan-African Saldania Belt, South Africa. Precambrian Research 97, 303-323.

Rubatto, D. (2017). Zircon: the metamorphic mineral. Reviews in mineralogy and geochemistry, 83(1), 261-295.

Rudnick, R. L., Gao, S. (2003). Composition of the continental crust. The crust, 3, 1-64.

SACS (South African Committee for Stratigraphy). (1980). Stratigraphy of South Africa. Part 1. Lithostratigraphy of the Republic of South Africa, South West Africa/Namibia, and the Republics of Bophuthatswana, Transkei and Venda, 690.

Sawyer, E. W. (1991). Disequilibrium melting and the rate of melt residuum separation during migmatization of mafic rocks from the Grenville Front, Quebec. Journal of Petrology 32, 701-738.

Sawyer, E. W. (2008). Atlas of migmatites (Vol. 9). NRC Research Press.

Scheepers, R. (1995). Geology, geochemistry and petrogenesis of Late Precambrian S-, I- and A-type granitoids in the Saldania belt, Western Cape Province, South Africa. Journal of African Earth Sciences 21, 35-58.

Scheepers, R. (2000). Granites of the Saldania mobile belt, South Africa: radioelements and P as discriminators applied to metallogeny. Journal of Geochemical Exploration 68, 69-86.

Scheepers, R., Armstrong, R. A. (2002). New U-Pb SHRIMP zircon ages of the Cape Granite Suite: implications for the magmatic evolution of the Saldania Belt. South African Journal of Geology 105, 241-256.

Scheepers, R., Schoch, A. E. (2006). The Cape Granite Suite. In: Johnson, M.R., Anhaeusser, C.R., Thomas, R.J. (Eds.). The Geology of South Africa. Geological Society of South Africa, Johannesburg, pp 421-432.

Schofield, N.J., Stevenson, C., Reston, T. (2010). Magma fingers and host rock fluidization in the emplacement of sills. Geology, 38, 63–66.

Schofield, N. J., Brown, D. J., Magee, C., Stevenson, C. T. (2012). Sill morphology and comparison of brittle and non-brittle emplacement mechanisms. Journal of the Geological Society, 169(2), 127-141.

Sibson, R.H. (2003). Brittle-failure controls on maximum sustainable overpressure in different tectonic regimes. American Association of Petroleum Geology, 87(6):901–908.

Sláma, J., Košler, J., Condon, D.J., Crowley, J.L., Gerdes, A., Hanchar, J.M., Horstwood, M.S.A., Morris, G.A., Nasdala, L., Norberg, N., Schaltegger, U., Schoene, B., Tubrett, M.N., Whitehouse, M.J. (2008). Plešovice zircon – a new natural reference material for U-Pb and Hf isotopic microanalysis. Chemical Geology, 241, 1–35.

Sleep, N. H. (1988). Tapping of melt by veins and dikes. Journal of Geophysical Research: Solid Earth, 93(B9), 10255-10272.

Spacapan, J.B., Galland, O., Leanza, H.A., Planke, S. (2017). Igneous sill and finger emplacement mechanism in shale-dominated formations: a field study at Cuesta del Chihuido, Neuquén Basin. Argentina. London Geological Society 174, 422–433.

Spear, F. S., Pattison, D. R., Cheney, J. T. (2017). The metamorphosis of metamorphic petrology. The Web of Geological Sciences: Advances, Impacts, and Interactions II, Geol. Soc. Am, 523, 31-73.

Spencer, C. J., Kirkland, C. L., Taylor, R. J. (2016). Strategies towards statistically robust interpretations of in situ U–Pb zircon geochronology. Geoscience Frontiers, 7(4), 581-589.

Steiger, R. H., Jäger, E. (1977). Subcommission on geochronology: convention on the use of decay constants in geo-and cosmochronology. Earth and planetary science letters, 36(3), 359-362.

Stephens, T. L., Walker, R. J., Healy, D., Bubeck, A., England, R. W. McCaffrey, K. J. (2017). Igneous sills record far-field and near-field stress interactions during volcano construction: Isle of Mull, Scotland. Earth and Planetary Science Letters, 478, 159-174.

Stevens, G., Villaros, A., Moyen, J.F. (2007). Selective peritectic garnet entrainment as the origin of geochemical diversity in S-type granites. Geology 35(1), 9 – 12.

Stevenson, D.J. (1982). Migration of fluid-filled cracks: Applications to terrestrial and icy bodies. Lunar and Planetary Science Conference 13, 768-769.

Streckeisen, A. (1976). To each plutonic rock its proper name. Earth-Science Reviews 12, 1-33.

Strong, D.F., Hanmer, S.K. (1981). Peraluminous granites: Canadian Mineralogist, 19, 163–176.

Taisne, B., Tait, S., Jaupart, C. (2011). Conditions for the arrest of a vertical propagating dyke. Bulletin of Volcanology 73, 191–204.

Tanaka, T., Togashi, S., Kamioka, H., Amakawa, H., Kagami, H., Hamamoto, T., Kunimaru, T. (2000). JNdi-1: a neodymium isotopic reference inconsistency with LaJolla neodymium. Chemical Geology, 168(3-4), 279-281.

Tankard, A. J., Martin, M., Eriksson, K. A., Hobday, D. K., Hunter, D. R., Minter, W. E. L. (2012). Crustal evolution of southern Africa: 3.8 billion years of earth history. Springer Science & Business Media.

Taylor, P. N., Jones, N. W., Moorbath, S. E. (1984). Isotopic assessment of relative contributions from crust and mantle sources to the magma genesis of Precambrian granitoid rocks. Philosophical Transactions of the Royal Society of London. Series A, Mathematical and Physical Sciences, 310(1514), 605-625.

Taylor, S. R., McLennan, S. M. (1995). The geochemical evolution of the continental crust. Reviews of geophysics, 33(2), 241-265.

Theron, J. N. (1984). The Geology of Cape Town and Environs: Explanation of Sheets 3318 CD and DC and 3418 AB, AD and BA, scale 1: 50 000. Department of Mineral and Energy Affairs, Geological Survey.

Theron, J.N., Gresse, P.G., Siegfried, H.P., Rogers, J. (1992). The geology of the Cape Town Area. Explanation of Sheet 3318. Geological Survey of South Africa, 140pp.

Tikoff, B., De Saint Blanquat, M., Teyssier, C. (1999). Translation and the resolution of the pluton space problem. Journal of Structural Geology, 21, 1109-1117.

Tommasi, A., Vauchez, A., Femandes, L. A., Porcher, C. C. (1994). Magma-assisted strain localization in an orogen-parallel transcurrent shear zone of southern Brazil. Tectonics, 13(2), 421-437.

Tourigny, G., Schwerdtner, W.M. (1991). Metre-scale band structures and associated veins in Archean metavolcanics: aubelle gold mine, central Canada. Journal of Structural Geology, 13, 913–918.

Vernon, R. H. (1986). K-feldspar megacrysts in granites—phenocrysts, not porphyroblasts. Earth-Science Reviews, 23(1), 1-63.

Vernon, R.H., Etheridge, M.A., Wall, V.J. (1988). Shape and microstructure of microgranitoid enclaves: indicators of magma mingling and flow. Lithos 22, 1–11.

Vernon, R. H., Clarke, G. L. (2008). Principles of metamorphic petrology. Cambridge University Press.

Vernon, R.H., Paterson, S.R. (2008). How late are K-feldspar megacrysts in granites? Lithos 104,327–336.

Vernon, R. H. (2018). A practical guide to rock microstructure. Cambridge university press.

Villaros, A., Stevens G., Moyen, J.F., Buick, I.S. (2009a). The trace element composition of S-type granites: evidence for disequilibrium melting and accessory phase entrainment in the source. Contributions to Mineralogy and Petrology 158, 543–561.

Villaros, A., Stevens G., Buick, I.S. (2009b). Tracking S-type granite from source to emplacement: clues from garnet in the Cape Granite Suite. Lithos, 112(3–4), 217–235.

Villaros, A. (2010). Petrogenesis of S-type Granite with particular emphasis on source processes: The Example of the S-type Granite of the Cape Granite Suite. PhD. Thesis. Stellenbosch University, Stellenbosch, South Africa.

Villaros, A., Buick I.S., Stevens, G. (2012). Isotopic variations in S-type granites: an inheritance from a heterogeneous source. . Contributions to Mineralogy and Petrology 163, 243–257.

Von Veh, M.W. (1982). Aspects of the structure, tectonic evolution and sedimentation in the Tygerberg Terrane, southwestern Cape Province. Precambrian Research Unit, University of Cape Town, Bulletin 32, 97pp.

Walker, F., Mathias, M. (1946). The petrology of two granite-slate contacts at Cape Town, South Africa. Quarterly Journal Geological Society of London 102, 499-521.

Weertman, J. (1971a). Theory of water-filled crevasses in glaciers applied to vertical magma transport beneath oceanic ridges. Journal of Geophysical Research, 76, 1171–1183.

Weertman, J. (1971b). Velocity at which liquid-filled cracks move in the Earth's crust or in glaciers. Journal of Geophysical Research, 76, 8544–8553.

Weertman, J. (1973). Can a water-filled crevasse reach the bottom surface of a glacier? IASH publishing, 95, 139-145.

Weis, D., Kieffer, B., Maerschalk, C., Barling, J., De Jong, J., Williams, G. A., Goolaerts, A. (2006). High-precision isotopic characterization of USGS reference materials by TIMS and MC-ICP-MS. Geochemistry, Geophysics, Geosystems, 7(8).

Wheeler, J., Mangan, L. S., Prior, D. J. (2004). Disequilibrium in the Ross of Mull contact metamorphic aureole, Scotland: a consequence of polymetamorphism. Journal of Petrology, 45(4), 835-853.

Whitney, J. A. (1988). The origin of granite: The role and source of water in the evolution of granitic magmas. Geological Society of America Bulletin, 100(12), 1886-1897.

Wiebe, R.A., Collins, W.J. (1998). Depositional features and stratigraphic sections in plutons: implications for the emplacement and crystallization of granitic magmas. Journal of Structural Geology, 20, 1273-1289.

Wiebe, R. A., Blair, K. D., Hawkins, D. P., Sabine, C. P. (2002). Mafic injections, in situ hybridization, and crystal accumulation in the Pyramid Peak granite, California. Geological Society of America Bulletin, 114(7), 909-920.

Wiedenbeck, M., Allé, P., Corfu, F. (1995). Three natural zircon standards for U-Th-Pb, Lu-Hf, trace element and REE analyses. Geostandards Newsletter, 19, 1–23.

Weinberg, R. F., Veveakis, E., Regenauer-Lieb, K. (2015). Compaction-driven melt segregation in migmatites. Geology, 43(6), 471–474.

Wilson, P. I., McCaffrey, K. J., Holdsworth, R. E. (2019). Magma-driven accommodation structures formed during sill emplacement at shallow crustal depths: The Maiden Creek sill, Henry Mountains, Utah. Geosphere, 15(4), 1368-1392.

Winchester, J. A., Floyd, P. A. (1976). Geochemical magma type discrimination: application to altered and metamorphosed basic igneous rocks. Earth and Planetary Science Letters, 28(3), 459-469.

Winkler, H. F., Schultes, H. (1982). On the problem of alkali feldspar phenocrysts in granitic rocks. Neues Jahrbuch für Mineralogie Monatshefte, 12, 558-564.

Winter, J.D. (2009). Fabrics and Folds. Retrieved from https: //courses.eas.ualberta.ca /eas233 /0809winter /EAS233Lab06webversion.pdf

Winter, J.D. (2010). Principles of Igneous and Metamorphic Petrology, 2. ed., New Jersey: Prentice-Hall, pp.702.

Yoshinobu, A. S., Wolak, J. M., Paterson, S. R., Pignotta, G. S., Anderson, H. S. (2009). Determining relative magma and host rock xenolith rheology during magmatic fabric formation in plutons: Examples from the middle and upper crust. Geosphere, 5(3), 270-285.

Žák, J., Holub, F.V., Kachlík, V. (2006). Magmatic stoping as an important emplacement mechanism of Variscan plutons: Evidence from roof pendants in the Central Bohemian plutonic complex (Bohemian Massif: International Journal of Earth Sciences, v. 95; no. 5, p. 771-789.

Zindler, A., Hart, S.R. (1986). Chemical geodynamics. Annual Reviews Earth Planetary Science. 14, 493-571.

Appendix list

Appendix A: Sample list and locations

Appendix B: General petrographic descriptions and interpretations not included in the lithological descriptions chapter

Appendix C: Bedding and foliation orientation data

Appendix D: Shape preferred orientation (SPO) data (for this study) and geological maps from the K-feldspar megacrystic study in the Bantry Bay, Clifton and Camps bay areas performed by Kumbe (2017)

Appendix E: Geochemistry data and plots not included in the main text

Appendix A

Table A1: List of samples collected at the Sea Point contact outcrop

Samples collected in 2016 for honours projects			
Sample no.	**Co-ordinates**	**Rock type**	**Granite sub-type**
SP1	S33° 55’18.2” E018° 22’38.5”	Spotted Malmesbury metamudstone	
SP2	S33° 55’18.8” E018° 22’38.56”	Spotted Malmesbury metamudstone with S_2 crenulation cleavage	
SP2B	S33° 55’18.8” E018° 22’38.56”	Spotted Malmesbury metamudstone	
SP3	S33° 55’18.3” E018° 22’38.6”	Microgranite	
SP4	S33° 55’18.9” E018° 22’37.5”	Medium-grained hybrid granite	Medium-grained porphyritic
SP5	S33° 55’18.45” E018° 22’37.81”	Mixed rock (coarse-grained porphyritic hybrid granite and Malmesbury)	Coarse-grained porphyritic
SP6	S33° 55’18.33” E018° 22’37.81”	Mixed rock (fine- to medium-grained porphyritic granite lenses within Malmesbury)	Medium-grained porphyritic
SP7	S33° 55.333’ E018° 22.618’	Coarse-grained porphyritic granite (main phase)	
SP8	S33° 55.317’ E018° 22.612’	Folded Malmesbury metamudstone with S_2 crenulation cleavage	
SP9	S33° 55.320’ E018° 22.610’	Foliated Malmesbury metamudstone	
SP10	S33° 55.324’ E018° 22.613’	Xenolith in granite - mixed zone	
SP11	S33° 55.318’ E018° 22.634’	Fine-grained semi-porphyritic hybrid granite	Fine-grained semi-porphyritic
SP12	S33° 55.318’ E018° 22.635’	Small metamudstone xenolith with S_1 foliation	

Samples collected in 2018 for the current MSc project			
Sample no.	**Co-ordinates**	**Rock type**	**Granite sub-type**
SP 13	S33° 55’18.2” E018° 22’37.5”	Biotite-rich coarse-grained granite	Coarse-grained porphyritic
SP14	S33° 55’18.7” E018° 22’39.0”	Malmesbury metamudstone with S_2 crenulation cleavage	
SP15	S33° 55’22.0” E018° 22’37.4”	Aplitic phase	
SP16	S33° 55’21.9” E018° 22’36.9”	Malmesbury metamudstone	
SP 17	S33° 55’21.9” E018° 22’36.9”	Banded rock of metasiltstone and metamudstone	
SP 18	S33° 55’21.6” E018° 22’36.6”	Coarse-grained porphyritic granite (main phase)	Coarse-grained porphyritic
SP 19	S33° 55’18.5” E018° 22’39.5	Microgranite	
SP 20	S33° 55’20.9” E018° 22’37.6”	Mixed rock (weathered, loose block) - megacrysts in Malmesbury	Medium-grained porphyritic
SP 21	S33° 55’18.9” E018° 22’38.0”	Medium- to coarse-grained porphyritic hybrid granite (with Malmesbury)	Medium-to- coarse-grained porphyritic

Samples collected in 2018 for the current MSc project

Sample no.	Co-ordinates	Rock type	Granite sub-type
SP 22	S33° 55’19.1” E018° 22’38.0”	Medium-grained porphyritic hybrid granite	Medium-grained porphyritic
SP 23	S33° 55’19.7” E018° 22’37.3”	Coarse-grained porphyritic granite (biotite-rich)	Coarse-grained bt-rich porphyritic
SP 24	S33° 55’19.2” E018° 22’37.8”	Medium-grained porphyritic hybrid granite (with Malmesbury)	Medium-grained porphyritic
SP 25	S33° 55’19.4” E018° 22’37.9”	Coarse-grained porphyritic hybrid granite	Coarse-grained porphyritic
SP 26	S33° 55’19.2 E018° 22’37.8”	Medium-grained porphyritic hybrid granite	Medium-grained porphyritic
SP 27	S33° 55’18.8” E018° 22’38.8”	Medium-grained porphyritic hybrid granite	Medium-grained porphyritic
SP 30	S33° 55’18.81” E018° 22’37.38”	Fine-grained non-porphyritic hybrid granite	Fine-grained non-porphyritic
SP 31	S33° 55’18.66” E018° 22’37.20”	Medium-grained porphyritic hybrid granite	Medium-grained porphyritic
SP 32	S33° 55’18.66” E018° 22’37.14”	Medium-grained porphyritic hybrid granite	Medium-grained porphyritic
SP 33	S33° 55’18.60” E018° 22’37.20”	Fine-grained porphyritic hybrid granite	Fine-grained porphyritic
SP 34	S33° 55’18.60” E018° 22’37.14”	Medium-grained porphyritic hybrid granite	Medium-grained porphyritic
SP 35	S33° 55’19.74” E018° 22’36.54”	Medium-grained porphyritic hybrid granite	Medium-grained porphyritic
SP 36	S33° 55’19.80 E018° 22’36.78”	Coarse-grained non-porphyritic hybrid granite	Fine-grained non-porphyritic
SP 37	S33° 55’19.92” E018° 22’37.02”	Medium-grained semi-porphyritic hybrid granite	Medium-grained semi-porphyritic
SP 38	S33° 55’16.8” E018° 22’41.1”	Microgranite	
SP 39	S33° 55’18.7” E018° 22’37.2”	Medium-grained porphyritic hybrid granite	Medium-grained porphyritic
SP 40	S33° 55’18.0” E018° 22’36.1”	Fine-grained non-porphyritic hybrid granite	Fine-grained non-porphyritic
SP 41	S33° 55’18.3” E018° 22’36.0”	Malmesbury metamudstone	
SP 42	S33° 55’18.4” E018° 22’35.9”	Medium-grained hybrid granite	F/g non-porphyritic & c/g porphyritic
SP 43	S33° 55’20.0” E018° 22’37.1”	Mixed sample – large Malmesbury block with well-defined granite lit-par-lit intrusions. Segmented into smaller blocks (i.e. 43A, B, C & D)	
43A	S33° 55’20.0” E018° 22’37.1”	Coarse-grained porphyritic hybrid	Coarse-grained porphyritic
43B	S33° 55’20.0” E018° 22’37.1”	Lit-par-lit	
43C	S33° 55’20.0” E018 ° 22’37.1”	Lit-par-lit	
43D	S33° 55’20.0” E018° 22’37.1”	Lit-par-lit	
SP 44	S33° 55’9.02” E018° 22’54.21”	Banded rock of metasiltstone and metamudstone	

***Samples SP38 and SP44 fall outside the area mapped (Fig. A1). Sample 38 is located approx. 80 metres away from the mapped area, whereas SP44 is approx. 480 metres away.**

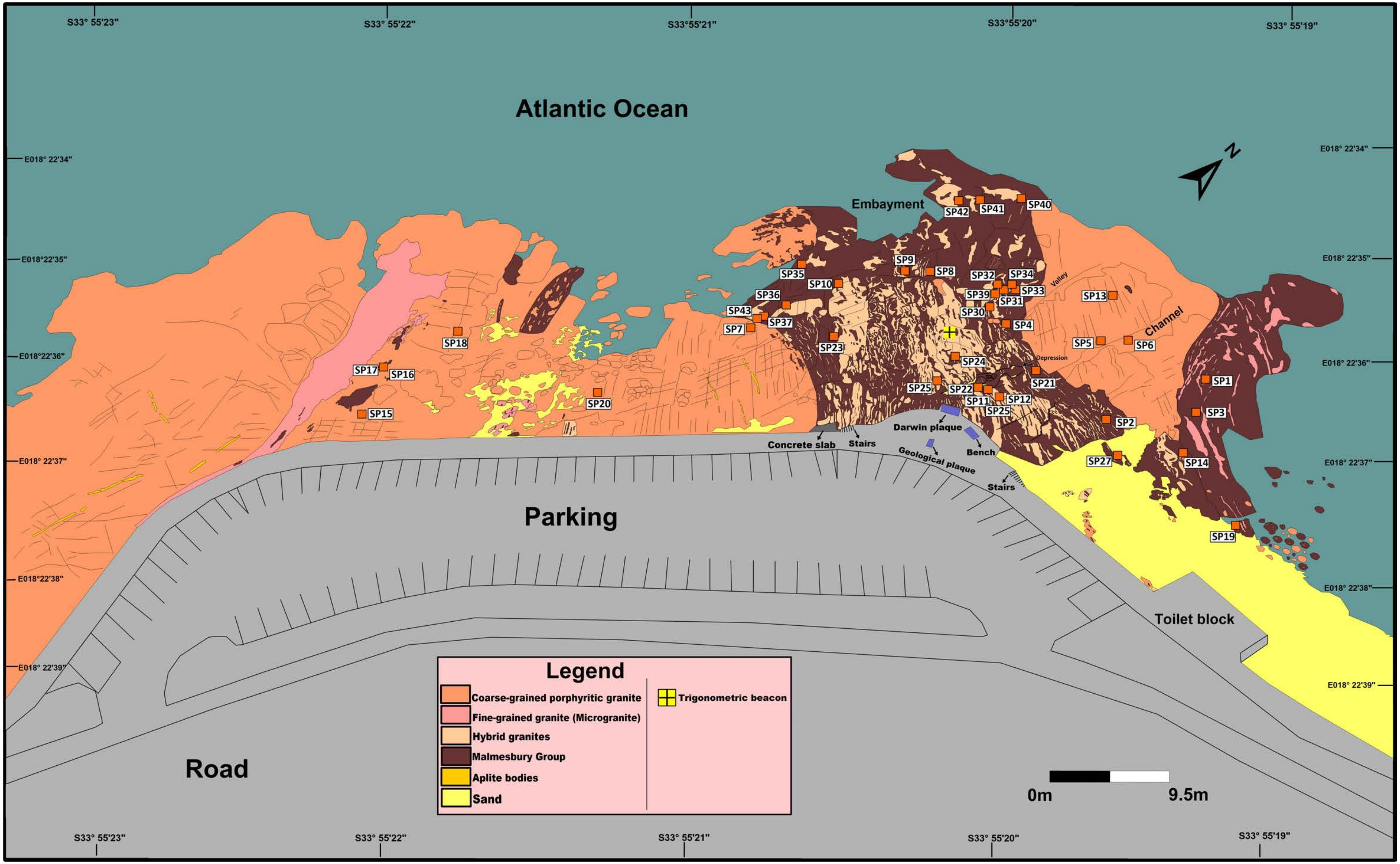

***Figure A1**: Sea Point geological map with the locations of the samples collected.*

Appendix B

Appendix B1

–Types of cordierite alteration in the metamudstone metasediments

The recognition of alteration type based on composition was done as far as possible because this aspect was limited by the very-fine grained nature of some alteration types which makes it close to impossible to recognize all constituents. The alteration types are as follows:

I. The first type (Type I) involves the replacement of cordierite by fine aggregates of phyllosilicates including muscovite (& sericite) (most dominant), biotite and chlorite (Fig. B1A, B). It is the most commonly occurring (or more widespread) alteration type and tends to completely alter or replace primary cordierite wherever present. Coarser grained, strongly aligned and variably chloritized biotite grains (i.e. those that define the dominant matrix foliation) not only anastomose around the cordierite grain but also show signs of being involved in the replacement process of some cordierite grains, starting from the outer edge toward the centre, alongside or together with the alteration products of Type I.

II. The second type (Type II) involves the replacement of cordierite by fine-grained isotropic to slightly birefringent alteration material (Fig. B1C, D). Whenever this alteration type is found to occur, it tends to only replace the cordierite partially, with full replacement being rare. Moreover, it is commonly accompanied or occurs with the Type I alteration. When this is the case, the Type II alteration is concentrated in the central portion of the cordierite grain and is rimmed or surrounded by the fine micaceous aggregates of Type I alteration (e.g. Fig. B1E).

III. The third type (Type III) resembles Type II alteration material in a sense that it is also defined by fine-grained isotropic material. The difference between the two is that Type III alteration material is concentrated with the various fractures, fissures, and pathways in the cordierite or occurs as very narrow rims around the cordierite (Fig. B1D, E). They occur sporadically with no preferred orientation and tend to encompass or include some of the mica and quartz inclusions present within the cordierite. In plane-polarized light, Type III alteration products have a brownish-yellow appearance (Fig. B1E).

IV. The fourth type (Type IV) involves the replacement of cordierite by relatively coarse-grained muscovite grains, which mostly lie oblique to the foliation, and intergrowths of biotite (Fig. B1G, H). Much like the Type I alteration, the muscovite grains from Type IV alteration tend to completely replace the cordierite grains. Moreover, there are occurrences of fine-grained biotite inclusions on the edge of the cordierite grains, oriented sub-parallel and continuous with the matrix foliation, that occur alongside both the alteration products of Type IV. The difference in the orientation of these fine-grained biotite grains relative to those involved in the alteration process suggests that both varieties are not involved in the same alteration process.

Appendix B2

–Petrographic descriptions of the types of biotite clots in the coarse-grained granite

I. Type I clots: where the central portions (or core) of the clots comprises euhedral to subhedral quartz and biotite grains similar in size to the biotite grains which surround them. This variety tends to resemble an aggregate or accumulation of biotite due to minor occurrence of quartz and they are also involved in the replacement of K-feldspar phenocrysts (Fig. 4.9F) and pinitized cordierite (Fig. 4.9G) starting from the margins of the aforementioned grains to their cores.

II. Type II clots: where the core of the clot is comprised of euhedral to subhedral quartz and biotite grains which are much smaller in size compared to the biotite grains which surround them (Fig. 4.9E).

III. Type III clots: where the biotite and quartz are present as symplectic intergrowths within a K-feldspar host.

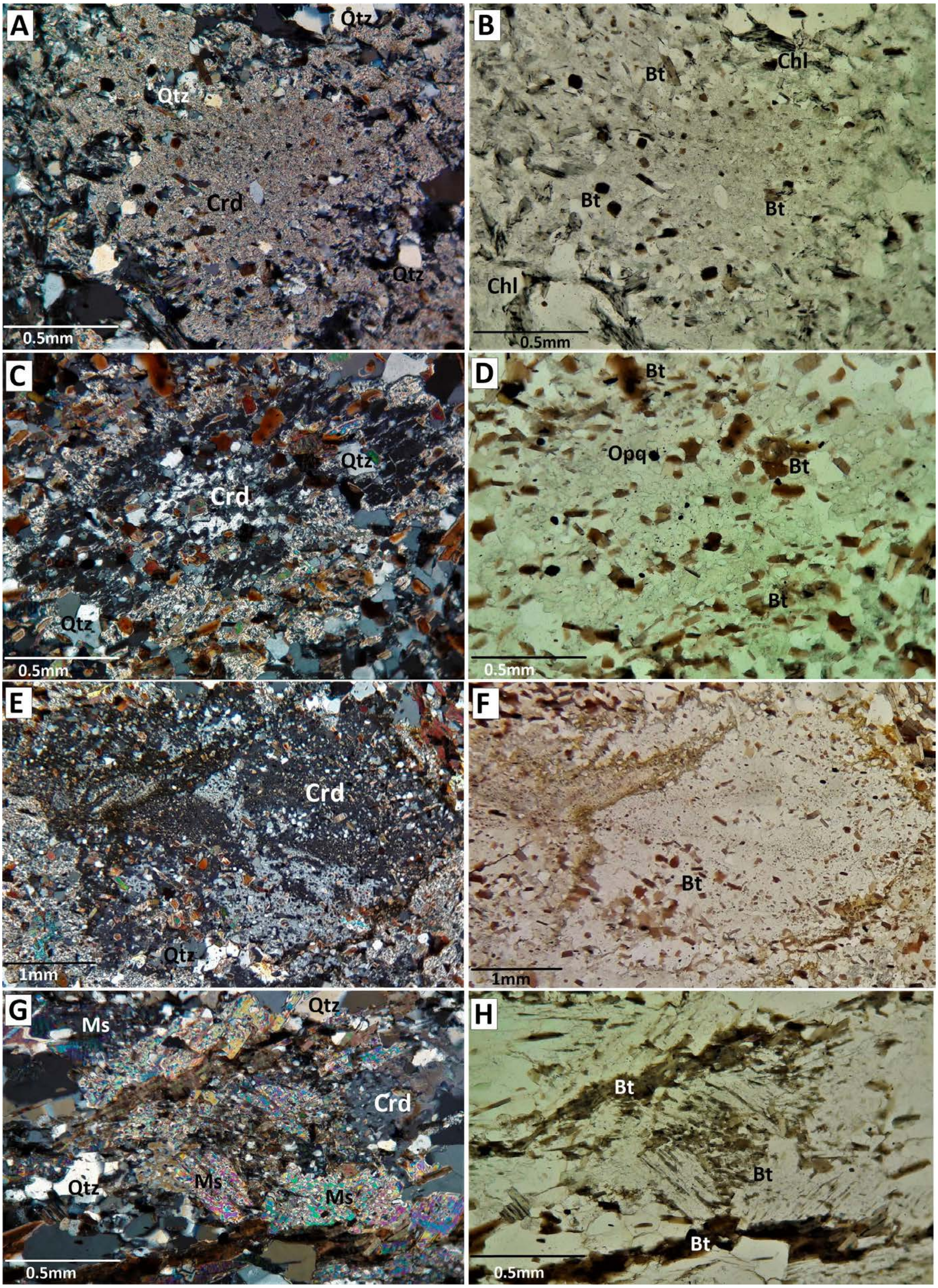

Figure B1*: Thin section photomicrographs, in cross polars and plane-polarized light, of the various types of alteration affecting the cordierite (Crd) grains within the metamudstone samples. (A) & (B) Type I alteration involving the replacement of Crd by fine-grained mats comprising muscovite (Ms), biotite (Bt), sericite and chlorite (Chl). (C) & (D) Type II alteration involving the replacement of Crd by an isotropic material, which, is in turn, mantled or rimmed by constituents involved in Type I alteration. (E) & (F) Sector twinned Crd affected by Type III alteration involving an isotropic material concentrated within the various fractures, fissures, and pathways of the Crd. (G) & (H) Crd grain affected by Type IV alteration involving replacement by fairly coarse-grained crystals of Ms.*

Appendix B3

–The varying sizes of enclaves and their contact relationship with the host porphyritic granite

The small-sized biotite-granite- and granodiorite-enclaves (Fig. 4.13C, D respectively) define fairly sharp contacts with the host granite due to their fine-grained sizes and having K-feldspar inclusions of much smaller size (< 1cm) compared to the host granite (e.g. Fig. 4.13C). Conversely, the larger sized enclave bodies show a relatively diffuse and gradual transition with the host granite and also have K-feldspar inclusion similar in size and texture relative to those in the host granite (Fig. 4.13A, B, E). These observations likely have to do with thermal effects and contrasts between the enclaves and host granites. The smaller enclaves are likely to have quenched to finer-grained solid enclaves in the host magma because small bodies lose heat quickly and so will likely cool rapidly against the larger, more voluminous granite host (Vernon et al., 1988; Wiebe et al., 2002; Paterson et al., 2004). This also serves to explain the sharper contacts they define with the host granite (Fig. 4.13C, D).

In contrast, the larger enclave bodies cooled at a slower rate, allowing for them to thermally equilibrate with the host granitic magma, precluding sharp contacts and retaining fairly coarse sizes in the process (Fig. 4.13A, E). The K-feldspar grains that are included in some of the enclaves (e.g. Fig. 4.13A, B, C, E), are likely to have originated from the host magma and became incorporated/entrained into the magma that later formed the respective enclave bodies (e.g. Elburg, 1996). Because of the quenching effect experienced by the smaller sized enclaves, the entrained K-feldspar grains cooled rapidly and did not get the opportunity to grow big in the enclave before the enclave cooled below the crystallization temperature of K-feldspar. The larger enclaves cool slower and so the entrained Kfs grains have more time and opportunity to grow bigger, hence why the K-feldspars included within them are similar in size and texture to those in the host granite.

Appendix B4

–The formation of magmatic structures

Magmatic structures characterizing the Peninsula Pluton include high concentrations of K-feldspar megacrysts (Fig. 4.15A, B), magmatic layering (Fig. B2), biotite-quartz clots (Figs.4.7B–D, 4.9E–G) and biotite accumulation in schlieren (Fig. 4.15C, D) (Farina et al., 2012). These magmatic structures are interpreted by Farina et al. (2012) as having formed by local flow and melt–crystals separation at a temperature not exceeding 750°C at the emplacement level of highly viscous crystal-rich magmas through magma mushes assembled from older batches.

The magmatic layering in Figure B2 occurs on a vertical surface (with an approximate height and horizontal extent of 7 m and 35 m respectively) within an S-type granite host between the Bantry Bay-Clifton areas (approx. 1.5 kilometres from the Sea Point contact). Other localities where such sheeted structures outcrop is along the coastline of the small town of Llandudno further to the south of the study area (Fig. 2.3B). Such magmatic layering has been covered by Farina et al. (2012) and more extensively by Ramphaka (2013). According to the aforementioned authors, the magmatic layers are formed by the repetition of zoned layers defined by a schlieren-like base (mafic layers) grading to a leucocratic upper part dominated by plagioclase, K-feldspar and quartz (Fig. B2). The difference in bulk rock composition, trace and rare earth elements compositions between the layers and host granite suggests that the layered rocks were not formed by magmas produced by differentiation of the host granite but, instead, each layer represents a separate magma pulse (Ramphaka, 2013). The mafic portions of the layers largely represent an accumulation of the crystals in the magma batch at the time of injection and mostly consist of orthopyroxene and biotite (Ramphaka, 2013).

***Figure B2**: Magmatic layering within an S-type granite outcrop between the Bantry Bay-Clifton areas. The outcrop is characterized by the repetition of zoned layers defined by a schlieren-like base (mafic layers or portions) grading to a leucocratic upper part dominated by plagioclase, K-feldspar and quartz. The traffic sign-post has a height is 2.25m.*

Appendix C

- **Bedding (S_0) and foliation (S_1 and S_2) orientation data**

Table C1*: All measured bedding orientation data from the northern end of the study area.*

S_0 bedding northern end (dip direction/dip) (n=35)			
050/82	070/68	056/78	038/70
058/78	066/66	030/72	026/64
038/72	072/68	028/70	214/70
034/82	074/70	026/74	224/76
042/72	072/74	030/74	224/72
032/80	040/84	028/78	210/78
034/88	036/82	032/70	220/74
050/72	040/90	032/68	218/80
034/70	062/80	042/62	

Table C2*: All measured bedding orientation data from the southern end of the study area.*

S_0 bedding southern end (dip direction/dip) (n=31)			
008/76	012/82	228/84	046/78
018/74	008/78	222/82	230/70
014/78	016/80	224/78	032/78
016/76	034/84	222/80	222/82
002/70	024/72	222/84	218/80
014/88	032/78	234/74	224/84
012/80	024/82	232/76	200/72
014/78	030/88	044/80	

Table C3*: All measured bedding orientation data from the lit-par-lit zone of the study area.*

S_0 bedding lit-par-lit zone (dip direction/dip) (n=13)	
354/72	012/76
358/58	018/60
008/58	008/82
010/78	002/84
354/70	002/86
356/74	016/84
014/62	

Table C4: *All measured S_1 foliation orientation data from the northern end of the study area.*

S_1 foliation northern end (dip direction/dip) (n=62)			
044/10	036/76	232/80	234/84
054/76	036/88	242/70	022/88
044/82	048/82	220/82	010/84
050/90	074/80	206/78	038/82
054/76	076/74	218/70	048/74
070/72	074/78	236/84	032/80
040/80	076/82	240/82	030/78
030/82	080/70	238/86	018/70
050/86	066/86	224/78	016/80
072/82	080/80	218/86	028/88
050/76	086/78	222/78	020/80
054/50	080/70	214/78	014/84
050/78	082/88	228/82	024/84
066/84	080/80	232/84	044/72
060/86	240/78	228/88	
042/70	044/66	064/86	

Table C5: *All measured S_1 foliation orientation data from the lit-par-lit zone of the study area.*

S_1 foliation lit-par-lit zone (dip direction/dip) (n=60)				
348/64	358/68	016/70	022/70	024/82
008/58	354/72	210/80	026/70	034/80
354/70	002/80	020/72	004/88	002/74
004/48	001/78	194/66	004/84	028/86
354/72	006/82	224/84	008/88	
002/80	008/64	232/80	038/84	
001/80	028/64	026/88	036/80	
006/82	340/62	356/84	030/88	
008/64	002/50	190/88	028/86	
340/62	018/66	196/74	032/84	
020/60	004/82	200/70	026/88	
028/64	002/64	194/82	042/86	
004/48	190/74	020/70	040/84	
020/60	186/80	022/74	342/66	

Table C6: *All measured S_1 foliation orientation data from the southern end of the study area.*

S_1 foliation southern end (dip direction/dip) (n=15)	
038/88	042/74
042/80	042/70
028/78	044/86
038/70	238/80
032/80	230/88
044/80	232/78
048/82	234/82
050/60	

Table C7: *All measured S_2 crenulation cleavage orientation data in the study area. Outcrops with an S_2 crenulation cleavage only outcrop in the northern end of the study area.*

S_2 cleavage (dip direction/dip) (n=13)				
322/08	348/12	314/08	310/12	292/16
322/06	320/08	290/20	302/02	
320/10	308/14	300/20	332/08	

Appendix D1

- **K-feldspar lineation data from SPO on two/three mutually perpendicular surfaces at the Sea Point contact outcrop**

Table D1: Measured orientation of K-feldspar grains on three mutually perpendicular surfaces at station SPO 1

Station SPO 1: 3 mutually perpendicular surfaces GPS location: S33°55'23.4" E018°22'39.0" Total no. of readings: 50					
Top surface		**West-facing surface**		**South-facing surface**	
Trend/Plunge	Size (cm): long axis/short-axis	Trend/Plunge	Size (cm): long axis/short-axis	Trend/Plunge	Size (cm): long axis/short-axis
366/18	6/2	294/84	9/4	334/14	5.5/1.5
350/10	4/2	232/40	4.2/2.5	336/18	3.5/1
344/02	2.5/1	312/80	4/2	328/20	4.4/2
344/10	3.7/2.1	222/42	4.5/2.5	338/30	6/5.8
308/10	3/1.1	236/58	2.5/1	326/28	3/1.5
346/10	2/0.8	362/62	4/1.3	210/78	6/2.4
292/06	3.8/2.2	212/24	3.3/1.2	190/80	3.5/1.5
292/04	3.5/1.5	214/16	4/1.4	252/82	3/1
010/12	5.5/2	314/78	4.5/2.5	246/80	2.5/1.5
062/02	3/1.8	216/20	3.5/2	168/22	5.5/2
046/06	4.8/2.2	220/44	4/2.2	176/26	4.2/2
020/10	4/2.5	252/50	4.4/2	170/40	7/2
362/08	2.3/1.8	244/38	2.5/1.2	346/16	4/2
344/10	3/1.2	208/78	4.2/2	316/12	4.5/1.5
012/08	4.5/2.5	238/30	3.5/1.5	270/80	3.2/1
356/10	8/2.2				
358/14	5/2.5				
368/10	3/1				
254/04	3.1/1.6				
310/06	2.8/2				

Table D2: Measured orientation of K-feldspar grains on two mutually perpendicular surfaces at station SPO 2

Station SPO 2: 2 mutually perpendicular surfaces GPS location: S33°55'23.3" E018°22'38.4" Total no. of readings: 32			
Top Surface		**West-facing surface**	
Trend/Plunge	Size (cm): long axis/short-axis	Trend/Plunge	Size (cm): long axis/short-axis
112/04	4.5/1.7	204/14	4/2.8
032/10	2.4/1.8	185/18	5.5/3.5
030/08	3/2	190/24	5.5/3.8
010/12	4.2/2.8	206/64	4/2
026/20	4/1.5	216/22	2/0.5
050/02	5/3	194/42	2/1.5
106/08	4/2	322/20	2.4/1.5
114/12	5.6/2.5	322/80	3.5/2
016/06	2.5/0.3	198/78	3.1/1
022/04	5.2/1.6	354/40	3/1
032/08	4/1.5	362/36	5/2
014/02	2.8/0.4	350/42	3.5/0.8
042/06	5/2.6	210/20	2.5/1.2
018/02	3/0.5		
300/06	5.4/2		
312/20	3.5/1.5		

***Table D3**: Measured orientation of K-feldspar grains on two mutually perpendicular surfaces at station SPO 3*

Station SPO 3: 2 mutually perpendicular surfaces GPS location: S33°55’23.2” E018°22’37.1” Total no. of readings: 30			
Top Surface		**West-facing surface**	
Trend/Plunge	Size (cm): long axis/short-axis	Trend/Plunge	Size (cm): long axis/short-axis
286/04	4/2	158/86	9/3
302/02	4/1.4	328/34	6.1/2.4
210/10	3/1.7	156/90	4/2
212/04	4.4/2.6	098/86	3/1.8
144/18	4/2	346/24	6/2
172/02	7/2.5	080/70	4.5/2
164/06	6/2.4	348/50	3.7/1.5
280/02	3.5/1.7	320/30	5/1.8
224/08	3/1.5	088/60	2.5/1.1
138/04	5.2/2.6	342/60	4.7/2
172/02	4/1.4	150/80	3.5/2
168/08	3/1.3	354/50	4.5/0.6
128/10	4.4/0.8	350/42	6/2.8
268/02	4.5/1.8	060/72	5/2.2
218/04	5.6/2	338/54	5.5/2.6

***Table D4**: Measured orientation of K-feldspar grains on two mutually perpendicular surfaces at station SPO 4*

Station SPO 4: 2 mutually perpendicular surfaces GPS location: S33°55’20.2” E018°22’37.2” Total no. of readings: 50			
Top Surface		**East-facing surface**	
Trend/Plunge	Size (cm): long axis/short-axis	Trend/Plunge	Size (cm): long axis/short-axis
075/10	5.6/2.5	036/10	4.2/2.3
072/04	3.5/2	130/78	3/1.5
082/08	6.5/4.5	290/76	2/1.5
080/16	8/3.8	104/54	4/2.1
080/02	5.5/2.8	214/04	6.5/2.5
090/02	4/2	038/04	5.8/1.3
132/20	3/2.5	056/20	3.5/1.2
114/30	3.2/2.4	312/60	4.5/2.3
068/04	3/2	040/08	5.4/1.6
160/12	3.8/2.2	210/26	7/2.5
086/04	8.5/2	044/20	5/2.5
042/12	3.7/2.5	060/60	7/2.5
150/10	6/2.5	032/60	6/2
338/02	3.5/2	026/30	3.6/1.2
236/10	4.7/2	044/14	4.2/2
240/06	5/2.3	232/30	4/1.5
340/04	4.2/1.9	038/50	6/2.5
010/02	4/1.4	262/20	6.8/1.6
088/12	4/2.5	050/20	3.8/1
210/02	3/2	046/08	5.4/1.6
110/06	6.2/3.4	080/56	4.6/1.4
348/02	5.2/1.8	302/82	6.2/3.6
356/10	4.2/1.6	162/52	3/1.5
124/16	4/1.5	028/80	4.8/2.8
096/02	5/2	120/20	3.6/2.1

***Table D5**: Measured orientation of K-feldspar grains on three mutually perpendicular surfaces at station SPO 5*

Station SPO 5: 3 mutually perpendicular surfaces GPS location: S33°55’20.3” E018°22’37.4” Total no. of readings: 70					
Top surface		**West-facing surface**		**South-facing surface**	
Trend/Plunge	Size (cm): long axis/short-axis	Trend/Plunge	Size (cm): long axis/short-axis	Trend/Plunge	Size (cm): long axis/short-axis
246/12	4/3.2	182/24	3.5/2	108/12	4/2
222/10	3/2.5	170/38	4.5/3.8	266/42	4.8/4
258/10	4.5/3.8	244/78	4.8/2.5	254/90	3.3/1.5
280/10	3/1.6	178/30	8/1.5	098/46	3.4/2
282/04	5/2.5	308/78	5.5/1.8	162/90	4.5/2
256/10	2.7/1.4	326/82	3/1	286/24	3/2
292/04	2.2/1	306/78	9/2	272/80	5/1.8
288/08	2/1	170/14	5.2/3.1	112/12	3.7/2
288/06	4.5/4.2	306/80	6/2.5	100/10	3.4/1
290/10	4/2	326/76	2.5/1	118/14	7/2.5
294/04	4/2.2	334/80	3.5/2	120/10	4.5/2
276/10	2.5/1.8	184/20	3/1	106/26	6.5/1.5
260/08	4.2/3.8	182/40	5/3	302/22	5/2.5
256/12	3/1.7	226/56	4.8/2	142/60	3.9/2.1
248/10	3.3/1.7	278/66	5.4/2.2	288/26	7/5.5
274/28	3.9/2.1	320/68	3.5/2.5	120/28	5/3
312/06	5.5/2.5	176/30	3.2/1	116/22	3/2
268/02	5/3.8	162/18	5/2	102/58	4.7/2
260/10	4/2.5	190/16	3.2/1.5	276/28	3.5/3
208/12	4/2.9	250/44	5.6/2.5	102/08	5/2.5
				124/18	4.5/2.2
				296/78	5/2.2
				100/42	3/1.7
				114/30	5/1.2
				120/36	3/2
				272/34	5/4
				106/32	3.5/2
				114/42	4/3
				278/16	5/2.5
				212/90	6/2.5

***Table D6**: Measured orientation of K-feldspar grains on two mutually perpendicular surfaces at station SPO 6*

Station SPO 6: 2 mutually perpendicular surfaces GPS location: S33°55’20.6” E018°22’37.9” Total no. of readings: 40			
Top Surface		**South-facing surface**	
Trend/Plunge	Size (cm): long axis/short-axis	Trend/Plunge	Size (cm): long axis/short-axis
274/02	4/2	100/18	5.2/2
284/02	3.8/2.6	102/12	3/1
292/04	3/2	120/20	6.5/3.5
094/12	3/2.0	118/78	3/2.4
098/20	5/3	100/14	3.5/1.5
256/04	6.4/2	116/40	2.5/2.3
336/24	2.1/1	104/16	2/1
326/08	3.5/1.4	298/30	3.2/1.2
262/34	7/1.5	118/58	2.5/1.5
270/04	5/2.5	114/40	4.6/2.8
280/10	2.2/2	208/90	3.5/3
036/40	5.2/2	106/22	4/1.8
270/06	5/3.5	181/70	2.4/2
310/08	3.5/1.7	140/48	4/1.5
290/02	1.2/1	110/14	3.5/1
260/04	6/4	106/12	8.5/4
310/06	6.8/2.2	112/60	3/2.5
320/04	4.7/1.8	108/20	2.1/1
318/10	5.4/2.2	280/28	3/1.2
284/14	2/1	284/14	2.5/0.5

***Table D7**: Measured orientation of K-feldspar grains on three mutually perpendicular surfaces at station SPO 7*

Station SPO 7: 3 mutually perpendicular surfaces GPS location: S33°55’20.1” E018°22’37.2” Total no. of readings: 66					
Top surface		**East-facing surface**		**North-facing surface**	
Trend/Plunge	Size (cm): long axis/short-axis	Trend/Plunge	Size (cm): long axis/short-axis	Trend/Plunge	Size (cm): long axis/short-axis
058/10	5.5/3	164/80	5.8/3.4	298/44	3.5/2
078/10	5.3/3.5	032/38	4.5/4.3	324/84	4.5/2.3
308/10	2.8/1.5	062/72	3.4/1.4	322/74	2.5/2
058/06	3.5/1.5	066/40	3.3/0.8	284/18	3.2/2
346/02	2.4/1.2	118/74	3.7/3.5	294/08	4.5/2
300/10	2.6/1.5	032/50	4/1.8	296/42	3.7/2.8
336/10	3/1.4	164/76	7.5/4	106/28	5/2.4
356/02	3/1.5	204/24	7.6/2	012/76	6/4.5
262/04	3.3/2.5	194/40	5/2	078/82	3.7/1
258/04	3.7/1.7	124/88	7.5/1.5	104/20	4.7/1.5
256/14	4.2/3	052/58	3/2.5	292/06	5.2/2.1
312/06	3/1.8	038/40	5/3	096/24	3/2
260/10	3.4/1.5	042/82	4/2.6	098/22	2.5/1.4
274/12	3.1/1.2	156/52	4/1.8	096/24	2.4/2
238/02	3.2/1.3	148/62	2/1.1	092/32	4.3/4
312/08	3.5/2.2	086/80	3/2.2	342/64	3.2/1
286/10	4/2			292/34	5/2
222/14	2.4/1.1			292/20	3.7/1.5
234/06	2.5/1.5			052/64	5/2.3
254/08	3/1.7			100/22	5.5/4.5
				292/44	4/2.4
				308/38	3/2.5
				298/42	5/3
				108/20	4.2/4
				102/20	4/1.5

***Table D8**: Measured orientation of K-feldspar grains on two mutually perpendicular surfaces at station SPO 8*

Station SPO 8: 2 mutually perpendicular surfaces GPS location: S33°55’19.0” E018°22’37.0” Total no. of readings: 45			
Top Surface		**North-facing surface**	
Trend/Plunge	Size (cm): long axis/short-axis	Trend/Plunge	Size (cm): long axis/short-axis
340/06	7/3	304/28	4.7/2.2
358/02	4.9/3	322/48	4.2/2.5
328/04	4/3.5	044/60	4.4/3.8
296/04	4.8/2.3	296/22	7.3/1.5
366/22	4/2	328/44	3.7/2.4
042/10	2/1	342/64	3/2
348/02	2.2/1.3	084/76	4/1
278/10	2.4/1	300/54	5.3/2.8
358/06	3/2.2	348/64	5/1.8
336/02	4/2.5	302/42	5/1.5
352/04	2.7/1.2	306/48	3.7/2.5
058/04	5.2/2.1	308/52	7/5
246/08	3.5/2	362/80	5.5/2
242/08	3.2/2	096/22	2.5/2
356/04	3/1.4	320/52	6/2.8
364/16	3.2/1	362/70	7.5/2.8
352/04	4.7/3	330/62	2.5/1
336/10	2.4/0.8	300/38	4.5/2.8
344/02	2/1	310/50	5.5/2
326/06	6/3.2	352/30	5.3/1.8
234/06	3.4/2		
320/02	2.6/1.2		
318/12	5.4/2.4		
332/08	2.5/1		
294/04	4.5/2		
354/04	5.8/3		

***Table D9**: Measured orientation of K-feldspar grains on two mutually perpendicular surfaces at station SPO* 9

Station SPO 9: 2 mutually perpendicular surfaces GPS location: S33°55'18.5" E018°22'37.5" Total no. of readings: 40			
West-facing surface		**South-facing surface**	
Trend/Plunge	Size (cm): long axis/short-axis	Trend/Plunge	Size (cm): long axis/short-axis
194/20	3.5/2.6	264/18	5/3
196/38	5/3	252/50	4/2.5
202/42	4/2	244/78	7/2.8
196/54	9/3.5	280/42	3/1.8
010/50	3/2	206/72	4.5/2.5
194/36	4.4/1.8	112/20	5/4
224/42	4.5/3	118/40	3.2/2.2
194/22	3.3/2	124/26	3.7/2.5
198/38	3.5/1.8	278/36	4/1.7
276/72	5/3	272/40	5.2/1
024/20	6.2/2.5	284/40	7/2.8
278/88	8.5/3.4	288/30	4.7/1.8
192/54	4.5/2	280/36	3.2/2.5
186/18	7.5/3.5	168/80	3.8/1.5
190/44	4.5/3	114/24	3.5/1
272/90	5/3	258/46	7.3/1.8
352/72	7/2.5	282/52	3/1.5
202/24	2/1.2	274/36	3.2/2
202/16	3.5/2.3	110/30	7.5/3
012/38	4/2	288/50	4.5/2

***Table D10**: Measured orientation of K-feldspar grains on two mutually perpendicular surfaces at station SPO* 10

Station SPO 10: 2 mutually perpendicular surfaces GPS location: S33°55'18.3" E018°22'38.3" Total no. of readings: 50			
Top Surface		**East-facing surface**	
Trend/Plunge	Size (cm): long axis/short-axis	Trend/Plunge	Size (cm): long axis/short-axis
116/12	5.6/2.5	108/10	4.5/3
022/06	3.5/2	018/90	4.2/2.5
292/16	6.5/4.5	112/18	4/2.3
302/10	8/3.8	110/20	6/4.5
290/08	5.5/2.8	012/88	5.6/3.5
298/02	4/2	026/90	3.2/1.5
318/24	3/2.5	106/14	3.5/2.8
286/04	3.2/2.4	112/12	5/2.5
294/02	3/2	104/14	3.1/2.5
010/12	3.8/2.2	114/16	5/3.5
268/14	8.5/2	114/22	5.5/2.2
296/02	3.7/2.5	288/24	5.5/2
294/06	6/2.5	026/82	5.5/1.5
338/04	3.5/2	032/86	4.5/2
060/10	4.7/2	028/80	4.4/1.8
		120/24	9.2/3.2
		110/22	5.8/2
		298/48	4/2.4
		096/74	6.6/2
		084/76	3/2.5
		300/40	8/3
		118/44	4/3
		122/30	4.3/3.2
		110/20	4.3/1.5
		116/20	2.7/1.5
		112/38	6.8/2.5

Station SPO 10: 2 mutually perpendicular surfaces GPS location: S33°55’18.3” E018°22’38.3” Total no. of readings: 50			
Top surface		**East-facing surface**	
Trend/Plunge	Size (cm): long axis/short-axis	Trend/Plunge	Size (cm): long axis/short-axis
		108/36	5/2
		114/50	6/4
		106/16	3.5/1
		026/90	4.5/2.6
		294/22	9.5/3.2
		116/40	7/4
		096/76	5/3.8
		302/28	6.7/1.5
		106/24	7/2.5

***Table D11**: Measured orientation of K-feldspar grains on two mutually perpendicular surfaces at station SPO* 11

Station SPO 11: 2 mutually perpendicular surfaces GPS location: S33°55’18.6” E018°22’38.3” Total no. of readings: 40			
Top surface		**North-facing surface**	
Trend/Plunge	Size (cm): long axis/short-axis	Trend/Plunge	Size (cm): long axis/short-axis
036/36	3.5/3	336/60	5/1
060/18	5.5/2	346/14	4.5/1.2
112/06	8/2.8	350/20	6/2.5
104/04	3/2	090/52	3/2.3
098/10	3/1.5	122/80	6/1.3
088/02	3.8/3	326/42	4.5/1.4
058/10	3.5/1	106/44	3/2
094/02	3.5/3	354/60	3/1
120/06	4/3.5	352/24	3.4/2.4
092/02	6/2	332/36	6.5/2
106/02	3.4/1.6	140/16	3.5/3
138/04	3/1.5	130/50	4.5/2.8
054/02	6/2	120/60	2.5/1.5
072/06	5.3/2.5	326/30	6.5/2.5
088/06	4/2	334/20	5.4/1.6
086/02	4.5/2	310/52	3.6/1.3
053/04	3/1.5	126/78	4/1.5
116/10	6.5/2	120/72	3.8/1
040/06	7/3	340/24	3.7/2.5
116/10	2.8/1.5	314/40	4.7/2

- **Appendix D2: Maps of the Sea Point- Bantry Bay-, Clifton- and Glens beach-Camps bay–areas depicting all the station locations used for SPO analysis and their associated preferred K-feldspar megacryst orientations and resultant magmatic foliation plane from the Kumbe (2017) honours project study**

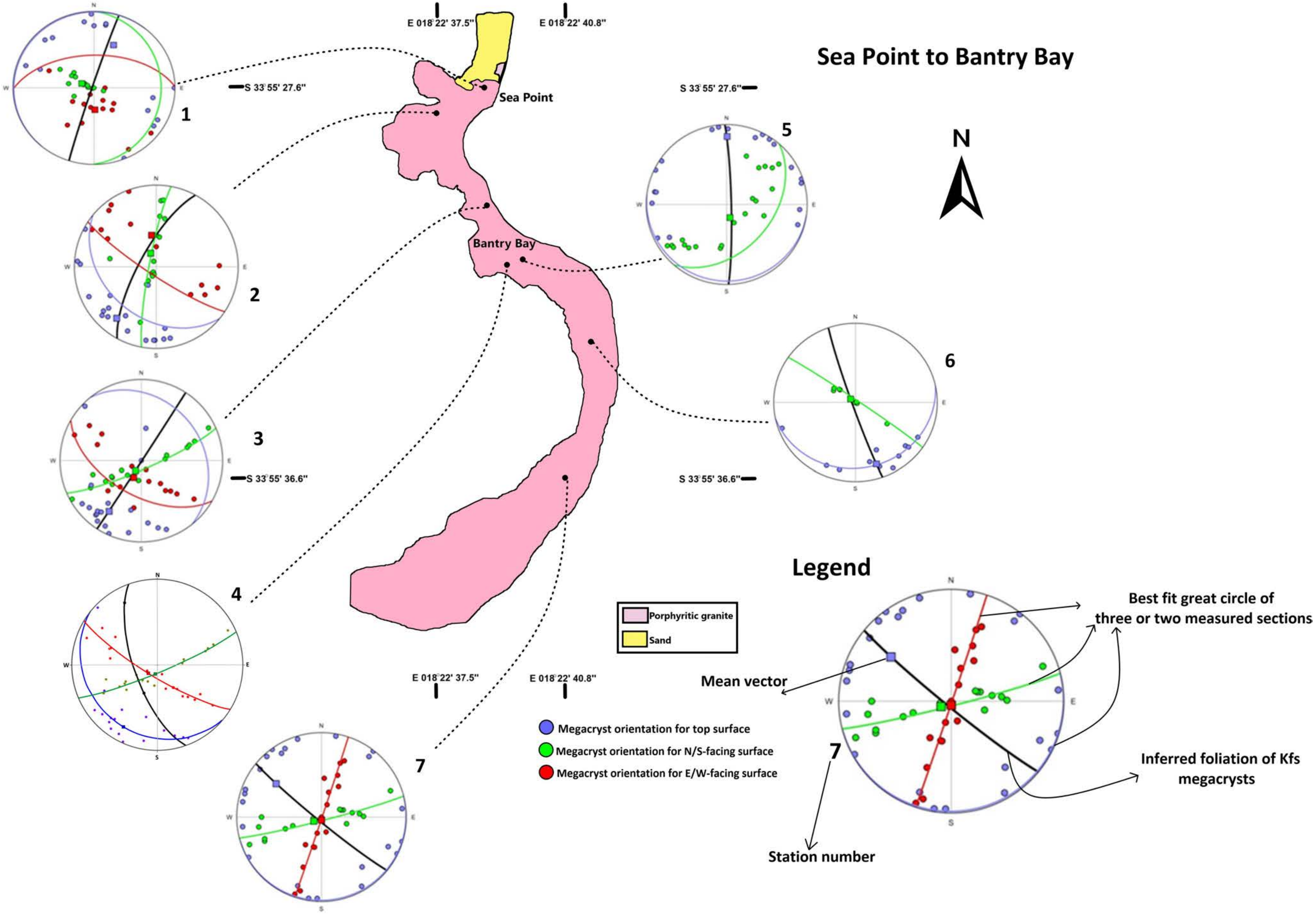

Figure D1: Sea Point-Bantry bay map. Stereoplot legend supplied in the bottom-right of the Figure also applies to Figures D2 and D3. Most of the stations have a Kfs-defined magmatic foliation that trends N-S (station 5) to NNW (NW) - SSE (SW) (stations 4, 6, 7).

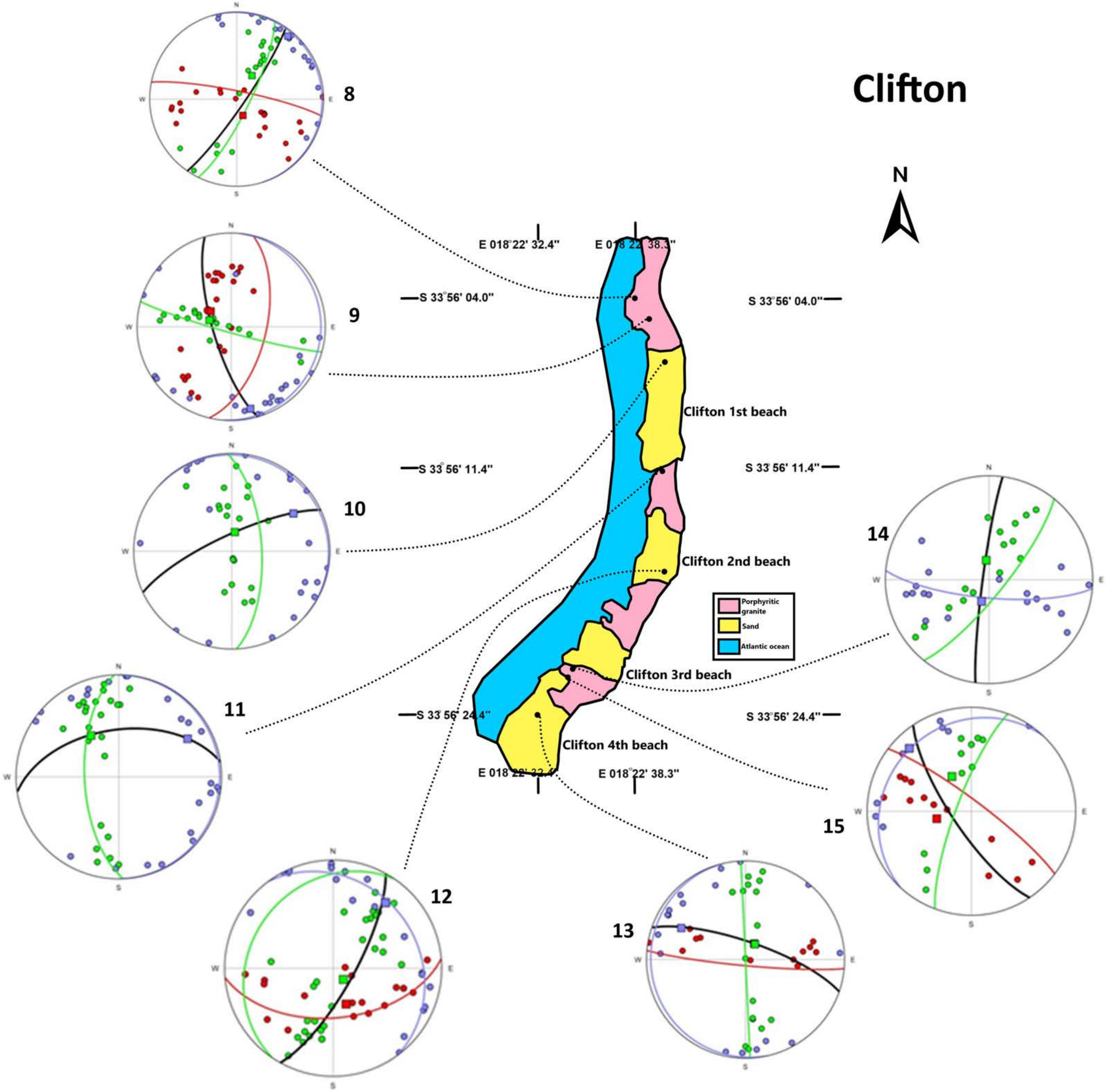

***Figure D2**: Clifton map. Stations 9, 14 and 15 have a Kfs-defined magmatic foliation that trends N-S (station 14) to NNW (NW) - SSE (SW) (stations 9, 15). The stations that show a different orientation to the predominant N-S and NNW-SSE orientation are those that form isolated outcrops on the respective beaches, by and large. These are stations 10 (in Clifton 1st beach), 12 (on the edge of Clifton 2nd beach) and 13 (in the middle of Clifton 4th). The outcrops at these stations could, possibly, not be in situ.*

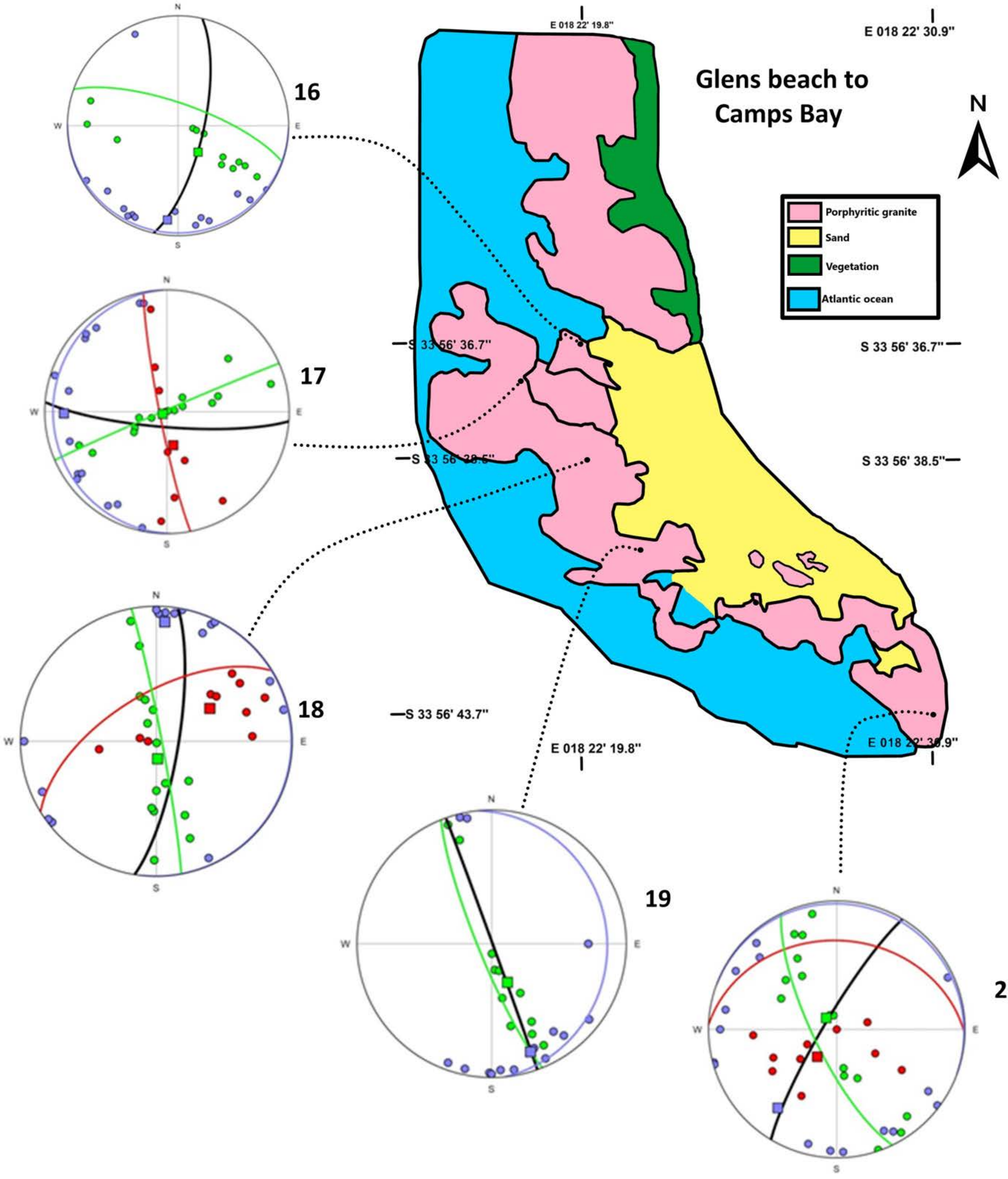

***Figure D3**: Glens beach-Camps Bay map. Most of the stations have a Kfs-defined magmatic foliation that trends N-S (stations 16, 18) to NNW (NW) - SSE (SW) (station 19).*

Appendix E1

- ## Sr and Nd radiogenic isotope geochemistry data from Buggisch et al. (2010) and Frimmel et al. (2013) for the Tygerberg Formation (Malmesbury Group) for comparison with the metasedimentary sample (SP16) of the study area

Table E1*: Sr and Nd radiogenic isotope geochemistry data for sample SP16 and the Tygerberg Fm samples of Buggisch et al. (2010) and Frimmel et al. (2013)*

Sample	**Rock type**	**Rb (ppm)**	**Sr (ppm)**	**Rb/Sr**	**(^{87}Sr/^{86}Sr)$_0$**	**^{87}Rb/^{86}Sr**	**Sr I**	**Sm**	**Nd**	**Sm/Nd**	**^{147}Sm/^{144}Nd**	**(^{143}Nd/^{144}Nd)$_0$**	**Nd I**	**εNd$_{(t)}$**	**T$_{CHUR}$**	**T$_{DM}$**	**Age (Ma)**
SP16 [a]	Metamudstone	297	84.2	3.52	0.802792	9.355237	0.728103	7.53	37.60	0.20	0.12818	0.511985	0.511515	-7.84	1.441	2.071	560
HFS-08-1[b]	Tygerberg greywacke	89	149.9	0.59	0.730980	1.724231	0.730980	5.69	27.70	0.21	0.12422	0.512144	0.511688	-4.45	1.039	1.711	560
HFS-08-5 [b]	Tygerberg siltstone	207	163.9	1.26	0.742371	3.665957	0.742371	8.53	44.50	0.19	0.11591	0.512041	0.511616	-5.87	1.126	1.726	560
HFS-08-6 [b]	Tygerberg siltstone	162	69.5	2.33	0.764461	6.775498	0.764461	4.65	26.00	0.18	0.10815	0.511990	0.511593	-6.31	1.115	1.673	560
HFS-08-7 [b]	Tygerberg siltstone	105	140	0.75	0.727347	2.164475	0.727347	9.31	48.10	0.19	0.11704	0.511987	0.511558	-7.01	1.245	1.831	560
HFS-08-10 [b]	Tygerberg mudstone	171	111.8	1.53	0.750934	4.435150	0.750934	9.60	46.00	0.21	0.12620	0.512006	0.511543	-7.29	1.365	1.988	560
RSA2 [c]	Tygerberg greywacke							6.34	31.36	0.20	0.12210	0.512072	0.511624	-5.71	1.156	1.791	560
RSA5 [c]	Tygerberg siltstone							7.96	43.81	0.18	0.10990	0.511975	0.511572	-6.73	1.163	1.723	560
RSA7 [c]	Tygerberg greywacke							10.05	58.51	0.17	0.10380	0.511951	0.511570	-6.76	1.127	1.661	560
RSA13 [c]	Tygerberg shale							4.94	23.81	0.21	0.12530	0.512010	0.511550	-7.15	1.339	1.961	560
RSA14 [c]	Tygerberg greywacke							6.13	30.15	0.20	0.12290	0.512006	0.511555	-7.06	1.304	1.917	560
RSA15 [c]	Tygerberg greywacke							5.50	27.23	0.20	0.12200	0.512003	0.511555	-7.05	1.294	1.903	560
RSA16 [c]	Tygerberg siltstone							3.98	19.52	0.20	0.12310	0.512001	0.511549	-7.17	1.318	1.929	560

a: Data from study area; **b**: Data from Frimmel et al. (2013); **c**: Data from Buggisch et al. (2010).

Rb-Sr isotope geochemistry data for **b** is not available for comparison.

Appendix E2

- **Harker plots for the granite phases of the study area**

Figure E1 shows a series of bivariate plots, known as Harker diagrams, which use wt. % SiO_2 plotted along the x-axis to illustrate variation with the other selected major (and minor) oxides of the dataset (also in wt. % and plotted along the y-axis).

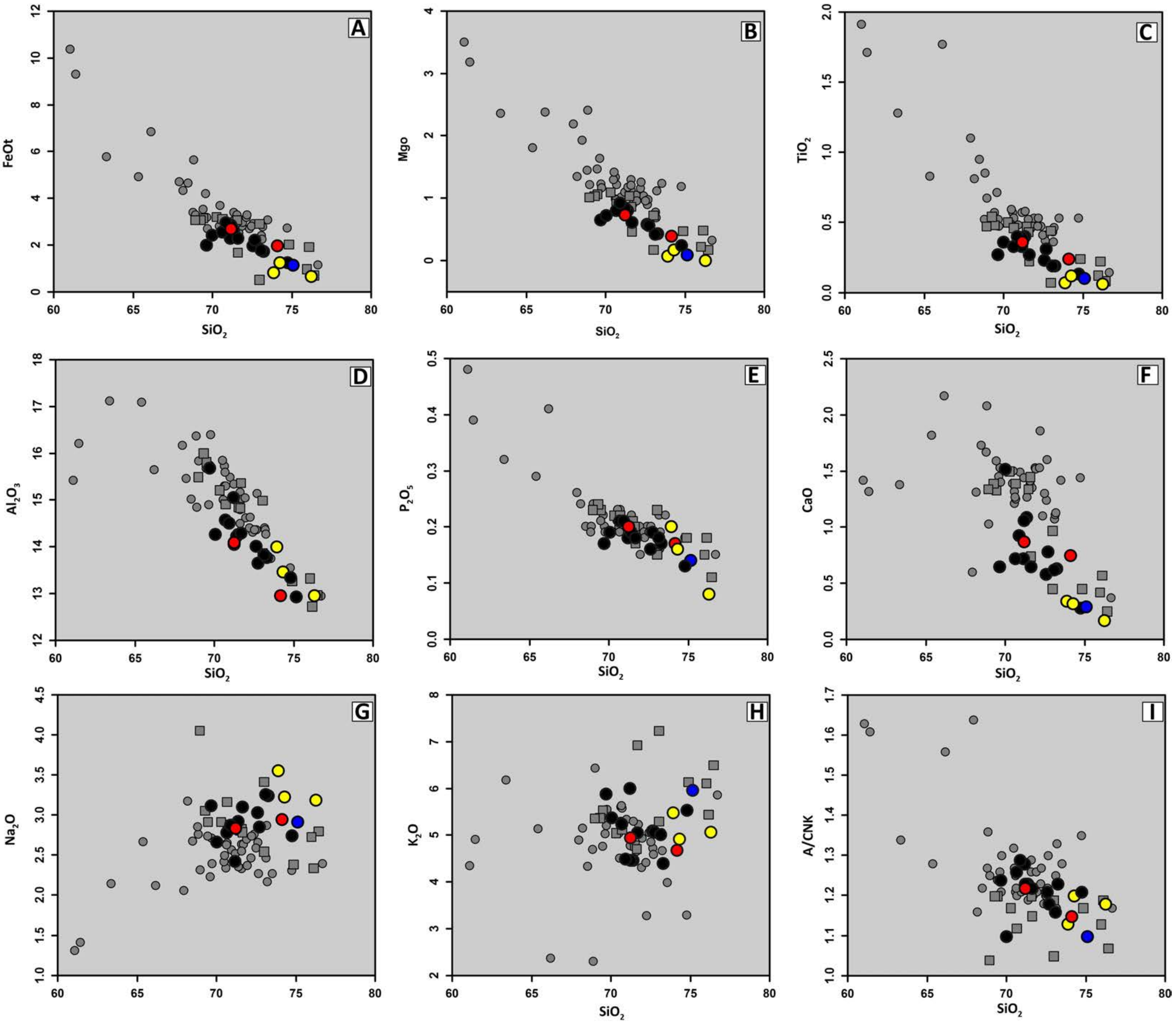

Figure E1*: Major element binary Harker diagrams for the various granite phases of the study area. Black dot: Hybrid granites; red dots: main phase granite; yellow dots: microgranite; blue dots: aplite. Data from Villaros et al. (2009a) (grey dots) and Farina et al. (2012) (grey squares) are shown for reference.*

The granites of the study area show fairly coherent overall trends of decreasing FeO^{tot}, MgO, TiO_2, Al_2O_3, P_2O_5, CaO and A/CNK as a function of increasing SiO_2 content (i.e. negative trends) (Fig. E1A–F, I). The FeO^{tot} (R^2 with SiO_2 = 0.84), MgO (R^2 with SiO_2 = 0.91), TiO_2 (R^2 with SiO_2 = 0.86) and P_2O_5 (R^2 with SiO_2 = 0.88) contents, in particular, display a well-defined linear negative trend or relationship relative to SiO_2 whereas the A/CNK parameter shows more scatter in its trend. In contrast, K_2O and Na_2O (Fig. E1G, H) show a larger scatter in their trend relative to SiO_2 especially for K_2O values, which plot as a cloud of non-coherent data points. Despite the scatter, the trend defined by Na_2O is a weak positive trend (R^2 with SiO_2 = 0.42) relative to increasing SiO_2 content. (Fig. E1G).

Appendix E3

- **REE and spider plots comparing the leucogranites (microgranites and aplite) with average leucocratic compositions of the Peninsula Pluton from Farina et al. (2012)**

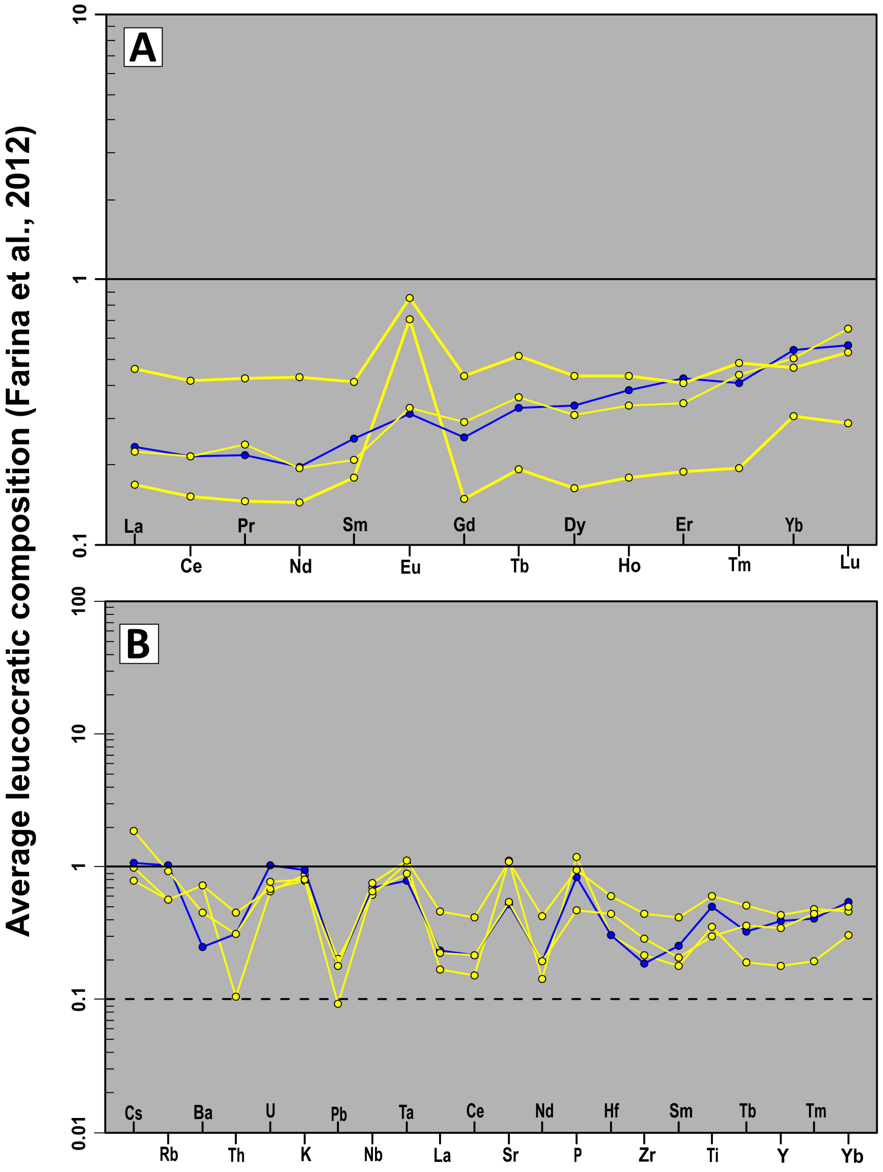

***Figure E2**: Rare earth element (A) and multi-element spider (B) plots for the leucogranites (microgranites, shown in yellow, and aplite, shown in blue) of the study area. (A) and (B) are normalized to the average leucocratic compositions of the Peninsula Pluton From Farina et al. (2012).*